Measurement of the effective diffusivity of gasoline compounds in coated monoliths and associated factors

Kim, Sungsoo

Award date:
2001

Awarding institution:
University of Bath

MEASUREMENT OF THE EFFECTIVE DIFFUSIVITY OF GASOLINE COMPOUNDS IN COATED MONOLITHS AND ASSOCIATED FACTORS

Submitted by

Sungsoo KIM

For the degree of PhD of the University of Bath, 2001

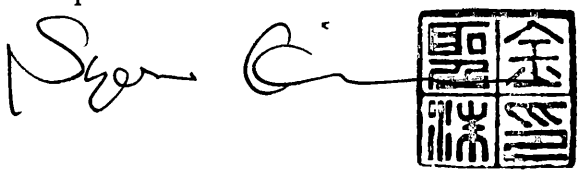

ProQuest LLC
789 East Eisenhower Parkway
P.O. Box 1346
Ann Arbor, MI 48106-1346

Abstract

The multichannel monolith is used as a catalyst support in a wide range of catalytic combustion applications. The walls of the channels are often coated with a very thin layer (10-50μm) of high surface area material (*e.g.* γ-Al_2O_3), in which the catalyst is dispersed.

In order to measure the effective diffusivity, D_e, of CH_4 and C_5 - C_8 *n*-paraffins in the catalytic layer, a section of cordierite (0.25 mm thick) was cut from a monolith, then coated and sealed in a Wicke-Kallenbach type of diffusion cell. The washcoat (1.5 μm to 10 μm) was formed by a sol-gel technique from an alumina suspension.

For the uncoated cordierite, when the experimental results were compared with the use of the parallel pore model and the random pore model, it was found that the predicted values of D_e were very much greater than experimental values. In order to obtain a good match, it was necessary to apply a model in which tortuosity factors could be inserted. Values of tortuosity ranged from 5.1 for methane to 17.5 for *n*-octane.

For the washcoated cordierite plate, in a variety of preliminary screening studies, the effects of doping with zirconia, addition of drying agent and catalyst, influence of calcination temperature and the number of coating were studied. In experiments with *n*-hexane, *n*-heptane and *n*-octane, it was shown that D_e decreases with an increase in the weight and hence thickness of washcoat loadings. Above a washcoat loading of 0.0012 g/cm^2 (corresponded to 1.5 μm), the decrease was linear with loading. The resistance in the interfacial layer can be significant at low washcoat thickness.

In a binary composite layer of washcoat and cordierite support, it was shown that higher values of D_e are obtained, if the hydrocarbon stream is on the cordierite side.

Finally, the diffusion of a mixture of hydrocarbons was briefly studied. These multicomponent diffusion experiments show that the D_e values of each diffusing species in a multicomponent diffusion system are close to the values obtained from binary diffusion experiments.

Acknowledgements

It is a great pleasure to have a chance to acknowledge those who were contributing to my PhD in many different ways. The first and the most thank goes to my supervisor, Professor Stan Kolaczkowski, for his advice and guidance throughout my study. I express my gratitude to all the friends and colleagues for their friendship and valuable discussion, who I have met during my stay in the UK. What I can do now is to list their names here: Mr Richard Hitchman, Dr Martijn Bezemer, Dr Frank Lipnizki, Dr Alexei Lapkin, Dr Viatcheslav Freger, Mr Gareth Williams, Dr Serpil Awdry, Korean friends and many more. Also I would like to thank to Mr Hugh Parrott for his help in electron microscopy and Mr Barry Chapman for XRD.

Finally, many thanks must go to my parent and also my brother and two sisters for their encouragement and support.

Sungsoo Kim, December 2000

Table of Contents

List of Figures

List of Tables

Nomenclature

A	= Cross-sectional area of a sample plate,	[cm^2 or mm^2]
C_0	= Tracer concentration in upper chamber of the diffusion cell	[mol/cm^3]
C_1	= Tracer concentration in upper chamber of the diffusion cell,	[mol/cm^3]
C_A	= Concentration of diffusing species A of the diffusion cell	[mol/cm^3]
C_p	= Intraphase tracer concentration,	[mol/cm^3]
D_0	= True diffusion coefficient defined in Equation (3.12),	[cm^2/s]
D_a	= Macro diffusion coefficient,	[cm^2/s]
D_{AB}	= Molecular diffusion coefficient,	[cm^2/s]
$D_{AB,eff}$	= Effective molecular diffusion coefficient,	[cm^2/s]
D_e or D_{eff}	= Effective diffusion coefficient,	[cm^2/s]
$D_{e,cord}$	= Effective diffusivity in cordierite substrate	[cm^2/s]
$D_{e,overall}$	= Overall effective diffusivity	[cm^2/s]
$D_{e,washcoat}$	= Effective diffusivity in washcoat	[cm^2/s]
D_i	= Micro diffusion coefficient,	[cm^2/s]
D_{KA}	= Knudsen diffusion coefficient of species A,	[cm^2/s]
$D_{KA,a}$	= Macro Knudsen diffusion coefficient,	[cm^2/s]
$D_{KA,i}$	= Micro Knudsen diffusion coefficient,	[cm^2/s]
d_p	= Average pore diameter,	[cm or m]
D_T	= Transition diffusion coefficient (=$(1/D_{KA} + 1/D_{KA})^{-1}$)	[cm^2/s]
F, v	= Volume flowrate over faces of the sample plate in diffusion cell,	[cm^3/s]
J_A	= Molar flux of species A	[$mol/(cm^2.s)$]
J_i	= Molar flux of species i	[$mol/(cm^2.s)$]
j_v	= Molar average velocity of the entire phase or the amount of convection,	[cm/s]
k	= External mass transfer coefficients,	[cm/s]
L	= Length of a pellet or thickness of a plate,	[cm]
l_1, l_3	= Thickness of washcoat layer	[cm]
l_2	= Thickness of substrate	[cm]
$l_{overall}$	= Total thickness	[cm]
M	$= \frac{A}{F_2}(\frac{\varepsilon}{D_e})^{\frac{1}{2}}$ defined in Equation (3.1)	
M_A	= Molecular weight of species A,	[g/mol]
M_{AB}	= $2[(1/M_A) + (1/M_B)]^{-1}$ defined in Equation (2.2)	
n	= Avogadro's number (= 6.02×10^{23})	
N	$= L(\frac{\varepsilon}{D_e})^{\frac{1}{2}}$ defined in Equation (3.1)	

N_A	= Molar flux of species A	[mol/(cm^2.s)]
N_{AS}	= Superficial molar flux,	[mol/(cm^2.s)]
N_B	= Molar flux of species B	[mol/(cm^2.s)]
P	= Pressure,	[bar]
p	= Vapour pressure over the meniscus in the capillary,	[bar]
p^o	= Saturation pressure,	[bar]
q	= Ratio of the average pore length to the thickness of the slab,	[dimensionless]
r	= Average pore radius,	[m or cm]
R	= Gas constant (= 8.314 J / mol·K)	
r_a	= Macropore radius,	[m or cm]
r_i	= Micropore radius,	[m or cm]
r_k, r_m	= Radius of capillary,	[m]
S	= BET surface area,	[m^2/g]
T	= Temperature,	[K or °C]
t	= Time,	[s]
u	= Average velocity,	[m/s or cm/s]
v	= Volume flowrate over faces of the sample plate in diffusion cell,	[cm^3/s]
V	= Volume of chambers in diffusion cell,	[cm^3]
V_g	= Pore volume of a solid	[cm^3/g]
V_L	= Liquid molar volume,	[cm^3/mol or m^3/mol]
x, z	= Axial co-ordinate in diffusion cell,	[cm or m]
x_i	= value of sample i	
$\bar{x}$	= Arithmetic mean of a sample	
y_A	= Mole fraction of component A,	[dimensionless]
Z	= Wall collision frequency per unit area in stationary gas,	

Greek letters

α	= Ratio of fluxes, $N_A/N_B = -(M_A/M_B)^{1/2}$	
γ_n	= The real part of the Laplace transform function,	
δ_n	= The imaginary part of the Laplace transform function,	
ΔC_i	= Concentration difference of component *i* across the plate	[mol/cm^3]
ΔP	= Pressure gradient across the porous solid	[mbar]
Δx	= Thickness of the plate	[cm]
E	= Effectiveness factor	
ε	= Total porosity,	[dimensionless]
ε_a, ε_M	= Macroporosity,	[dimensionless]
ε_i	= Microporosity,	[dimensionless]

ζ	= Half time required for tailing to vanish,	
η	= Coefficient of viscosity,	[pa·s]
θ	= The angle of contact angle between an adsorbent and the wall of capillary	
θ_{Hg}	= Contact angle of mercury (= 130°).	
κ	= Geometrical constant (=$1/\tau$)	
λ	= Mean free path,	[m]
σ	= Surface tension of adsorptive,	[mN/m]
μ	= Mean	[dimensionless]
σ_{AB}	= Characteristic length,	[Å]
σ_{Hg}	= Surface tension of mercury (= 0.485 N/m),	
σ_{N2}	= Surface tension of liquid nitrogen, 8.72 mN/m	
ρ	= Gas density,	[kg/m^3]
ρ_p	= Apparent (bulk) density of a solid	[g/cm^3]
τ	= Tortuosity factor,	[dimensionless]
χ	$= \frac{j_v\, l}{D} = \frac{\omega\ \Delta P\, l}{D}$ defined in Equation (3.19)	
ω	= Permeability,	[mol/(cm^2.s.bar)]
Ω_D	= Diffusion collision integral,	[dimensionless]

Subscripts

0	= of coordinate $x=0$ or $z=0$
1, 2	= at the upper chamber and the lower chamber, respectively
i, A, B	= with respect to chemical species *i, A, B,* respectively
j	= of capillary segment *j*
L	= of coordinate $x=L$ or $z=L$
S	= of catalyst external surface

Abbreviation

BET	: Brunauer-Emmerit-Teller
BJH	: Barret-Joyner-Halenda
DCCA	: Drying control chemical additive
DIC	: Differential interference contrast
EDS	: Energy-dispersive spectrometry
FID	: Flame ionisation detector
HSG	: High speed generator
J-S	: Johnson-Stewart model

LAB2 or Lab2: Alumina sol prepared from aluminium *i*-propoxide

LAB3 or Lab3: Alumina sol prepared from aluminium *s*-butoxide

SCR : Selective catalytic reduction

SEM : Scanning electron microscopy

TCD : Thermal conductivity detector

TEM : Transmission electron microscopy

W-K : Wicke-Kallenbach

W-S : Wakao-Smith model

XRD : X-ray diffraction

Chapter 1. Introduction

Background to the project

Catalytic combustion

The use of a heterogeneous catalyst on a monolith support to facilitate the combustion of gaseous hydrocarbons and carbon monoxide (CO) is well known. Clear advantages can be gained which include the reduction in emissions of environmental pollutants, such as hydrocarbons, CO, NO_x, particulates.

The catalytic converter as a gas clean-up device to control emissions from a vehicle is well established. However, the use of catalytic combustion in primary combustion applications is less well known. The background to the development of catalytic combustion and potential applications are described in a textbook by Hayes and Kolaczkowski (1997).

Application of catalytic combustion in a gas turbine

From a number of recent review articles (*e.g.* Trimm, 1983; Touchton, 1983; Kolaczkowski, 1995; Dalla Betta, 1997; Beebe, 2000), it is clear that there is increasing interest in the use of catalytic combustors in stationary gas turbines for power generation. According to McCatrty *et al.* (1999), the commercialisation of catalytic (gasoline) turbo-generators (~50kW) and catalytic (natural gas) small (1-5 MW) gas turbine engines is an important goal.

This work has evolved as a result of a particular interest at the University of Bath, to develop a catalytic gas turbine system for transport applications (alternative engine for land vehicle, like a van). Trials of conventional gas turbine powered vehicles were done in the early 1970s (*e.g.* Anderson, 1979; Sjöblom and Rehn, 1997). However, the use of catalytic combustor in a gas turbine for an automobile engine has not yet been thoroughly tried even though the concept may offer many advantages, such as reduction of pollutants and improvement in fuel economy.

The use of petrol as a fuel is of interest to this work, as the infrastructure to supply this liquid fuel to support transport applications is already in place.

Operating temperatures for a catalytic gas turbine combustor

In selecting catalysts for the gas turbine engine applications, one of the important features of the catalyst is the range of temperatures over which it can operate. In general, there is an optimum temperature range at which catalytic reactions will occur and these are normally catalyst-specific. As a gas turbine engine operates over a wide range of operating temperatures, an appropriate catalyst system will be needed. However, there is no known catalyst which has an acceptable level of activity across the entire range of operating temperatures in a gas turbine combustion chamber (Kolaczkowski *et al.*, 1999). There are two main causes of catalyst deactivation during combustion. Firstly, it may be caused by the deactivation of the active catalyst. For example, at elevated temperatures above 800 °C, palladium oxide decomposes to metallic palladium as results of oxidation reaction, the latter being relatively inactive for the catalytic combustion of methane (*e.g.* Ferrauto *et al.*, 1990). Secondly, it may be due to a change in the pore structure of the catalyst support. For example, γ-alumina experiences a phase changes to α-alumina at 900 °C and loses its surface area from *ca* 300 m^2/g to *ca* 5 m^2/g. Because of the phase change, the closure of the opening of the pore and/or blocking of the pore occurs and hence the active catalyst is buried in the support and hence cannot be accessed.

When exposed to high temperatures, the catalyst coated layer may start to peel off during use, lowering the performance of the catalyst. Adhesion may be improved by the use of an inorganic binder. However, this may also decrease the surface area of the washcoat; it may cover the catalyst surface, and it may react with the catalyst, thereby decreasing the performance of the system (*e.g.* Agrafiotis & Tsetsekou, 2000).

There are a number of methods that could be used to coat the surface of a monolith with a washcoat to act as a high surface area support for the catalyst. In order to explore the influence of this process, the use of alumina and the sol-gel technique as a method of preparing the washcoat to act as a catalyst support are explored. This method has many advantages over other techniques, in particular, its relatively high thermal resistance and its superior adhesion to the substrate. However, there is lack of data in the literature on the method and its application onto a catalyst support. Also, in many of the studies on catalyst coated monoliths reported in the literature, experiments have been prepared on samples of monolith prepared by a catalyst supplier. The method of coating has not

been a factor that has been varied in these studies.

Intraphase diffusion

Since the appearance of the classical work of Thiele (1939), it has been recognised that intraphase mass transfer resistance in porous catalyst structures can affect the rate of reaction under certain circumstances. In a catalytic monolith, catalytic active sites are distributed throughout the porous support (*e.g.* γ-alumina). Pore diffusion has an important role in the global rate of reaction. This is known as intraphase diffusion resistance, and the importance of the diffusion effect is represented by the effectiveness factor (*e.g.* Levenspiel, 1972):

$$Effectiveness\ \ factor\ (E) = \frac{reaction\ rate\ affected\ by\ intraphase\ diffusion}{reaction\ rate\ unaffected\ by\ intraphase\ diffusion}.$$

For an isothermal catalyst layer, the magnitude of the effectiveness factor generally lies between zero and unity. Therefore, neglecting diffusional resistance can lead to an overestimation of the performance of the reactor.

In a monolith catalytic system, the mass transfer can be divided into two parts: external mass transfer from the bulk into the channel wall, and the internal mass transfer in the catalytic washcoat layer. The importance of the diffusional resistance of the catalytic layer has often been neglected due to its thinness (*e.g.* Hegedus, 1975; Lee & Aris, 1977; Bennett *et al.*, 1992). However, Zygourakis & Lee (1983) and Hayes & Kolaczkowski (1994) investigated the problem of reactions and diffusion in the catalytic washcoat of monolith reactors. Zygourakis & Lee (1983) demonstrated by numerical analysis that the thin catalytic washcoats of the commercial monoliths would present significant diffusional resistance even at moderately high temperatures. Hayes & Kolaczkowski (1994) reported that effectiveness factors for the oxidation of carbon monoxide at temperatures above 800 K were well below unity in a washcoat, which was 10 μm thick at the centre of the channel and 150 μm thick at the corners. Because of the nature of the coating process, the thickness of the washcoat varied from the side to the corners in the monolith cells. In square monolith channels, the washcoat tends to accumulate on the corners, giving them a round appearance. Leung, *et al.* (1996) presented numerical solutions of diffusion/reaction in the washcoat of a catalytic monolith reactor for the CO oxidation and demonstrated that the rate of reaction may be strongly influenced by the diffusion limitation at temperatures at which such a reactor

can operate.

The mass transfer in porous catalyst is commonly described by an effective diffusivity (D_e). The theoretical prediction of effective diffusivity has been an important issue in heterogeneous catalysis for a number of decades and a lot of theoretical models (*e.g.* parallel pore model, random pore model) have been reported. However, depending on the model used, the predicted effective diffusivity could deviate from a measured value by up to a factor of two and in some cases, by several orders of magnitude (Haynes, 1988). Thus, when selecting a theoretical model for a particular catalyst structure, it is important to perform some experimental measurements to check the validity of the model used. In the case of catalytic monoliths, diffusion in the catalyst washcoat is likely to be important, as effectiveness factors can become quite low (less than 0.1) (Hayes & Kolaczkowski, 1994). Therefore, a correct D_e value is required to calculate a correct rate expression.

Aim of the study

Having introduced the interest in the use of gasoline as a liquid fuel in a catalytic combustor on a small gas turbine, the following three aspects were selected for further study in order to progress the understanding of the appropriateness of a particular model and to advance knowledge of the influence of the method of coating:

- The investigation of the use of the sol-gel method to washcoat a monolith.
- The development of an experimental method to determine the effective diffusivity of a component in the washcoat of a monolith.
- The measurement of the diffusion of gasoline-based species in the washcoat on a monolith support.

Structure of the thesis

In Chapter 2, a brief review is provided to illustrate how catalytic combustion could be utilised in a gas turbine for transport applications. This includes a description of diffusion limitations, models for the prediction of effective diffusivity and measurement

methods. In order to progress with the work, it was necessary to have samples of coated monolith. To be able to vary the properties of the washcoat, it was decided to prepare these samples in the laboratory using a sol-gel method.

In Chapter 3, the design of the experimental apparatus and the development of a procedure for the measurement of effective diffusivity in a coated monolith support are described. The method is based on the well-established Wicke and Kallenbach type of cell (*e.g.* Smith, 1956), but it had to be modified for experiments on a thin layer of catalyst support and to enable measurement to be made at elevated temperatures.

In Chapter 4, the preparation of the alumina washcoat by the sol-gel method is described and the methods used to characterise the samples are explained. The results of a number of key parameters that affect the properties of the alumina washcoat are also presented, *e.g.* change in pore structure as a result of calcination temperature, cracking, doping with zirconia, addition of active catalyst.

In Chapter 5, experimental results are presented and discussed. Diffusion measurements in both uncoated cordierite substrate and washcoated substrate are reported.

In Chapter 6, conclusions and recommendations for further works are provided.

A simplified diagram of the work done in this thesis and their relationship to the future work is presented in Figure 1.1 and the links between the events in this thesis are illustrated in Figure 1.2

	Work described in this thesis	Future work
Chapter 2	• Introduction to catalytic combustion and intraphase diffusion • Experimental measurement of effective diffusivity • Sol-gel method	

Chapter 3	• Experimental set-up of Wicke-Kallenbach method
	  • Development of the method of mounting samples into diffusion cell
	  • Feasibility test of the method of both steady-state measurement and transient measurement
	  • Investigating the optimum operating conditions	

Chapter 4	• Preparation of washcoated specimen by the sol-gel method
	  • Washcoating on monolith support
	  • Washcoating on a plate
	• Parameters influenced the physical properties of washcoat
	  • Use of different drying methods
	  • Use of doped zirconia
	  • Addition of catalysts (Pt) into the washcoat	

Chapter 5	• Measurement of effective diffusivity in uncoated cordierite substrate
	  • Effective diffusivity of C5-C8 paraffins
	  • Comparison with the models
	• Measurement of effective diffusivity in the alumina washcoat
	  • Effect of concentration gradient on effective diffusivity
	  • Effect of alumina loading on effective diffusivity
	  • Effect of direction of flux in composite binary structure on effective diffusivity
	  • Effect of calcination temperature on effective diffusivity
	  • Multicomponent diffusion
		• Investigation of the effect of adsorption on effective diffusivity - Sorption experiment using gravimetric methods
		• Further investigation of multicomponent diffusion

Figure 1.1. Simplified structure of thesis.

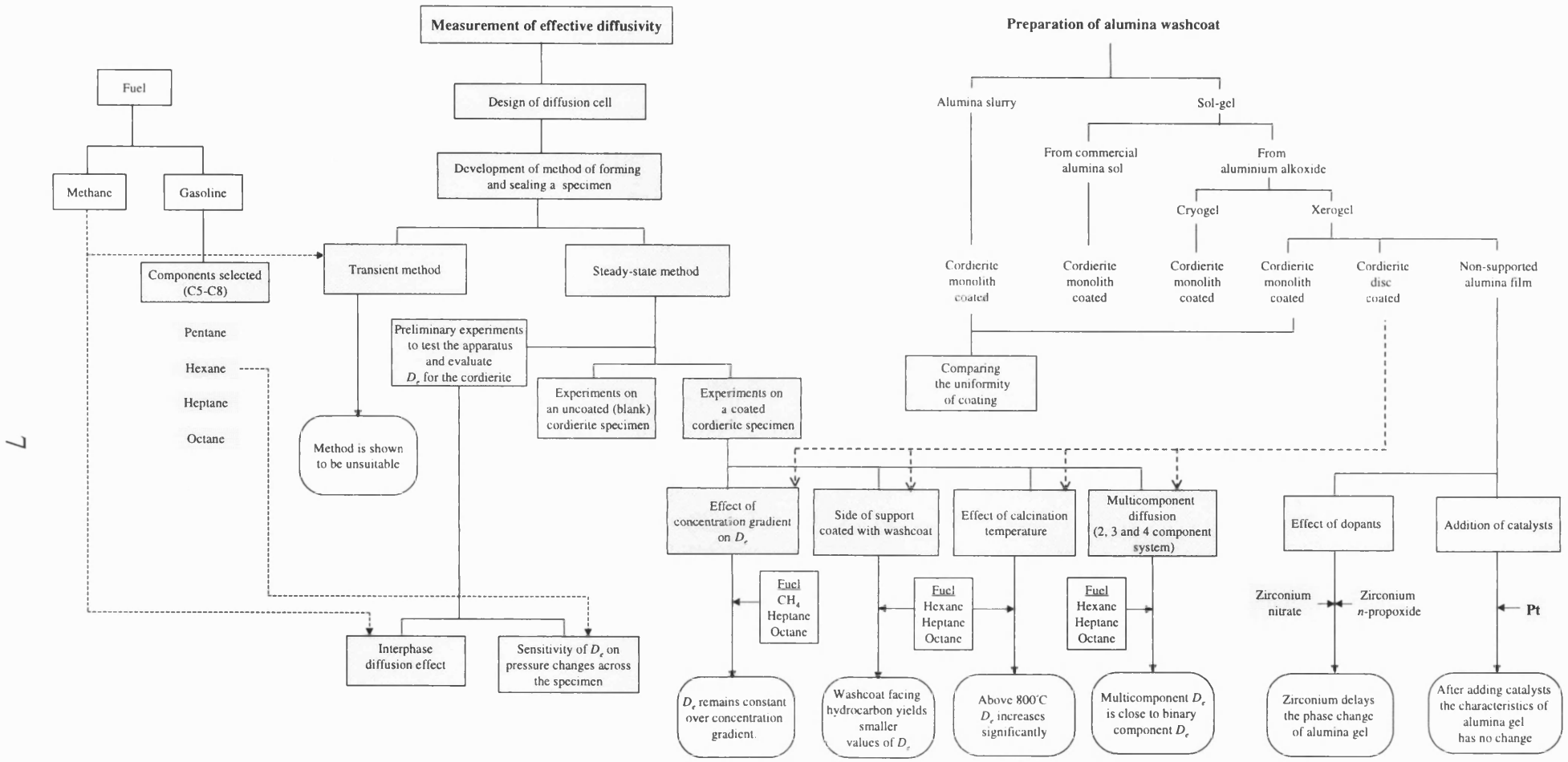

Figure 1.2. Schematic illustrating the link between events in this thesis

Chapter 2. Literature Review

Introduction

There are three main different types of applications where gas turbine technology could be used: (1) aircraft gas turbines, (2) stationary gas turbines and (3) ground-based transport (*e.g.* automobile) gas turbines. Gas turbines have been successfully exploited in aircraft and power generation industries, but their application in ground-based transport is still questionable although this has been studied since 1970. This is due to the complexity of operating conditions, particularly, transient conditions. The work in this thesis supports early development of a catalytic combustor for a gas turbine engine to power a small van.

2.1 Gas turbine engine for transport applications

In the automotive industry, the possibility of using a gas turbine as an alternative engine to the internal combustion engine has been considered. The reasons for seeking an alternative in the 1960s and 1970s were not to improve vehicle power and comfort, but the need to achieve lower exhaust emission levels and higher fuel economy took precedence as time went on (Sjöblom and Rehn, 1997). Although minimum emission levels remain the main priority to date, optimum fuel economy, comfort, driving performance and handling are still the prime considerations.

According to Sjöblom and Rehn (1997), a gas turbine can be manufactured at about the same cost as a piston engine and can be produced at the same volume. Although it contains a higher proportion of expensive materials, the gas turbine is relatively simple in its design with fewer parts.

An example of a gas turbine, which could be used to provide power in a car, through a conventional manual or automatic gearbox, employs two shafts, see Figure 2.1. This arrangement affords an excellent torque characteristic and enhances driving performance. However, since typical shaft speeds range from 50,000 to 100,000 rpm, reduction gearing is necessary when using a conventional transmission (Hartley, 1978).

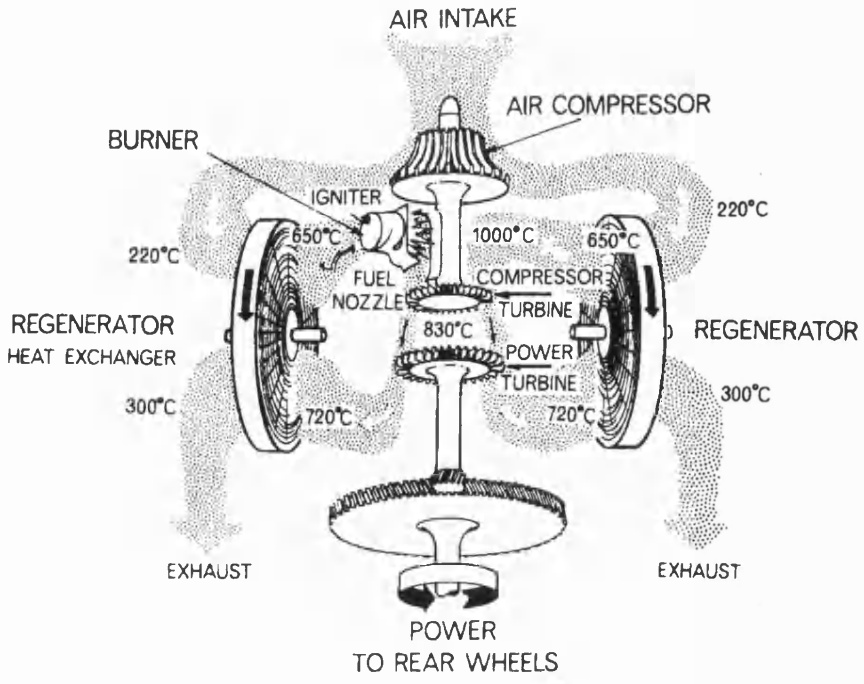

Figure 2.1. Basic layout of automotive gas turbine engine (adapted from Hartley, 1978).

Instead of transferring the power directly to the wheels, Volvo has considered the use of a high-speed generator (HSG) and an efficient electric motor, see Figure 2.2.

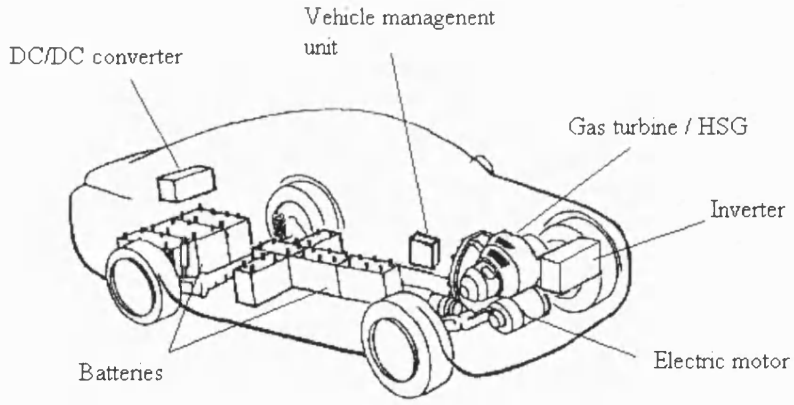

Figure 2.2. Main components in a Volvo environment concept car (adapted from Sjöblom and Rehn, 1997).

Automotive catalytic gas turbine

In a conventional combustion process, the formation of oxides of nitrogen (NO_x) is one of the major concerns. This could be reduced by a variety of methods (*e.g.* Gupta & Lilly, 1992; Dharmadhikari, 1989), for example:

- Adjusting fuel to air ratio.
- Decreasing residence time of gases in the combustor.
- Modifying combustor configuration.
- Applying staged combustion.
- Controlling the extent of combustion zone cooling by injection of water or steam.
- Exhaust gas clean-up.

However, these add to the cost and require complex control schemes. Increasing awareness of the problems caused by air pollution and the decrease in fossil fuel reserves, has resulted in great interest in combustion techniques that reduce pollutant emission levels from combustors, particularly, if an increase in combustion efficiency can be achieved.

The development of a catalytic combustor for an automobile has four primary objectives. Firstly, it has to attain levels of NO_x emissions substantially below those possible in a conventional combustor, secondly, to burn a liquid fuel like gasoline that is readily available, thirdly, to sustain stable combustion over a wide range of low concentrations of fuel in air, and finally to reduce emissions of particulates.

In reviewing the literature, it is clear that a considerable amount of effort has been devoted to the development of catalytic combustors for large gas turbines for stationary power generation. Very little has been published on small turbines (50-200 kW) for transport applications. A review of research on catalytic combustions for stationary applications is available in the literature (*e.g.* Trimm, 1983; Touchton, 1983; Kolaczkowski, 1995; Dalla Betta, 1997; Beebe, 2000). Although many application studies of this concept to gas turbine combustors have been carried out since having been proposed by Pfefferle *et al.* (1987), its commercialisation has been hindered by the difficulty of designing a viable system to cope with varying power loads (Kolaczkowski, 1995).

As an example, Figure 2.3 illustrates the catalytic combustor concept that was presented in Kajita *et al.* (1990). A homogeneous diffusive type pre-combustion burner is used for the engine start-up and for preheating inlet air to about 450°C in the steady state operating mode. An air bypass valve at the back of the catalyst is used to achieve

control of the catalytic combustor at various turbine loads. The operating temperature of catalytic combustion at the rated turbine load was set at 1200°C. The target durability was more than 8000h and 400 on-off cycles.

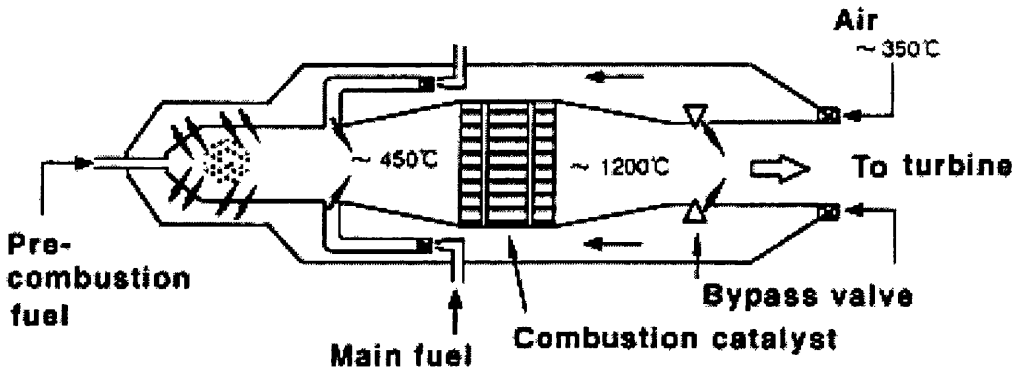

Figure 2.3. Schematic construction of the catalytic combustor for a gas turbine (adapted from Kajita *et al.*, 1990).

As an example of a possible control strategy, Figure 2.4 shows the basic control concept for the commercial catalytic combustor turbine reported in Kajita *et al.* (1990). Applicability of the concept was confirmed by another test measuring the response of the turbine speed and the catalyst outlet temperature to a stepwise change of the fuel control valve and the air bypass valve, respectively, at different turbine loads.

NoMac Energy Systems developed a gas turbine-driven generator as a range extender for a major automobile manufacturer's hybrid electric vehicle. The 24 kW continuous rating is sufficient to propel the automobile at the maximum legal speed in the United States (Mackay, 1992). There is no gearbox as the magnet generator is mounted on the gas turbine shaft and there is no lubrication system since the rotor group shaft runs on air bearings. The complete generator set weighs 36 kg and the price would be around 1000 $US (in 1992) if supplied to a mass automobile market. Their catalytic combustor burned natural gas, and for a power output of 50 kW, consistently achieved emissions below 2.0ppm both for NO_x and CO. The hydrocarbons were less than 0.1 v/v%. Using unleaded gasoline as a fuel, emissions will be less of a challenge than natural gas, as gasoline is three times more reactive than natural gas (Mackay, 1992).

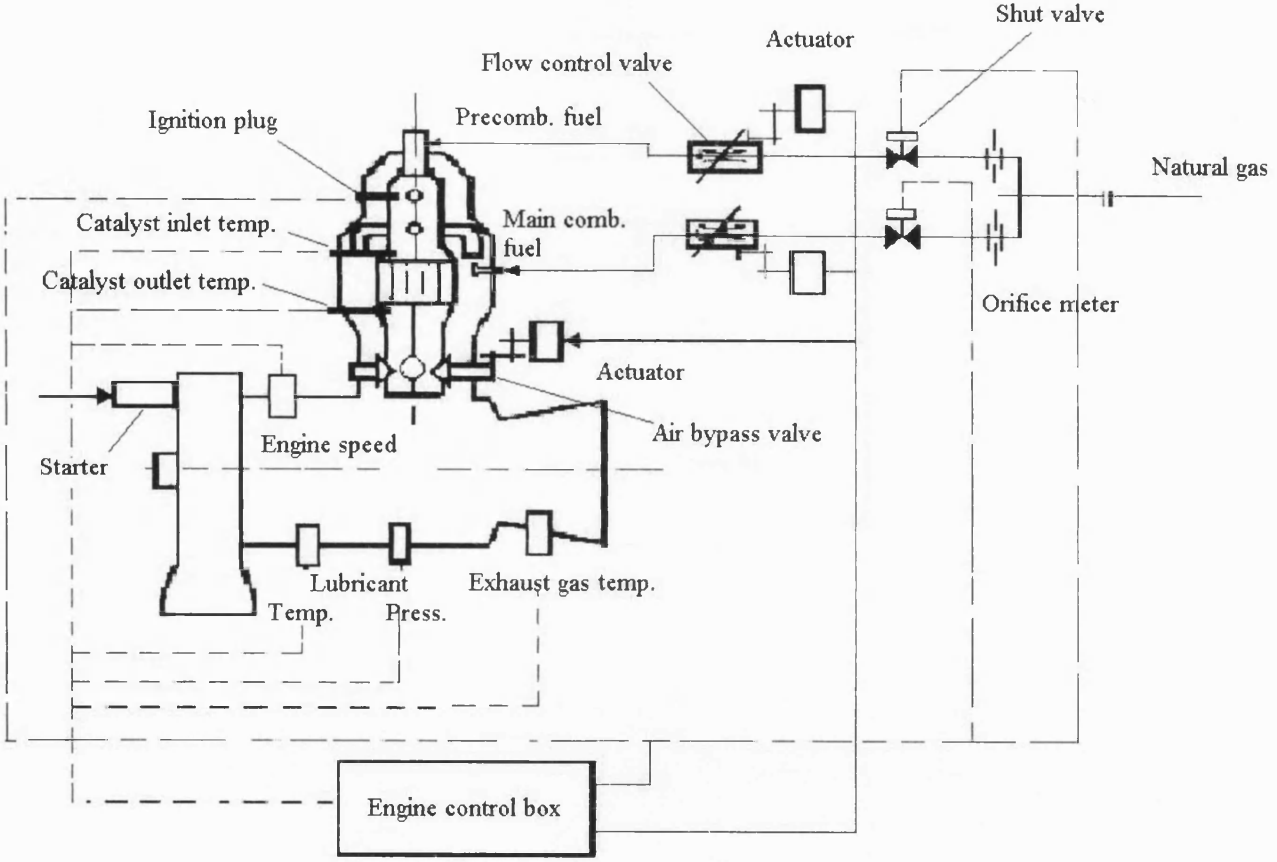

Figure 2.4. Basic controls for catalytic combustor turbine (adapted from Kajita *et al.*,1990).

2.2. Catalytic combustion

Catalytic combustion is a heterogeneous oxidation reaction that occurs on the surface of a catalyst. Using a suitable catalyst, the activation energy for the reaction is lowered compared to that for homogeneous non-catalytic reactions (105-210 kJ/mol → 42- 84 kJ/mol). (Prasad *et al.*, 1984). Consequently, heterogeneous oxidation reaction rates can be achieved at temperatures and fuel concentrations much lower than those required for the typical flame combustion to proceed. As a result of this, catalytic combustors can sustain stable combustion at fuel concentrations much below those possible in conventional combustors.

2.2.1 Catalyst system

A catalyst system is generally composed of two components, the catalyst and the support system (substrate and washcoat). Choice of both components has a significant influence on the development of a successful catalytic combustor. To obtain optimal performance from the combustor, the catalyst system should possess the following properties (Prasad, 1984):

1. Low light-off temperature.
2. High catalytic activity at lowest levels of air preheat and the highest values of mass throughput.
3. The support should have a large geometrical surface area, low pressure drop, excellent thermal shock resistance and high working temperature.
4. Thermally stable washcoat.
5. It should maintain high activity after prolonged use at elevated temperatures.

The washcoat should also be highly resistant to attrition (*e.g.* Agrafiotis & Tsetsekou, 2000).

2.2.2.1 Choice of catalyst

There is a vast amount of data in the literature on the performance of a wide variety of materials that exhibit catalytic activity. In this section, a brief review is provided to illustrate the type of materials considered and the link with the choice of support. Common approaches to choosing catalysts for complete oxidation have been summarised in the works of several Russian scientists (*e.g.* Boreskov, 1982).

Typical combustion catalysts are based on precious metals (mainly Pt, Pd), transition metal oxides, and metal oxide composites, *e.g.* spinels (Guilhaume & Primet, 1994) and perovskites (Ciambelli *et al.*, 1999). Platinum has received the most attention for catalytic combustion. This metal is not only extremely active for combustion of many fuel types, but it maintains much of its activity in the extreme high temperature regions used for catalytic combustion catalysts (DeLuca & Campbell, 1977). Moreover, platinum metal is advantageous over oxide catalysts for the following reasons: (a) high specific activity, (b) resistance to sulphur poisoning at temperature below 800K, (c) possibility of being supported in highly dispersed form on various supports, and (d) low content of the active component (0.1-0.5 wt%) (Prasad, 1984). However, problems in the operation of precious metal catalysts may arise (Kesselring, 1986). For example, growth of platinum crystallites, and at temperatures above about 1000K, a palladium oxide may start to decompose to metallic palladium that is less active.

Metal oxide catalysts have also been used in catalytic combustion even though their catalytic activities are generally known to be lower than precious metals. The main advantage of metal oxides over precious metal catalysts is the lower cost of the raw material. Furthermore, higher thermal stability can be achieved (Zwinkels *et al.*, 1993). The order of catalytic activity of oxide catalyst for the oxidation of hydrocarbons and other organic substances coincides with only few exceptions (Boreskov, 1986):

$Co_3O_4 > MnO_2 > NiO > CuO > Co_2O_3 > Fe_2O_3 > ZnO > V_2O_3 > TiO_2 > Sc_2O_3$.

2.2.2.2. Choice of the support

The high cost of precious metals encourages manufacturers to find means to use low precious metal loadings while simultaneously maintaining catalytic activity and durability. The research for improving catalyst performance and durability include the selection of supports with optimum porosity and surface area, and with particular attention to the location of the precious metal within the support.

Substrates

The substrates were usually fabricated from low surface area ceramics or metal alloys. Table 2.1 presents the widely used ceramic monolith substrates.

Table 2.1. Materials of commercial ceramic monolithic substrates.

Name	Composition	Thermal Expansion rate* (10^{-6} K^{-1})
α- and γ-Alumina	Al_2O_3	8.5
Cordierite	$2MgO{\cdot}2Al_2O_3{\cdot}5SiO_2$	0.5-1
Cordierite-mullite	$2MgO{\cdot}2Al_2O_3{\cdot}5SiO_2$ — $2Al_2O_3{\cdot}2SiO_2$	-
Magnesium aluminate-spinel	MgO — $MgO{\cdot}Al_2O_3$	-
Mullite	$3Al_2O_3{\cdot}SiO_2$	5.0
Mullite-aluminum titanate	$3Al_2O_3{\cdot}2SiO_2$ — $Al_2O_3{\cdot}TiO_2$	-
Silica	SiO_2	-
Silicon carbide	SiC	-
Silicon nitride	Si_3N_4	-
Spinel	$MgO{\cdot}Al_2O_3$	8.6
Titania	TiO_2	-
Zeolites	Al_2O_3 —SiO_2	-
Zirconia	ZrO_2	11.4
Zirconia - spinel	ZrO_2 —$MgO{\cdot}Al_2O_3$	-

* Source: Komeya and Matsui (1994), Temperature range: 293- 1273 K

Washcoat

The low surface area of the monolith substrate can be increased by the application of a thin coat of metal oxide material, such as alumina. This washcoat adheres strongly to the ceramic support and provides a high surface area. The most commonly used washcoat material is γ-alumina. Figure 2.5 shows the change in the alumina phase with temperature. γ-Alumina is the most frequently used support as it has a very high surface area (*ca* 300 m^2/g), compared to α-alumina which has a low surface area, *ca* 5 m^2/g. When γ-alumina is transformed to the α phase, both the specific surface area and the pore volume decrease. Such morphological changes in a catalyst support are accompanied by a loss of catalytic activity due to encapsulation of the metal (*e.g.* Arai & Machida, 1996; Djuricic *et al.*, 1997). This loss of activity is permanent, because the transformation of the metastable γ-alumina is irreversible.

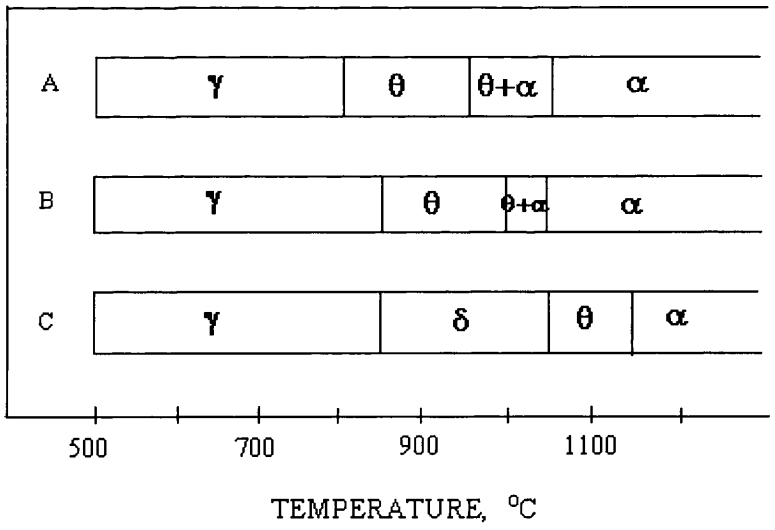

Figure 2.5. Phase transformations of alumina: (A) γ-Al_2O_3 + 3% Pt, (B) γ-Al_2O_3 + 0.1% Pt, and (C) γ-Al_2O_3 (adapted from Trimm, 1980).

At temperatures above 900°C, the alumina undergoes a phase change to low surface area α-alumina (300 $m^2/g \rightarrow 5\ m^2/g$). This results in pore closure and a burying of active catalysts in the alumina washcoat. The problem associated with phase change can be reduced by stabilising alumina washcoats with CeO_2 or CsO_2, or more thermally resistant washcoat such as ZrO_2 (Kesselring, 1986). These processes reduce the surface area, but it may not be necessary to maintain a high surface area in high temperature catalytic combustion (Prasad *et al.*, 1984).

There are generally four methods to prepare monolithic catalysts (DeLuca & Campbell, 1977):

(a) Catalyst incorporation during manufacturing of monolithic supports.
(b) Deposition of active material directly onto the monolithic support.
(c) Washcoating (*i.e.* laying down a high surface area coating) the monolith first and then depositing on this layer the active material.
(d) Depositing the washcoat and the active material at the same time.

Process (c) is the most widely used method. This procedure is frequently used with precious metals in order to locate them such that they are strongly anchored to the surface (Stiles, 1983).

There are three major ways to produce a high surface area washcoat on a monolith substrate:

a) One can simply take fine powder of a high surface area metal oxide (*e.g.* γ-Al_2O_3), make a slurry, and then dip the monolith.
b) A second method involves dipping the support into a salt solution (*e.g.* aluminium nitrate) containing the desired metal ions, and then heating the system to decompose the salt to form metal oxides.
c) The last method is the sol-gel method which involves contacting the support with the desired organic (*e.g.* aluminium alkoxides) or inorganic salt (*e.g.* aluminium chloride), and then contacting this system with a precipitating agent to produce a solid, for example, the hydroxide, which is subsequently heated to give the oxide form.

The requirements of a washcoat are that it be uniform, have a high surface area, be adherent to the monolith and have high thermal resistance. Operating temperatures are dependent on the operating temperature of the catalytic combustor. It was decided to adopt the sol-gel method of coating in this work and this will be described in more detail later in this chapter and Chapter 4.

2.2.2.3 Choice of fuel

The composition of gasoline is very complicated. If diffusion experiments were performed with gasoline, then they would be very difficult to interpret.

Figure 2.6 shows a schematic of the composition of gasoline. As can be seen, gasoline consists of C_4 - C_9 hydrocarbons, which can be categorised into three main groups, saturated hydrocarbons (paraffins), unsaturated hydrocarbons (naphthenes) and aromatic hydrocarbons. In general, the boiling range of gasoline lies between 60 and 200 °C, which is equivalent to the C_4 -C_9 *n*-paraffins.

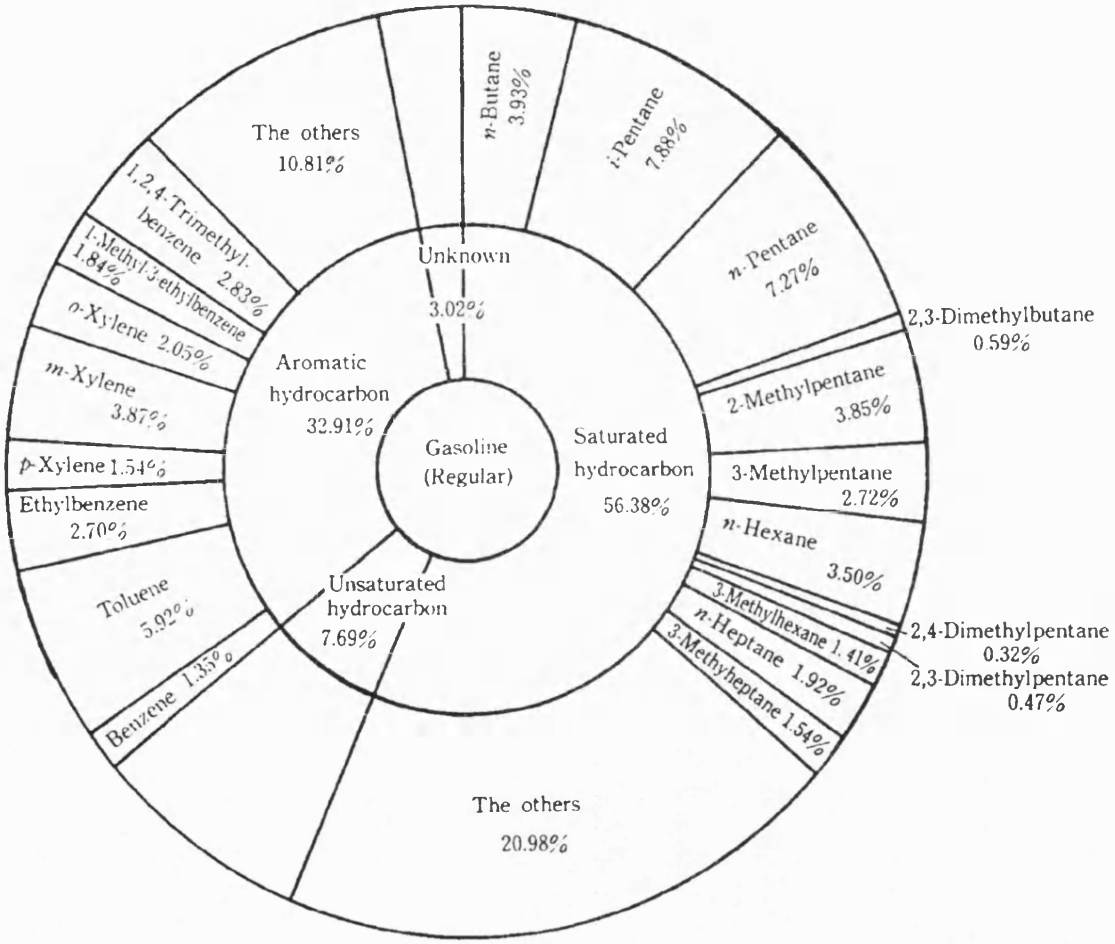

Figure 2.6. Typical composition (wt %) of gasoline (adapted from Hirao & Petfrey, 1988).

2.3 Diffusion in catalytic reaction

Catalytic combustion is a heterogeneous catalytic reaction which requires the presence of two phases, a solid phase (catalyst system) and a gas phase (reactants). In heterogeneous systems, the rate of a chemical reaction may be affected by many variables. It is not only dependent on temperature, pressure and composition, but also on the rate of mass transfer. In addition, the rate of heat transfer may also become important. For example, considering an exothermic reaction taking place at the interior surface of a porous catalyst pellet if the heat generated by reaction is not removed fast enough, then a severe non-uniform temperature distribution can occur within the pellet. Therefore, heat and mass transfer effects become increasingly important, especially in a fast reaction, such as catalytic combustion.

To optimise the performance of the catalyst, the surface area of the catalyst per unit volume of support must be maximised. It is generally accepted that it is good to have a well-dispersed system. Large specific surface areas can be obtained by creating an extensive network of very small pores within the catalyst support. However, the resistance to mass transfer in a network of small pores can be appreciable. This is important because the reactant must be transported from the medium surrounding the catalyst support, through the porous structure to reach the active site at which the reaction is taking place. Understanding both the physical structures of catalyst supports and physical processes occurring within the catalyst is fundamental to determine the effect of pore size on the mass transfer rate and catalytic activity.

The porous structure of the catalyst enables a high internal surface area per unit reactor volume to be obtained. Due to the complex mechanisms involved in catalysts, both the structure and the internal surface area of the catalyst pores influence parameters, like catalytic activity, permeability, diffusivity, thermal conductivity, and mechanical strength. This becomes clear when considering that solid-catalysed reactions occur on the catalyst surface by means of adsorption and desorption processes and diffusion through the pores.

The activity of a catalyst cannot be satisfactorily characterised in terms of the specific surface area alone, because the texture of the structure is also important. To study the

accessibility of the surface, the shape and the dimensions of the pores presented in the matrix need to be known.

The reaction process in heterogeneous catalysis can be separated into the following steps (*e.g.* de Boer, 1959), see Figure 2.7:

1. Transport of the reactants from the reaction mixture to the external surface of the catalyst particles.
2. Transport of the reactants from the external surface of the catalyst particle to the internal surface.
3. Adsorption of the reactants on the active centres of the catalyst.
4. Reaction between adsorbed reactants.
5. Desorption of the reaction products.
6. Transport of the products from the internal surface of the catalyst to the external surface.
7. Transport of the products from the external surface of the catalyst to the reaction mixture.

Because the slowest step will determine the overall reaction rate, it is important to know which step is controlling the overall process. For example:

1. If the surface chemical reaction at the active catalyst site is controlling the process, the porosity of a catalyst becomes very important because the internal surface is generally larger than the external surface.
2. If the pore diffusion process is the controlling step, then reactions in the external layer at the surface of the catalyst are dominant and the porosity becomes less important (as all of the internal surface area cannot be utilised efficiently).

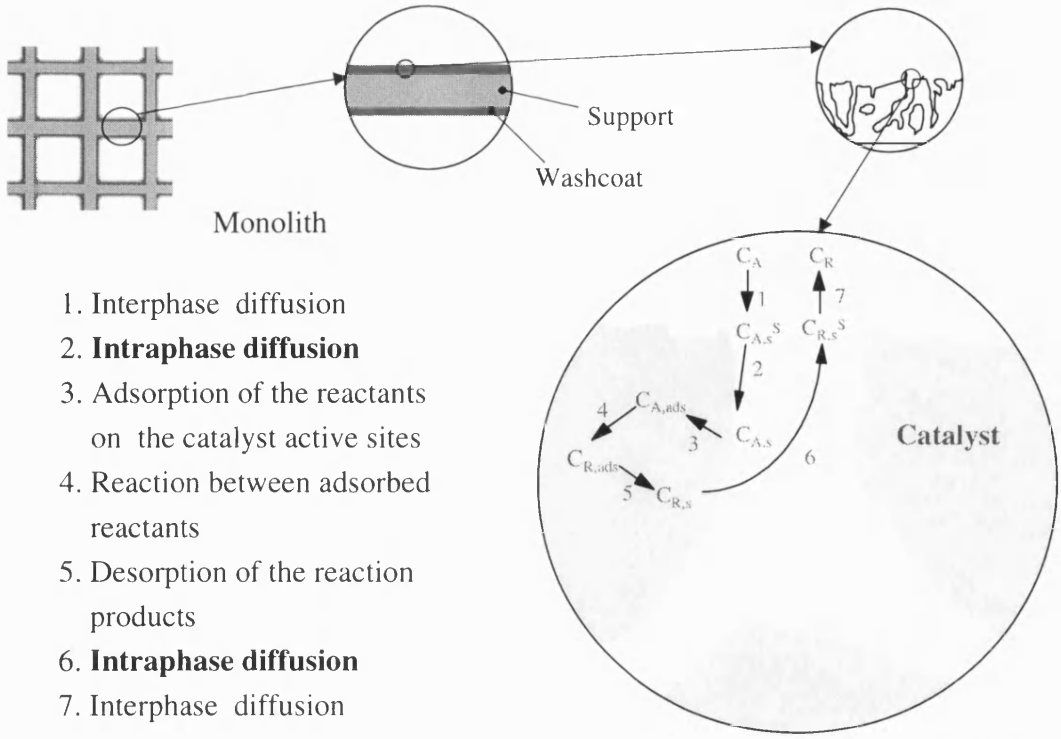

Figure 2.7. A reaction process in monolithic catalysts (Reaction: A → R).

Resistance to pore diffusion in a catalyst can be reduced by using a catalyst with a smaller particle size, thus shortening the diffusion path. Similarly, in a monolith system resistance to pore diffusion can be reduced by decreasing the thickness of the catalytic layer.

Diffusion in porous media of a component in a gaseous mixture can be described as consisting of:

1) Molecular diffusion.
2) Knudsen diffusion, if the pore size is smaller than the length of the mean free path of gas molecules.
3) Surface diffusion in a mobile adsorbed layer.

In porous catalysts, the transfer of reactants and products may be taking place by the combined contribution of the three diffusion schemes as shown in Figure 2.8. The surface diffusion contribution is regarded of little importance, provided that the reaction

is taking place well above the boiling point of the reactants and the products. However, this can be important for components with high adsorption strength and can be comparable in magnitude to Knudsen diffusion (Doong and Yang, 1986).

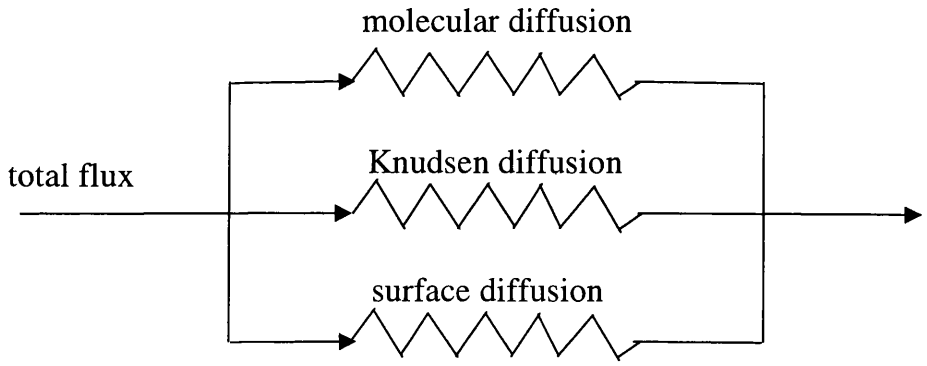

Figure 2.8. Electric analogue circuit picturing the flux of the diffusing species in a porous solid (adapted from Mason and Malinauskas, 1983).

In many cases of diffusion in porous media, the diffusion type is intermediate between molecular diffusion and Knudsen diffusion. According to Youngquist (1970), this so-called "intermediate diffusion (or transition diffusion)" was first discussed by Bosanquet, who considered the process as a random walk in which the successive steps of individual molecules are determined either by collisions with other molecules or with the tube wall (Hewitt and Sharratt, 1963).

Surface diffusion

Surface diffusion implies movement of molecules over a surface and is considered as the most important mode of transport for many adsorbates. It cannot be significant unless appreciable adsorption occurs, yet if adsorbed molecules are held so strongly as to be essentially immobile, surface diffusion will be significant (Satterfield, 1970). The contribution of surface diffusion increases with lager and heavier molecules because these molecules are most easily condensed and adsorbed due to their higher density (Do, 1998).

Ash *et al.* (1963) found that as the monolayer coverage is approached, then measure values of surface diffusion in the steady state increases rapidly. As the monolayer is exceeded, the diffusivity shows a minimum and then rises sharply again in the region of capillary condensation. The surface diffusivity generally shows a nonlinear relationship with surface loading and it can be divided into three regions: (a) a monolayer region, (b)

a multilayer region and (c) a capillary condensation region as shown in Figure 2.9 (Do, 1998).

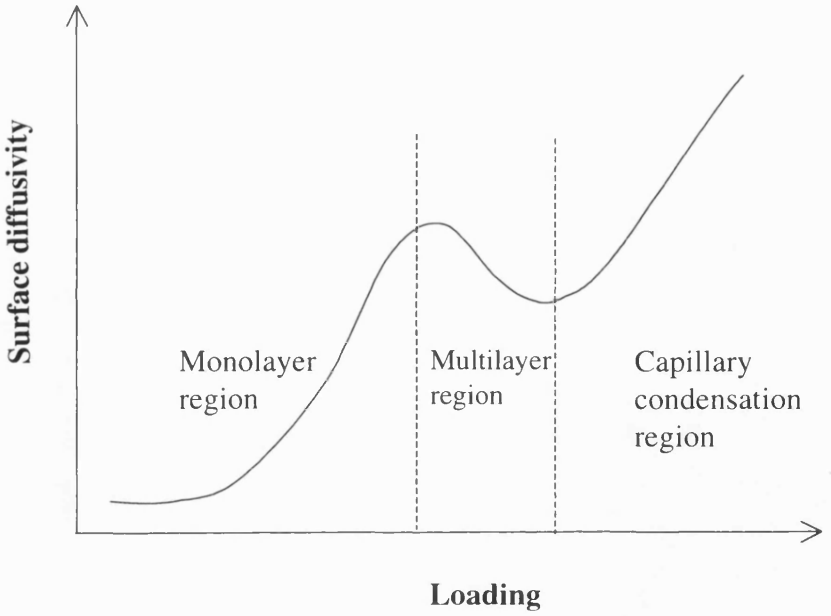

Figure 2.9. Surface diffusivity as a function of loading (adapted from Do, 1998).

When less than a monolayer coverage exists in a system, the surface diffusivity increases rapidly with loading (Carman, 1956). It is caused by the heat of adsorption which varies over the adsorbent surfaces, and the surface diffusion which takes place by the most loosely bound molecules. At low coverage, adsorption occurs on high energy sites where the adsorbed molecules moves very slowly. When the monolayer coverage is exceeded, molecules can be adsorbed more onto lower energy sites and because of the loose bonding these molecules will diffuse faster than the molecule bound in the high energy sites.

Surface diffusion is greatly influenced by temperature as surface mobility is related to strength of adsorption. In general, the influence of surface diffusion becomes less important as the temperature increases. When temperature is increased, the amount adsorbed on the surface decreases faster than the increase in surface diffusivity.

An important point that should be noted is that if surface diffusion is significant, then if this is neglected, it may cause the theoretically predicted effective diffusivity to be smaller than the measured experimental value. This is because most of the existing

models that predict effective diffusivity (as described in Section 2.3.1) do not take surface diffusion into account (Satterfield, 1970).

Diffusion that occurs in porous catalysts usually includes molecular diffusion and Knudsen diffusion. The usual criteria for Knudsen diffusion is that the mean free path of the gas molecules is larger than the pore diameter ($r_p < \lambda$). In the case of molecular diffusion, the mean free path is smaller than the pore size ($r_p >> \lambda$). Weisz (1973) introduced an additional diffusion term, called 'configurational' diffusion. This mechanism may be considered when the pore size is still larger than molecular dimensions (usually, collision diameter), but much smaller than the mean free path ($r_p \approx \sigma$) (Froment & Bischoff, 1990). The collision diameter and mean free path can be obtained from the kinetic theory (*e.g.* Kemp, 1979).

The flux in a porous structure, in respect to a concentration gradient may be represented by:

$$N_A = -D_e \frac{dC_A}{dx} \tag{2.1}$$

where D_e is the effective diffusivity.

The molecular diffusion coefficient, D_{AB}, can be estimated by the theoretical equation based on the kinetic theory and Lenard-Jones expression for binary gas mixtures. This is (*e.g.* Reid *et al.*, 1986):

$$D_{AB} = \frac{0.00266T^{3/2}}{PM_{AB}^{1/2}\sigma_{AB}^2\Omega_D} \tag{2.2}$$

where $M_{AB} = 2[(1/M_A) + (1/M_B)]^{-1}$

T = temperature, K

P = pressure, bar

σ_{AB} = characteristic length, Å

Ω_D = diffusion collision integral, dimensionless.

If pores are small and the gas has a lower density, collision will occur frequently between gas molecules and pore wall, rather than between molecules. This type of transport is referred to as Knudsen diffusion. Knudsen showed that the diffusion flux is given by (*e.g.*Youngquist, 1970):

$$J_A = -D_{KA} \frac{dC_A}{dx} \tag{2.3}$$

The Knudsen diffusivity, D_{KA}, (*e.g.* Smith, 1981):

$$D_{KA} = \frac{2}{3} r \sqrt{\frac{8RT}{\pi M_A}} \tag{2.4}$$

Porous substances can be classified into three sub-groups, macroporous, mesoporous and microporous substances. The classification officially adopted by International Union of Pure and Applied Chemistry (IUPAC) is summarised in Table 2.2.

Table 2.2. Classification of pores according to their widths (Gregg & Sing, 1982).

	Width
Micropores	< 20 Å (2 nm)
Mesopores	20 Å - 500 Å (2 - 50 nm)
Macropores	> 500 Å (50 nm)

Real catalysts do not have a single size pore, but consist of a variety of different pore sizes. It is sometimes necessary to know the pore size distribution which can be represented, *e.g.*, by a histogram. The pore size distribution can be determined by two methods:

(a) Mercury porosimetry for macropores.

(b) Low temperature nitrogen adsorption for micro- and mesopores (< 500 Å).

In general, the mean value of the radius of the pores is used to describe a catalyst, which can be obtained by dividing the pore volume by the surface area using the assumption that the pores are interconnected cylindrical capillaries which have some effective radius. It should be noted that neither method provides information regarding the shape or length of the pores.

Pores can be categorised by two groups, 'through' pores and 'dead-end' pores, according to their accessibility. Pore spaces having at least one passage to the exterior are called 'through' pores and those with only one passage are known as 'dead-end' pores (or 'ink-bottle' pores) (McBain, 1935). The pores are sometimes interconnected with others. In electric conduction or in simple diffusion of non-reaction gases the 'through' pores are only active. However, in a porous catalyst the dead-end pore can be also active, due to

inward diffusion of reactant(s) and outward diffusion of product(s). In the second case, knowledge of the relative proportion of 'dead-end' and 'through' pores is necessary in order to obtain a full understanding of the catalytic performance in porous media. Simple structural models for solids, based on cylindrical-shaped capillaries have been used in many studies (*e.g.* Johnson and Stewart, 1965). Other shapes of capillaries are discussed by Barrer (1953) who examined the influence of pore shape on the form of the sorption isotherms.

The composition of a gas in pores can be represented by a smooth function of its position in the medium. However, it may not be necessarily so in the real system. In a reactive catalyst with non-branching pores, the composition at any point in a pore is determined by the location of the point along the axis of the pore, rather than by its position relative to the axis in the pellet. The relation between these two is influenced by the shape of the pore (Jackson, 1977). In Figure 2.10, points A and B are close together in space, but the composition at these points is very different. Because a lies in the entrance of the pore, the composition is reactant-rich, while B, in the middle of the pore, has a composition that is richer in reaction products and leaner in reactant.

Petersen (1958) introduced a labyrinth factor, tortuosity, to account for the length of the pores. For the diffusion of gases in porous catalysts, it is common to define a tortuosity, τ, for a pore of radius, r, by the expression presented in Equation 2.5 (Satterfield, 1970).

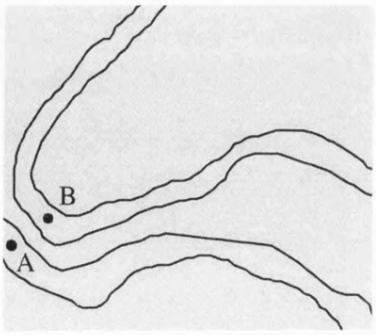

Figure 2.10. Porous pellet not described by smooth composition fields (adapted from Jackson, 1977)

For molecular diffusion in a porous solid, an effective diffusion coefficient D_e can be expressed as:

$$D_e = \frac{D_T \varepsilon}{\tau} \qquad (2.5)$$

where $\frac{1}{D_T} = \frac{1}{D_{AB}} + \frac{1}{D_K}$ (2.6)

Here, D_T is transition diffusion coefficient, ε is the void fraction in the porous media, and τ is a tortuosity factor. Tortuosity factor is often a parameter to describe the pore structure of a catalyst. Therefore, the accurate estimation of this value is essential in fundamental design of catalytic reactors using sophisticated models (*e.g.* Froment and Hoffman, 1986). The tortuosity factor accounts for the fact that the actual diffusion path between two points within a porous medium is generally greater than the distance between the points. The tortuosity of actual catalysts is generally larger than unity, so the actual diffusion path is longer than the distance in the direction of net flow. Sharma *et al.* (1991) measured the effective diffusivity of 13 commercial catalysts and supports under nonreacting conditions and reported that the tortuosity factors are between 1 and 6 and they vary strongly with the particle porosity.

2.3.1 Models for predicting diffusion rates in porous solids

The important role of diffusion in catalysis has promoted the search for a reliable model for predicting effective diffusivities in porous catalysts.

Many different models have been reported over the last few decades, see Figure 2.11. They can be categorised in three groups: 1) models based on total porosity, 2) models based on the pore size, and 3) network models. In the following sections, these will be briefly described and the more commonly used models will be described in more detail.

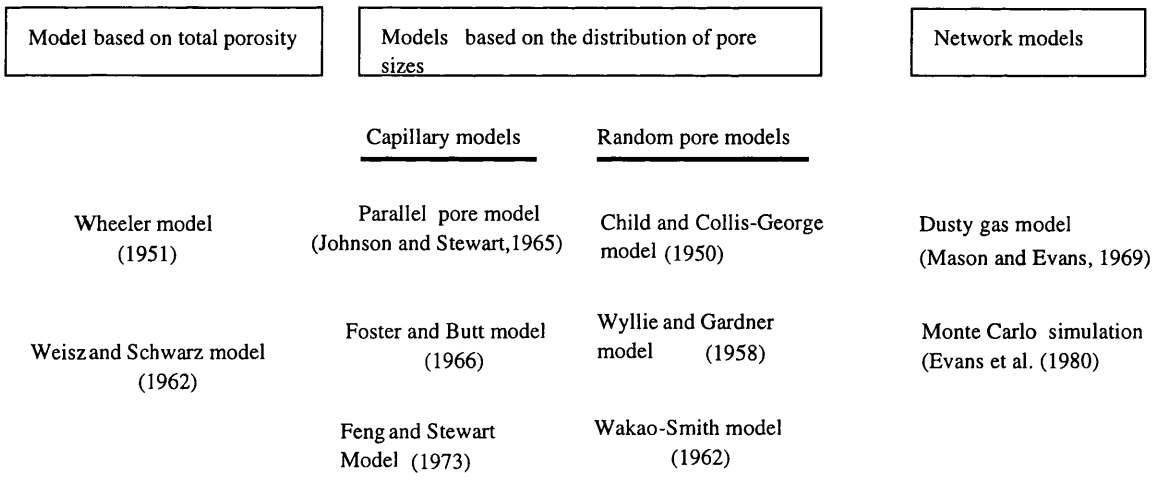

Figure 2.11. Classification of models for predicting effective diffusivity.

2.3.1.1 Models based on total porosity

The simplest models for predicting effective diffusivities in porous media are based on total porosity. These models are only applicable to porous materials consisting of pores with a single size. If the porous medium contains a broad distribution of pore sizes, the applicability of these models is questionable. An early attempt at characterising the pore structure of catalysts was made by Wheeler (1951). Later, Weisz and Schwartz (1962) suggested a three-dimensional model to give improved predictions.

2.3.1.2 Models based on the pore size distribution

Since the models based only on total porosity are not applicable to porous solids containing pores of many different radii, a considerable amount of effort has been directed toward incorporating the pore size distribution into an effective diffusivity model. The widely used models are:

- Wakao and Smith model – this is based on a bi-disperse pore structure (Wakao and Smith, 1962).
- Johnson and Stewart's model (Johnson and Stewart, 1965) – this is based on a mono-disperse parallel pore structure.
- Foster and Butt's model – this is based on convergent and divergent parallel pore arrays (Foster and Butt, 1966)
- Feng and Stewart's model developed from the earlier work by Johnson and Stewart (Feng and Stewart, 1973).

(a) Parallel pore model

An equation for describing the transfer rate of gas through a porous solid catalyst is presented in Evans *et al.* (1961).

$$N_A = -D_{AB} \cdot \frac{dC_A}{dx} + y_A \cdot (N_A + N_B) \tag{2.7}$$

If Equation (2.7) is integrated at constant pressure, then the diffusion flux of gas, *A*, through a porous pellet of length, *L*, represents as:

$$N_A = D_{AB,e} \cdot \frac{P}{R \cdot T \cdot L \cdot \alpha} \cdot \ln \frac{1 - \alpha \cdot y_{AL}}{1 - \alpha \cdot y_{A0}} \tag{2.8}$$

where

$$\alpha = 1 + \frac{N_A}{N_B} = 1 - \sqrt{\frac{M_B}{M_A}} \tag{2.9}$$

Johnson and Stewart (1965) reported a model for predicting the rate of diffusion in a binary mixture trough a porous solid at constant temperature and pressure. In the development, the following expression for the diffusion flux of species A through porous media is obtained:

$$N_A = -\kappa \frac{dC}{dx} \int_0^\infty \frac{1}{\frac{1-\alpha y_A}{D_{AB}} + \frac{1}{D_{KA}}} f(r)dr \tag{2.10}$$

with D_{AB} calculated from Equation (2.2)and D_{KA} calculated from Equation (2.4). The geometric constant (κ) (or the reciprocal of tortuosity factor, $1/\tau$) would have the value of 1/3 for isotropic pore systems by assuming that pores are straight and nonconnecting, with no dead volume (Johnson & Stewart, 1965).

The integration of Equation (2.11) with respect to pore radius, *r,* can be completed either numerically or graphically as there is a distribution in the size of pores. The integral can be evaluated directly with the following equation:

$$\int f(r)dr = \varepsilon = V_g \rho_p \tag{2.11}$$

where V_g is pore volume, cm^3/g

ρ_p is the apparent density, g/cm^3

Expressing the total diffusion flux through the pellet in the terms of an effective diffusivity as

$$N_A = -D_e \frac{dC}{dx} \tag{2.12}$$

and combining Equation (2.10) with Equation (2.1) gives:

$$D_e = \kappa \int_0^\infty \frac{1}{\frac{1-\alpha y_A}{D_{AB}} + \frac{1}{D_{KA}}} f(r)dr \tag{2.13}$$

The term can be neglected with respect to unity, so Equation (2.13) can be:

$$D_e = \kappa \int_0^\infty \frac{1}{\frac{1}{D_{AB}} + \frac{1}{D_{KA}}} f(r)dr \tag{2.10}$$

Taking the value of κ as 1/3 and using the macropore sixe distribution curves for porous solid, the effective diffusivity of species can be predicted by numerical integration of Equation (2.14).

(b) Random pore models (Wakao and Smith's model)

A random pore model was suggested by Wakao and Smith (1962). Many porous materials are produced by compressing powder particles which are themselves porous, so the resulting materials may basically have two different size of pore structure, micropores (pores within each powder particle) and macropores (spaces between the powder particles). This combination of both micropores and macropores leads to a bidisperse pore structure as shown in Figure 2.12 and diffusion through the porous solid could occur by three parallel paths:

1. Through the macropores of average radius, r_a.
2. Through the micropores of average radius, r_i.
3. Through macropores and micropores in series.

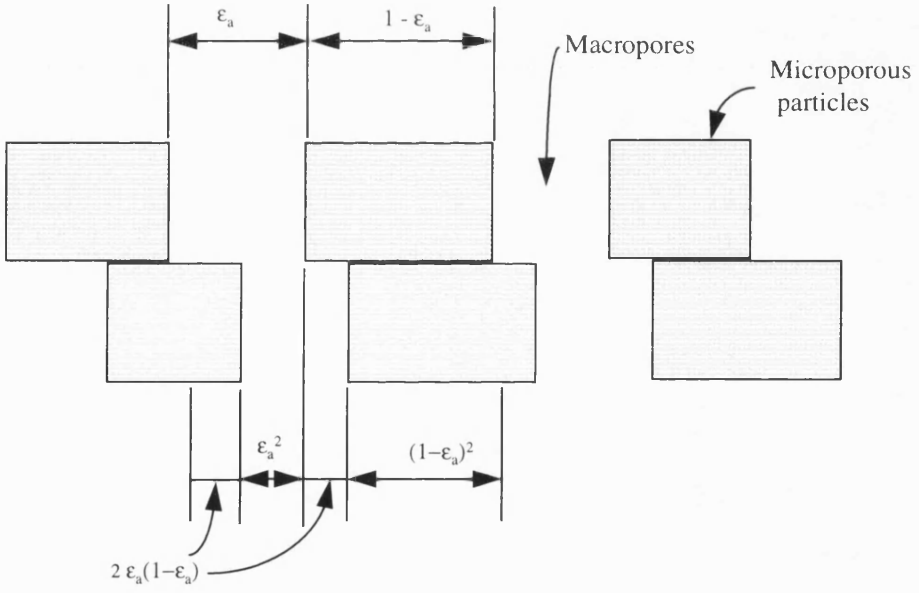

Figure 2.12. Random pore model for bidisperse solids (adapted from Wakao and Smith, 1968)

The flux is the sum of three contributions due to probability of lining-up macropores with macropores, macropores with micropores, and micropores with micropores. For diffusion at constant pressures, the flux for diffusion at constant pressure can be described as (Youngquist, 1970):

$$N_{AS} = -\left(\varepsilon_a^2 . D_a + (1-\varepsilon_a)^2 . D_i + 2\varepsilon_a . (1-\varepsilon_a) \frac{2}{1/D_a + 1/D_i} \right) \frac{P}{RT} \frac{dy_a}{dx} \qquad (2.11)$$

where

$$D_a = \frac{D_{AB}}{\left(1 - \alpha \cdot y_A + \frac{D_{AB}}{D_{KA,a}} \right)},$$

$$D_i = \frac{D_{AB} \cdot \varepsilon_i^2}{(1-\varepsilon_a)^2 \cdot \left(1 - \alpha \cdot y_A + \frac{D_{AB}}{D_{KA,i}} \right)}$$

Pure gases, *A* and *B*, are exposed over the two boundaries (*e.g.* $x = 0$, $x = L$). Using this condition, the working equation for calculating effective diffusivity from this model can be obtained:

$$D_e \frac{\ln[1/(1-\alpha)]}{D_{AB}} = \varepsilon_a^2 \ln\left\{ \frac{1 + D_{AB}/D_{AKa}}{1 - \alpha + D_{AB}/D_{AKa}} \right\} + \frac{\varepsilon_i^2 \alpha}{1 - \alpha + D_{AB}/D_{AKi}} + \frac{4\varepsilon_a(1-\varepsilon_a)}{1 + [(1-\varepsilon_a)^2/\varepsilon_i^2]} \times \alpha / \left\{ 1 - \frac{\alpha}{2} + \frac{D_{AB}}{D_{AKi}(1+\varepsilon_i^2)/(1-\varepsilon_a)^2} \right\} \qquad (2.12)$$

where $\alpha = 1 - (M_B / M_A)^{1/2}$.

(c) Forster and Butt's model

Forster and Butt (1966) proposed a more complicated model for the prediction of diffusion fluxes in porous solids. In comparison with the parallel model (which assumed that the pores consist of smooth capillaries), this model proposed that the entire pore volume be represented by two conical ducts shown in Figure 2.13, centrally convergent ducts and centrally divergent ducts. The exact shape of these ducts is obtained from the pore size distribution of the solids by assigning the pore volume corresponding to a given pore radius to capillary segments of that radius in the two ducts. For a given gas

composition at opposite ends of a solid sample, the diffusion flux can be calculated by an interactive procedure. Using estimation for the flux, the capillary equation describing the diffusion flux in the transient region is given by:

$$N_A = \frac{-D_{AB}\frac{dC_A}{dx} + (N_A + N_B)y_A}{1 + \frac{D_{AB}}{D_{KA}}} \qquad (2.13)$$

This can be rearranged to give the change in composition across each capillary segment. For the *j*th segment, this can be described as:

$$y_{Aj+1} = \frac{1}{\alpha}\left\{\left[(1 - y_{Aj}) + \frac{D_{AB}}{D_{KA}}\right]e^{\frac{N_A RTL_j \alpha}{PD_{AB}}} - (\frac{D_{AB}}{D_{KA}} + 1)\right\} \qquad (2.14)$$

Starting at one end, Equation (2.18) is applied consecutively to each capillary segment. Mixing between the two ducts can be allowed at various points and the extent to which it is allowed provides an adjustable parameter for data correlation. The calculations are carried out through the total length of the ducts, and correctness of the assumed flux is determined by comparing the calculated and given end compositions.

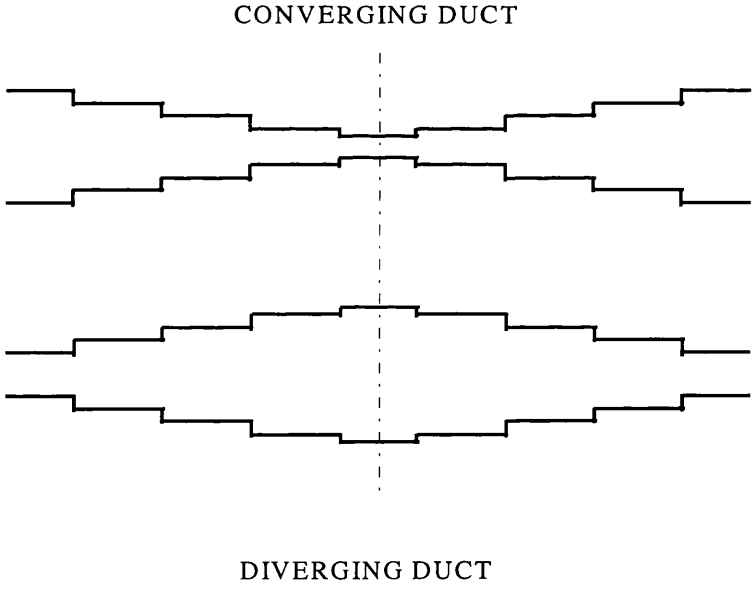

Figure 2.13. Converging-diverging pore model (adapted from Foster and Butt, 1966).

2.3.1.3 Network models

A formula for the mass transfer in porous media can be obtained simply from momentum transfer considerations. These are introduced in terms of motion of gas mixtures given by Maxwell and Stefan and also in Knudsen's work on the flow of a rarefied gas through a capillary. Their approaches are, however, based on assumptions which cannot be entirely justified within the framework of the argument (*e.g.* pore structure), so they may be only regarded as a means of developing physical concepts for the underlying phenomena (Mason & Malinauskas, 1983). Frequently, tortuosity factor which measures the increases in diffusion path length imposed by the presence of solid obstacles, becomes adjustable parameters that compensate for inadequacies in evaluating the mass transfer in porous media (*e.g.* Reyes and Iglesia, 1991).

Evans *et al.* (1980) attempted to provide correlation for predicting gaseous diffusivities without the need for tortuosity factor or similar parameters. A Monte Carlo simulation of the diffusion of gas molecules within various porous solids was carried out to obtain values of pore diffusivity. A Monte Carlo method is any procedure that involves the use of statistical sampling techniques to approximate the solution of a mathematical and physical problem (Brown, 1956). Therefore, two tasks were involved in the simulation: the numerical representation of a porous solid with the computer, and the calculation of molecular trajectories within the solids. However, the simulation did not include entire diffusion regimes, but is confined to the Knudsen diffusion regimes.

2.3.1.4 Dusty gas model

It is assumed that the diffusion in porous solids illustrates the flow of gas in the aggregate of small particles. Based on this, Maxwell suggested as early as 1860 a model for gas flow and diffusion in porous media. In this model the porous medium is visualised as a random collection of large particles fixed in space ('dust'). This work was however ignored for many years until it was introduced in 1957 by Deriagin and Bakanov, who proposed to treat the particles of a porous medium as giant molecules using Chapman-Enskog's theory. The complete model was independently re-invented by Evans *et al.* (1961), who avoided the complicated mathematics and used the model only to determine the flux equations. By formal variation of the mole fraction of the dust particles, the whole pressure range from the free-molecule to the continuum region

could be covered. In this form, the model has been applied to a variety of diffusion and flow problems (Mason *et al.*, 1967).

The one-dimensional equation for the flux of species A in a binary system through a porous medium by Evans *et al.* (1961), can be described as:

$$N_A^0 = \frac{-D_{AB}\frac{dC_A}{dx} + (N_A^0 + N_B^0)y_A}{1 + \frac{D_{AB}}{D_{KA}}} \qquad (2.15)$$

by assuming that there is no convective flow resulting from pressure gradients and no surface flow or surface diffusion.

A diffusion model based on dusty-gas theory requires knowledge of the volume fraction of solids or particle size distribution. However, this would be of little value at the present since the physical properties of porous media are practically determined by analysis of pore volume through use of capillary-surface tension, for example, mercury porosimetry. Scheidegger (1957) has pointed out that there is no unique relationship between the distribution of pore sizes and the distribution of particle sizes.

2.3.2 Intraphase diffusion in combustion reaction

The catalyst used in catalytic combustion is often contained within a washcoat. If the rate of pore diffusion is slow compared to the intrinsic reaction, the reaction becomes diffusion limited with effectiveness factors different from unity. Recent papers (*e.g.* Leung *et al.*, 1996, Hayes & Kolaczkowski, 1994) have demonstrated that reactor configurations employed may be operated in the region of significant diffusion limitation. To quantify the extent of diffusion limitation and calculate reliable values of effectiveness factors, it is necessary to obtain accurate values of effective diffusivity for the species of interest (Hayes *et al.*, 2000). Most of the investigators who have modelled diffusion in washcoats have assumed a value, or have estimated a value with one of the established models. Some examples of modelling studies in which intraphase diffusion in a washcoat has been considered are listed in Table 2.3. As can be seen, the random pore model of Wakao and Smith (1968) has been often used.

Table 2.3. Modelling of catalytic monoliths - Examples of model selected for effective diffusivity, D_e.

Author	**Catalytic monolith & reaction studied**	**Estimation for D_e**	**Is there any evidence that the choice of model for D_e was validated with experimental data?**
Oh & Cavendish (1983)	Catalyst: Pt on washcoated monolith. Reaction: Oxidation of CO, C_3H_6, and H_2.	Random pore model of Wakao-Smith model. D_e values were assumed to increase the 1.4 power of temperature.	No
Zygourakis & Aris (1983)	Catalyst: catalytic washcoat on ceramic monolith. Reaction: Oxidation of hydrocarbon and CO.	Random pore mode of Wakao-Smith model.	No
Svatular *et al.* (1993)	Catalyst: honeycomb commercial-type SCR catalysts (<2 wt% V_2O_5). Reaction: reduction of NO_x by NH_3.	Wakao-Smith model.	No
Tronconi *et al.* (1994)	Catalyst: V_2O_5-WO_3/TiO_2 on a monolith. Reaction: NO reduction and SO_2 oxidation.	Wakao-Smith model.	No
Kyriacopoulou *et al.* (1994)	Catalyst Pt-Rh/γ-alumina on a cordierite monolith. Reaction: NO reduction by CO.	Knudsen diffusion.	No
Nakhjavan *et al.* (1995)	Catalyst: modified alumina with Pt or Pd on a monolith. Reaction: combustion of fuel.	Factorial design for effective diffusivity with the value of between 0.1 cm^2/s and 0.01 cm^2/s for the + level and the - level, respectively.	No

Table 2.3. Modelling of catalytic monoliths (continued ...)

Author	**Catalytic monolith & reaction studied**	**Estimation for D_e**	**Is there any evidence that the choice of model for D_e was validated with experimental data?**
Hayes *et al.*(1995)	Ceramic tube (Alumina-silicate) coated on the inside wall with a platinum catalyst washcoat. Reaction: CO oxidation.	Wakao-Smith model.	No
Kolaczkowski *et al.* (1996)	Catalyst Pd/ γ-alumina on monolith. Reaction: Oxidation of methane.	Mean transport model of Fott & Petrini (1982).	No
Holmgren & Andersson (1998)	Catalyst: 1wt% Pt/γ-alumina on cordierite monolith. Reaction: CO oxidation.	Random pore mode of Wakao-Smith model.	No

2.4 Measurements of effective diffusivity

A large number of techniques have been employed to measure the effective diffusivity of porous structures. The classical physical methods have been reviewed by Haynes (1988), who categorised them into two major groups: steady state and unsteady-state (or transient) methods.

In the discussion that follows, these methods and their potential applicability to a catalytic monolith will be considered.

2.4.1 Steady state methods

2.4.1.1 Wicke-Kallenbach experiment

Since Wicke and Kallenbach (1941) introduced a steady-state counter-diffusion method to measure the effective diffusivity of CO_2 in the porous catalyst, the method has been widely used for the measurement of effective diffusivity in catalyst pellets. Figure 2.14 presents an experimental set-up, which may be used for steady state measurements on single pellets. The diffusion cell has one or more cylindrical sample pellets and both end-faces are exposed to streams which differ in composition. Pressures are equalised across the pellet so that mass transfer is achieved by diffusion resulting from the concentration gradient. Flow rate and composition are measured on each side of a diffusion cell. In the binary gas system, a thermal conductivity detector (TCD) is usually used for continuous monitoring of compositions.

The most important component of the Wicke-Kallenbach apparatus is the diffusion cell. To ensure that the flux across the pellet occurs only a result of the concentration difference and not the pressure gradient, any pressure differences between the two sides of the cell should be eliminated. The pressure difference is monitored by a sensitive differential pressure transducer. Stagnant layers and boundary layer resistance in series with the pellet resistance must also be eliminated. To achieve this, the gases are fed tangentially across the faces of the pellet at a high flow rate, or alternatively, mixed thoroughly with a stirrer in both chambers of the cell.

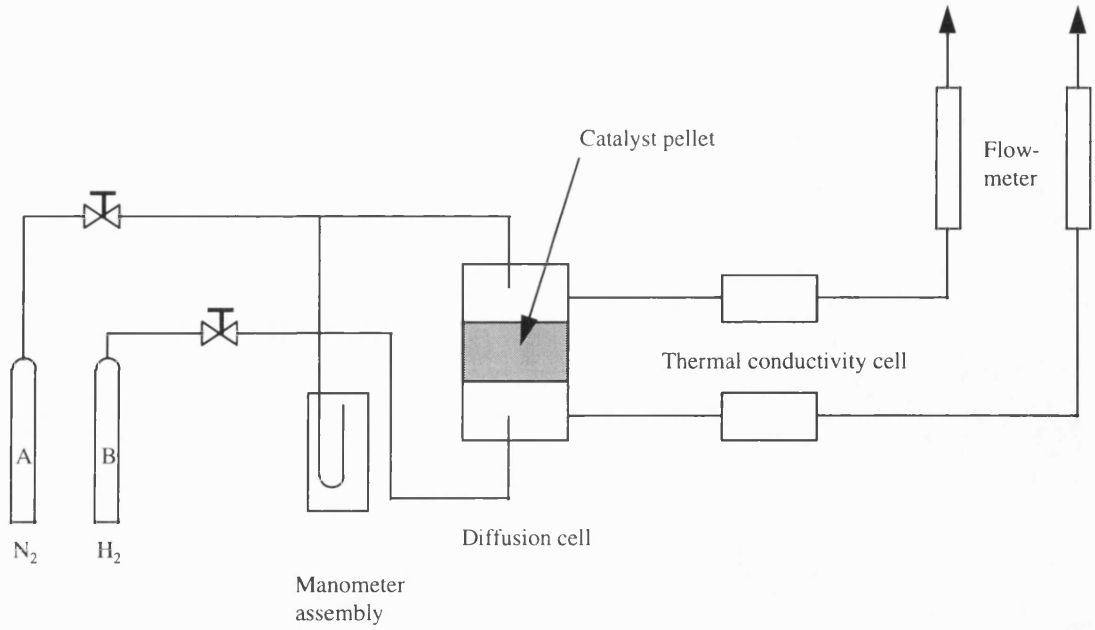

Figure 2.14. The schematic diagram of Wicke-Kallenbach measurement (adapted from Smith, 1982).

Although valuable information can be gathered from a specially formed model catalyst pellet, the results can be very different for an industrial catalyst. Therefore, it is necessary to develop a way of mounting industrial catalyst into the diffusion cell. Also as catalytic reactions generally take place at elevated temperatures, the measurements need to be made at similar conditions. However, there are temperature limitations to the method, mainly, because of the problem of sealing the pellet in the cell. A number of researchers (*e.g.* Al-Rqobar, 1981; Paravar & Hayhurst, 1984; Yang & Liu, 1982) have attempted to measure diffusion at high temperatures. Al-Rqobar (1981) used a polymer called Silastomer provided by Dow Corning, Co., to cast it around pellet. Yang & Liu (1982) used an electroplating technique to deposit metal on a graphite pellet. Paravar and Hayhurst (1984) determined the unidirectional diffusion coefficient for *i*- and *n*-butane in a single large crystal. The crystal used was 0.3×0.14×0.12 mm and embedded length-wise in epoxy to fabricate a membrane.

However, one major limitation of the steady state technique is that it has often been criticised for a lack of inclusion of the effect of dead-end pores.

2.4.2 Unsteady-state methods

The steady state method has been used extensively, and it is possible to detect dead end pores, which could contribute to the chemical reaction. A variety of transient techniques have been developed, such as:

(a) Continuous adsorber (*e.g.* Frost, 1981; Kelly & Fuller, 1980).

(b) The transient uptake in a single particle (*e.g.* Ruthven & Louglin, 1971; Ma & Ho, 1974; Do, 1983).

(c) The batch adsorber (*e.g.* Ma & Lee, 1976; Rice, 1982).

(d) The chromatographic methods (*e.g.* Haynes & Sarma, 1973; Hashimoto & Smith, 1973; Shah & Ruthven, 1977).

However, all of the techniques have the same disadvantage, *i.e.* the response used to measure the effective diffusivity is dependent on many different factors, such as residence time, amounts of solids in the reservoir, external mass transfer resistance, axial dispersion, non-uniform flowrate in the packed column, *etc.*

The advantages of unsteady-state techniques over the steady-state method can be summarised as follows. Firstly, the unsteady-state methods will detect diffusion in dead-end pores, and hence the effective diffusion coefficient obtained is known to reflect that in a reaction system more closely than those obtained in steady-state methods. Secondly, unsteady-state methods are suitable to measure effective diffusivities in bi-disperse structured catalysts. However, the time scale in the unsteady state method is often small so that determination of the effective diffusivity is difficult or even impossible, and requires complicated test methods and procedures to interpret the data.

2.4.2.1 Transient Wicke-Kallenbach method

The Wicke-Kallenbach (W-K) diffusion cell can be operated in transient mode, and this technique was developed by Smith and co-workers (*e.g.* Hashimoto & Smith, 1973, Dogu & Smith, 1975). The response for species was asserted to be only a function of the effective diffusivity of the porous solid and it was analysed with the moment technique. Examples of papers describing the use of the transient W-K method are listed in Appendix 2. It is interesting to compare the experimental conditions in each study, particularly, the size of the solid pellet. The design of the experimental apparatus may limit the amount of useful information which may be obtained from a pulse test,

irrespective of the method of analysis used. Dead volume in the apparatus may have a significant effect on the accuracy of the results.

The moment analysis may introduce serious errors in analysing diffusion data. The second moment of the response, which is sensitive to micropore diffusivity, is relatively inaccurate due to tailing of the experimental data. Time domain has been shown to be more accurate. However, most of the transient data obtained in the Wicke-Kallenbach type of diffusion cell has been analysed by using the moment technique because of the mathematical and/or numerical intractability (unruliness) of the diffusion cell in the time domain. There are a few exceptions, which take advantage of time domain fitting for the evaluation of effective diffusivity from transient diffusion measurements (*e.g.* Wakao & Kaguei, 1982; Do & Smith, 1984).

A number of workers (*e.g.* Clements, 1969; Curl and McMillan, 1966) have pointed out the practical disadvantages of the moment analysis of pulse experiments. Clements (1969) has shown that curve fitting of the single parameter axial dispersion model to Fourier transformed pulse data leads to a lower root mean square error than those obtained using parameters from moment analysis.

Al-Rqobar *et al.* (1988) used a time domain method using convolution integral and Fourier series (Wakao and Kaguei, 1982), to measure the effective diffusivity from a pulse response in a transient Wicke-Kallenbach diffusion cell. They proposed a combined moment technique and time domain fitting to improve the estimation of diffusion parameters.

2.4.2.2 Sorption rate experiments (or gravimetric method)

Adsorption experiments are suitable for the measurement of effective diffusivity in powder and granule materials. These experiments can be devised to be at constant volume and/or at constant pressure (Haynes, 1988).

By using a small sample of adsorbent exposed to a gas stream of constant composition in a flow system, the constant pressure technique has been used by Kondis and Drannoff (1971) to study sorption kinetics by measuring the weight gained or lost as a function of time. They used the single particle technique rather than the more traditional fixed bed

technique because of its greater sensitivity, both in the accumulation of experimental data and the differentiation of mathematical models.

Figure 2.15 shows a diagram of typical apparatus for sorption rate measurements. An important feature in this apparatus is the need for a highly sensitive microbalance. This consists of a small sample holder connected to a fine calibrated spring, in which motion is measured by an electric transducer and recorded continuously. The sample holder is contained within a Pyrex vessel of a sample tube through which gas is circulated. The sample tube can be submerged easily in either an electric furnace or an oil-filled constant temperature bath.

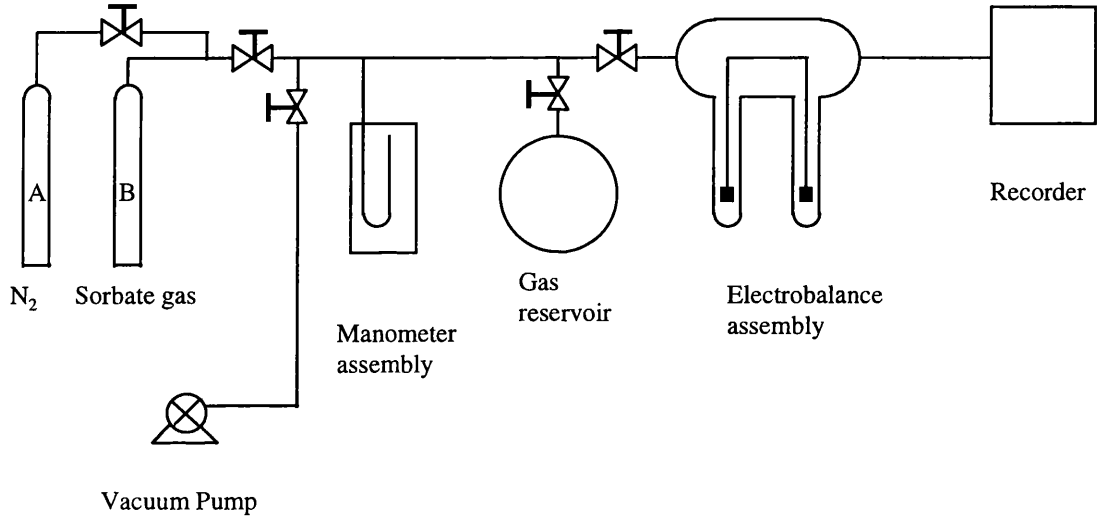

Figure 2.15. Schematic diagram of equipment for sorption rate measurements (adapted from Ruckensten *et al.*, 1971).

The usual pattern followed in such experiments is to regenerate a given adsorbent sample and then follow with an adsorption-desorption cycle, with continuous monitoring of the sample weight (which is indicated by the deflection of the spring on the microbalance). When thermal equilibrium is reached through the regeneration operation, an adsorption run is initiated by replacing the inert gas stream (usually, helium) with a predetermined mixture of helium and a target gas. The feed is maintained until the sample is saturated which is indicated by a constant weight. Desorption is then carried out by changing the feed gas to pure helium gas until the weight of the sample has returned to its initial value. A graph of the fraction of the target gas adsorbed and desorbed as a function of time is then constructed directly from

points on the recorded spring deflection-time trace. It is followed by a correction, which is made for the effects of buoyancy and drag by the gas stream flowing in the holder. Equilibrium loading data can be extracted directly from the final sample weight during adsorption.

The sorption uptake can also be measured volumetrically using a gas burette arrangement (Nelson & Walker, 1961). In principle, the procedure consists of charging the sample under investigation up to some fixed pressure (in excess of atmospheric), and then measuring the unsteady-state release of gas after a sudden reduction of the pressure to atmospheric.

2.4.2.3 Time lag experiments

To investigate porosity, tortuosity factor, mean capillary radius or the internal area of porous media, the time-lag method has been introduced by Barrer (1953). By applying Henry's law, this method can be extended to study adsorption and surface diffusion of adsorbed gases. The diffusion cell designed by Barrer and Barrie (1952) is shown in Figure 2.16. One side of the pellet is first evacuated and then the pressure increase downstream is observed over a certain time period while the upstream pressure is held constant. The change in pressure drop across the pellet during the course of the experiment is held to an insignificantly small value. There is a time lag before a steady state flux develops, so effective diffusion coefficients can then be calculated from either the unsteady-state or the steady-state data. Under unsteady-state conditions, correct analysis must allow for accumulation or depletion of material by adsorption, even if surface diffusion is insignificant.

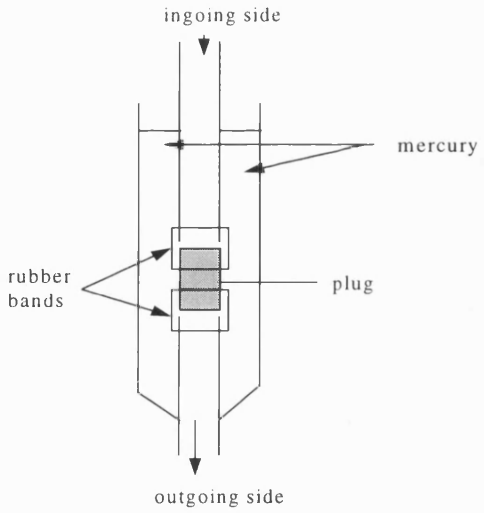

Figure 2.16. Schematic of a diffusion cell (adapted from Barrer & Barrie, 1952).

When measuring the flow rate of a gas through a thin slab of material (or membrane) in which the gas dissolves, there will be a time lag from the moment which the gas comes in contact with the slab until it emerges at a constant rate at the other side. It is possible to measure the diffusion coefficient in the porous catalysts by analysing stationary and unsteady-state flows. Barrer and Grove (1952) introduced an effective diffusivity calculated from the time lag observed in a plot of cumulative flow-through *versus* time. The surface area, which was determined by the time-lag method, is larger compared to the steady-state method (Barrer & Grove, 1952). During the time lag period (*i.e.* before the steady state is established), the penetration of gas involves every part of the surface and pore structure of the medium. In the steady state, dead-end pores contribute little to the rate of flow, so the surface area derived from steady state data can be negligible. The time lag method provides a good measure of the total surface area and of the average pore radius (Barrer & Grove, 1952). Explicit expressions for the time lag can be derived from Firsch's (1957) work, which can also be applied to systems with a concentration dependent diffusion coefficient without explicitly solving the diffusion equation.

2.4.2.4 Chromatographic experiments

A carrier gas (usually helium) is passed continuously though a chromatographic column packed with catalysts. A pulse of the diffusing component is injected into the inlet system and the effluent is measured by a detector and recorder. The concentration pulse of the injected gas is of a square form; thus, the time of injection can be calculated from

the known volume of the sampling loop and the flow rate of the carrier gas. Most of the parameters including partition coefficient, adsorption rate constant, interphase mass transfer coefficient can be obtained in theory, but in practice experimental conditions need to be adjusted for each target parameter. The sampling valve, the column outlet and the thermal conductivity detector inlet need to be connected in such a manner as to minimise dead volumes, but even in a carefully designed system, dead volume correction is usually required.

The calculation of the aforementioned parameters is generally completed by analysing the moment of the chromatogram (Kucera, 1965; Schanel & Schneider, 1971). It can be also achieved by comparing theoretically obtained curves and experimental curves. The curve fitting is to be time domain (Boersma-Klein & Moulijn, 1979) or obtained by Laplace transform or Fourier analysis (*e.g.* Ramachandran & Smitz, 1978; Gangwal, *et al.*, 1971). Figure 2.17 shows an example of the gas chromatography apparatus for measuring effective diffusivity (Hsu & Haynes, 1981).

This method has advantages as the experimental set-up is relatively simple and it is possible to perform experiments at high temperatures. However, if a catalytic monolith was to be used, then the mass of washcoat per unit volume of the bed may be too small to affect the measured output. Also, it would be difficult to coat and quantify the uniformity and thickness of the washcoat layer on which diffusion experiments has been performed.

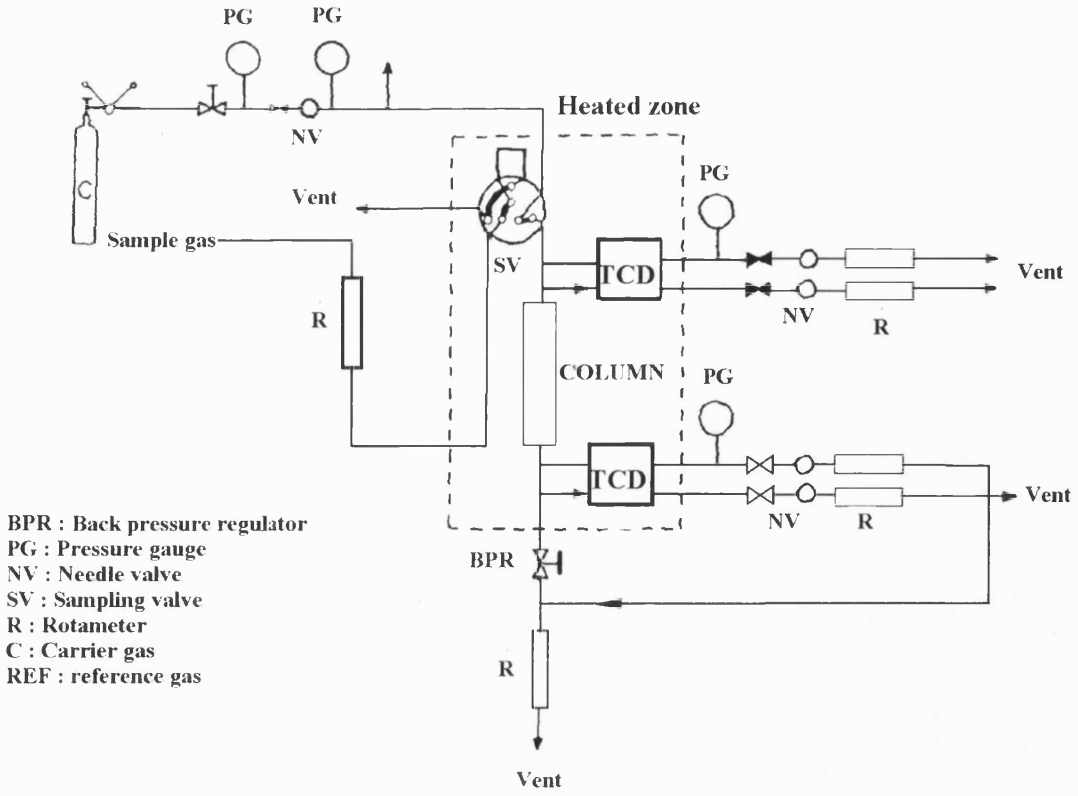

Figure 2.17. Pulse gas chromatography apparatus (adapted from Hsu & Haynes Jr., 1981).

2.4.3 Experimental measurements relevant to monolith catalyst

Unfortunately, there are very few studies in the literature that describe work on catalytic monoliths. Table 2.4 lists examples of experimental measurement of effective diffusivity in catalytic monoliths. The work by Beeckman (1991) is interesting as an actual sample of monolith is used and the construction of the diffusion cell resembles the well-known Wicke and Kallenbach cell (1941). The monolith had catalytic material incorporated into the structure of the monolith, and the catalyst was used for the selective catalytic reaction (SCR) of oxides of nitrogen. The incorporation of an actual monolith into the structure of a diffusion cell has attracted other researchers, *e.g.* Li (1997) and Roduit *et al.* (1998). This is because the technique has an advantage that the structure of monolith remains undisturbed so that the characteristics of the monolith are unchanged. Whereas, in the technique reported in Santos *et al.* (1996), (who also studied an SCR catalyst), they used particle of an SCR catalyst that they packed into a column (4.36 m in length; 0.0107 m in internal diameter) and then they used the chromatographic technique.

Table 2.4. Experimental measurement of D_e - Examples of measurements relevant to this thesis.

Author	Description of system and Materials studied	Measurement method and components	Comments
Beeckman (1991)	The catalyst is used to reduce NO_x from exhaust emissions and is an integral part of the monolith wall. It is not a coated system. Cell dimensions: 6 mm in diameter.	Steady state method. Modified form of Wick-Kallenbach type of cell. Counter current flow in a single channel cut from a monolith. Component: NO/N_2.	Experiments performed at room temperature. Equimolar counter diffusion was assumed. When compared with theoretical values calculated using random pore model by Wakao & Smith (1962) model the match was within ±10%. Tortuosity is close to 2.
Santos *et al.* (1996)	The catalyst is employed as SCR for NO_x and is a V_2O_5+WO_3+TiO_2 with an agglomerating agents based on a magnesium silicate (sepiolite).	Chromatography method. The catalyst pellets were packed in a copper column (4.36m in length and 0.0107 m ID). Component: Ar, O_2, N_2/He.	Operating temperature: 298-473 K. Tortuosity values (2.62 - 3.61) obtained were larger than those obtained by Beeckman (1991).
Li (1997)	The catalyst is used to oxidise methane for catalytic combustor and consists of a washcoat of γ-alumina on cordierite monolith. Cell type and dimension: hexagonal, 2.4 mm ID, thickness of support: 0.4 mm and thickness of washcoat 0.1 mm.	Steady state method. Modified form of Beeckman's method. Co-current flow in 7 channels cut from a monolith. Component: CH_4/N_2.	Experiments performed at room temperature. Equimolar counter diffusion. Experimental values of D_e for cordierite support and the washcoat were 3.1 and 6.9 time smaller that the values predicted by Wakao-Smith model, respectively. The tortuosity factors were 8.5 and 8.1 for the support and the washcoat respectively.

Table 2.4. Experimental measurement (continued .....).

Author	**Description of system and Materials studied**	**Measurement method and components**	**Comments**
Roduit *et al.* (1998)	The catalyst is for selective catalytic reduction (SCR) reaction of NO with NH_3 and contains TiO_2 (70%), V_2O_5 (5%), WO_3, and MoO_3 as integral part of monolith. Characteristic: geometry: honeycomb with square ducts; wall thickness: 0.78mm; channel pitch: 3.45 mm.	Experiment: same as Beeckman's method.	Experiment performed at different temperatures of 200-450°C.

In Beeckman's technique, a single cell is used as a catalyst, which is cut out from an industrial-sized monolith. A stainless steel tubing with a square shape on one end is inserted into the single channel and glued with epoxy to the catalyst. The catalyst and tubing are then inserted into a Pyrex glass enclosure of a diffusion cell and sealed tight using a clamp on the centre o-ring closure shown in Figure 2.18.

A schematic diagram of a diffusion cell is shown in Figure 2.19. The diffusion equation derived by Beeckman is based on the material balance over the axial distance, *dx*, along the cell. The diffusing species, NO, was introduced in counter current flow.

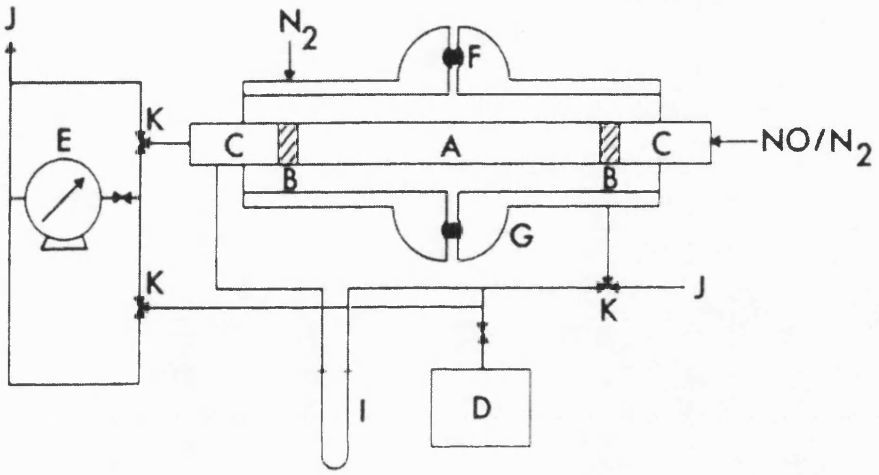

A:catalyst channel B:Epoxy glue C:1/4 inch steel tubing D:NO analyser
E:gas meter F:O-ring closure I:manometer J:vent K:3-way valve

Figure 2.18. Experimental set-up of the Beeckman's diffusion cell (adapted from Beeckman, 1991).

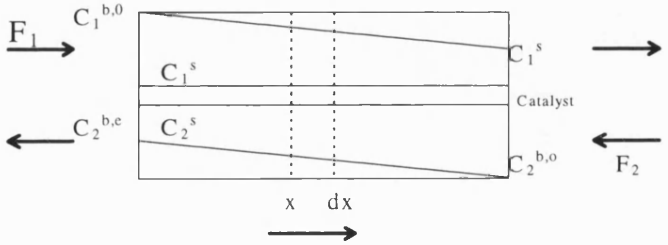

Figure 2.19. Schematic of a diffusion cell (adapted from Beeckman, 1991).

This approach by Beeckman (1991) was later extended by Li (1997) in order to measure the effective diffusivity of methane in a commercial monolith catalyst. There are a few modifications in Li's approach, see Figure 2.20:

- Instead of using a single channel, Li used seven channels, and the shape of channel was hexagonal, consisting of a central channel surrounded by six channels
- The hydraulic diameter of a channel is much smaller than that used in Beeckman's experiment.
- The two gas streams, N_2 and CH_4, flowed co-currently
- The walls of the channel consisted of composite layers of alumina washcoat on a cordierite substrate.

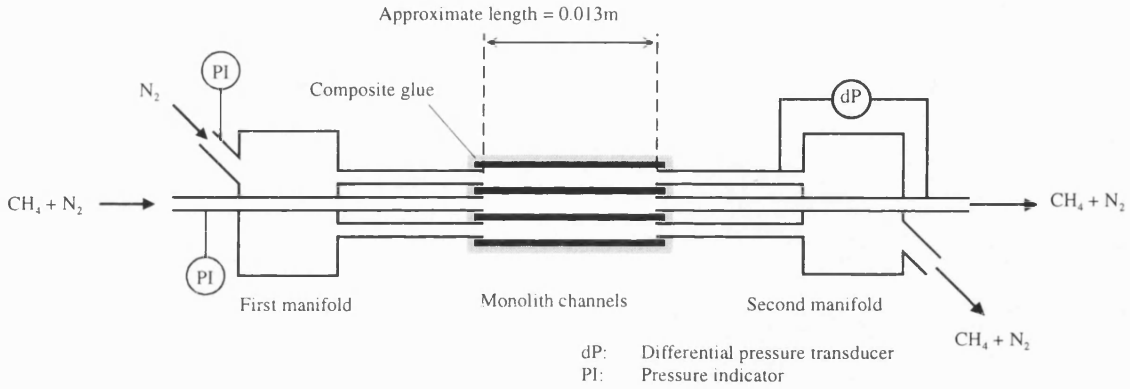

Figure 2.20. Schematic of the diffusion cell used in Li (1997).

Moreover, by using a hexagonal monolith, a relatively uniform thickness of washcoat could be obtained, as the angle of the corner is greater in hexagonal monoliths than in rectangular ones. For example, the catalyst monolith studied by Hayes and Kolaczkowski (1994) has a washcoat which was 10 μm thick at the centre of the channels and 150 μm at the corners, whereas in Li's experiment it was 40 ± 20 μm.

Monoliths are manufactured in a wide range of sizes and shapes. The shapes are mostly square, hexagonal and triangular. The design of the diffusion cell will depend on the size and shape of the monolith. Li (1997) measured the effective diffusivity of methane through honeycomb ceramic monoliths and selected a total of seven channels namely a central channel and the six surrounding channels. In a square monolith a total of five channels can be selected and three in a triangular configuration, see Figure 2.21.

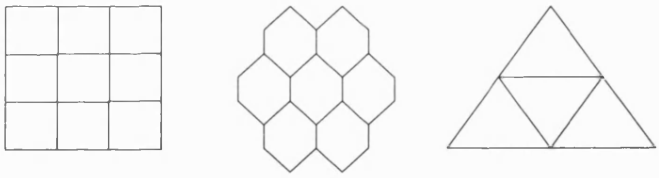

a) Square b)Hexagonal c)Triangular

Figure 2.21. Cross-sectional views of typical cell geometry of monolith.

The experimental apparatus shown in Figure 2.22 is similar to the Wicke-Kallenbach cell and is operated at a steady state. The main component of the apparatus is the selected monolith channel, which is used as a diffusion cell. The selected channel is connected and sealed to stainless tubing. Selection of the right sealing material is important to prevent gas leakage. The sealing material must be applied to both the connections and the surroundings of the selected channels. If the experiment is operated at high temperature and high pressure, temperature-resistant and pressure-resistant materials have to be chosen. The diffusing component, *e.g.* CH_4, was fed into the central channel and the other gas was fed into the surrounding channels. Pressures in the surrounding channels were equalised by joining them together with manifold at both ends. Flowrate and composition were monitored in the central channel and in the manifolds. The thermal conductivity detector from a gas chromatograph was used for continuous monitoring.

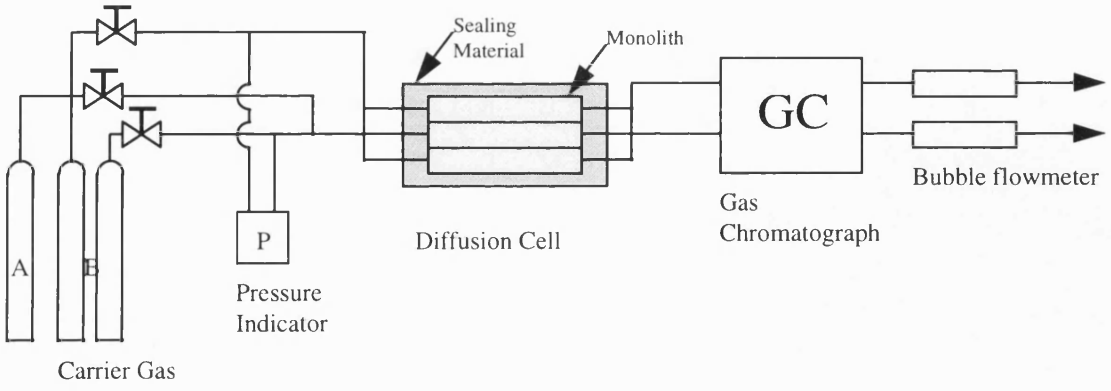

Figure 2.22. Schematic diagram of an apparatus.

2.5 Sol-gel method

Over the last decade, the sol-gel process as a method of preparing a washcoat has attracted considerable interest. A comprehensive review on sol-gel chemistry of metal oxides has been carried out by Livage *et al.* (1988). The chemistry of the sol-gel process is based on hydroxylation and condensation of molecular precursors. Two different routes are usually described in the literature depending on whether the precursor is an aqueous solution of an inorganic salt or a metal organic compound. The most versatile precursors of the sol-gel synthesis of oxide are undoubtedly metal alkoxides, which are very reactive toward nucleophilic reagents, mainly water.

Sol-gel technique has mainly been used for the preparation and/or fabrication of glass and ceramic products. Some selected examples of applications are:

1. Preparation of glass and ceramic fibres (*e.g.* Kamiya *et al.*, 1980).
2. Coatings and films (*e.g.* Abraham, 1975).
3. Porous solids and microballoons (*e.g.* Zarzycki *et al.*, 1982; Yoldas, 1975, Wehrenberg, 1978).
4. Nuclear fuels and radioactive wastes (*e.g.* Anold *et al.*, 1982).
5. Transition metal oxide gels (*e.g.* Bullot *et al.*, 1980).

Porous solids prepared by sol-gel methods may be attractive for chemical engineering application, *e.g.* membranes and filters, and supports for catalyst. It is because the gel calcined at relatively low temperatures (>300°C) is an extremely porous solid and the pores are predominantly interconnecting and open (*e.g.* Zarzycki *et al.*, 1982). The porosity and pore size distribution can be controlled by conditions such as precursor material, peptising reagent and peptisation temperatures (*e.g.* Leenaars *et al.*, 1984; 1985). For example, in a silica gel, the pore diameters can range from 20 to 80Å, and the porosity can be greater than 50%. Surface areas in excess of 900 m^2/g have been reported for silica gels dried at 40°C and even after heating at a couple of hundred degrees, a great deal of porosity is retained (Brinker *et al.*, 1982).

Table 2.5 lists some examples of catalytic applications where the sol-gel technique has been used. Application of the sol-gel technique on monolith supports has also been reported. According to DeLuca and Campbell (1977), the first application was reported by Foster and Meissner (1973) who developed a method of coating on monolithic

supports by in situ hydrolysis of various metal alkoxides. The procedure involves impregnating a monolith with alkoxide solution, which contains the desired metal.

Table 2.5. Examples of applications of sol-gel method in catalysis.

Author	Type of sols	Catalysts	Reactions or application
Carturan & Collegues (1978,1980,1984)	Al_2O_3, SiO_2 , NaO	Pt, Pd	Hydrogenation of Olefins
Guilhaume & Primet (1994)	Spinels	CuO	Combustion of methane
Seker & Gulari (1998)	Alumina	Pt	Catalytic reduction of NO_x
Li & Gonzalez (1996)	-	Sulphated Zirconia	Isomeration of butane
Cho *et al.*(1998)	Alumina	Pt	Investigation of physico-chemical properties
Hirashima *et al.* (1998)	-	Al_2O_3,ZrO_2, V_2O_5	Reduction of NO_x
Lange *et al.*(1998)	Titania	Pt	Selective hydrogenation
Wang & Lin(1998)	Alumina	CuO	Flue gas desulphurisation

To prepare an alumina layer, aluminium *i*-propoxide may be used. Then, the impregnated monolith is heated with water vapour to precipitate a hydroxide or oxihydrate, and then dried and calcined to obtain the oxide. Nelson *et al.* (1981) prepared coating of metals with ceramic oxides using colloidal intermediates. Then, they performed catalytic combustion experiment. In the paper a catalyst consisting of platinum dispersed in a high surface alumina, was prepared in a form suitable for bonding to Fecralloy^{TM} steel by using an aggregated alumina sol. By testing the ability of the catalyst to oxidise propane at various temperatures, they demonstrated that complete combustion of propane could be achieved at a temperature of 300°C. The catalyst was shown to have excellent thermal durability (due to the stable pore structure and surface area of the alumina produced from the aggregated sol).

Zwinkels *et al.* (1995) prepared by dip coating, a washcoat on whisker-covered metal monoliths with a silica suspension consisting of silica powder mixed with a colloidal

silica sol by dip coating. They reported that the use of colloidal sols with varying particle size distributions provided a way to control the specific surface area and pore size distribution of the washcoat. Increasing the thickness and hence internal surface area also leads to increased activity. However, the preparation procedure strongly influences the activity of the prepared catalysts.

2.4.1 Thermal resistance materials

γ-Alumina and its transition forms have often been used in catalytic applications where high specific surface area and catalytically active sites are needed. However, the transition aluminas are metastable phases and above a temperature of about 900°C there is a transformation to α-alumina with a catastrophic loss of specific surface area and a change of surface chemistry, which diminishes their usefulness in catalysis. Such morphological changes in catalyst support are accompanied by a loss of catalytic activity occasioned by encapsulation of the metal (*e.g.* Arai & Machida, 1996; Djuricic *et al*, 1997). The loss of activity is permanent, because the transformation of the metastable γ-alumina is irreversible.

Therefore there is considerable interest in improving the thermal stability of transition aluminas so that processes can be operated at higher temperatures with a corresponding gain in efficiencies. The stabilisation of the metastable phases depends on inhibiting nucleation of γ-alumina. Nucleation cannot occur as long as the primary particle sizes of the transition aluminas are smaller than the critical nucleus size for the α-alumina.

Since the sintering of transition aluminas occurs thermodynamically, the most convenient method of stabilisation is kinetically to inhibit sintering by adding dopants. The effect of dopants on surface area of alumina support has been extensively studied for use as automotive emission controls, steam reforming and catalytic combustion. Table 2.6 presents some study of use of these elements as a dopant to improve the thermal stabilisation of alumina.

Recent studies have focused on using heterometallic alkoxides as precursors (Caulton & Hubert-Pfalzgraf, 1990). In some applications, it is desirable to incorporate at least one other metal atom in the aluminium oxide material. For example, it has been found desirable when employing the aluminium oxide material as a catalyst support to include

atoms of lanthanum, cerium, calcium, strontium, barium, or all, in the aluminium oxide (alumina) matrix. Incorporating any of these metal atoms in the alumina matrix tends to prevent structural changes that occur in unstabilised γ-alumina at high temperatures. In addition, some of these metals (*e.g.* CeO_2, ZrO_2) are included to provide oxygen storage in the alumina for catalytic applications involving oxidation.

Table 2.6. Examples of thermal stabilisation of alumina by dopants (adapted from Arai & Machida, 1996).

Researcher	Dopant	Remark
Revy & Bauer (1967)	Li, K, Mg-activated alumina	*ca.* 600°C, 240 m^2/g
Amoto *et al.* (1975)	Ba-γ-Al_2O_3	*ca.* 1200°C
Amoto *et al.* (1975)	Si-γ-Al_2O_3	*ca.* 1200°C
Burtin *et al.* (1987)	Zr, Ca, La, Th doped alumina	Kinetic model of stabilisation
Schaper *et al.* (1987)	La-γ-Al_2O_3	1000°C, 120 m^2/g
Oudet (1988)	Latanide (La,Pr,Nb)-alumina	1150°C, 63 m^2/g
Johnson (1990)	Ba, Sr, La, Sn, SiO_2, PO_4+ γ-Al_2O_3	*ca.* 600°C
Niwa *et al.* (1990)	SiO_2 coated alumina	1220°C, 91 m^2/g
Beguin *et al.* (1991)	La-γ-Al_2O_3	1050°C,51 m^2/g
Beguin *et al.* (1991)	La-γ-Al_2O_3	900°C, 92 m^2/g
Konan *et al.* (1992)	SiO_2-Al_2O_3, mullite	1400°C, 31 m^2/g
Horiuchi *et al.* (1993)	SiO_2-Al_2O_3	1300°C, 46 m^2/g
Duricic *et al.* (1997)	ZrO_2-Al_2O_3	1200°C, 36 m^2/g

In this thesis, the addition of zirconia to alumina will be briefly considered, as it is a recognised method of improving the thermal stability of the washcoat. As illustrated in Figure 2.23, the surface area of zirconia decreases relatively slowly with temperature, compared to alumina, which has a dramatic change with temperature in the range of 673K - 1173K. Some metal catalysts (*e.g.* Cu, Rh), when supported on zirconia, have shown higher activity relative to being supported on other oxides, such as, ZnO, Al_2O_3, SiO_2 (Amenomiya, 1987; Iizuka *et al.*, 1982) and also in their selectivity (Bruce, *et al.*, 1983).

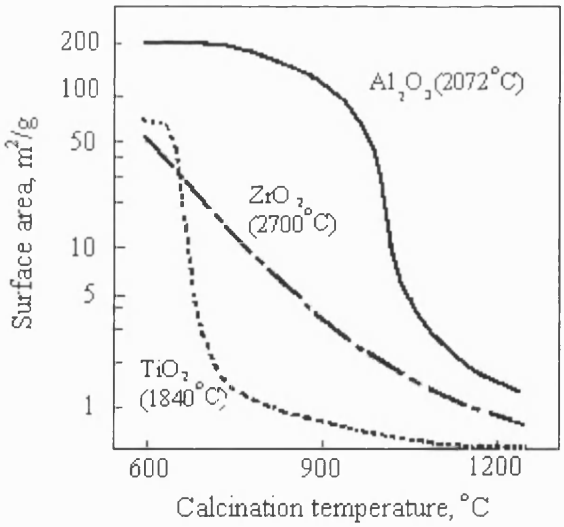

Figure 2.23. Temperature dependence of specific surface area of metal oxide supports (adapted from Arai & Machida, 1991). Melting point shown in the parentheses.

2.4.2 Cracking of washcoat

Shrinkage of the coating film upon heating is considered to be one of the main causes of cracks appearing in the washcoat. Shrinkage is a general problem in the sol-gel methods.

Sakka (1989) speculated that when the gel film is too thick, the coherent force within the film would cause shrinkage of the film in the direction parallel to the substrate plane. If this coherent force exceeds the bonding of the film to the substrate surface, the film may come off. It is expected that the bonding energy between the film and the substrate is large compared with the coherent force in thinner films. In this case, the film is supposed to shrink in the direction perpendicular to the substrate plane, resulting in the formation of a film that bonds firmly to the substrate.

Sherer (1989) reported that the drying stress in the film is nearly equal to the surface tension in the liquid. Until present, the rapid and reliable production of gel has been difficult to realise because of the lack of control over drying stress and cracking. The phenomenon can be described in the relationship between the tension in the film and the capillary stress. The stress (θ) in a film is approximately equal to the tension in the liquid when it existed in the form of a suspension. As the film becomes rigid due to evaporation of liquid, the tension in the film becomes equal to the capillary stress,

which would shatter a macroscopic gel. However, according to the liteature, inorganic films thinner than ~0.5mm do not crack, regardless of the drying rate, whereas films thicker than ~1mm are virtually impossible to dry without cracks (*e.g.* Sakka *et al.*, 1984; Strawbridge & James, 1986).

Zarzycki (1986) described the drying stress as a function of pore size and rate of evaporation of the pore liquor, which depends on the liquid vapour pressure. A few researchers (*e.g.* Sherer, 1989; Zarzycki *et al.*, 1982) have reported that cracking of the film can be reduced by controlling the rate of evaporation of liquid. Therefore the peeling-off may be reduced in the same manner.

Hench and Ulrich (1984) has introduced the use of organic additions to alkoxide sols, termed drying control chemical additives (DCCAs), to control the rate of hydrolysis and condensation, pore size distribution, pore liquor vapour pressure, and drying stresses. The possible DCCAs include formamide (NH_2CHO), glycerol ($C_3H_8O_3$), and several organic acids, such as oxalic acid ($C_2O_4H_2$).

Figure 2.24 illustrates how the use of organic DCCAs can control crack formation (Ulrich, 1988). Without a DCCA a wide range of pore sizes and diameter of solids network are produced when gelation occurs. Differential growth of the solid network will therefore occur during ageing due to local variations in solution-precipitation rates. The net effect is an aged gel structure with many regions susceptible to cracking during drying.

Addition of a basic DCCA such as formamide produces a large sol-gel network with uniformly large pores. An acidic DCCA, such as oxalic acid, in contrast results in a somewhat smaller scale of network after gelation, but also with a narrow distribution of pores. Thus, either basic or acidic DCCAs can minimise differential rates of evaporation and ensure a uniform thickness of the solid network that resists the drying stress. Achieving a uniform scale of structure at gelation also results in uniform growth of the network during ageing which thereby increases the strength of the gel and its ability to resist drying stresses.

Artaki *et al.* (1986) dealt with the effect produced by the addition of chemical additives on the polymerisation stage of the sol-gel process. The medium in which the condensation reaction occurs has been shown to be of critical importance in the determination of the structural state before and after gelation.

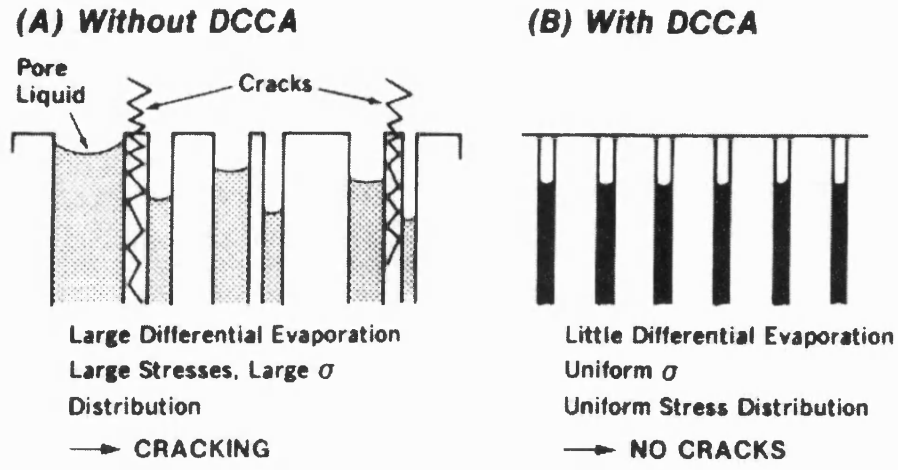

Figure 2.24. Control of sol-gel process with organic DCCAs (adapted from Ulrich, 1988).

The size and shape of the polymeric particles produced in the presence of the various solvents have been shown to be strongly dependent on the hydrogen bonding and electrostatic interactions in the sol-gel system. A strong network of hydrogen bonding, as in the case of the formamide system, sterically shields the reaction centres, promoting the formation of branched structure of larger or more uniformly distributed micropores. They concluded that the solvent medium should be included among the better studied control parameters (*e.g.* pH, temperature, metal concentration, water/alkoxide ratio).

2.4.3 Factors affecting the thickness of washcoat

According to Sakka (1989), the following factors might affect the thickness of crystalline dip-coating films (within the thickness range where uniform films form that are attached to the substrate):

(a) The viscosity of the coating solution: the thickness of the film increases with increasing viscosity. It is proportional to the square root of the viscosity.

(b) The rate of withdrawal: the thickness increases with increasing the rate of withdrawal. It is proportional to the square root of the rate of withdrawal.

(c) The oxide concentration of the solution: the thickness increases with increasing oxide concentration of the coating solution.
(d) Heating temperature and time: gel coated films are porous and sintered when they are heated. Accordingly, the film thickness decreases with increasing heating temperature and time.

A thicker film can be obtained by repeating the coating procedure. In this case, it is essential to repeat the whole procedure consisting of dipping of the substrate, its withdrawal and heating. Omitting the last step in process (*i.e.* heating) would lead to peeling of the film. It is assumed that the film becomes a part of the original substrate after heating.

2.4.4 Sol-to-gel transition

The textural properties of a gel depend upon the method of drying. There are three methods that can be used. The first method is drying at atmospheric conditions and the dried gels are called xerogel. The second method is drying in supercritical conditions and the dried gel is known as aerogel. The third method involves eliminating the solvent by freeze drying by sublimating the frozen solvent in order to prevent the formation of menisci between the solid-liquid and liquid-vapour interfaces. The freeze-dried gel is called cryogel. Their textural properties are very close to those of aerogel and xerogel.

The fabrication of finely divided powder or monoliths via a sol-gel process requires at least four steps: hydrolysis, peptisation, ageing and finally drying. The last step may either conserve or destroy the qualities obtained during the three previous steps (*e.g.* Brinker & Scherer, 1990).

2.4.5. Advantage and disadvantage of the sol-gel methods

Based on the review of literature, the advantages and disadvantages of sol-gel methods are summarised in Table 2.7. Compared to commercial alumina, sol-gel processed materials are expensive. There is some cost reduction because the washcoat can be loaded on the honeycomb substrates as a uniform layer without filling up the corners of the channel (Narula *et al.*, 1993).

Table 2.7. Some advantages and disadvantages of sol-gel methods.

Advantages

1. Easy to control the physical properties by calcination.
2. Distinct texture due to different drying step.
   (xerogel, aerogel, cryogel).
3. Uniform layer of washcoat.
4. Relatively good thermal stability.
5. Strong adhesion to monolith substrates.
6. High specific surface area.

Disadvantages

1. High cost of raw materials.
2. Long processing time.
3. Large shrinkage during processing (gelling, calcining).
4. Lack of information and unfamiliarity.

Conclusions

From the review of the literature it is clear that there have been very few published experimental studies on the measurement of effective diffusivities in catalyst coated monoliths. Also, it appears that there has been no published work on the diffusion of gasoline components in monoliths.

Recognising that the characteristic properties of the washcoat depend on the method of preparation, it was decided to coat samples of cordierite with alumina, using the sol-gel method. Measurements would then be performed on a structure that more closely resembled commercial application of this technology.

In the application of interest, gasoline is a potential fuel, however, its composition is complex. It was therefore decided to select the hydrocarbons: *n*-pentane, *n*-hexane, *n*-heptane and *n*-octane as model compounds to represent the range of species encountered. This will pose certain experimental difficulties, as they are liquid at room temperature. To act as a reference base, experiments will also be performed with methane. This is a gas at room temperature, so potential problems of vaporisation and condensation will not be encountered. Also it will be possible to compare the results with methane with other published experimental data.

As catalytic combustion occurs at elevated temperatures, it was decided to design an experiment where the effect of temperature could be assessed. Within the constraints of available equipment, a temperature range of 100 to 300°C was selected. This in itself posed a challenge, as the maintenance of a seal around a fragile sample of the washcoated monolith would be difficult.

In looking at the published literature on the way in which the effective diffusivity, D_e, has been calculated in a model of a catalytic combustor, it is clear that intraphase diffusion should be modelled and that very little has been done to check the validity of the method used to calculate D_e value. Hayes *et al.* (2000) showed that the experimentally measured D_e values are significantly smaller than those obtained from random pore model. However, experiments were not performed with hydrocarbons representing gasoline and neither were the properties of the washcoat varied. So it is clear that there is a need to study the link between the properties of the washcoat and D_e values.

In order to select and/or develop an experimental technique for measuring diffusion in a catalyst, the following issues were considered:

- What precision and accuracy are required?
- What will cause interference?
- Acceptability of the technique.
- Geometrical shape of the catalyst.
- Ease and convenience in operation.
- Speed.
- Cost and availability of the equipment.

Furthermore, it was necessary to assess if the selected technique can be applied to a real catalyst (or commercial catalyst) and whether the characteristics of the catalyst can be retained during the preparation of the specimen.

The Wicke-Kallenbach (1941) experiment is a classical experimental technique that is extensively used to evaluate the effective diffusivity of catalyst pellets. This technique has been used widely to measure the effective diffusivity in catalysts because it offers the convenience of a simple design and ease of operation. Many theoretical and

experimental studies using this technique have been described in the literature over the last few decades (Park *et al.*, 1996). However, this steady-state method has been criticised, as it cannot detect the contribution of dead-end pores. By extending the method to include an analysis of transient response (*e.g.* Hashimoto & Smith, 1973; Dogu & Smith, 1976), the contribution of dead-end pores could be considered.

Using the Wicke-Kallenbach type of cell, experiments have generally been performed on catalyst pellets that are 5mm thick. The catalyst coated monolith wall is only 0.25mm thick, so this posed a number of problems. One option considered was to crush the monolith and then form a pellet by pressing the powder into a desired shape to fit the cell. This was rejected, as the characteristics or texture of the pellet would differ from the washcoat on a substrate. Beeckman (1991) and Li (1997) adapted the Wicke-Kallenbach technique to perform measurements on actual samples of monolith. Although this looked interesting for the controlled series of experiments planned in this thesis, it would be difficult to coat the perimeter of the cell in a uniform manner and to ensure uniformity along the axial length of the channel. Also, sealing the ends of the channel for experiments at 300°C would be difficult.

It was therefore decided, to cut a section from the cell wall of the monolith, into the form of a plate. Although the manufacture of this plate is difficult (because of fragility due to thinness of the wall structure, 0.25mm thick), the characteristics of the structure are not changed. This support would then be coated with the washcoat material, and then the plate would be sealed in a cell.

Chapter 3. Design of Experimental Apparatus and Techniques for Diffusion Measurements

In this chapter, the design of the experimental apparatus, and the results of preliminary experiments are presented. The sequence of events is summarised in Figure 3.1.

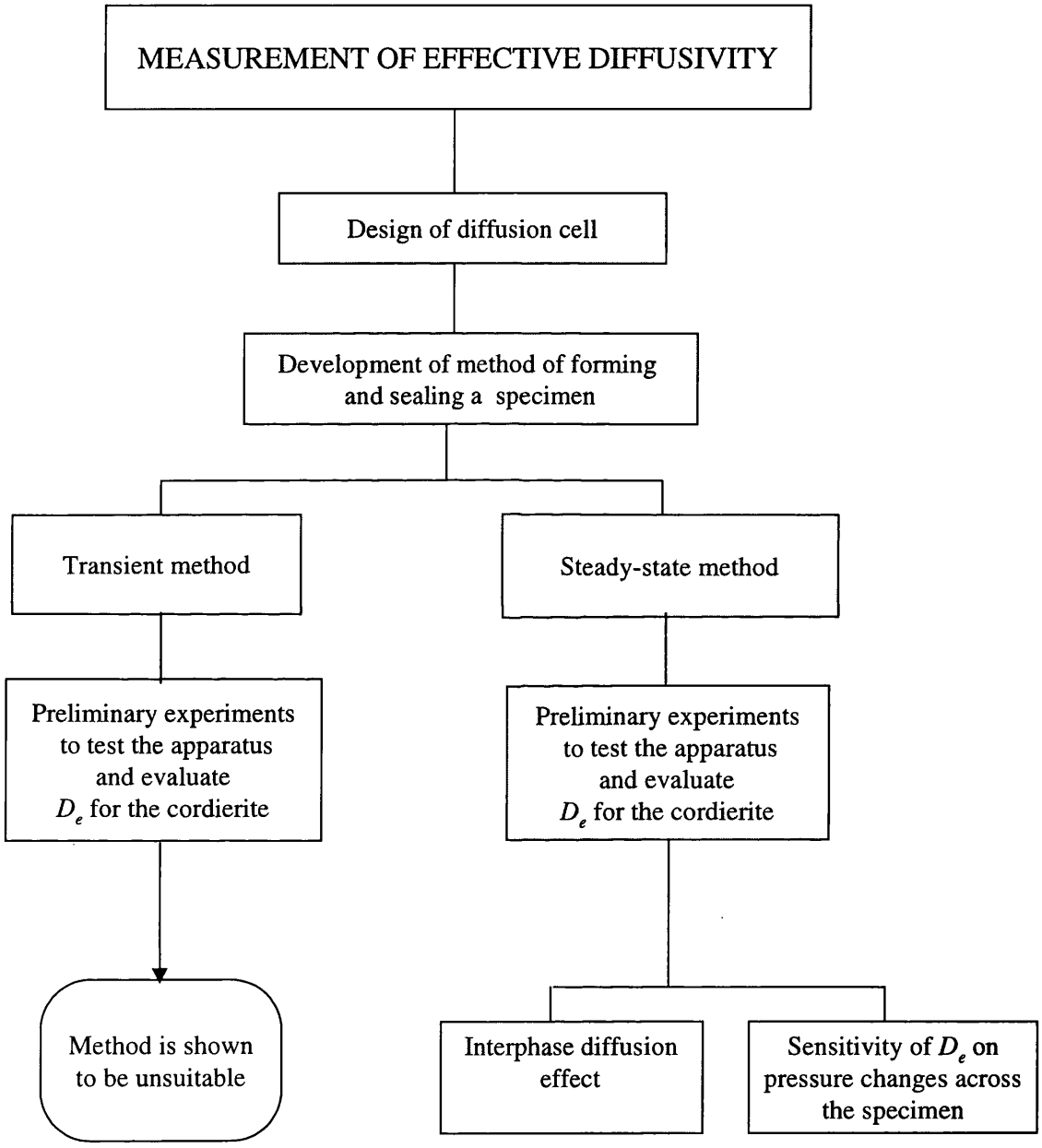

Figure 3.1. Schematic illustrating the link between events described in Chapter 3 (note: this links with Figure 1.2 in Chapter1).

3.1 Introduction

Having decided to design a diffusion cell where a sample of coated cordierite plate (or wafer) could be sealed in a cell, see Figure 3.2, the possibility of performing both steady state and transient methods of analysis were considered. The general advantages and disadvantages are summarised in Table 3.1.

Besides having to face the problem of sealing a fragile plate, where the catalyst layer is very thin (1-10 μm) on a 250 μm support, when planning experiments with gasoline, additional challenges are faced:

(a) At ambient temperatures gasoline is a liquid.

(b) Problem of sealing the specimen for measurements at high temperatures.

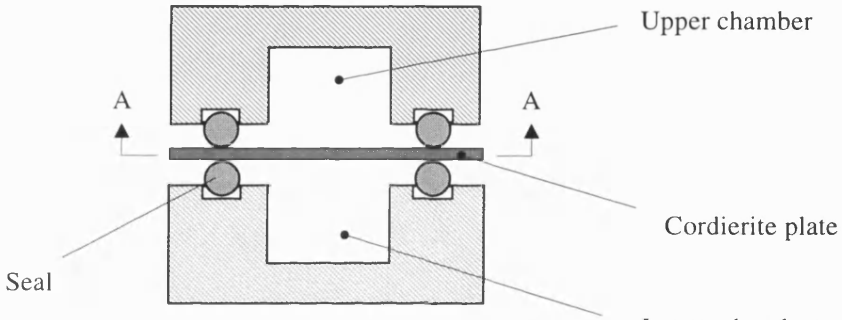

(a) Schematic

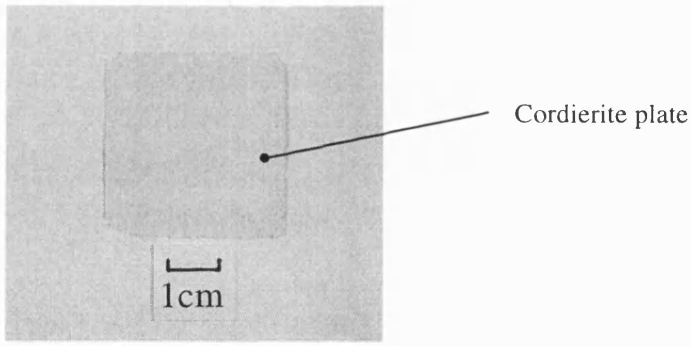

(b) Section view A-A

Figure 3.2. Schematic illustrating the concept of using a thin plate cut from a cordierite monolith.

In this chapter, the following aspects are considered: (a) the preparation of specimen consisting of a suitable washcoat support and development of sealing techniques, (b) a description is provided of the experimental apparatus and procedure, and (c) results are

presented of preliminary experiments and performance tests to assess the characteristics of the experimental rig.

Table 3.1. Advantages and disadvantages of diffusion cell measurements.

Type	Advantages	Disadvantages
Steady-state experiments	(a) Axial dispersion, gas flow maldistribution, gas-to-solid mass transfer can be eliminated. (b) Direct measurement of D_{eff}. (c) Not affected by finite heat transfer.	(g) Dead-end pores are inaccessible.
Transient experiments	(d) Same as No. 1 above. (e) Data collection is fast. (f) The contribution of dead-end pores can be assessed.	(h) Mathematical interpretation of results is more tedious.

3.2. Preparation of cordierite plates

In preliminary experiments, it was quickly realised that the cordierite plate cut from the monolith was too thin and fragile to mount directly in the diffusion cell. An electroplating technique was therefore considered to build a metal layer on the plate, which would act as a seal and provide rigidity. However, the ceramic plate has a very low electrical conductivity, and it is necessary to increase its electrical conductivity so that metal would grow on the surface. To do this, gold was selected as a conductive material and this was first deposited on the ceramic plate by using a sputter machine (*Edwards 5150B sputter coater*). In order to maintain a section of the plate clear, a paper disc was attached to both sides of the plate before sputtering with gold. This section remains free of gold, and hence metal cannot grow on it during the electroplating process, see Figure 3.3. The gold-deposited plates were then loaded into an electrochemical cell.

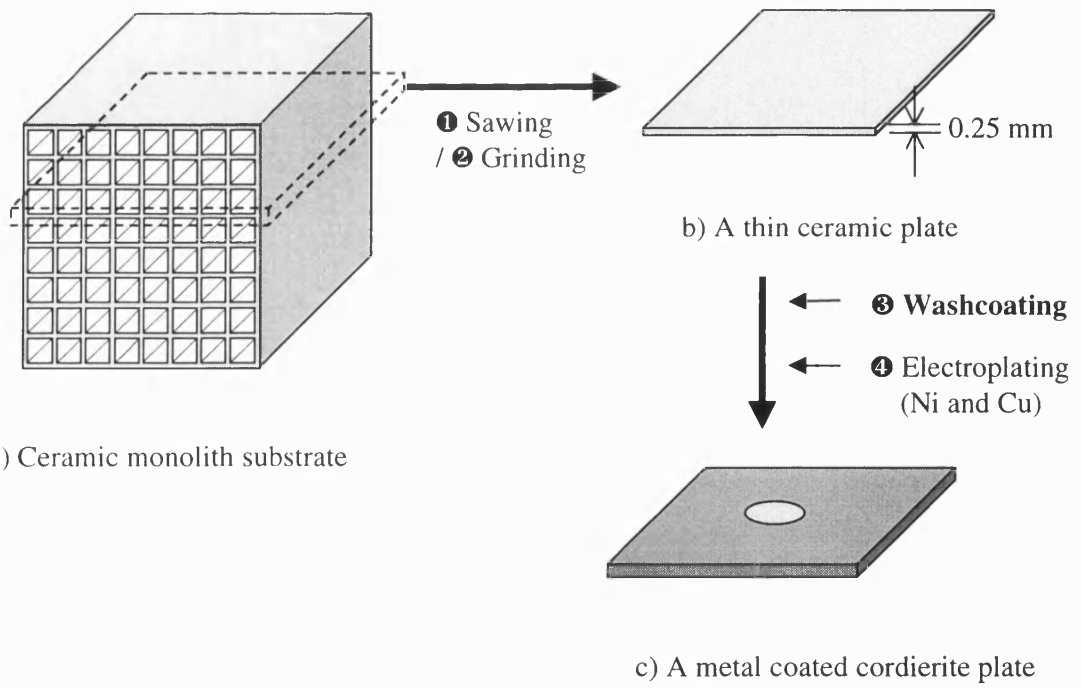

Figure 3.3. The preparation procedure for a sample: ❶ sawing, ❷ grinding, ❸ washcoating, and ❹ electroplating.

In order to ensure success with the electroplating process, it was necessary to pre-treat the cathode, and to select anode material, plating bath, current density and other electrolysis conditions (*e.g.* temperature, pH). The following types of layers may be formed during electroplating (Pletcher & Walsh, 1993):

(a) Single metals: *e.g.* Sn, Cu, Ni, Cr, Zn, Cd, Pb, Ag, Au, and Pt.

(b) Alloys: *e.g.* Cu-Zn, Cu-Sn, Pb-Sn, Sn-Ni, Ni-Co, and Ni-Fe.

Ideally, the metal should have the same coefficient of thermal expansion as the ceramic in order to avoid cracking. However, many of the metals with a low thermal expansion, were unsuitable because of their poor deposition properties as a result of their low current efficiency. For example, copper has very high current efficiency, but its thermal expansion is also high (17.0×10^{-6} in/in·K^{-1}), while in case of chromium with a low thermal expansion (6.5×10^{-6} in/in·K^{-1}) it has a low current efficiency. After screening and testing, two kinds of metals, nickel and copper, were found to be suitable for this work. Nickel was found to be suitable because its thermal expansion is relatively low (13×10^{-6} in/in·K^{-1}) and its current efficiency is good. However, producing a thick and hard nickel layer was very difficult because the layer of nickel was found to shrink and bend when it become thicker. Therefore, nickel was firstly electroplated as a thin layer

(« *ca* 1 mm) and then copper was deposited in order to increase the strength of the plate. The electroplating conditions for copper and nickel used in this study are listed in Table 3.2.

Table 3.2. Electroplating conditions used.

Metal	Electrolyte Composition (g/l)	T (°C)	I (mA/cm^2)	Current efficiency (%)	Additives	Anode
Cu*	$CuSO_4$ (200-250), H_2SO_4 (25-50)	20-40	20-50	95-99	Dextrin, gelatine	P-containing Cu
Ni**	Ni sulphamate (300), $NiCl_2$ (30), H_3BO_3 (30)	20-75	20-150	98	Naphthalene-1,3,6-tri-sulphonic acid (7.5 g/l)	Ni pieces

* Based on method described in Pletcher & Walsh (1993)
** Based on method described in Diggin (1954)

For copper electroplating, the electrolyte consisted of: sulphuric acid (98%, Aldrich), copper sulphate (98%, Aldrich). For nickel plating, the electrolyte consisted of: nickel (II) chloride (Aldrich), boric acid (99%, Aldrich), nickel sulphamate (98%, Aldich). Naphthalene-1,3,6-tri-sulphonic acid (Aldrich) and dextrin (Sigma) were used as an additive in the electrolyte for nickel and copper, respectively. Copper rod was used as the cathode in copper deposition, and nickel foil was used as a cathode in nickel deposition.

To create an annular ring around the cordierite, with a thickness of 2mm, it was necessary to operate the cell for several days as the rate of metal deposition is usually much slower than 75 μm/h (Pletcher & Walsh, 1993). To obtain a smooth surface to ensure a good seal between the copper plated surfaces and stainless steel O-rings, the electroplated specimens were ground with silicon carbide paper on a rotor. Examples of specimens prepared are shown in Figure 3.4.

Although it was desirable to have a large exposed area of cordierite in the plate, the strength of the structure decreased with an increase in diameter. After a number of trials, it was decided to form supports with a number of small circular openings (about 4mm in diameter) in the plate, thereby retaining strength and surface area for the experiment.

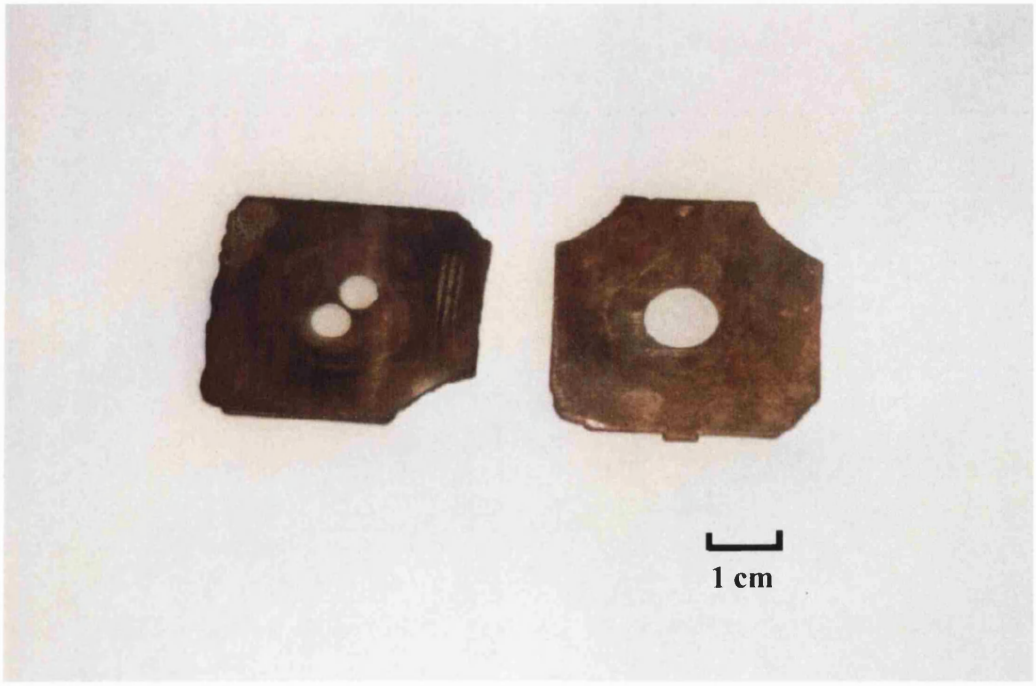

Figure 3.4. Examples of electroplated specimens for diffusion experiment.

A cross section of the interface between the cordierite and the metal-coated annular ring is shown in Figure 3.5. This image was generated by an optical microscope (Model: ICM405, Zeiss, Germany) with DIC (Differential Interference Contrast) lenses. The interface between the metal layer and the ceramic plate can be seen clearly. It can be further observed that the nickel layer has very close contact with the ceramic surface, even in the crevices.

The thin ceramic plates were directly cut from a commercial cordierite monolith substrate obtained from Corning Inc. (New York, USA) and the thickness of the plate is 0.25 mm, the same as the walls of the channel. The composition and physical properties of the ceramic are listed in Table 3.3. Although the difference between the thermal expansion of ceramic (12.5×10^{-7} in/in·K^{-1}) and nickel (13×10^{-6} in/in·K^{-1}) was relatively small, it was necessary to restrict the maximum temperature to a value of 320°C, to avoid fracture of the cordierite.

In commercial applications, as the layer of the washcoat can vary from 10 μm to 150 μm (*e.g.* Hayes & Kolaczkowski, 1996), it was decided to prepare samples where the thickness of the washcoat could be as high as 10 μm.

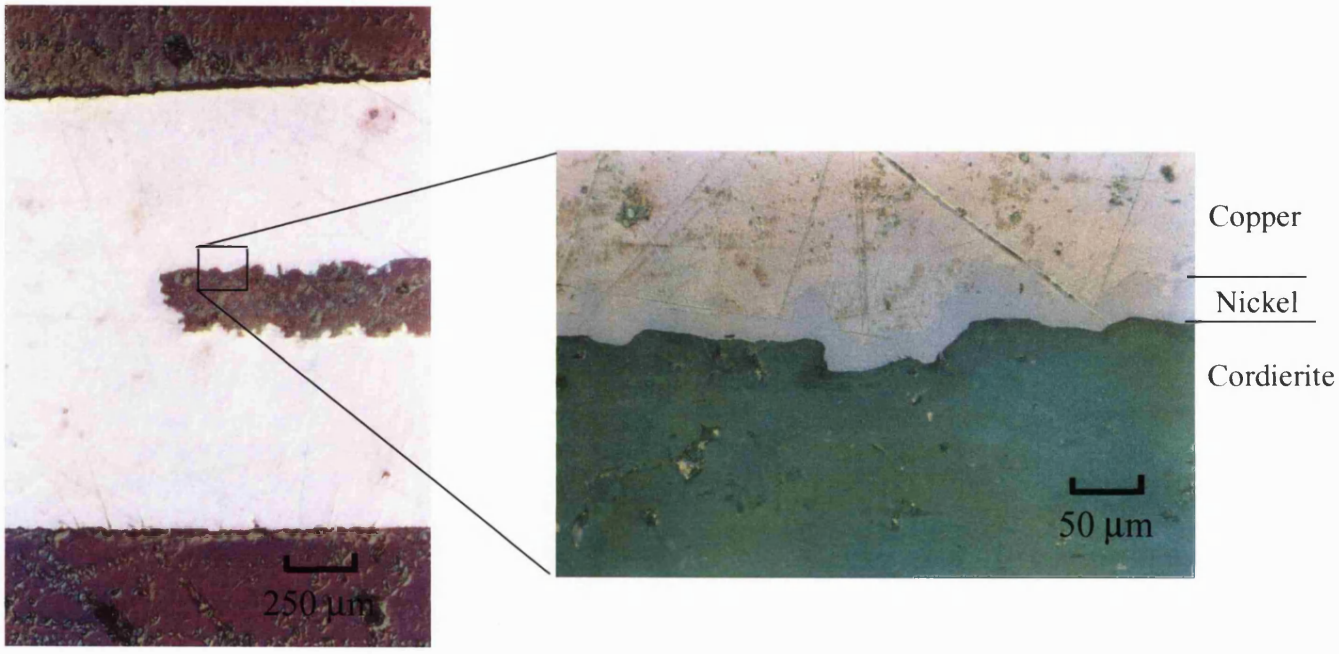

Figure 3.5. Optical microscopic images (DIC) of the section of an electroplated cordierite plate.

Table 3.3. Specification of the cordierite substrate supplied by Corning, Inc.

1. Cell density: 400 square cells per square inch.
2. Chemical composition:

Major oxides:	MgO	13.5% ± 1.0%
	Al_2O_3	35.4% ± 1.5%
	SiO_2	49.7% ± 1.5%
Impurities:	K_2O	1.0 %
	TiO_2	1.0 %
	CaO	0.5 %
	Fe_2O_3	1.0 %
	Na_2O	0.4 %

3. Crystalline phase:
   Major phase (Minimum = 90%):
   Cordierite 2 MgO - 2 Al_2O_3 - 5 SiO_2
   Minor phase (Maximum = 10%)
   - ♦ Mullite (3 Al_2O_3 - 2 SiO_2)
   - ♦ Alumina (Al_2O_3)
   - ♦ Spinel (MgO- Al_2O_3)
4. Physical properties:
   Water adsorption: 15% water adsorption
   Coefficient of thermal expansion: 12.5×10^{-7} cm/cm K
   Minimum softening temperature: 1410 °C

For experiments with a washcoat, the cordierite plate has to be coated with washcoat before electroplating, see Figure 3.3.

3.3. Design of diffusion cell

The diffusion cell consists of two identical stainless chambers, which have a cavity of 15 mm in diameter and 6 mm in depth, and several connection ports. The metal plated sample was placed between the two sections of the cell, and then the two parts were assembled by means of four screws. Stainless steel O-rings supplied by Wills Polymer Co. (Bridgewater, UK) were used on both sides of the plate to form a gas tight seal.

After performing preliminary experiments on a diffusion cell with a:

- cross-section cell area: 1.23 cm^2,
- upper chamber volume: 0.8 cm^3, and
- lower chamber volume: 0.8 cm^3,

it was decided to construct a cell with the dimensions illustrated in Table 3.4. Decisions on size of tubing and position in the two chambers, were based on examples of designs

of the Wicke-Kallenbach type of cell reported in the literature (*e.g.* Dogu & Smith, 1968).

The gas flow to both sides of the sample was introduced perpendicularly through two jets to minimise the concentration barrier that exists between the gas phase and the solid phase. Stainless steel tubing (dimension: 3.175 mm (1/8") OD and 1 mm ID) was used for the gas inlet and the end had a cone shape in order to distribute the gas evenly onto the face of the plate, see Figure 3.6.

A pressure tapping in the upper and lower chambers was used to measure the pressure differential across the plate. In order to monitor the temperature in the cell, two thermocouples were located in each side of the cell, one in the gas stream and the other was positioned close to the sample. The general configuration of the diffusion cell is summarised in Table 3.4. A schematic of the cell is shown in Figure 3.6, and a photo image is presented in Figure 3.7.

Table 3.4. Summary of diffusion cell configuration.

The cell was constructed from: Stainless steel; Type 316
Connection ports:
4 ports for thermocouple connections 2 ports for gas inlet and outlet 2 ports for pressure transducer
2 O-rings (supplied by Wills polymer Co.):
Material: stainless steel; Type 321 Dimension : 22.45 mm OD × 1.6 mm high
Dimension of the upper and lower chamber: (15 mm in diameter × 6mm in depth) Upper chamber: 1.06 cm^3 Lower chamber: 1.06 cm^3

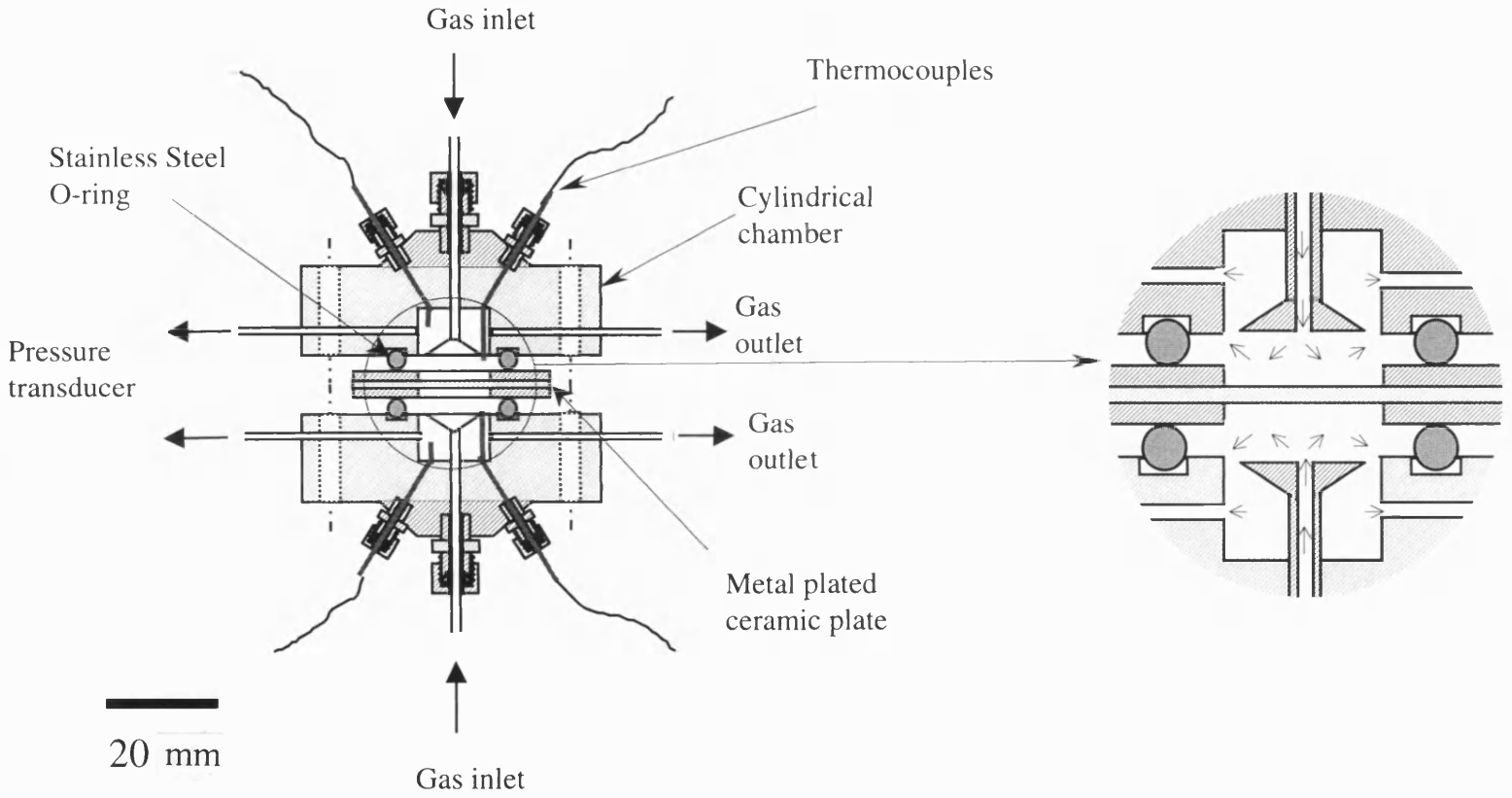

Figure 3.6. Schematic of diffusion cell assembly.

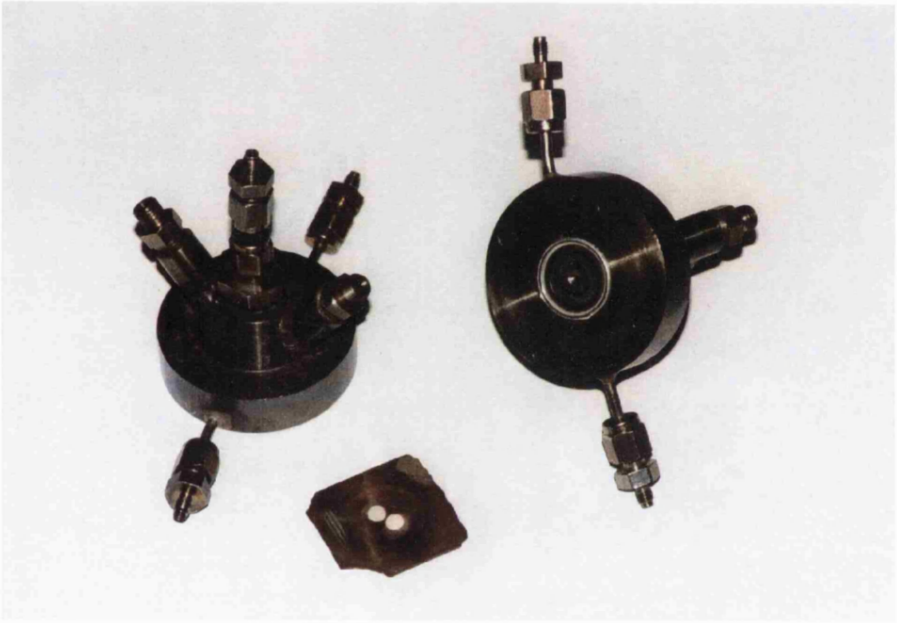

Figure 3.7. A photo image of the diffusion cell

3.4 Experimental apparatus and procedure

3.4.1 Transient measurements

A flow diagram of the equipment for the transient experiments is illustrated in Figure 3.8. The apparatus consists of a diffusion cell, a constant temperature oven, gas flow lines (carrier gas, reference and sample gas), a gas sampling valve and a gas chromatograph equipped with a thermal conductivity detector (TCD).

The same carrier gas flows on both sides of the ceramic substrate. A portion of carrier gas, which carries the trace gas to the plate, flows across one face of the sample plate while the reference carrier gas flows across the other, carrying the outlet tracer to the detector.

A differential pressure transducer (Druck Ltd., Leicester, UK) was connected between both sides of the plate in order to confirm that the pressure was equalised on either face of the plate, to avoid flow as a result of pressure gradient.

Trace gas was introduced into the carrier by means of a gas sampling valve. Several different sampling loops were used to obtain pulse inputs. In order to introduce a pulse input of hydrocarbon in liquid form, a certain amount of liquid hydrocarbon was introduced into an injection port (by means of a microliter syringe), the injector was then heated up to a desired temperature to vaporise the hydrocarbon and this was then fed into the cell.

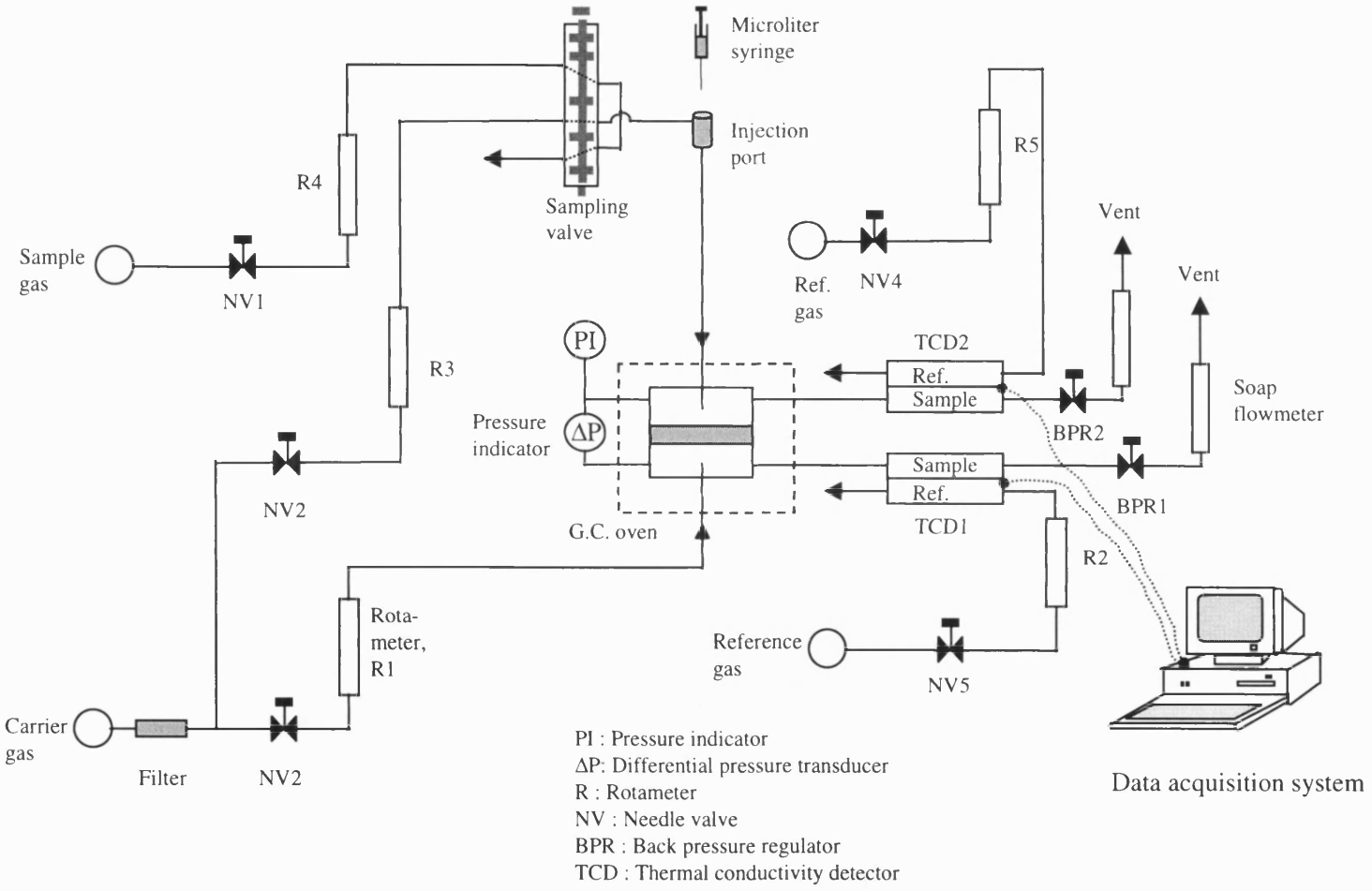

Figure 3.8. Schematic of experimental apparatus for transient measurements.

3.4.2. Steady state measurement

A flow diagram of the experimental apparatus is illustrated in Figure 3.9, and consists of the diffusion cell (see Figure 3.6) housed in a constant temperature oven, a gas chromatography system equipped with a flame ionisation detector (FID), and a hydrocarbon vapour generating system (see Figure 3.10).

Nitrogen gas flows onto both upper chamber and lower chamber as a carrier gas. A portion of N_2 containing the diffusing species flows across one surface of the plate, while the reference N_2 flows across the other side. Two pressure transducers (Model: PDCR 810-0799, Druck Ltd., Leicester, UK) were connected in both side of the plate in order to monitor the pressures in both chambers, combined with a differential pressure transducer (Model: PDCR 2111, Druck Ltd). It is crucial to equalise the pressures across the sample plate so that the convective flow is eliminated. The concentration on both sides of the plate was measured using a flame ionisation detector (FID). The diffusion cell was located inside a constant temperature oven, which had previously been a part of a gas chromatograph. The temperature of the oven was kept constant (maximum variation of ±2°C at 200°C).

The line work and connections in the delivery line were made of stainless steel. Stainless tubing of 1.59mm (1/16") O.D. was mainly used in order to reduce the dead volume, particularly at points where pressure transducers were connected.

3.4.2.1 Vapour generating system

As the *n*-paraffins, C_5-C_8, are liquid at room temperature, it was necessary to design a vapour generating system. It was important to generate a constant flow of hydrocarbon vapour. The development of a uniform vapour generating system was crucial in this work. To achieve this, the vapour generating system shown in Figure 3.10(a) was designed and constructed. It consists of a high precision liquid pump and two pressure vessels with a tubular heater. The high precision liquid pump with two piston heads (Model: ConstaMetric IIIG) was purchased from ThermoQuest (Manchester, UK). To improve vaporisation efficiency, an evaporator with a cross-flow nebuliser was manufactured as shown in Figure 3.10(b).

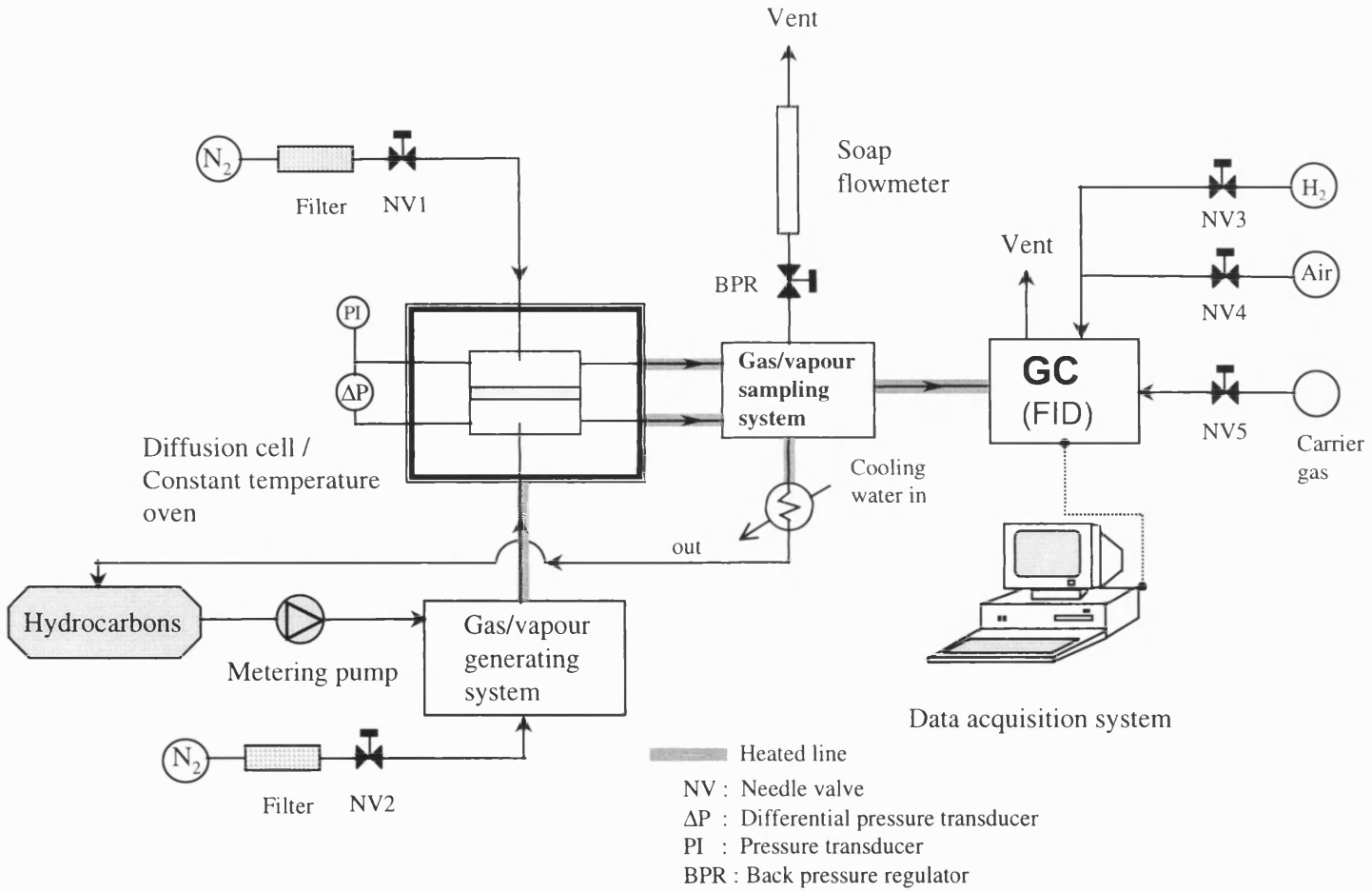

Figure 3.9. Schematic of experimental apparatus for steady state measurements.

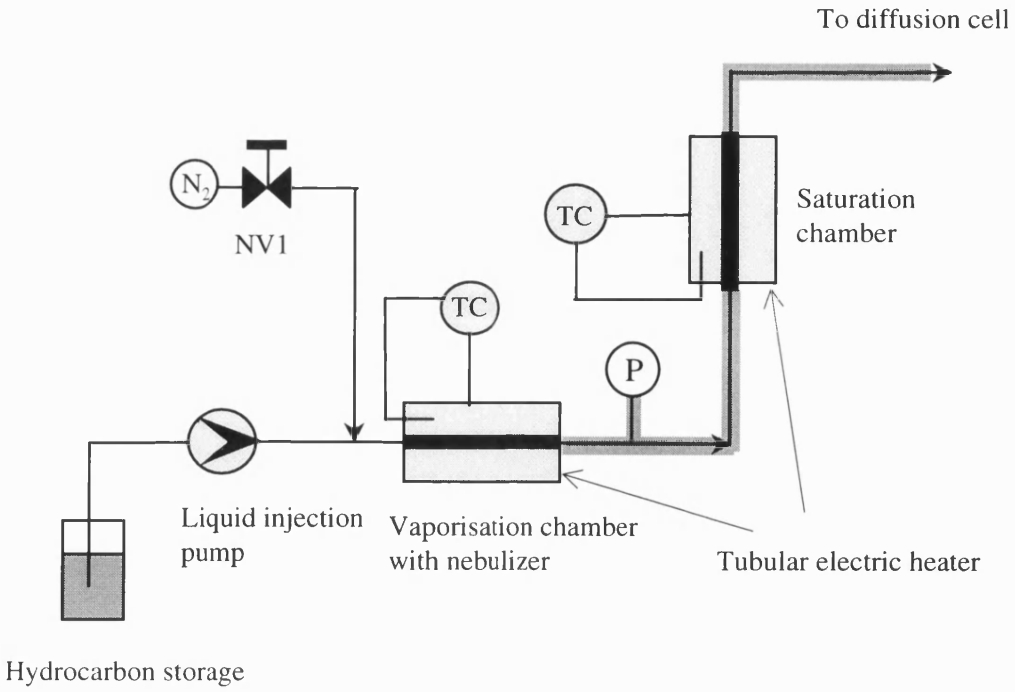

(a) Schematic

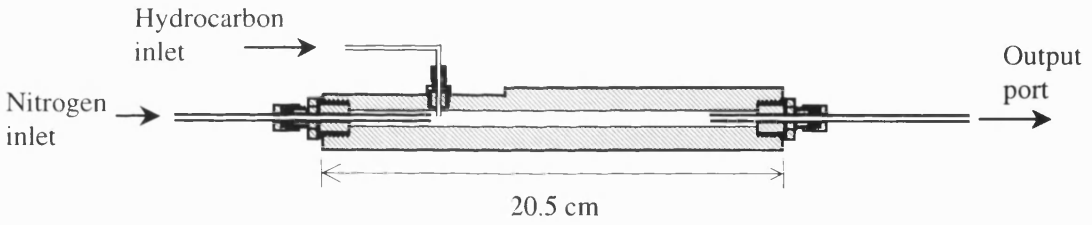

Dimension : 1 cm I.D. × 2.54 cm O.D.

(b) Detail of vaporization chamber with nebulizer

Figure 3.10. Schematics of the gas mixing/hydrocarbon vapour generating system, in Figure 3.9.

The nebuliser should help to reduce the size of the liquid droplet of hydrocarbon. Consequently, it can increase the rate of vaporisation. Furthermore, another vessel, labelled as the saturation chamber, was added after the vaporisation chamber. The saturation chamber (50 ml in volume) was kept at a temperature lower than the vaporisation chamber. This ensures that the vapour was saturated. Residual condensate dripped down to the vaporisation chamber. Before the saturated vapour was introduced

into the diffusion cell, another cylinder (15 ml) was added just before the diffusion cell (located inside the constant temperature oven), so as to keep the temperature the same as the diffusion cell.

Furthermore, all the delivery lines were heated with a heating coil, and then insulated to prevent condensation of hydrocarbon vapour.

3.4.2.2 Gas chromatography

The diffusing species were analysed with a gas chromatograph (GC Unicam 204 series, ATI Unicam, Cambridge) equipped with a thermal conductivity detector and a flame ionisation detector. The GC was modified in order to analyse the vapour samples from both chambers of the diffusion cell. Two gas sampling valves with 6 ports were used to take samples from both chambers in the diffusion cell. In addition, a switching valve was also used to divert the sample to a gas chromatography column.

The performance of the GC was calibrated with a number of standards. In the case of methane, a known amount of this gas was mixed with a nitrogen diluent and then injected using a gas sampling valve. The liquid hydrocarbon standards were prepared in a methanol solvent and then injected into the column with microlitre syringes (Hamilton Co., Nevada). The GC column used was a packed column with 10% CP-Sil5/Chromosorb WHP (Chrompack, the Netherlands).

The thermal conductivity detector (TCD) was used in the transient method and the flame ionisation detector (FID) was used in the steady state method. The FID exceeds the sensitivity of TCD (~ 10^{-8} g solute/ml carrier gas) by factors as large as 10^4, but it is used to analyse only organic compounds which produce ions and electron that can conduct electricity through a flame (when pyrolysed at the temperature of a hydrogen/air flame).

3.4.3. Experimental conditions

The investigation was started with experiments using *n*-pentane, *n*-hexane, *n*-heptane and *n*-octane, to represent components found in gasoline. In addition, an experiment was performed with methane.

The gases used in this work were nitrogen, hydrogen, methane and compressed air, these were obtained from BOC gas and were of a technical grade. The nitrogen used as carrier gas for both GC and diffusion experiment was filtered with oxygen and moisture filters.

The physical properties of hydrocarbons used in the study are listed in Table 3.5. Their purity was: pentane (99%), hexane (98.5%), heptane (99%) and octane (99%), and they were obtained from Sigma-Aldrich Co. Methanol, which was used for making standard solutions of the hydrocarbons, was 99% GC grade.

The operating temperature for the diffusion experiments of the gasoline-based hydrocarbons had to be above their boiling points. The self-ignition temperatures of the hydrocarbons are below 300°C, as listed in Table 3.5. As it was found that cracks could arise in the electroplated sample at temperatures above 300°C, the operating temperature range was set between 100°C and 300°C.

Table 3.5. Physical properties of the hydrocarbons used.

Hydrocarbon	M.W., g/mol	Density*, g/cm^3	Boiling point, °C	Self-ignition temp.**, °C
n-Pentane (C_5H_{12})	72.15	0.630	36.3	258
n-Hexane (C_6H_{14})	86.17	0.659	69	296
n-Heptane (C_7H_{16})	100.2	0.684	98.4	214
n-Octane (C_8H_{18})	114.2	0.703	125.7	208

* at T=20°C

** Referred from Glassman (1987). The temperatures are the lowest value presented in the reference.

It is well known the resistance to transfer between the bulk gas in the chamber to the surface of the plate could be significant. This is known as interphase diffusion resistance. By performing experiment at various flowrates, this aspect can be quantified and minimised. This is discussed in more detail in Section 3.5.2.1.

The operating pressure of the cell is directly linked to the flowrate in the diffusion cell and the back pressure across the control valves. By adjusting a back pressure regulator (BPR), see Figure 3.9, this pressure can be controlled.

3.5 Preliminary experiments

3.5.1.Transient experiment

In preliminary experiments, a 2ml pulse of methane was injected into the upper chamber. The operating conditions are summarised in Figure 3.11 and the results are represented in Figure 3.12. The output response in lower chamber is much smaller than the response in upper chamber as it represents the methane flux diffused across the cordierite plate.

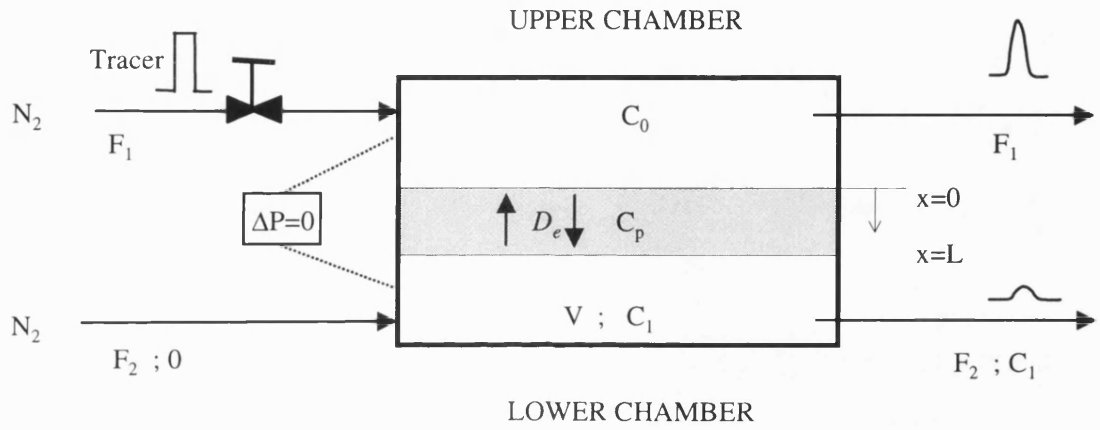

UPPER CHAMBER	LOWER CHAMBER
Inlet flow of N_2 (F_1) = 1.43 ml/s Size of methane pulse = 2 ml	Inlet flow of N_2 (F_2) = 2.1 ml/s
Operating temperature = 25 °C, Pressure differential = ±1mbar	Operating pressure = 1.04 bar

Figure 3.11. Operating conditions of transient experiment of methane diffusion.

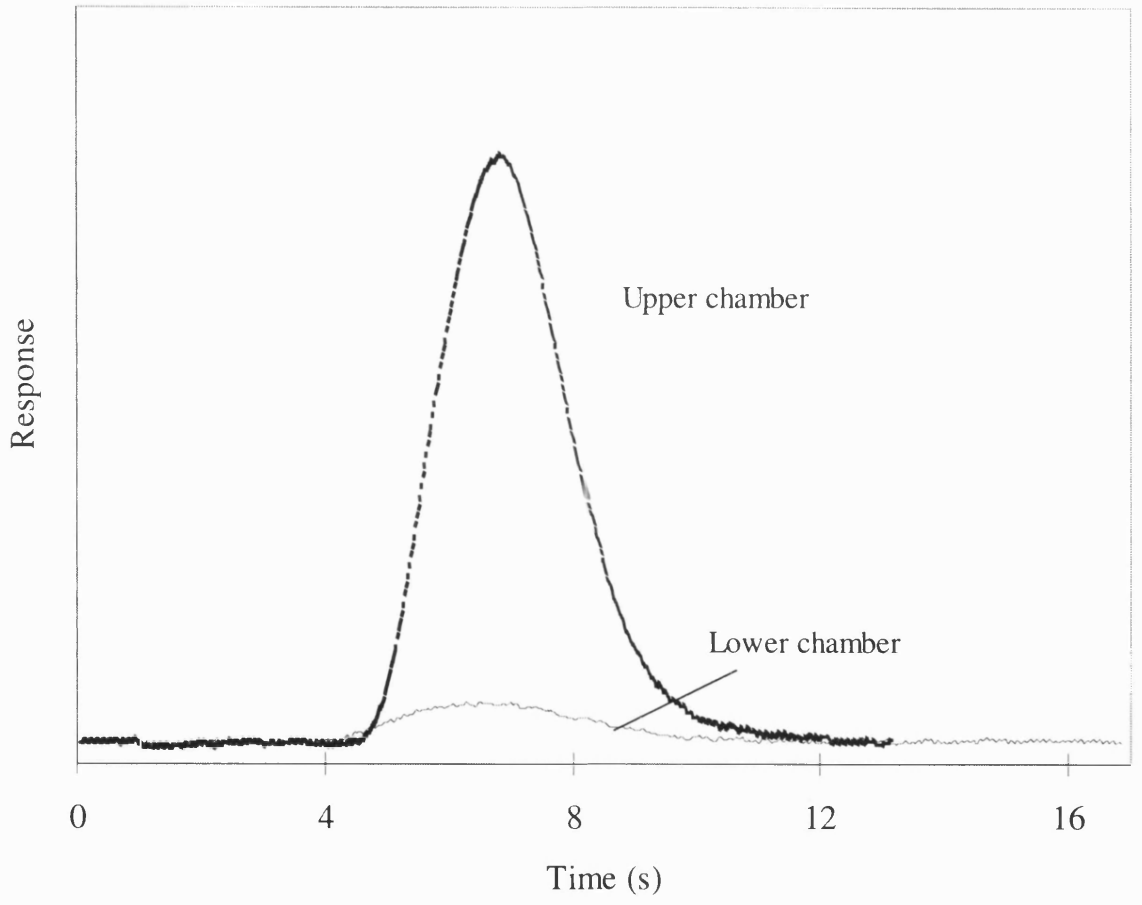

Figure 3.12. The measured response of methane tracers in both upper and lower chamber when introducing 2ml of methane as a pulse (specimen: uncoated cordierite, T=25°C).

In this work, the Fourier series method of analysis was employed. The normalised response signal is (Al-Rqobah *et al.*, 1988):

$$\frac{[c_2(t)]_{calc}}{[c_2]_{s\to 0}} = \frac{1}{2\zeta} + \frac{N+M}{\zeta M} \times \left[\sum_{n=1}^{\infty} \left(\gamma_n cos \frac{n\pi t}{\zeta} - \delta_n sin \frac{n\pi t}{\zeta} \right) \right] \qquad (3.1)$$

where $N = L(\varepsilon/D_e)^{0.5}$, $M = \frac{A}{F_2}(\varepsilon/D_e)^{0.5}$, ζ is the half time required for tailing to vanish, and γ_n and δ_n are the real and imaginary parts of the Laplace transform function, respectively.

The effective diffusivity of methane was predicted from the Fourier series method for a cordierite plate, see Figure 3.13. It can also be calculated by moment method and the value obtained by this approach is close to the value from the Fourier series method (Al-Rqobah *et al*, 1988).

The effective diffusivity of methane was approximately 6.5 $\times 10^{-6}$ cm^2/s and deviates from the value (9.2 $\times 10^{-3}$ cm^2/s) measured by the steady state method (described in Section 3.4.2) by a factor of more than 10^3. The cordierite plate is very thin, and the use of the transient method on this kind of thin porous sample has not been reported in the literature, see Appendix 2.

It can be concluded that this transient measurement is not suitable for such a thin sample. One more thing to note is that when detecting heavier hydrocarbons the sensitivity of the thermal conductivity detector (TCD) is very poor.

A number of additional experiments were then performed with the other hydrocarbons. Figure 3.14 shows the response of heptane tracer in the upper and lower chamber when introducing a pulse of 0.1 ml heptane into the same system as that in which the methane measurements were made. As heptane is liquid at room temperature, the experiment was carried out at 175°C and the other operating conditions are listed in Table 3.6. It can be seen that the response is very poor.

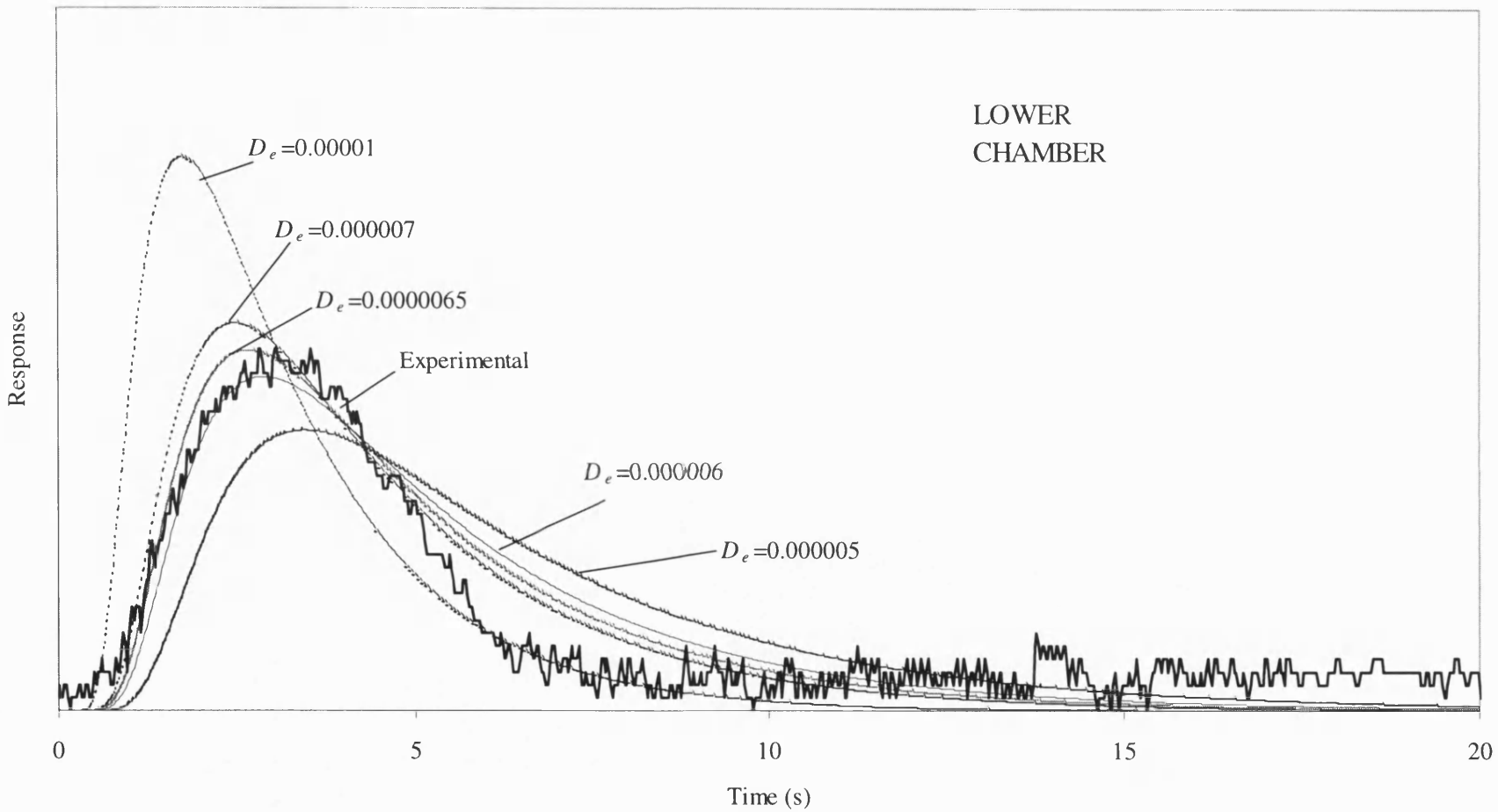

Figure 3.13. Determination of the effective diffusivity of methane by the Fourier series method. The experimental curve is the normalised curve of the response in the lower chamber.

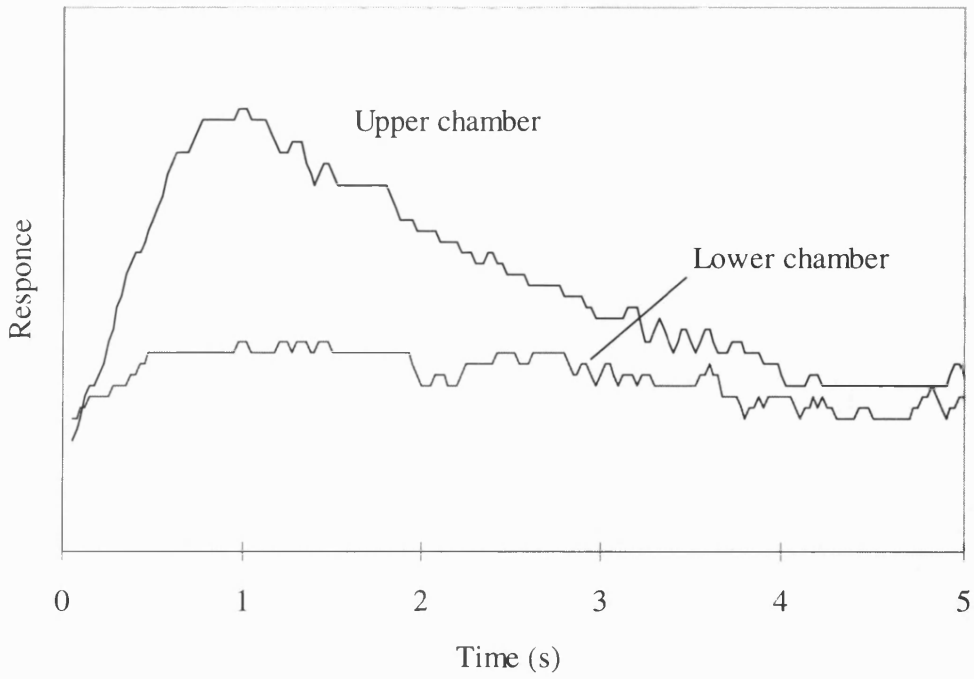

Figure 3.14. The response of heptane tracer in both upper and lower chamber.

Table 3.6. Operating conditions for transient measurements with liquid hydrocarbons.

Specimen : cordierite substrate	
Cross sectional area :	45 mm^2
Thickness :	0.25 mm
Flowrate of N_2 in upper chamber:	1.42 cm^3/s
Flowrate of N_2 in upper chamber:	1.06 cm^3/s
Operating temperature :	175 °C
Operating pressure :	1.067 bar
Size of pulse input :	0.1 ml

Figure 3.15 shows the output responses in upper chamber for the C5-C8 *n*-paraffins when 0.1 ml pulse was introduced into the injection port with a microlitre syringe. As the carbon number increases, the response decreases. For *n*-octane, the peak in the output is almost unrecognisable. Furthermore, the diffusion flux in the washcoated cordierite substrate is likely to be very much smaller than that in the uncoated substrate. On closer examination of this experimental method, it is clear that the accuracy of the analysis of the data is clearly dependent on the length of the diffusion path, or the thickness of the plate. For very thin plates of ~0.25mm, the delay is insufficient to discriminate from other small time delays and distortions of the signal in the system, *e.g.* in line, instruments.

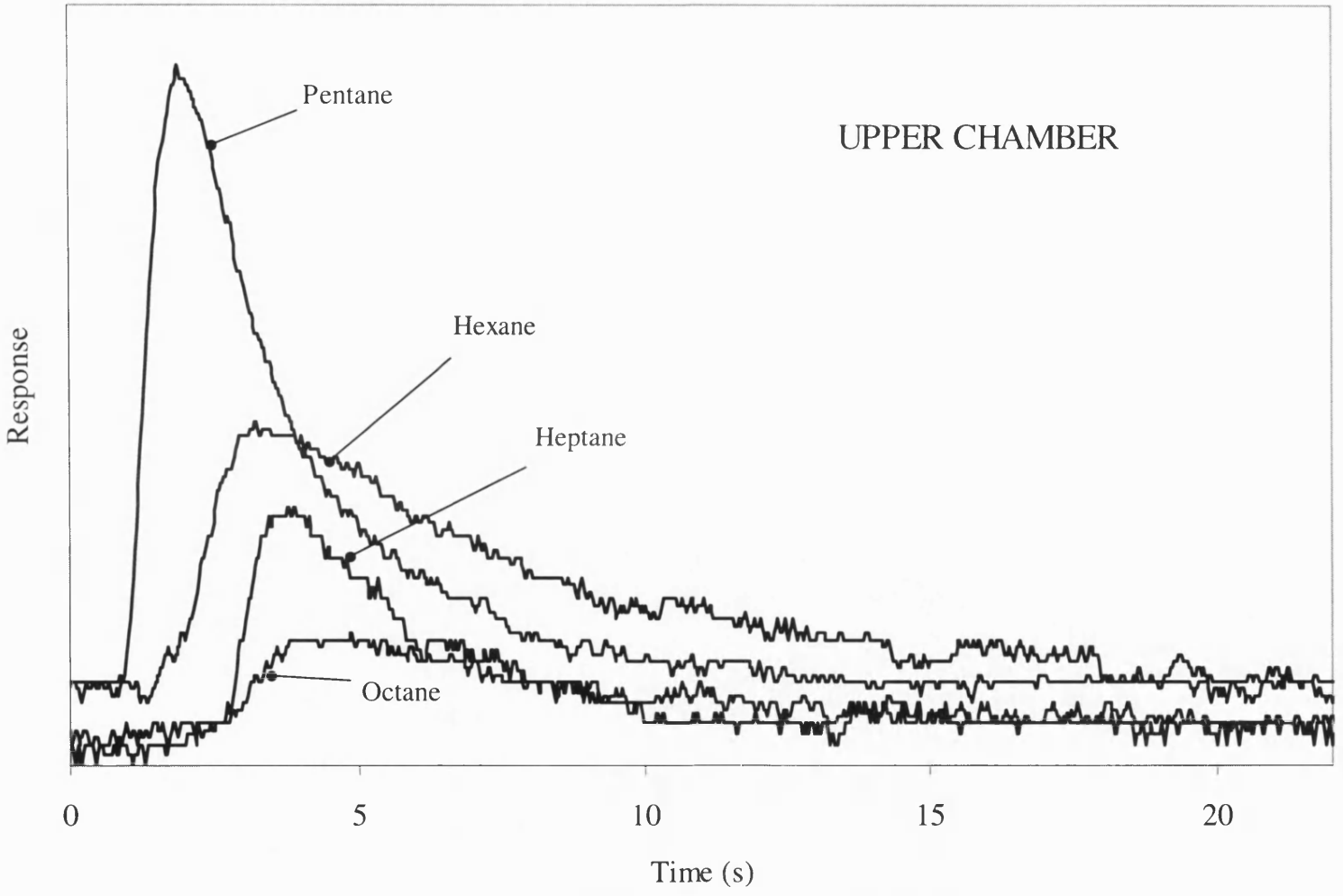

Figure 3.15. Output response in upper chamber for hydrocarbons (specimen: uncoated cordierite, T=175°C).

3.5.2. Steady state method

3.5.2.1. Interphase and intraphase resistance in the diffusion cell.

The transport of diffusing gas can be treated as taking place in three successive steps as shown in Figure 3.16: 1) diffusion between the bulk gas stream and the sample surface (interphase diffusion), 2) diffusion through the porous sample (intraphase diffusion), and 3) diffusion between the sample surface and the bulk gas stream (interphase diffusion). The resistance of the first and third step can be combined and described in terms of a single resistance.

The differential equation of diffusion in an isotropic medium is derived from Equation (2.1) and is given by, if the diffusion coefficient, D, is constant:

$$\frac{\partial C}{\partial t} = D_e\left(\frac{\partial^2 C}{\partial x^2} + \frac{\partial^2 C}{\partial y^2} + \frac{\partial^2 C}{\partial z^2}\right) \tag{3.2}$$

If there is a gradient of concentration only along the x-axis, then Equation 3.2 becomes:

$$\frac{\partial C}{\partial t} = D_e \frac{\partial^2 C}{\partial x^2} \tag{3.3}$$

If steady state conditions apply, then:

$$D_e \frac{d^2 C}{dx^2} = 0 \tag{3.4}$$

Considering the existence of a boundary layer on the surface of a porous solid, then the differential equation is subject to two boundary conditions (Crank, 1956; Cussler, 1984):

$$\begin{aligned} x = 0, \quad & \frac{dC}{dx} + k_1(C_{1,s} - C_1) = 0 \\ x = l, \quad & \frac{dC}{dx} + k_2(C_2 - C_{2,s}) = 0 \end{aligned} \tag{3.5}$$

The solutions are:

$$C = \frac{k_1 C_{1,s}(1 + k_2(l - x) + k_2 C_{2,s}(1 + k_1 x)}{k_1 + k_2 + k_1 k_2 l} \tag{3.6}$$

and

$$J_A = -D_e \frac{dC}{dx} = D_e \frac{k_1 k_2 (C_{2,s} - C_{1,s})}{k_1 + k_2 + k_1 k_2 l} = \frac{(C_{2,s} - C_{1,s})}{\frac{1}{k_1 D_e} + \frac{1}{k_2 D_e} + \frac{l}{D_e}}. \tag{3.7}$$

If k_1 and k_2 are large relative to D_e, then, $\frac{l}{D_e} >> \frac{1}{k_1 D_e}, \frac{1}{k_2 D_e}$.

Therefore, an expression for the diffusion flux can be written as:

$$J_A = -D_e \frac{\Delta C}{\Delta x} = \frac{C_{1,s} - C_{2,s}}{l / D_e} \tag{3.8}$$

and J_A can be determined from (see Figure 3.16):

$$J_A = \frac{C_2 v}{A} \tag{3.9}$$

where v= inlet flowrate, cm^3/s

A= cross sectional of the plate for mass transport, cm^2

Preliminary experiments were performed in which the flowrate of methane in the upper chamber and the flowrate of nitrogen in lower chamber were increased. An effective diffusivity can be obtained in terms of experimentally measurable quantities. The example calculation of effective diffusivity and diffusion flux using Equation (3.8) is illustrated in Appendix 1.

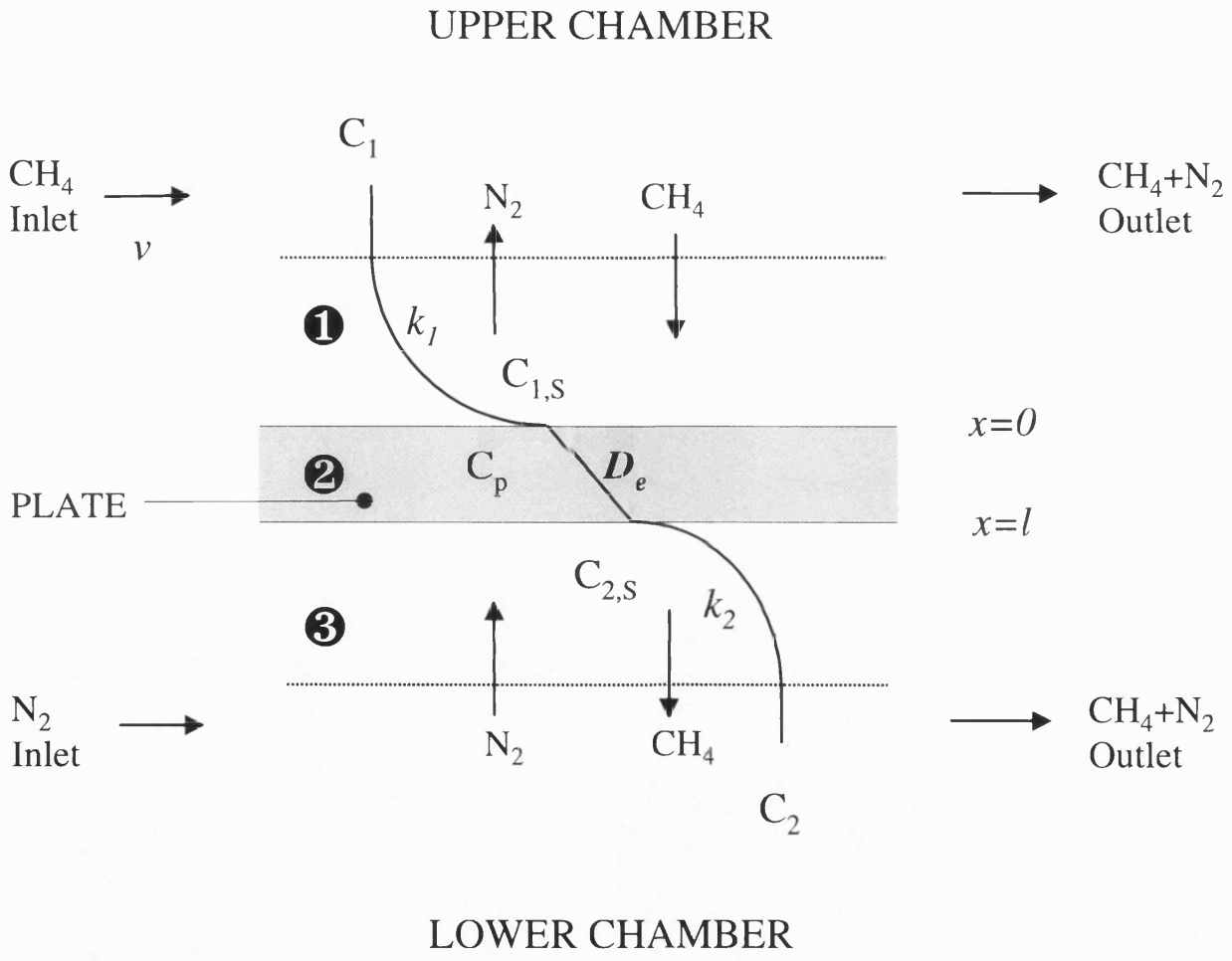

Figure 3.16. Mass transfer process in porous plate: ❶ interphase diffusion, ❷ intraphase diffusion, ❸ interphase diffusion.

The results of this experiment are shown in Figure 3.17 and in Table 3.7. It can be observed that the molar flux of methane across the plate increases linearly with the flowrate, and then becomes constant above a flowrate of 9 cm^3/s at S.T.P. At flowrates above 9 cm^3/s, $1/D >> 1/k_1D + 1/k_2D$. Under this condition then the molar flux is proportional to the effective diffusivity. Therefore, all the measurements of effective diffusivity were carried out at flowrates above 9 cm^3/s.

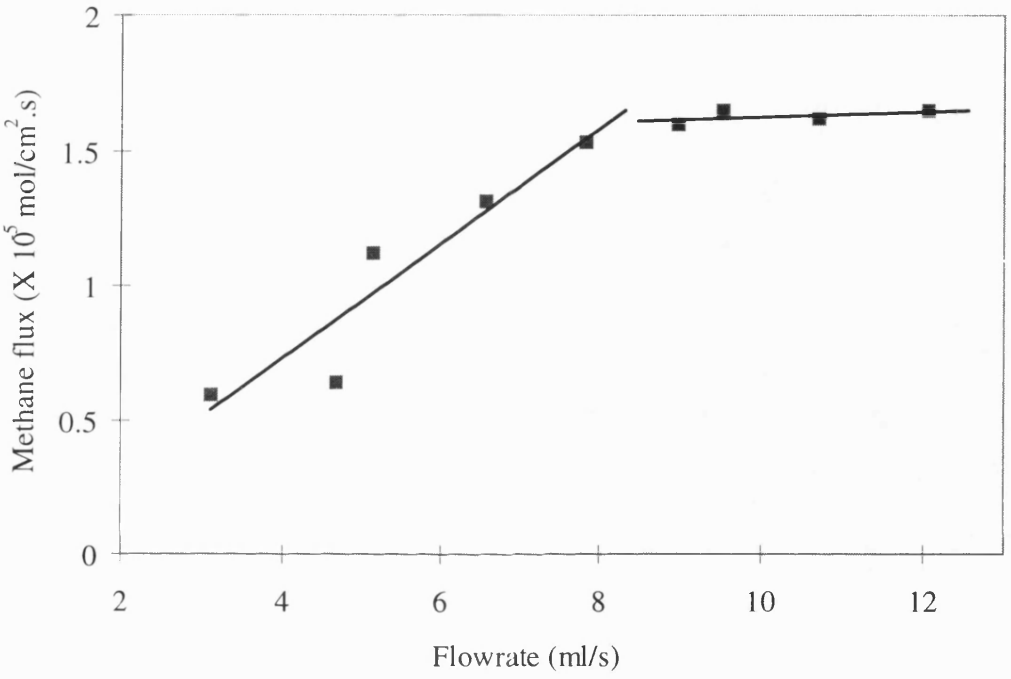

Figure 3.17. Interphase diffusion effect in CH_4-N_2 diffusion system (specimen: uncoated cordierite, T=25°C).

Table 3.7. The diffusion flux of methane across the cordierite substrate at different flowrates of methane (T=25°C).

Flowrate, cm^3/s	Flux, $mol/(cm^2.s)$	Flowrate, cm^3/s	Flux, $mol/(cm^2.s)$
3.10	5.94×10^{-6}	8.97	1.60×10^{-5}
4.67	6.41×10^{-6}	9.52	1.65×10^{-5}
5.13	1.12×10^{-5}	10.71	1.62×10^{-5}
6.56	1.31×10^{-5}	12.07	1.65×10^{-5}
7.82	1.53×10^{-5}		

3.5.2.2. Sensitivity of measurements to pressure gradient across the plate.

In the presence of a pressure gradient, the flow of component A can be considered as a combination of diffusion and convection, see Figure 3.18.

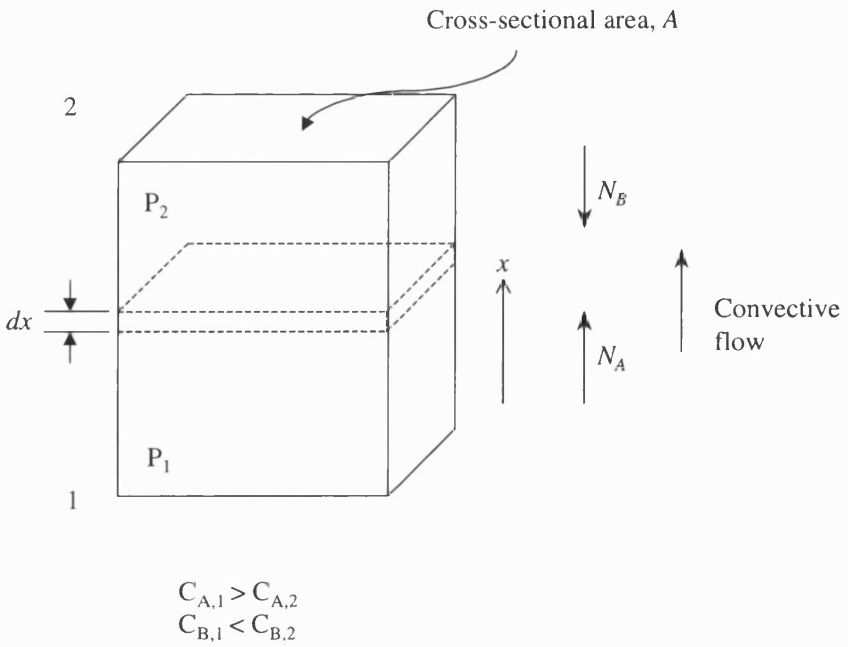

Figure 3.18. Diffusion of A and B in binary mixture.

The total flux of component A relative to a stationary point will be equal to the sum of the diffusion flux of A plus the convective flux of A:

$$N_A = C_A j_v + J_A \qquad (3.10)$$

(total molar flux) (convective flux) (diffusion flux)

where the quantity j_v represents the molar average velocity of the entire phase. For a membrane, j_v often represents the amount of convection and has a dimension of length/time. Also, it is convenient to write the quantity j_v as (Cussler, 1984):

$$j_v = \omega \Delta P \qquad (3.11)$$

where ω is permeability and ΔP is pressure gradient across the porous solid. This is also known as Darcy's law.

The following equation can be obtained by substituting Fick's diffusion equation (Equation 2.1) into Equation (3.10):

$$N_A = j_v C_A - D_0 \frac{dC_A}{dx} \qquad (3.12)$$

where D_0 is the true diffusion coefficient, *i.e.* when there is no pressure gradient across the plate (ΔP=0).

On introducing the following equations:

$$N_A = \frac{C_{A,2} v}{A}, \tag{3.13}$$

$$C_{A,p} = \frac{N_A}{j_v} = \frac{v}{j_v A} C_{A,2}, \tag{3.14}$$

where v = flowrate of N_2, cm^3/s

A = available area for mass transport, cm^2

$C_{A,p}$= concentration of diffusing species A in the pore, mol/cm^3

Equation (3.12) becomes:

$$j_v C_{A,p} = j_v C_A - D_0 \frac{dC_A}{dx} \tag{3.15}$$

and on integrating Equation (3.15) with respect to x with boundary conditions ($x=0$, $C_A(0)=C_{A,1}$; $x=l$, $C_A(l)=C_{A,2}$, the result is:

$$C_{A,2} = \frac{C_{A,1} e^{j_v l / D_0}}{1 - \frac{v}{j_v A}(e^{j_v l / D_0} - 1)} \tag{3.16}$$

Expressing the total diffusion flux through the plate in terms of an effective diffusivity, ($J_A = -D_e \, dC_A/dx$) is described as:

$$D_e = \frac{v \, C_{A,2} \, l}{A(C_{A,1} - C_{A,2})}. \tag{3.17}$$

Substituting Equation (3.16) into Equation (3.17):

$$D_e = \frac{j_v \, l \, e^{j_v l / D_0}}{(1 - \frac{j_v A}{v})(e^{j_v l / D_0} - 1)} \approx \frac{j_v \, l \, e^{j_v l / D_0}}{(e^{j_v l / D_0} - 1)} = \frac{\omega \, \Delta P \, l \, e^{\omega \Delta P l / D_0}}{(e^{\omega \Delta P l / D_0} - 1)} \tag{3.18}$$

By defining $\chi = \frac{j_v \, l}{D_0} = \frac{\omega \, \Delta P \, l}{D_0}$ (3.19)

, Equation (3.18) can be simplified as:

$$D_e = D_0 \frac{\chi \, e^{\chi}}{e^{\chi} - 1} \tag{3.20}$$

From Equation (3.20), the relationship between effective diffusivity, D_e, and pressure differential, ΔP, can be shown. There are three cases to be considered in respect of ΔP (see in Figure 3.19):

Case ❶: when $\Delta P < 0$ ($P_1 << P_2$), $j_v < 0$, $D_e \approx 0$

Case ❷: when $\Delta P \cong 0$ ($P_1 \approx P_2$), $j_v \rightarrow \pm 0$. Using Taylor's series and neglecting higher order terms, Equation 3.20 can be expressed as:

$$D_e = D_0 \frac{\chi(1+\chi+\frac{\chi^2}{2!}+\frac{\chi^3}{3!}+\cdots)}{(\chi+\frac{\chi^2}{2!}+\frac{\chi^3}{3!}+\cdots)} \approx D_0 \frac{1+\chi}{1+\frac{\chi}{2}} = \frac{(1+\chi)(1-\frac{\chi}{2})}{(1+\frac{\chi}{2})(1-\frac{\chi}{2})} = \frac{1+\frac{\chi}{2}-\frac{\chi^2}{2}}{1-\frac{\chi^2}{4}} \approx D_0(1+\frac{\chi}{2})$$

on reintroducing the original term (Equation 3.19),

$$D_e = D_0 + \frac{J_v\, l}{2} = D_0 + \frac{\omega\ \Delta P\ l}{2} \qquad (3.21)$$

Case ❸: when $\Delta P >> 0$ ($P_1 << P_2$), $j_v > 0$, Equation (3.20) becomes

$$D_e \approx D_0 \chi = j_v\ l = \omega\ l\ \Delta P \qquad (3.22)$$

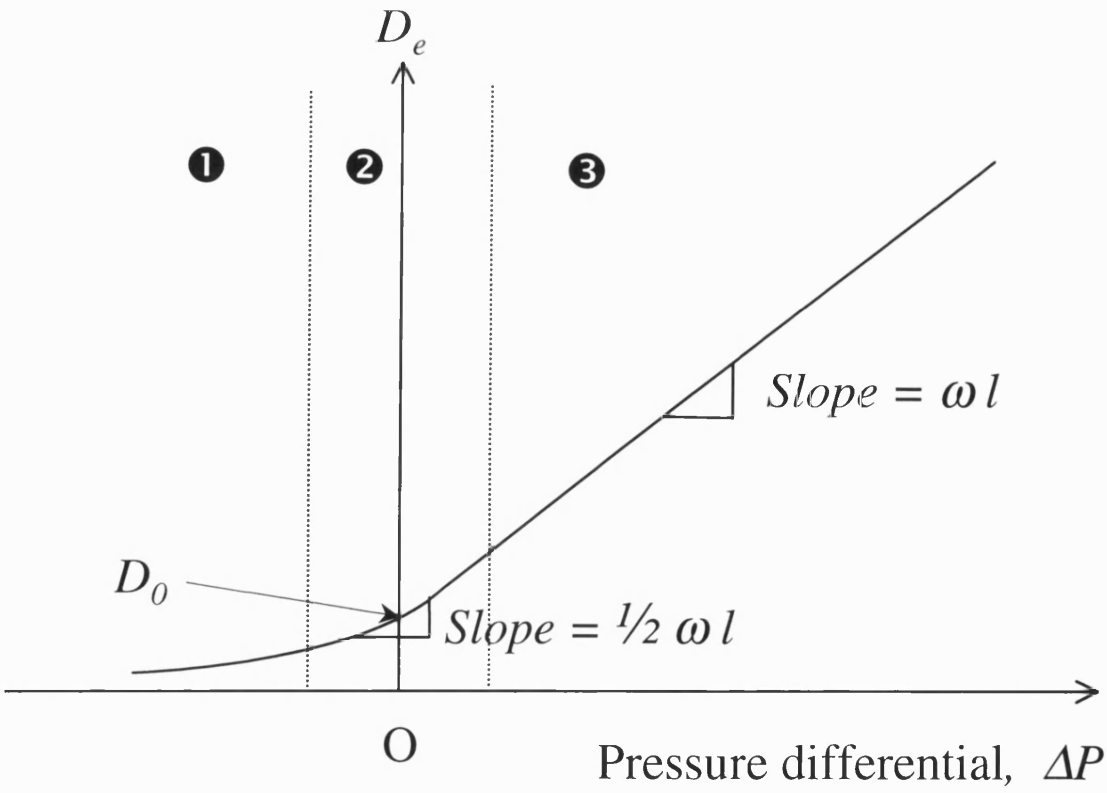

Figure 3.19. Effect of pressure differential, ΔP, on effective diffusivity, D_e (drawn from Equation 3.20).

The influence of the pressure change on effective diffusivity is dependent on the value of $\frac{\omega l}{2}$, as described in Equation (3.21). The accuracy of the differential pressure transducer used in this experiment was ±0.2 mbar, so the discrepancy between the experimental D_e value and D_0 value from this model will be $\pm 0.1\ \omega l$. In the particular experiment shown in Figure 3.20 and Table 3.8, the curve in the region ❸ is linear and the slope is 1.4×10^{-3} cm^2/(s·mbar), so the discrepancy of D_e due to inaccuracy of ΔP is 1.4×10^{-4} cm^2/s. The average effective diffusivity of hexane and the standard deviation of its effective diffusivity obtained from the experiment were 0.00218 and 0.00017, respectively. It can be found that the discrepancy calculated from the model is very close to the standard deviation of the experimental D_e based on repetition of the single measurement.

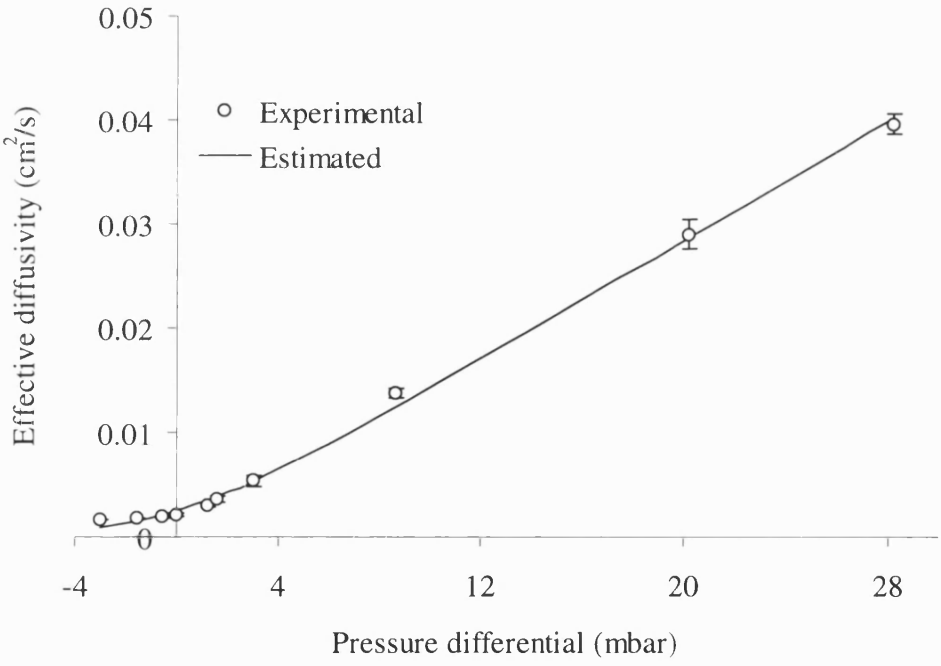

Figure 3.20. Sensitivity of the effective diffusivity of hexane on the pressure differential across the washcoated substrate (T=125°C).

Table 3.8. Effect of pressure differential, ΔP, on effective diffusivity, D_e, of hexane in a washcoated cordierite support (T=125°C).

ΔP, mbar	D_e, cm^2/s	ΔP, mbar	D_e, cm^2/s
-3.0	0.00167 $\pm 3.1\times10^{-5}$	1.6	0.00355 ± 0.00028
-1.6	0.00176 $\pm 3.0\times10^{-5}$	3.0	0.00531 ± 0.00057
-0.6	0.00191 $\pm 5.8\times10^{-5}$	8.6	0.0138 ± 0.00047
0	0.00213 ± 0.00017	20.2	0.0290 ± 0.00142
1.2	0.00300 ± 0.00022	28.2	0.0396 ± 0.00101

("-" sign represents that the pressure in upper chamber is greater than that in lower chamber)

In summary, this model was developed to investigate the effect of pressure gradient on effective diffusivity. It was shown that it could used to estimate the error in measurements that may arise from inaccurate pressure equalisation across the plate. Furthermore, by performing the flux measurement at varying positive pressure gradients, the model could be used to determine the permeability and the effective diffusivity could also be estimated.

3.5.2.3 Measurements of D_e as a function of the temperature.

The results of measurements of the effective diffusivity of methane in the cordierite substrate at different temperatures are presented in Table 3.9. Comparing these with values reported by Li (1997), who used the modified Beeckman's method described in Chapter 2. At room temperature, Li (1997) reported a value of $9.2\times10^{-3} \pm 3.8\times10^{-3}$ cm^2/s, while the value measured in this thesis is $8.7\times10^{-3} \pm 7.1\times10^{-4}$ cm^2/s. The two values are close to one another, with only a 6 % deviation.

Table 3.9. The measured effective diffusivity of methane in an uncoated cordierite substrate at different temperatures.

Temperature, K	Effective diffusivity, cm^2/s
294	0.0087 ± 0.0007
323	0.0114 ± 0.0018
373	0.0129 ± 0.0012
423	0.0144 ± 0.0013
448	0.0163 ± 0.0011
473	0.0175 ± 0.0010
523	0.0185 ± 0.0023
573	0.0246 ± 0.0030

Furthermore, the temperature dependence of the effective diffusivity was investigated in this thesis and it is illustrated in Figure 3.21. As shown in the figure, the exponent of the effective diffusivity of methane for an uncoated cordierite substrate is 1.36.

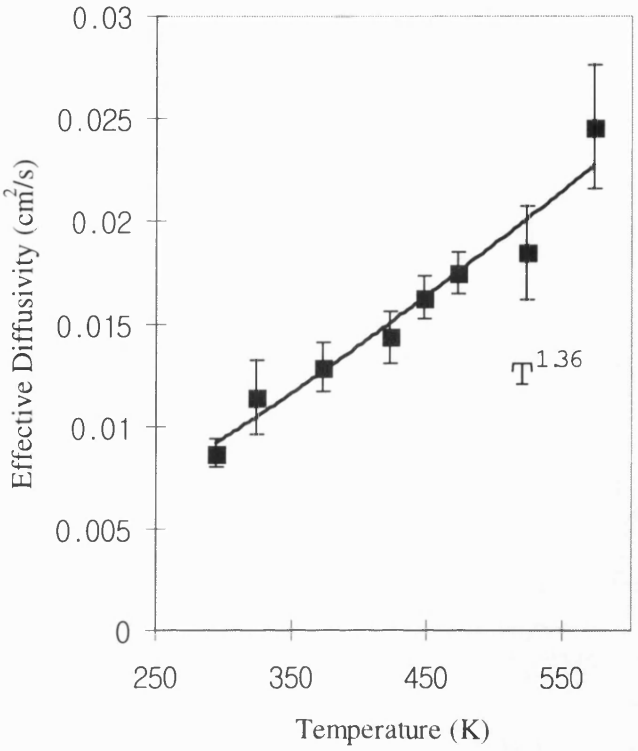

Figure 3.21. Effective diffusivity of methane in cordierite substrate measured at different temperatures (ν= 9-10 cm^3/s, P= 1.3-1.4 mbar).

The error presented here was obtained from standard deviation. Although the standard deviation gives a measure of the spread of a set of results about the mean value, it does not indicate the way in which the results are distributed. To illustrate this a large number of measurements are needed. Table 3.10 gives the result of 242 measurements of the effective diffusivities of methane in a cordierite support measure at a temperature of 448 K. These results arise from a variation in operating conditions. Experiments were performed at various permutations of concentration and flowrates (in upper and lower chambers). For example, if experiments were performed at 11 different concentrations (in the upper chamber and lower chambers), and at two different flowrates in each chamber, then the total number of experiments is 242 (=11×11×2).

Table 3.10. Frequency table for measurement of effective diffusivity of methane in cordierite support (T=448K)

Effective diffusivity (cm^2/s)	Frequency	Effective diffusivity (cm^2/s)	Frequency
0.0138	1	0.0170	25
0.0142	4	0.0174	16
0.0146	11	0.0178	13
0.0150	16	0.0182	8
0.0154	22	0.0186	9
0.0158	32	0.0190	1
0.0162	44	0.0194	2
0.0166	38	0.0196	-

The mean of these results is 0.0162 cm^2/s and the standard deviation is 0.00105 cm^2/s. The distribution of the effective diffusivity data is illustrated in the histogram, see Figure 3.22. This shows that the distribution of the measurement is roughly symmetrical about the mean, with the measurements clustered towards the centre.

The 95% confidence interval of the sample means will lie in the range given by (Miller & Miller, 1993):

$$\mu - 1.96(\sigma/\sqrt{n}) < \overline{D}_e < \mu + 1.96(\sigma/\sqrt{n}) \qquad (3.23)$$

where n= the number of sample,

μ= mean value,

σ= standard deviation ($=\sqrt{\frac{\Sigma(x_i - \bar{x})^2}{n-1}}$).

As the number of samples is 242, the 95% confidence limit is as:

$D_e = 0.0162 \pm 1.37\times10^{-4}$ cm^2/s.

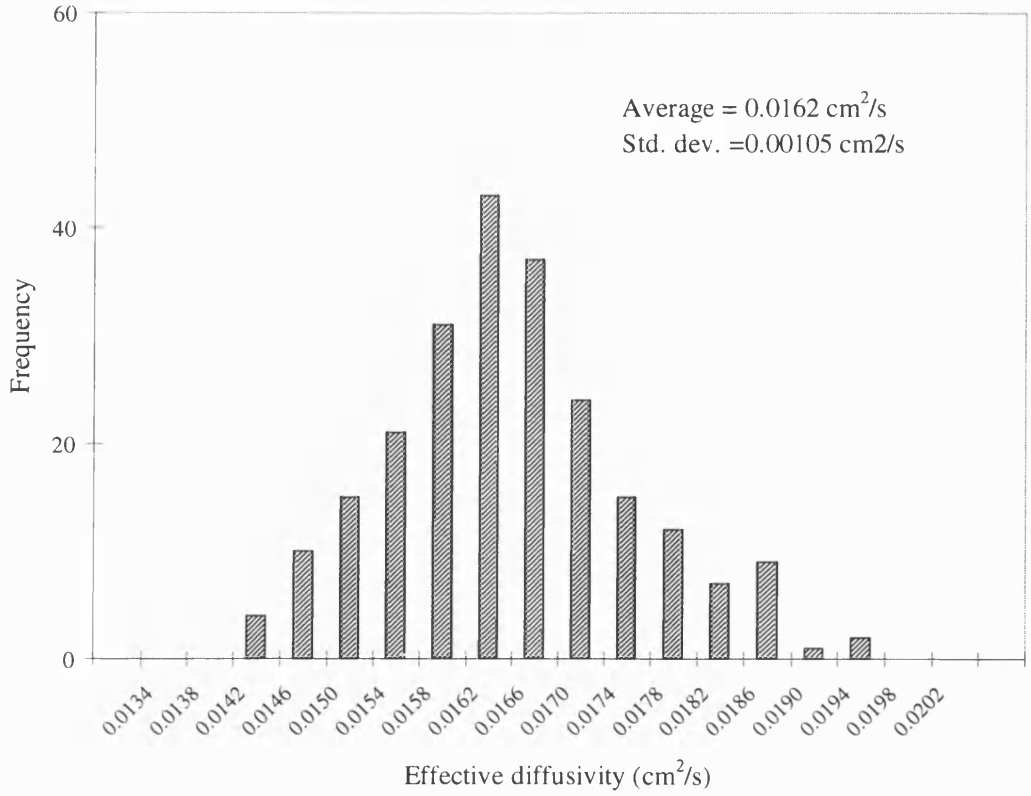

Figure 3.22. Histogram of the effective diffusivity data of methane in Table 3.10.

It should be noted that in the work reported by Li (1997), the relative error was ±41%, whereas in this thesis this has been reduced to ±0.8%.

Conclusions

A method was developed to form a metal ring around the perimeter of a sample of cordierite such that it could be sealed in a diffusion cell. The method involved electroplating and the sample could be tested at temperatures up to 320°C without fear of fracture.

Both transient and steady state experiments were performed to measure the effective diffusivity of hydrocarbons in a cordierite substrate. The transient method was shown to be unsuitable for such a thin sample, as the time delay for diffusion is insufficient to discriminate from the other time delays in the system.

The pressure difference between the two chambers can be regulated to ±0.2 mbar. This corresponds to an error of ±0.8% in value of D_e.

The steady-state method was shown to be suitable for this study and the results for uncoated cordierite plate compared well with earlier work by Li (1997). Therefore, the steady state method will be used to measure the effective diffusivity of hydrocarbons in the washcoat. Based on the results of the preliminary experiments, the following operating conditions are proposed:

1. Temperature: experiments can be performed from above the boiling point of the diffusing species and below 300°C to avoid fracture of the plate.

2. Flowrate: should be maintained above 9 cm^3/s at S.T.P. so as to minimise interphase resistance.

3. Pressure: subject to the flowrate (due to pressure drop)

In the following chapter, the influence on D_e of the physical/chemical properties of the washcoat is investigated. Also, the use of the sol-gel method to coat a cordierite plate support is studied in more detail.

Chapter 4. Washcoat Preparation Using the Sol-Gel Method and Characterisation Techniques

Introduction

Having gained experience in the method of preparing samples for the diffusion experiments, a number of issues surfaced that were explored further:

- How effective is the method of coating?
- What is the effect of doping with zirconia?
- What is the effect of adding catalyst?

To explore these aspects further, a number of preliminary experiments were performed and these are summarised in Figure 4.1.

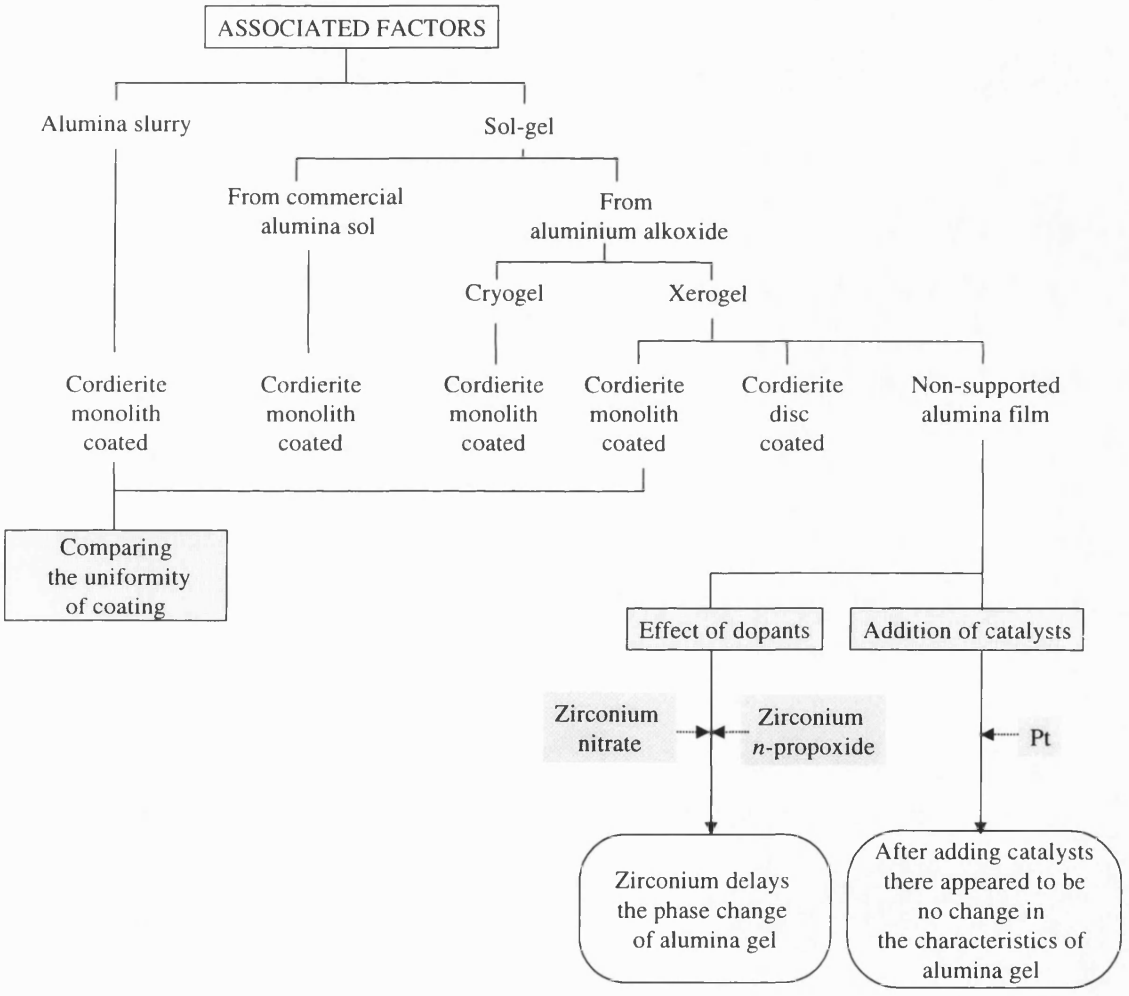

Figure 4.1. Schematic illustrating aspects studied in Chapter 4 (note: this links with Figure 1.2 in Chapter 1).

In this chapter, a description is provided of:

- The method used to characterise the washcoat.
- The method of preparing an alumina washcoat on a cordierite substrate in the form of a plate (for the diffusion cell) as a monolith.
- The use of doped zirconia to increase the thermal stability of the alumina washcoat.
- The method of adding active catalysts (Pt) to the alumina washcoat.

4.1. Characterisation techniques

4.1.1. Porosity measurements

The porosity of the specimens was measured by helium displacement using a pycnometer (*AccuPyc 1330, Micrometrics Instrument Co.*). The pycnometer determines density and apparent volume by measuring the pressure change of helium in a calibrated volume. Analysis measures the volume of solids of irregular shape by gas displacement, for which density can considered automatically if sample weight has been entered. Before the analysis, the samples were dried at 110°C for 2 hours.

4.1.2. Nitrogen adsorption experiment

The technique of gas adsorption is widely used to characterise a porous solid and solid catalyst by determining the specific surface area (mainly, BET) and the pore size distribution of the materials. The adsorption of a gas on a solid can provide information about the nature of the solid surface. Adsorption is defined as the enrichment of a component in the interfacial layer by physi-sorption, which occurs when an absorbable gas is in contact with the surface of a solid. It is possible to experimentally determine the amount of gas (mostly, nitrogen) adsorbed on the surface of a solid as a function of the equilibrium gas pressure. When measured at a constant temperature the relationship between these two quantities is know as the adsorption isotherm. The shape of the isotherm (Figure 4.2) is a characteristic of the type of adsorption process occurring which is in turn dependent on the nature of the surface and the specific pore structure as described in Chapter 2. Pores are classified into three groups, micropores, mesopores, and macropores, in Table 2.2 (in Chapter 2). Type IV shown in Figure 4.2 is associated with adsorption on a mesoporous solid and exhibits a characteristic hysteresis loop. The hysteresis loop is associated with capillary condensation and its shape is thought to be

dependent on the specific pore structure. However, this method cannot give information on the specific pore structure, notably, pore shape.

There are a number of methods by which the amount of gas adsorbed at various pressures is used to determine the specific surface area. The Brunauer-Emmett-Teller (BET) gas adsorption method is most widely used (Gregg & Sing, 1982). According to Gregg and Sing (1982), nitrogen adsorption is a valuable non-destructive tool for the examination of porous materials, but owing to limitations in computational methods it must be appreciated that there are uncertainties in the method. They reported that the degree of uncertainty is of ±10 %, but BET still provides a means of determining the specific surface of a mass of a porous material large enough to constitute a representative sample.

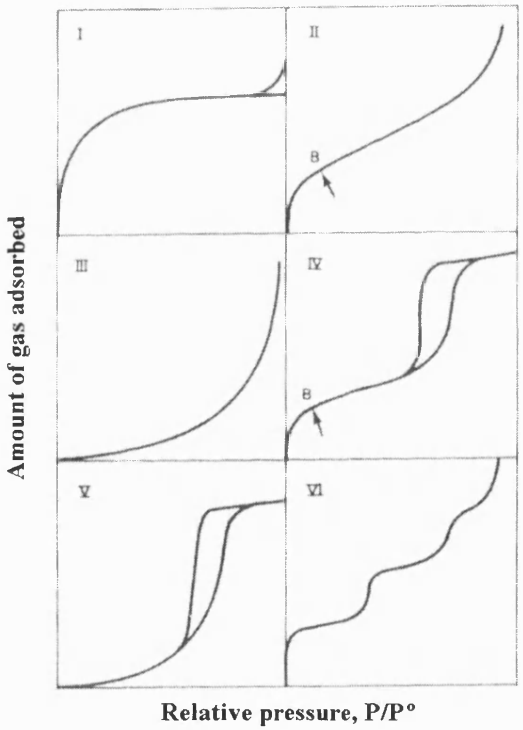

Figure 4.2. The five types of adsorption-desorption isotherms, I-VI (adapted from Gregg & Sing, 1982)

This type of experiment does not only give the specific surface area, but it also provides information on pore size distribution and the average pore diameter. There are also few methods to compute the pore diameter, but the BJH (Barrett-Joyner-Halenda) method is widely used. The basic equation used is the Kelvin equation as follows (Barrett, *et al.*, 1951):

$$\log(p/p^{\circ}) = \frac{-2\sigma_{N2}V_L}{RTr_k} = \frac{-4.14}{r_k} \qquad (4.1)$$

where

p = vapour pressure over the meniscus in the capillary, mbar

p° = saturation pressure, mbar

σ_{N2} = surface tension of nitrogen at T=77K, mN/m

V_L = liquid molar volume, m^3/mol

r_k = radius of capillary, nm

T = 77 K

R = the gas constant, 8.314 J/(mol·K).

Although average pore diameter and the pore size distribution obtained by this method is useful, there is a limitation that this method cannot provide geometrical information of the actual pore, such as type of pores and connectivity.

An ASAP 2010, from the Micrometrics Instrument Co (USA), was used in this work. The adsorbent used was nitrogen and the adsorption isotherm was obtained by measuring the relationship between the amount of nitrogen adsorbed and relative pressure at a constant temperature of 77 K. A procedure for the preparation of samples for gas adsorption analysis was adopted to get reproducible data. A certain amount of sample was dried overnight in an oven at 120°C and then transferred to a sample tube for degassing. The sample was evacuated at 200°C for at least 5 hours in a vacuum of 5 μm Hg. After cooling, the mass of the degassed adsorbent is weighed for use in subsequent calculations.

4.1.3. Mercury penetration

Mercury porosimetry is a technique which was originally developed to determine the macropore range of porous solids where the gas adsorption method is not applicable due to practical reasons, particularly, the Kelvin equation (Equation 4.1) is limited in the range of pore radius between 20 Å and 500 Å. The basic equation to compute pore size is (Ritter & Drake, 1945):

$$r_a = \frac{-2\sigma_{Hg}\cos\theta}{p} \qquad (4.2)$$

where r_a is the pore radius, p the pressure, σ_{Hg} surface tension of mercury (= 0.485

N/m), and θ the contact angle of mercury (= 130°).

Although this method can measure the pore diameter below 60 Å, it is generally accepted for characterising macroporous material, because high-pressure penetration causes destruction of pores (Gregg and Sing, 1982).

The instrument used in this study was a mercury porosimeter (Model: AUTOPORE II 9220) built by Micrometrics Instrument Co. It is capable of reaching a pressure 60,000 psi (4082 bar) and, therefore, of measuring pores down to a radius of about 60Å. The identical sample used in the nitrogen adsorption experiment was analysed with the mercury porosimeter. As only the macropores are involved, no rigid degassing was necessary. After placing the sample in the penetrometer, sample analysis was carried out by two runs, a low-pressure run (between vacuum and atmospheric pressure) and a high pressure run (from atmospheric pressure to 60000 psi (4082 bar)).

4.1.4. X-ray powder diffraction (XRD)

X-ray powder diffraction patterns were recorded with a Philips diffraction equipment (Philips, Netherlands). An X-ray generator (PW 1730/10, 4kW) and a diffractometer control unit (PW 1710) were used. The radiation used was Cu K_α, which has a wavelength of 0.1542 nm.

4.1.5. Scanning electron microscopy (SEM)

Scanning electron microscopy (SEM) was used to examine the pore structure of the sample, to observe the morphology of the powder used and also to examine formation of cracks after the samples had been electroplated and then heated. The instrument used was a JEOL T330 (JEOL, Japan) operated at 15 kV and a JEOL 6310, which was equipped with an energy-dispersive spectrometry (EDS) facility.

Specimens were prepared for SEM examination according to the following procedure. A section from the samples was mounted in Epoxy cold-setting resin (Struers A/S, Denmark) and then it was ground flat using silicon carbide paper on a Motopol 12 machine (Buehler Ltd, USA). The specimen was then ground for 2 minutes using a Perftex surface with a 30 micron diamond slurry, and then for 4 minutes with a 6

micron diamond slurry. They were then polished for 2 minutes on a Texamet 1 cloth with 1μm diamond, and finally polished with colloidal silica (0.3 μm) on Texamet 1 cloth for a sufficient time until a scratch free surface was obtained. To make the surfaces electrically conductive and prevent charging under the electron beam, a gold coating was added to the polished samples in an Edwards 5150B Sputter (BOC Edwards, England).

4.1.5. Transmission electron microscope (TEM)

The transmission electron microscope (TEM) used in this study was a JEOL 1200EX (JEOL, Japan), operated at 120 kV. Specimens were prepared by drying the alumina sol on a petri dish at atmospheric and by calcining the gel at the desired temperature. The specimens were reduced in thickness in the central region by an ion-milling machine until perforation at the centre occurs.

4.2. Washcoat preparation by the sol-gel method

In this thesis, preparation of an alumina washcoat by the sol-gel technique consists of a route using a metal alkoxide as a precursor and consists of the following three steps: alumina sol synthesis, washcoating, and addition of catalyst, see Figure 4.3.

4.2.1. Alumina sol synthesis step

The term "alkoxide-derived support" means a material prepared by depositing a thin layer of sol from metal alkoxide on a core material, converting the sol to gel by drying and finally converting the gel to metal oxide by calcination. The alkoxide-derived support comprises a monolith support material having on its outer surface a thin layer of a metal oxide produced from a precursor metal alkoxide. The monolith support material can be any material, such as a refractory oxide, which will not be decomposed or melt when subjected to calcination. One of the most commonly used materials as monolith supports in catalytic combustion applications is cordierite, which is a mixture of magnesia, alumina and silica. Table 4.1 shows typical properties of a cordierite ceramic monolith.

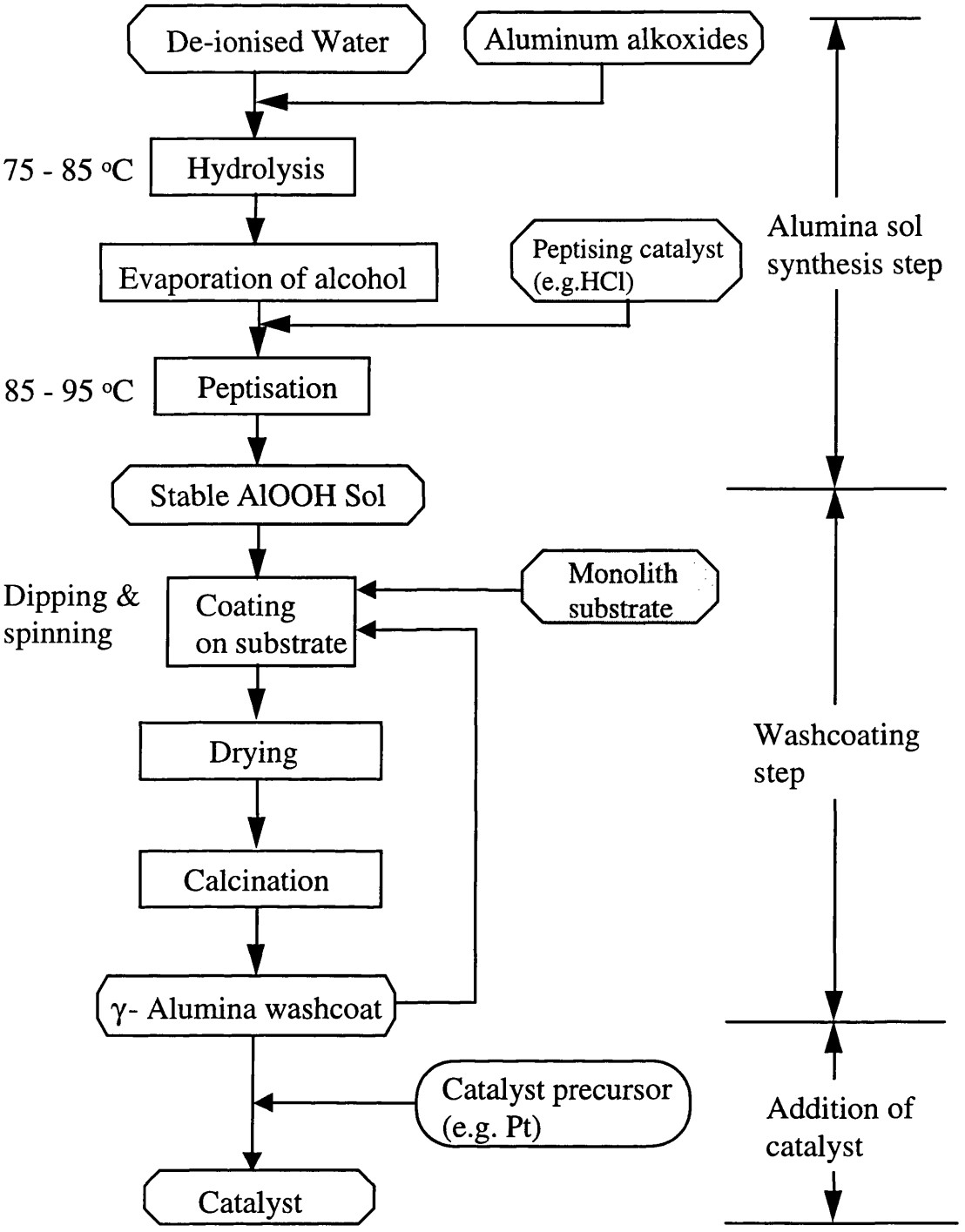

Figure 4.3. The procedure followed in the preparation of catalyst by the sol-gel method.

Table 4.1. Properties of cordierite ceramic monolith (adapted from Komeya and Matsui, 1994).

Crystalline phase	Main phase: cordierite Other Phases: mullite, spinel, alpha alumina	
Property	Units	Value
Thermal expansion coefficient(25-800°C)	10^{-6}/°C	0.8
Specific heat (25 °C)	cal/g °C	0.2
Thermal conductivity (25 °C)	W/(m.K)	1.1
Softening temperature	°C	1390
Water adsorption ratio	%	22
Total porosity	cm^3/g	0.2
Microporosity for ≥ 10μm	%	45
Mean pore diameter	μm	9
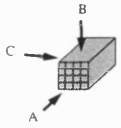 A direction	Mpa	>14
B direction	Mpa	>1.5
C direction	Mpa	>0.15

Alumina sol-gel is produced from a metal alkoxide and will be used in this work. A frequently cited process for the making of alumina gels is that described in Yoldas (1973; 1975).

In this study, aluminium *i*-propoxide and aluminium *sec*-butoxide are hydrolysed in a large excess of water, with an acid catalyst in the ratio of 0.07 mol acid/mol alumium alkoxide. The steps in the sol-gel alumina reaction are shown in Figure 4.4.

(a) Hydrolysis

Hydrolysis was performed by introducing the alkoxides into a known quantity of water that was stirred. The molar ratio of water to alkoxide was kept at *ca* 100. Double-distilled, deionised water at an initial temperature of 75°C was used. The water-alcohol-aluminium slurry was vigorously stirred for 15 to 20 minutes over a hot plate before the addition of acid.

(b) Peptisation

To initiate peptisation reaction, a peptising catalyst is normally required. Both acid and alkali can be used, but acid is more often used. Peptisation involves the addition of a

critical amount of certain acid into the slurry, which is then kept above 80°C for a sufficient time. Following the work of Yoldas (1975), 0.03 mole of acid per mole of alkoxide must be added to the slurry to peptise the system to a clear sol and the critical range of inorganic acids (*e.g.* HNO_3, HCl and $HClO_4$) is 0.03 to 0.1 mole per mole of the alkoxide.

Hydrolysis

Aluminum *i*-propoxide → *i*-Propanol

$$Al[OCH(CH_3)_2]_3 + H_2O \xrightarrow[80°C]{} Al[OCH(CH_2)_3]_2(OH) + C_3H_7OH$$

Peptisation

$$2Al[OCH(CH_3)_2]_2(OH) + 2H_2O \xrightarrow[HCl]{>80°C} C_3H_7O\text{–}\underset{\displaystyle OH}{\underset{|}{Al}}\text{–O–}\underset{\displaystyle OH}{\underset{|}{Al}}\text{–}OC_3H_7 + 2C_3H_7OH\uparrow$$

$$n\,Al(OC_3H_7)_2(OH) + nH_2O \xrightarrow[HCl]{} C_3H_7O\left(\begin{array}{c}OH\\|\\Al\text{-}O\text{-}\\\end{array}\begin{array}{c}OH\\|\\Al\\\end{array}\right)_n -OC_3H_7 + nC_3H_7OH\uparrow$$

Gelation

$$AlOOH\ sol \xrightarrow{drying} AlOOH\ gel + xH_2O\uparrow$$

High temperature reaction (Calcination)

$$AlOOH\ gel \xrightarrow[400°C]{} \gamma\text{-}Al_2O_3 + xH_2O\uparrow$$

$$\gamma\text{-}Al_2O_3 \xrightarrow[1000°C]{} \theta\text{-}Al_2O_3 \xrightarrow[1100°C]{} \alpha\text{-}Al_2O_3$$

Figure 4.4. Sol-gel alumina reactions: Hydrolysis, peptisation, and calcination in alumina derived from aluminium *i*-propoxide peptised with HCl (adapted from Brinker and Scherer, 1990).

Acid additions are generally specified in terms of pH (Brinker and Scherer, 1990). However, in the case of alumina gel synthesis, the type of acid played a much more important role than the pH of the system (Yoldas, 1975). For example, H_2SO_4 or HF did not produce the desired effect, regardless of the range of pH. The type of acid suitable for the peptisation of the hydroxide were thoroughly investigated by Yoldas (1975), who specified two general requirements:

(a) The anion of the acids must be non-complexing with aluminium ions at the low concentrations (H_2SO_4 and HF form complexes with aluminium.).
(b) The acid must also be sufficiently strong to produce the necessary charge effect in relatively small quantities with respect to aluminium concentration.

Heat treatment is needed to start peptisation of the slurry. Yoldas (1975) reported that the suspension must be heated above 80°C and this temperature held until a clear sol is formed. Below 80°C the rate of peptisation drops drastically, which tends to form a less stable sol at room temperatures.

4.2.2. Washcoating step

The washcoat is prepared by dip-coating the substrate with the metal oxide sol. In dip coating, a substrate is dipped into a homogeneous suspension containing the desired metal compounds, which would finally form the desired simple or complex oxides. The metal oxide suspension is contacted with the monolith substrate for a sufficient time to deposit the metal oxide precursor material onto the substrate by selective adsorption. A liquid film on the substrate becomes a gel film upon withdrawal of the substrate from the solution as a result of the gelling reaction during dying. The substrate with the gel film is heated to a high temperature (above 400°C) in order to produce chemical bonding between the film and substrate. The chemical bonding, **-Al-O-Al'-**, may be formed as a result of dehydration. Subsequent heating at a higher temperature will change the film to a crystalline washcoat with desired crystalline species.

In order to form washcoats which are firmly bound to the substrate upon heating, the thickness of one coating should be in the range of 0.1-0.3 μm (Sakka, 1989). If conditions exist at which the film becomes thicker than 0.3 μm, then the film may peel off the substrate wholly or partially. The underlying physics and chemistry of sol-gel thin film formation by dip coating can be found in a review by Brinker *et al.* (1992).

Other liquid-phase coating procedures, such as spin coating and dripping of a solution on the substrate can also be considered. Particularly, spin coating is the common method of applying uniform, thin coatings on many types of support, particularly, the plate. This method differs from dip coating in that the depositing film thins by centrifugal draining and evaporation. Levinson *et al.* (1993) found that the film

thickness was greatly affected by process parameters, such as, spinning rate, spinning time, density and viscosity of suspension, and volatility of the solvent.

However, the practicality of these methods may depend on the geometrical shape of the substrate. These methods are unlikely to be used for preparing a washcoat on a monolith substrate.

Drying and calcining

A composite prepared using any of the above techniques can be dried at a temperature ranging from room temperature to 300°C, to remove the excess solvent and then converted into the oxide form by calcining at temperatures from 150°C to 800°C. The physical properties of a resulting gel are relatively easy to control by changing the calcination temperature. In particular, the pore size distribution of a calcined washcoat is very narrow.

4.3. Preparation of alumina washcoats by sol-gel method

The alumina sol was dried in two different ways, air-drying and freeze-drying. The sample preparation scheme studied in this thesis is summarised in Figure 4.5. Zirconia-doped alumina was also produced in two different ways by either using zirconium alkoxide or zirconium nitrate.

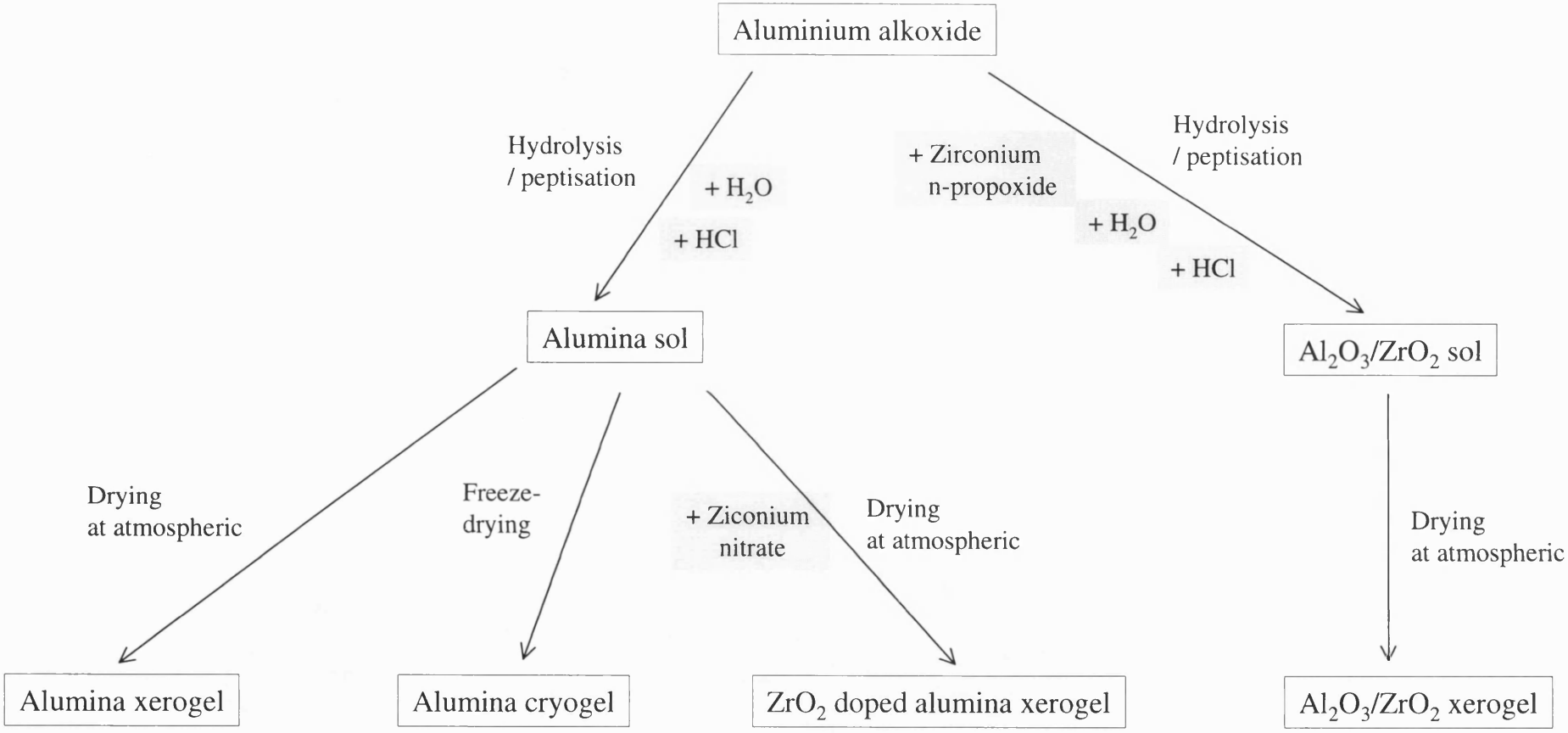

Figure 4.5. An illustration of the various types of samples that were prepared.

4.3.1. Preparing alumina sol

The alumina sol was prepared in the apparatus illustrated in Figure 4.6. The apparatus consist of a glass vessel, magnetic stirrer/heater and condenser. The glass vessel used was a flat-bottom flask (1 *l*) with a thermometer.

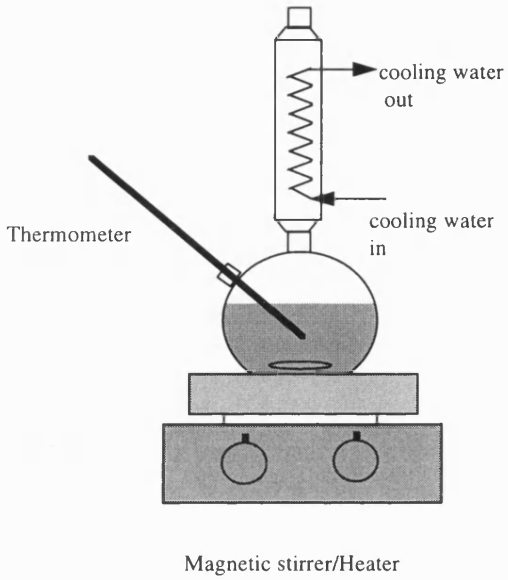

Figure 4.6. Alumina sol synthesis apparatus

Aluminum *i*-propoxide (98 %, Alfa chemical, Germany) and aluminum *sec*-butoxide (98 %, Alfa) were used as starting materials. Deionised-distilled water was required for the hydrolysis. *i*-Propanol (99%, Aldrich, USA) was used for diluting the alkoxides and HCl (1N, Aldrich, USA) was employed as a catalyst for hydrolysis. The alumina sol prepared from aluminium *i*-propoxide was labelled LAB2 and the alumina sol prepared from aluminium *s*-butoxide was labelled LAB3.

The ratio of water to the alkoxides and the ratio of HCl to the alkoxide were 100 and 0.05, respectively, according to Yoldas (1975). The hydrolysis was carried out at 80°C or over in the open glass container until the alumina content reached 10 wt% Al_2O_3 or higher. After hydrolysis, the resulting alumina sol was aged at around 90°C with complete reflux for a time in excess of 50 hours

It was possible to purchase an alumina sol, but its commercial use was as a ceramic binder and not as a catalyst support. This alumina sol, REMAL®A20 alumina dispersion, was obtained from REMET (New York, USA) and its applicability as a catalyst support was investigated. The physical and chemical properties as provided by the manufacturer are listed in Table 4.2.

Table 4.2. Physical and chemical properties of Remal A20 (Source: RAMET, Co)

Al_2O_3, wt%	20.0
pH, at 20°C	4.0
Specific gravity, at 20 °C	1.10
Electric charge to particles	positive
Crystalline size, Å	70
Viscosity, at 25 °C	< 50 cps
Surface area, m^2/g	180

4.3.2 Coating alumina sol onto a ceramic support

The ceramic monolith substrate was made of cordierite and obtained from Corning Inc. (New Jersey, USA). The typical properties of this material are listed in Table 3.3 (in Section 3.2).

Samples of monolith were dip-coated in the alumina (AlOOH) gel. After withdrawal, the excess sol was removed by blowing with air. The samples were then dried at room temperature and calcined at a desired temperature.

4.3.2.1. Uniformity of coating and adhesion: washcoat prepared from an alumina slurry *versus* the sol-gel method

Figure 4.7 presents the SEM images for washcoated monoliths prepared using two different methods. In one case the washcoated monolith is prepared with alumina slurry, in another the sol-gel method was used. An alumina slurry is usually a suspension of alumina powder or of dispersible precursor such as aluminium hydroxide, $Al(OH)_3$ or boehmite, γ-AlOOH. Therefore the properties of the washcoat may be highly dependent on the powder characteristics, particularly particle size.

The washcoat prepared from alumina slurry usually has a round shape in the corner of the cell because alumina accumulates in the corner of the channel due to the formation

of a meniscus in the coating process, but the washcoat prepared using the sol-gel method is evenly coated on the channel wall. Considering the economy of use of washcoat materials, the material in the corner may be a waste. Also, a thicker layer of washcoat may cause an increase in pressure drop across the monolith because the channel size is reduced by washcoating. A SEM image of a monolith coated with alumina slurry is illustrated in Figure 4.7(b) and Figure 4.7(d). The cracks in the washcoat have also been reported in the SEM images illustrated in Hayes and Kolaczkowski (1997). There is a risk that under operating condition these thin layers could fracture, resulting in loss of catalyst/activity.

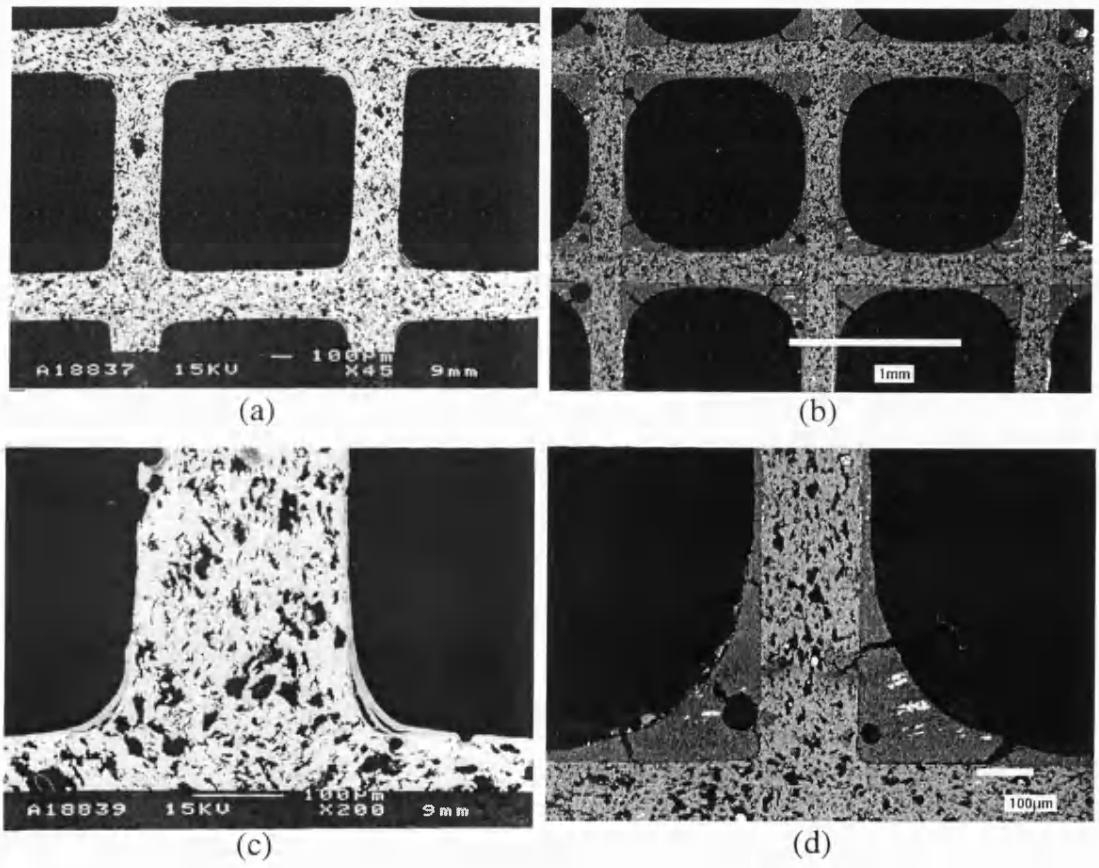

Figure 4.7. SEM images of cells: comparison between a washcoat prepared using the sol-gel method (a) and (c), and a washcoat prepared by a catalyst manufacturer from an alumina slurry (b) and (d).

Adhesion of the washcoat on the porous support takes place by a mechanical mechanism, such as anchoring and interlocking of the washcoat particles among them as well as with the surface irregularities of the support, and the interfacial forces between the washcoat and support material. Agrafiotis and Tsetsekou (2000b) reported

that the interfacial forces among the powder particles can be increased by reducing the particle size of the washcoat material and may improve the adhesion of the washcoat layer on the support. They also reported that there exists a certain threshold value - around 5 μm- below that the agglomerate's size has to be reduced.

On the other hand, by using a sol-gel method, a well-adhered washcoat layer can be formed *in situ* upon the walls of the support. The sol has strong interfacial forces with the porous support as well as among neighbouring particles. However, there are low washcoat loadings per impregnation. Also cracking and subsequent peeling-off of the washcoat layer can occur due to the loss of large amounts of volatile compounds during the calcination. Sarraco and Montanaro (1995) argued that the penetration of the sol in the porous structure of the support could be a problem in applications where the structure acts as a filter. However, in catalytic monoliths this may be an advantage as the penetration of the sol will act as an anchor for the washcoat layer and consequently improve the adhesion of the washcoat to the support.

Figure 4.8 shows SEM images of a washcoat on a cordierite monolith substrate prepared using the sol-gel method. It can be seen that the thickness of the washcoat is very even, around 3 μm in thickness (Figure 4.8(a) and Figure 4.8(c) shows each side of washcoat on the substrate). Some non-uniformity of washcoat is found in the crevice of the monolith substrate where the pores have been filled, see Figure 4.8(d) and Figure 4.8(d). However, this would increase the adhesion of the washcoat layer on the monolith substrate by anchoring and interlocking of the washcoat particles with the surface irregularities of the support.

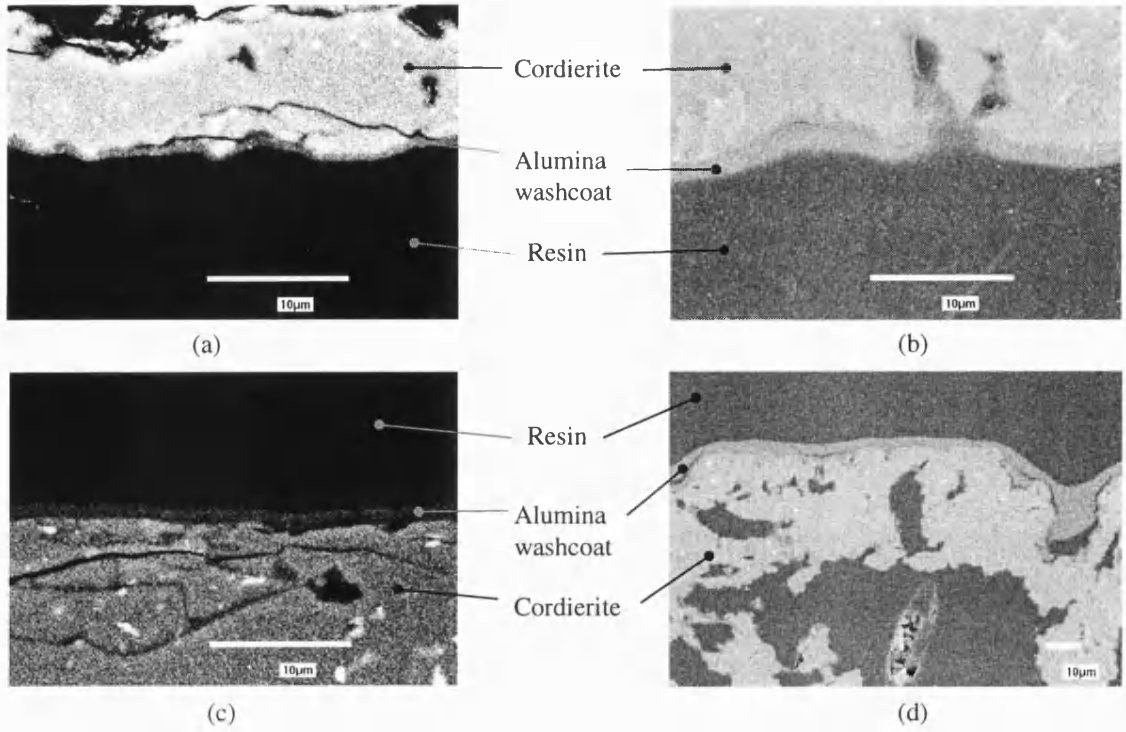

Figure 4.8. Alumina washcoat on cordierite substrate by sol-gel method.

The dip-coating method followed by air blowing was also used to coat the plate samples used in the diffusion cell. However, the thickness of the coating was found to be uneven. Thus, the method was modified by dipping the plate into the alumina sol and then using a spinning technique, which used the centrifugal force to remove excess sol from the support. Figure 4.9 shows the apparatus for preparing a washcoat on a cordierite plate. The speed of the motor was in the range of 2500 - 3000 rev/min.

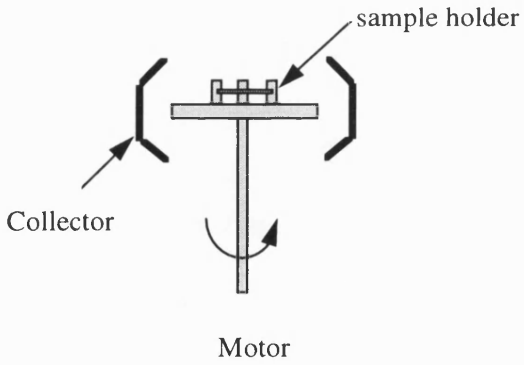

Figure 4.9. Schematic of spinner.

4.4. Physical properties of the samples

4.4.1. Physical properties of cordierite substrate

The apparent density, the macropore porosity, and the macropore size distribution of the cordierite substrate were obtained by mercury porosimetry. The mercury porosimeter used was Autopore II (Micrometrics, USA) and the experimental method was described in Section 4.3.2. The macroporosity and the pore size distribution were determined from the cumulative pore volume data obtained by mercury porosimetry. The experimental cumulative pore volume data are given in Appendix 3. Table 4.3 lists the physical properties of the cordierite substrate used.

The pore size distribution of the cordierite substrate measured by mercury porosimetry is shown in Figure 4.10. The median pore diameter was 3.3 μm and the average pore diameter was 0.54 μm. The pore volume and the pore area were 0.088cm^3/g and 0.652 m^2/g, respectively.

Table 4.3. Physical properties and pore size characteristics of a cordierite substrate.

Composition (wt%)*	MgO 13.5 ± 1.0% Al_2O_3 35.4 ± 1.5% SiO_2 49.7 ± 1.5% Impurities (K_2O 1.0%, TiO_2 1.0%,CaO 0.5%, Fe_2O_3 1.0%,Na_2O 0.4%)							
Surface area**, m^2/g	Apparent density****, g/cm^3	Pore volume, cm^3/g	Porosity			Pore diameter, μm		
			total***	macro	micro	average***	macro***	micro**
0.65*** (0.33**)	2.48	0.088	0.299	0.297	0.002	0.54	0.54	0.003 6

* Supplied by Corning Inc (New York).
** Obtained by N_2 adsorption-desorption measurement
*** Obtained by mercury porosimetry
**** Obtained by a pycnometer

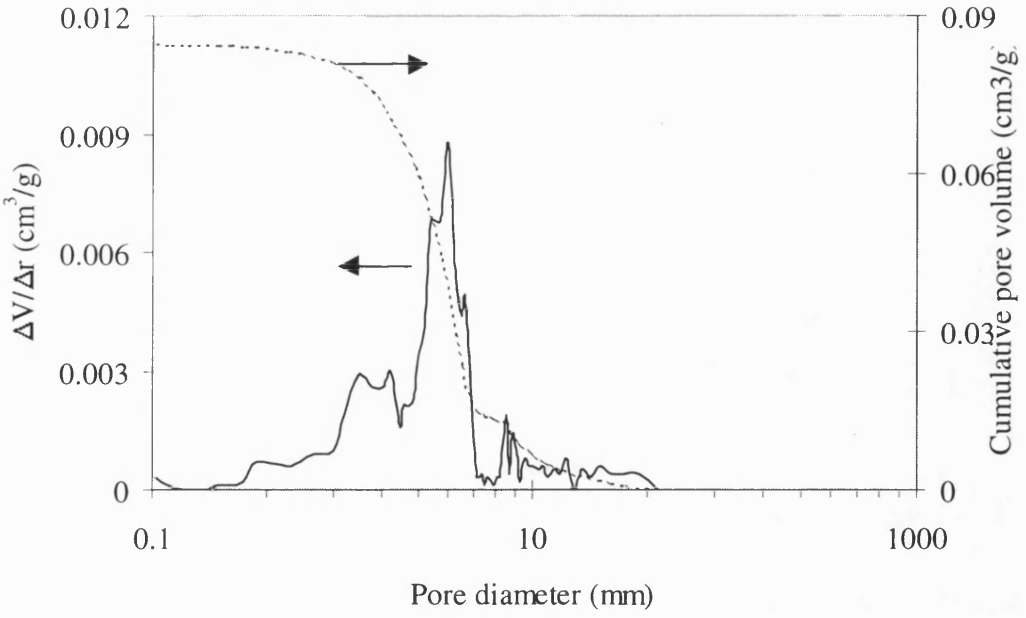

Figure 4.10. Pore size distribution of the cordierite monolith substrate obtained by mercury porosimetry.

4.4.2. Physical properties of washcoated cordierite substrates

After washcoating the alumina on the cordierite substrates (both monolith and plate), the pore size distribution was measured by mercury porosimetry. Figure 4.11 shows the comparison between macropore size distribution between washcoated and non-washcoated cordierite substrates (calcined at 600°C). It was found that the macropore sizes decreased after washcoating. The median pore diameter of the coated cordierite monolith decreased from 3.3 μm to 2.7 μm and the average pore diameter decreased from 0.54 μm to 0.16 μm. For the coated plate, the median pore diameter decreased to 2.2 μm and the average pore diameter was 0.16μm after washcoating. There was a difference between these two coated samples, but in both case there was a shift in the pore size distribution curve. This may have been caused by the filling of pores with alumina gel particles. This can be seen in the SEM images shown in Figure 4.12. The alumina gel was found in the macroporous structure of the cordierite substrates.

A nitrogen adsorption experiment was carried out to measure the pore size distribution in the range of pore diameters between 1 nm and 100 nm. Figure 4.13 presents the pore

size distribution for washcoated cordierite substrates including macropores and mesopores.

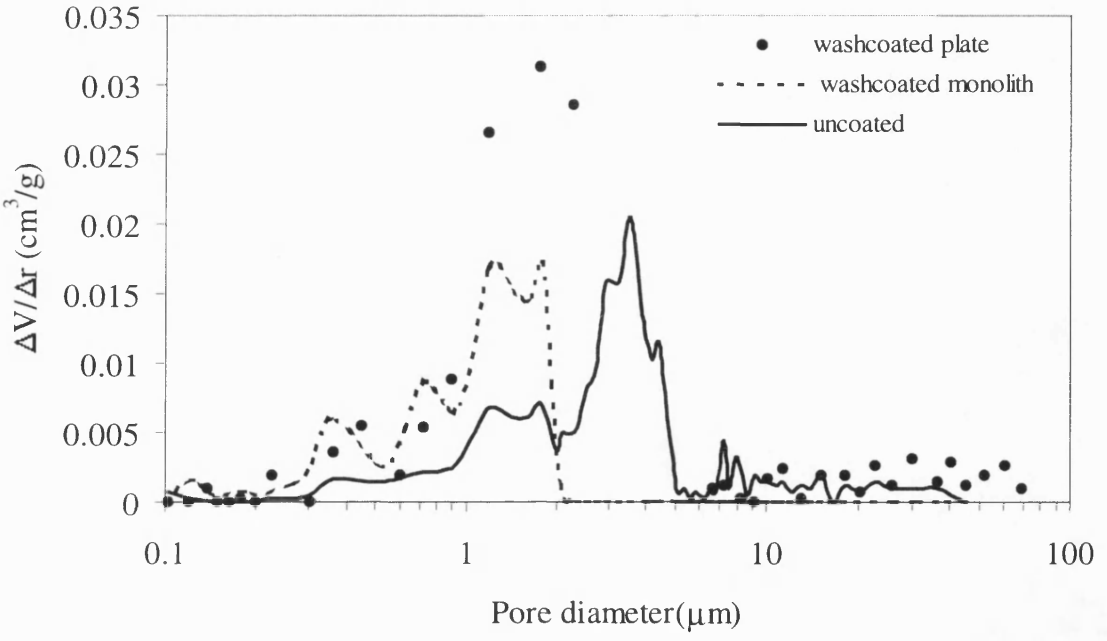

Figure 4.11. Pore size change as a result of washcoating. The samples were coated once and calcined at 600°C. Porosity of cordierite substrate obtained by mercury porosimetry: 29.9 ± 1.2 %.

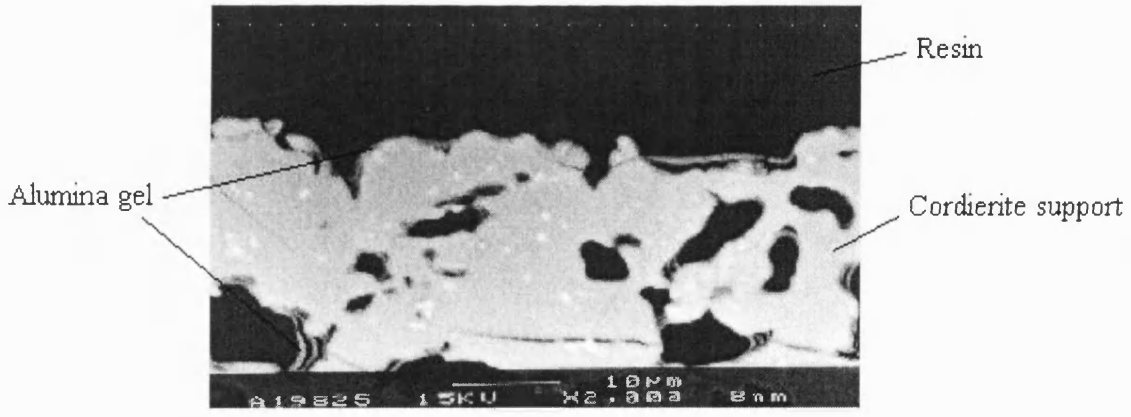

Figure 4.12. SEM images showing washcoated cordierite substrates showing the presence of alumina gel in the substrate macropores.

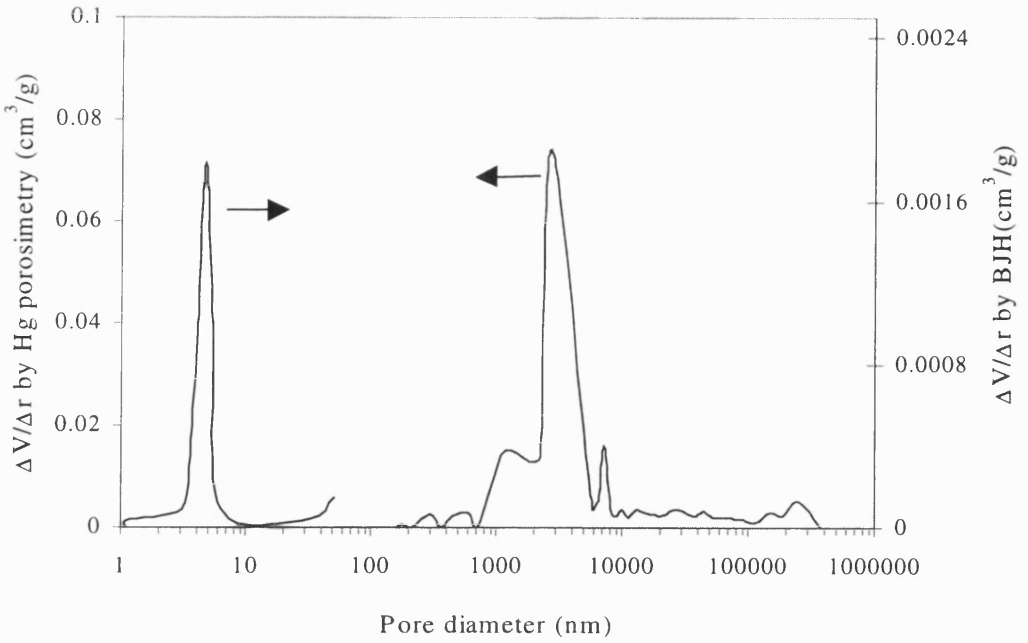

Figure 4.13. Pore size distribution of washcoated cordierite (1st coated) calcined at 600°C: Macropores obtained by mercury porosimetry and mesopores obtained by BJH method with nitrogen adsorption.

4.4.2.1. Increasing film thickness by the number of coatings

Dip coating followed by spinning was used to prepare the washcoat. The thickness of the washcoat and the weight of the sample increased with the number of coatings, see Figure 4.14. It was found that the weight increased linearly, but the washcoat hardly appeared in the first coating. This may be due to the filling of pores, see Figure 4.10 and Figure 4.11. After the first coating, the mouth of the pore in the monolith substrate became blocked, and then after subsequent coatings a linear increase of thickness was observed.

The change of specific surface area and pore volume, as a result of washcoating, was also investigated. Figure 4.15 presents the BET specific surface area and pore volume of a cordierite plate with different thicknesses of washcoat layers. The surface area and the pore volume are increasing linearly with increasing number of coatings.

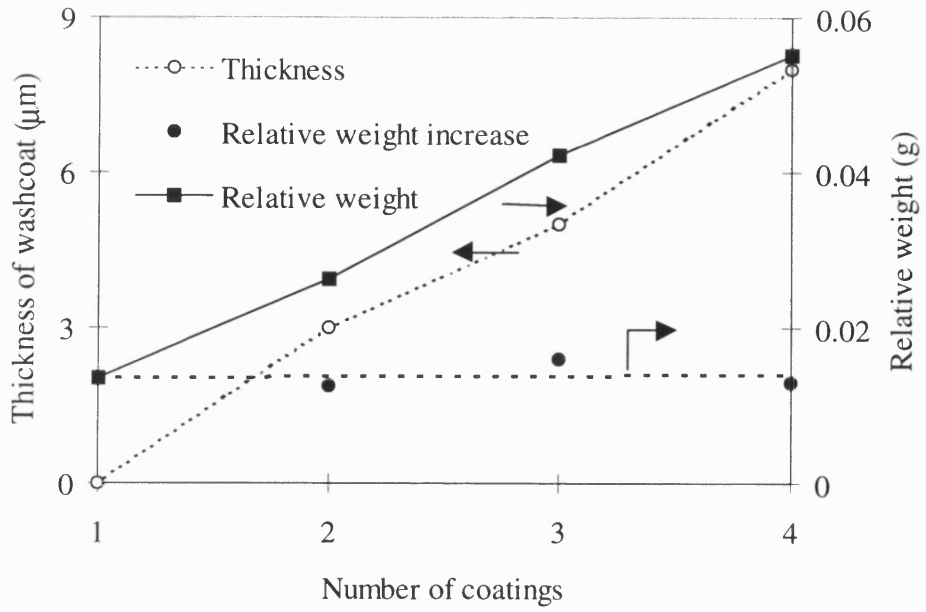

Figure 4.14. Number of coating vs. relative weight and thickness of washcoat.

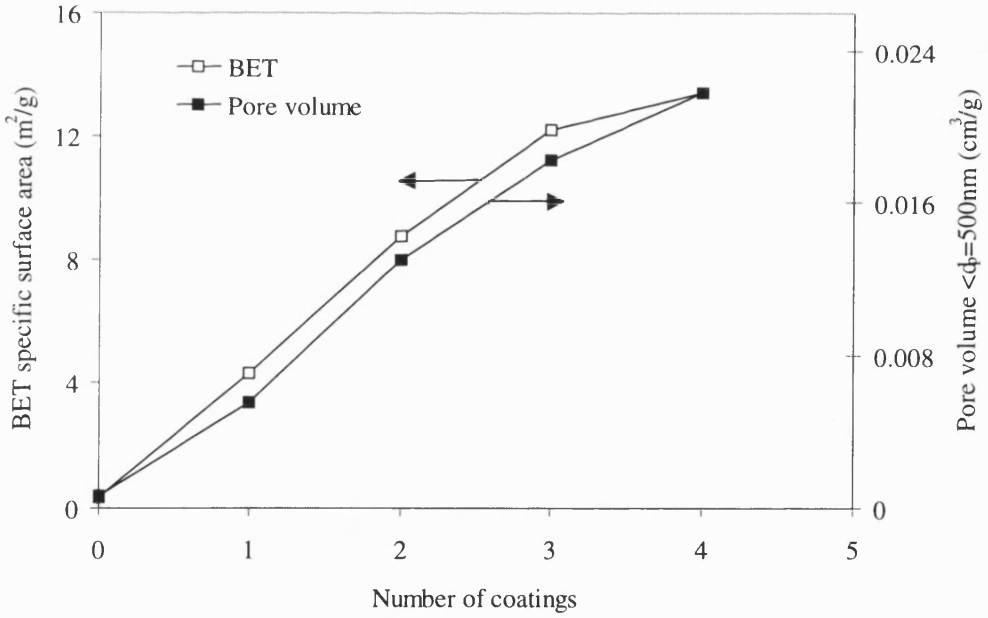

Figure 4.15. The increase of specific surface area and pore volume (for a pore diameter below 500nm) with an increase in the number of coatings.

Figure 4.16 shows SEM images for a washcoat on a cordierite plate prepared using the sol-gel method. The two images, Figure 4.16(a) and Figure 4.16(c), are the washcoated cordierite coated twice and the images in the right represent the washcoated plate coated four times. It can be seen that there are open cavities in the surface as the surface image shows a big pore opening, see Figure 4.16(c). By further coating the surface cavities in the porous support become filled and the surface is then covered with a layer of alumina washcoat, see Figure 4.16(d).

Figure 4.17 shows the change in the pore size distribution of a washcoated cordierite substrate as the number of coating is increased. The pore size distribution was calculated using the BJH method from nitrogen adsorption-desorption experiment. The average pore size was in the range of mesopores and there was no big change after increasing the number of coatings, but the pore volume was increased by the number of coatings.

The washcoat layer can be clearly distinguished from the cordierite substrate, see Figure 4.18. The marked layers in the SEM image were identified by performing EDS (Energy disperse spectrometry) analysis. The layer labelled A only contains aluminium (this results from the alumina in the spectrum, see Figure 4.18(b)). Figure 4.18(c) illustrates the spectrum of the layer labelled B and shows that the layer consists of the cordierite ($Mg_2Al_4Si_5O_{18}$) substrate as it contains the three major elements in this material, Al, Si, and Mg.

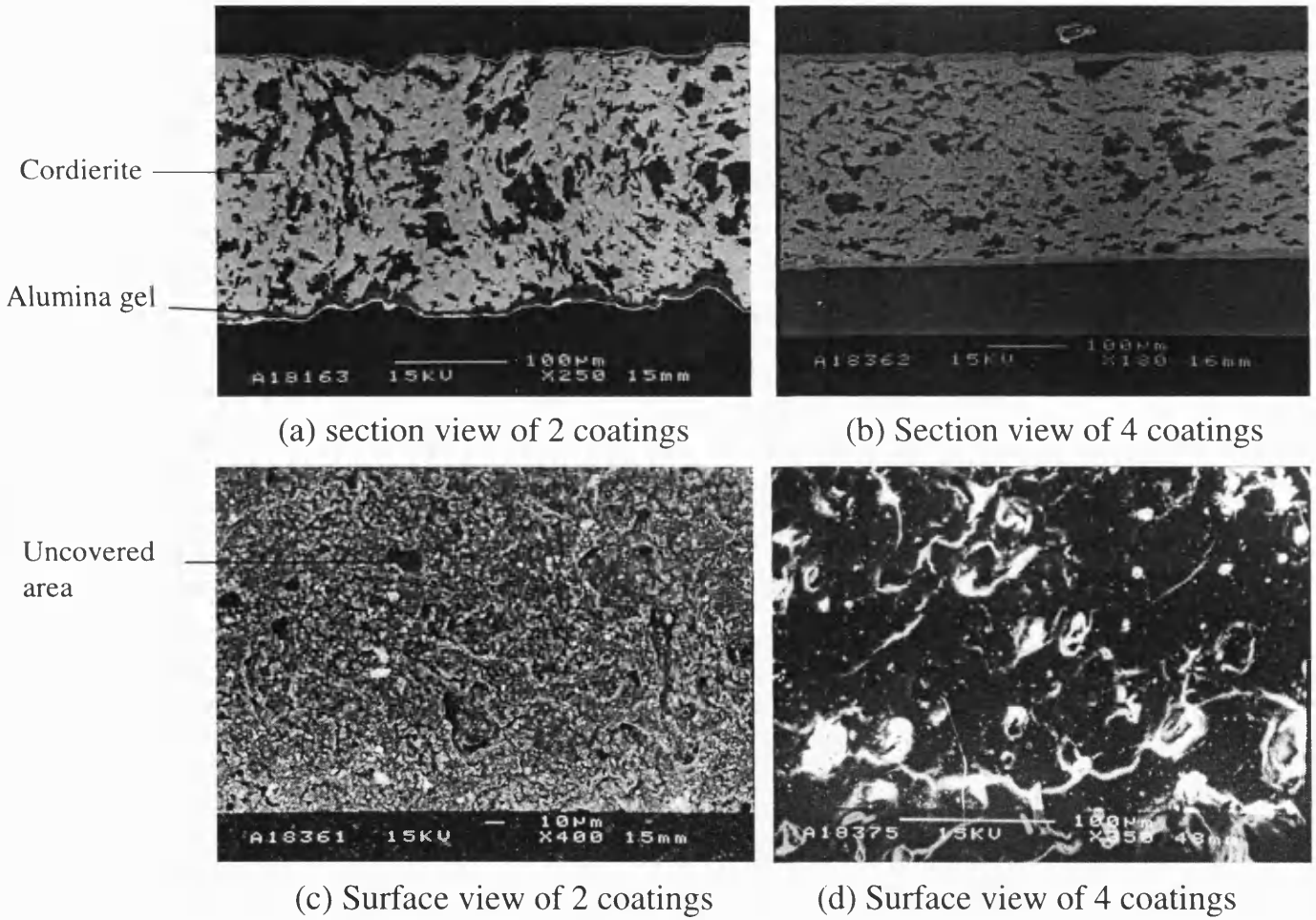

Figure 4.16. Washcoat on cordierite plate prepared from alumina sol (LAB2).

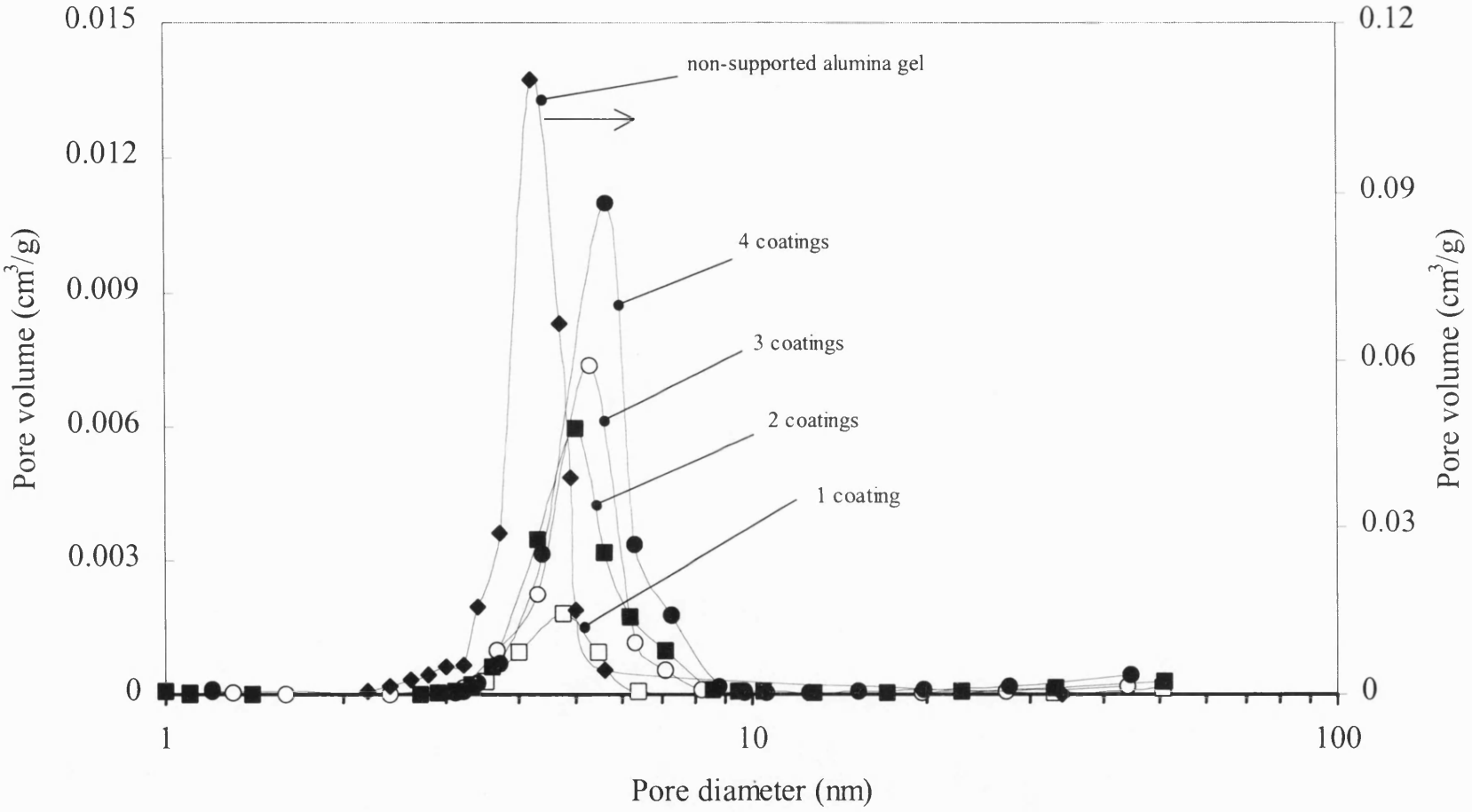

Figure 4.17. Pore size distribution of a non-supported alumina (Lab2) and alumina washcoated cordierites (calcined at 600°C for 20hrs).

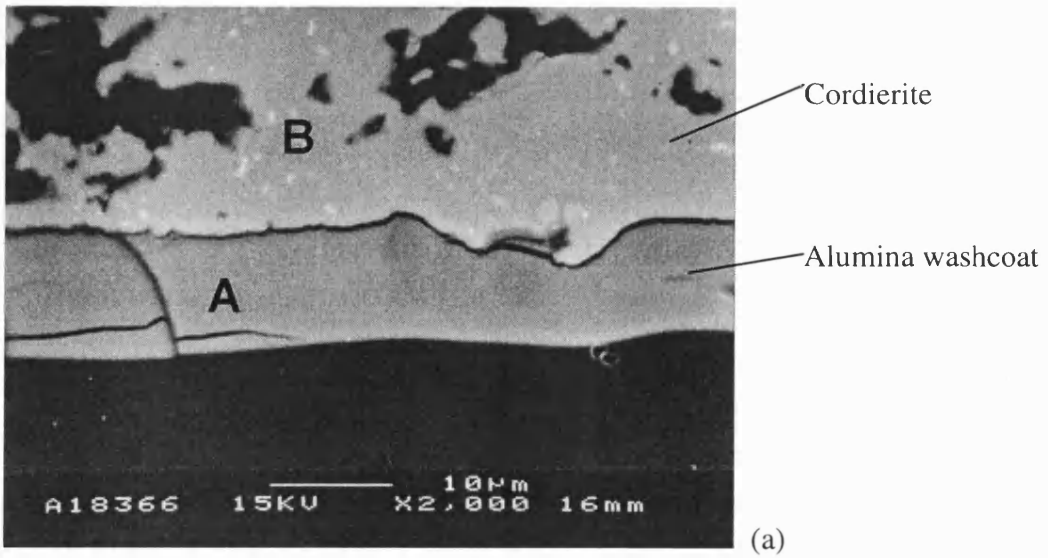

(a)

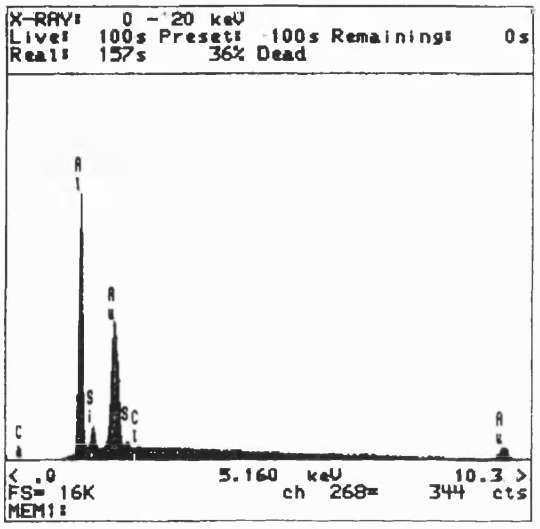

(b)

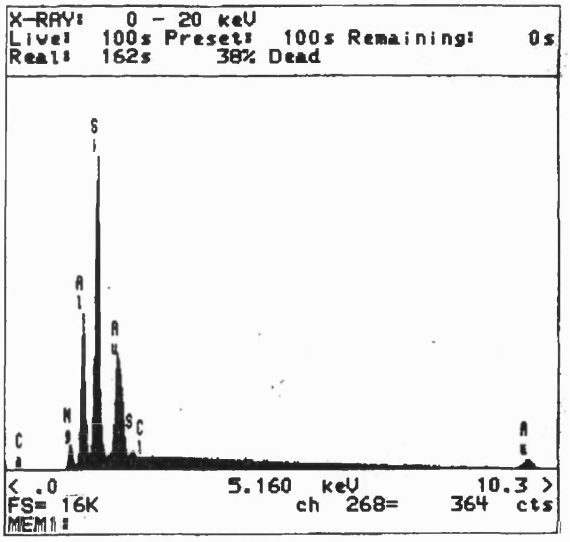

(c)

Figure 4.18. X-ray analysis of washcoated cordierite substrate. (a) SEM image A: alumina washcoat, B: cordierite substrate, (b) X-ray spectrum of the washcoat labelled "A" and (c) X-ray spectrum of the support labelled "B".

4.5. Parameters studied

4.5.1. Effect of gel preparation method on washcoat properties

Figure 4.19 illustrates how the physical property of the alumina gel changes with an increase in calcination temperature obtained by nitrogen adsorption experiment. Two alumina gels (LAB2 and LAB3) were compared with a commercial gel (Remal A20) obtained from REMET Co. Both LAB2 and LAB3 were prepared by the method reported by Yoldas (1976), but different forms of the alkoxides were used as a precursor, aluminium *i*-propoxide for LAB2 and aluminium *sec*-butoxide for LAB3.

X-ray diffraction patterns of alumina gels, LAB2 and LAB3, calcined at different temperatures are shown in Figure 4.20 and Figure 4.21, respectively.

The XRD patterns for alumina prepared using the sol-gel method and calcined at different temperatures were compared with the commercially available γ-alumina powder. As can be seen in Figure 4.22, the alumina gel (LAB3) calcined at 450°C has a similar pattern as the γ-alumina, but the gel calcined at 1000°C is different from the γ-alumina powder calcined at the same temperature. The alumina gel prepared at 1000°C was found to be θ-alumina, but the γ-alumina powder was transformed to α-alumina after calcined at 1000°C. It can be concluded that the alumina prepared by sol-gel method has a higher thermal resistance than the commercially available form of alumina.

Transmission electron microscopy (TEM) was used to investigate the pore structure of the alumina gel. Figure 4.23 presents the TEM images of alumina gel (LAB3) calcined at 600°C. It is difficult to find any particular structure from this alumina gel calcined at 600°C, compared with the TEM images (Figure 4.24) for the alumina gel (LAB3) prepared by sol-gel method and calcined at 1000°C. This shows a variety of sizes and shapes of pores. The largest pore is around 100nm, but the rest are much smaller. As can be found in the pore size distribution calculated by BJH method, the pore sizes lie between 5nm and 20nm with an average value of 10 nm.

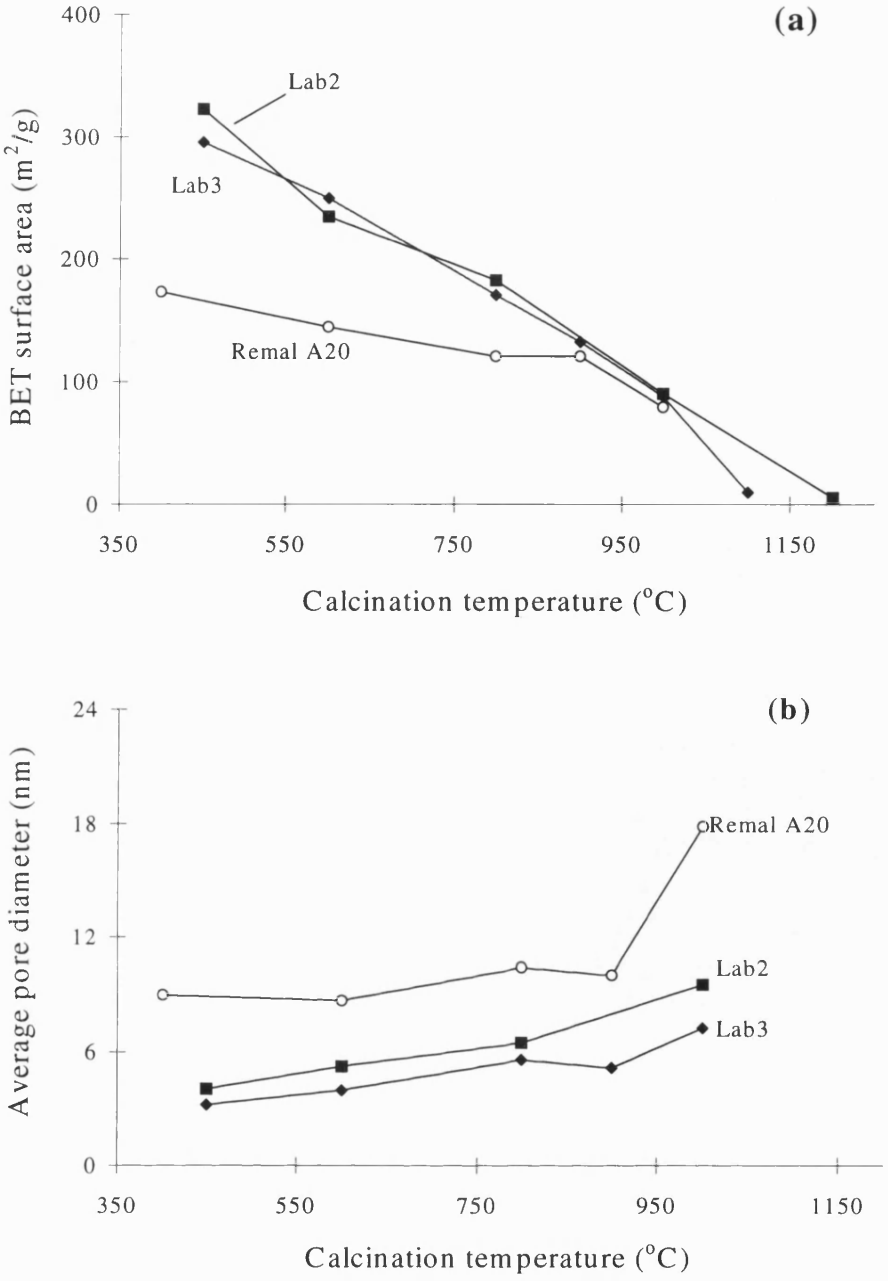

Figure 4.19. Comparisons between a commercial alumina gel (Remal A20) and two alumina gels (LAB2 & LAB3) prepared in this work. (a) BET surface area, (b) Average pore diameter obtained BJH method.

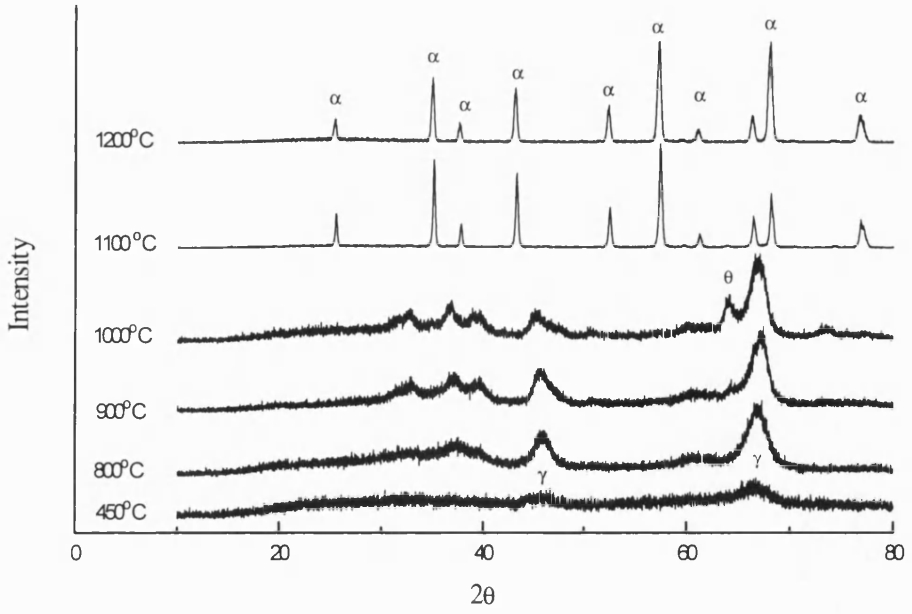

Figure 4.20. XRD patterns of alumina gels (LAB2) calcined at different temperatures.

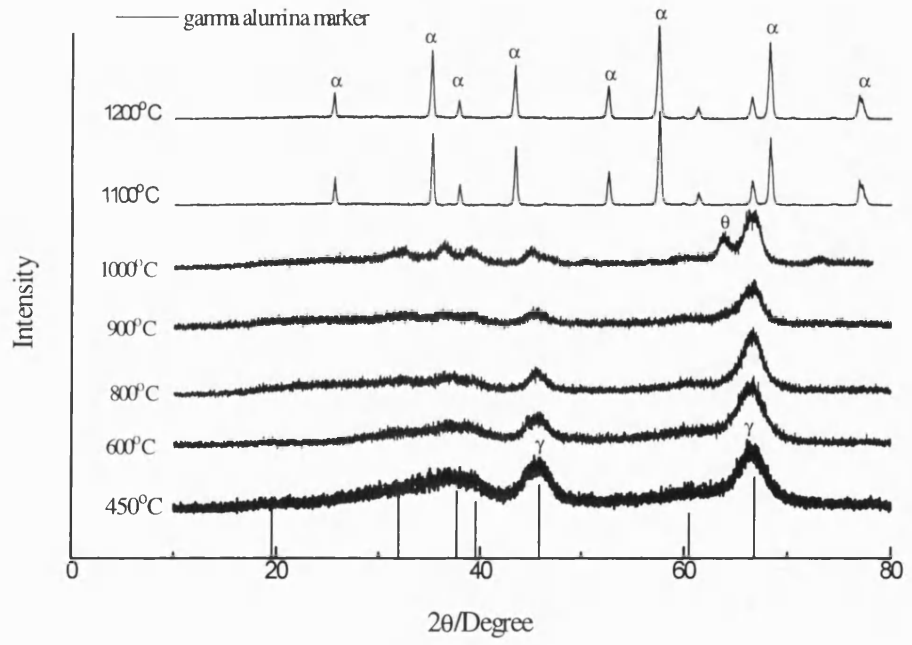

Figure 4.21. XRD patterns of alumina gels (LAB3) calcined at different temperatures.

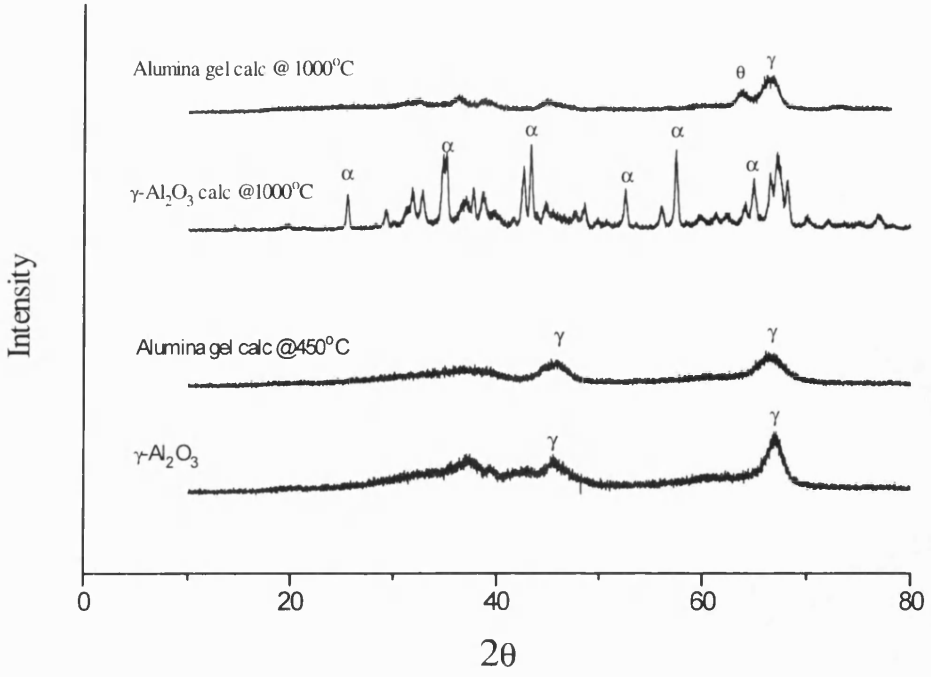

Figure 4.22. Comparison between alumina gel prepared by the sol-gel method and alumina powder obtained from Alfa chemical Co.

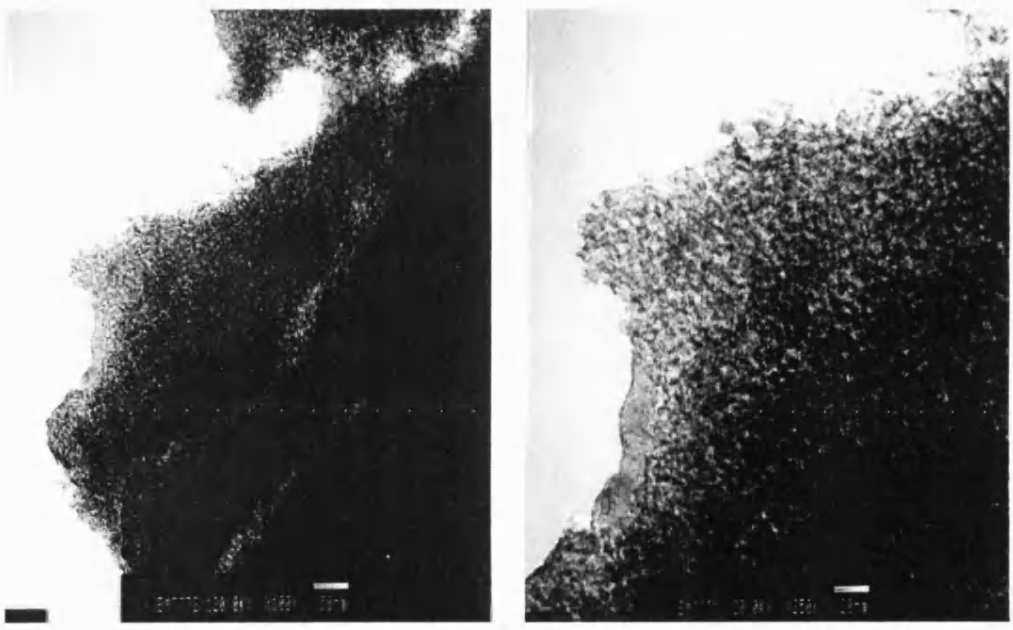

(a) (b)

Figure 4.23. TEM images of alumina gel (LAB3) calcined at 600°C: (a) Magnification: ×100,000, (b) Magnification: ×250,000.

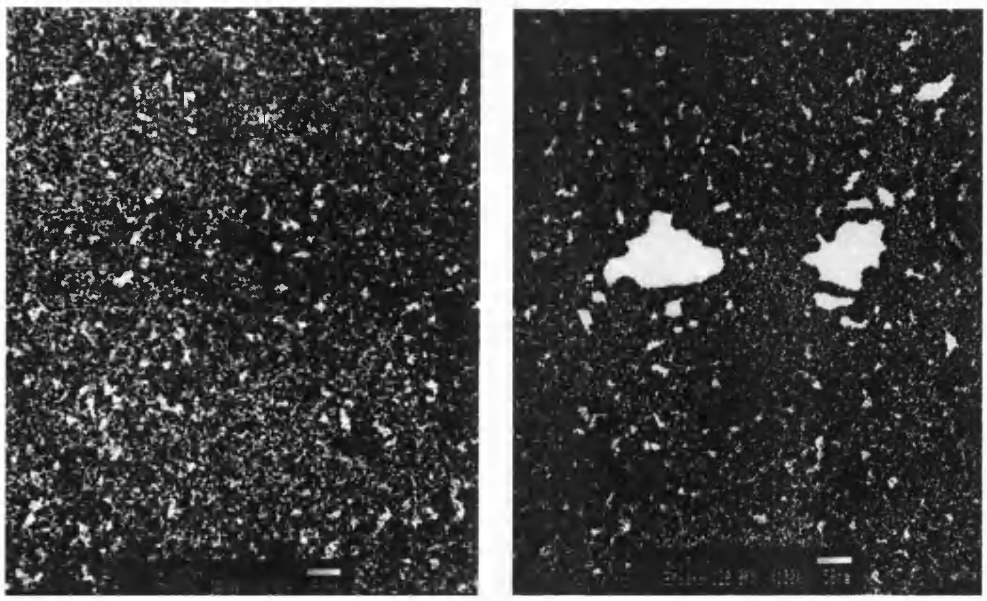

(a) (b)

Figure 4.24. TEM images of non-supported alumina washcoat, LAB3 calcined at 1000°C (Magnification: ×100,000).

Finally, the change in porosity with calcination temperature was also studied. The apparent density of the alumina gel (LAB2) was measured using the pycnometer (Appendix 5) and the pore volume was obtained from the nitrogen adsorption experiment (Appendix 4). The apparent density and the pore volume of the alumina gel calcined at different temperature are presented in Table 4.4. The apparent density of the alumina gel measured in this study was found to be similar as the density of alumina found in the literature. Within experimental errors, the density is constant. The average density of the alumina gel (LAB2) and the value found in literature was 4.01 g/cm^3 and 3.96 g/cm^3, respectively.

Based on the two parameters, the porosity was also presented in Table 4.4 and Figure 4.25. It can be seen that the porosity of the alumina gel decreases at a calcination temperature of about 1000°C. It is postulated that this is due to the phase change of the alumina, as γ-Al_2O_3 is transformed to θ- Al_2O_3 and then transformed to α- Al_2O_3.

Table 4.4. Physical properties of alumina gel (LAB2).

Calcination temperature, °C	Apparent density, g/cm^3	Pore volume, cm^3/g	Porosity*	Average pore diameter, nm	BET surface area, m^2/g
450	3.93	0.360	0.591	3.65	285.3
600	3.91	0.372	0.599	4.29	235.1
800	4.24	0.353	0.586	5.2	176.1
1000	4.27	0.229	0.480	7.5	90.5
1100	3.89	0.056	0.184	20.95	9.3
1200	3.84	0.018	0.067	37.86	5.3

* Porosity = pore volume/(pore volume + 1/average apparent density). Note: the average value of apparent density is 4.01 g/cm^3.

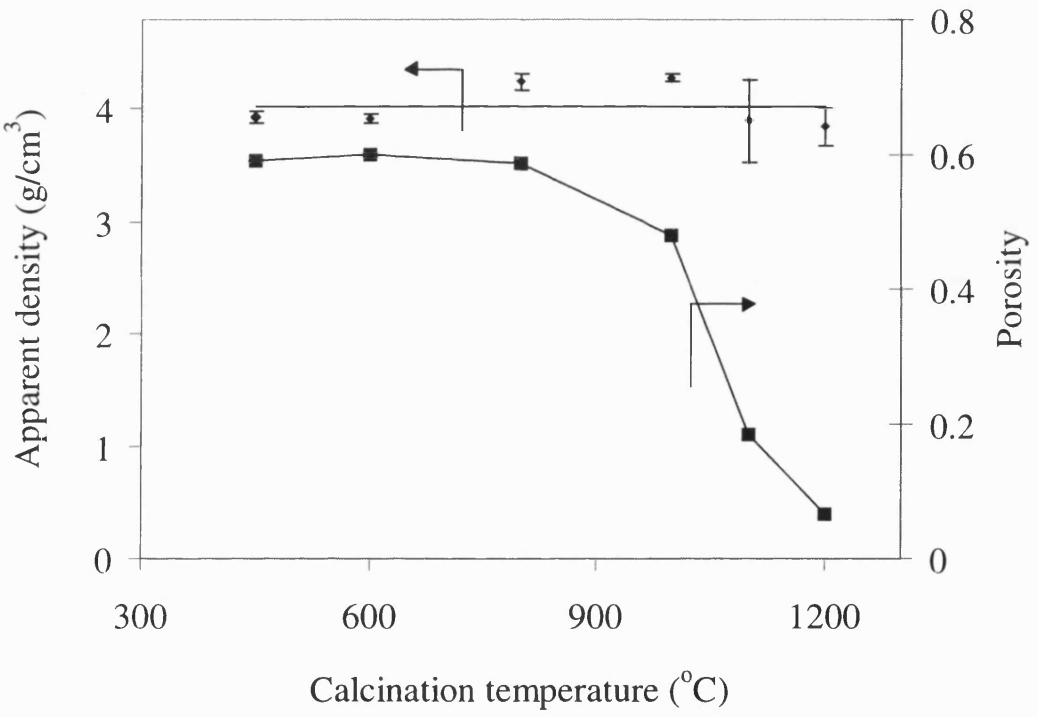

Figure 4.25. Porosity change of alumina gel with an increase of calcination temperature. Average density: 4.01 g/cm^3.

4.5.2. Investigation of a freeze-dried alumina gel

In order to investigate the effect of drying (gelation) conditions on the properties of the gel, two extreme different drying conditions were studied, drying at atmospheric (xerogel) and freeze drying (cryogel). Xerogels were prepared by drying about 20 *ml* of pure alumina sol in a petri dish at room temperature in air for a few days. To prepare cryogels, about 1*ml* of pure alumina sol was poured into a metal container (10 mm in diameter, 10 mm long) and this was then dipped into liquid nitrogen (T=77K) to freeze the sol. Then the solvent (water) was sublimated with phosphorous pentoxide (Aldrich, 98%) in a freeze drying unit (BOC Edwards, England). The sublimation was made under a residual pressure of 10^{-3} mmHg and lasted for about 15 hours at a temperature of about -60°C.

The purpose of experimenting with freeze-drying, was to see whether an alumina washcoat could be produced that did not shrink or crack. However, the resulting gel produced a gigantic flake structure of a quite different appearance as shown in Figure 4.26. Attempts to freeze-dry gels typically result in flakes or in translucent bodies with large pores that are the fossils of the crystal (Brinker and Sherer, 1990). Mostly, freeze-dried gels have been used to produce a fibre of ceramic materials by freezing uni-directionally, such as silica fibres (Mahler and Bechtold, 1980), alumina fibres (Maki and Sakka, 1986), and zirconia fibres (Kokubu *et al.*, 1988).

Although it is not intended that this study be limited to any particular theory relevant to freezing gels, the alumina freezing gel may be formed in the following manner. Growth of ice in a cellular substructure is accomplished by advancing the solid-liquid interface through the body of aqueous boehmite (AlOOH) particles at a rate, which provides a region of constitutional supercooling ahead of the advancing interface. As ice forms at the interface, it rejects the solute thus increasing the concentration of solute in the body of aqueous boehmite peptide ahead of the solid-liquid interface. Since the concentration of solute in the body of aqueous boehmite peptide is greatest at the interface, the temperature at the interface is below the freezing temperature of the body of aqueous boehmite peptide everywhere except at the interface.

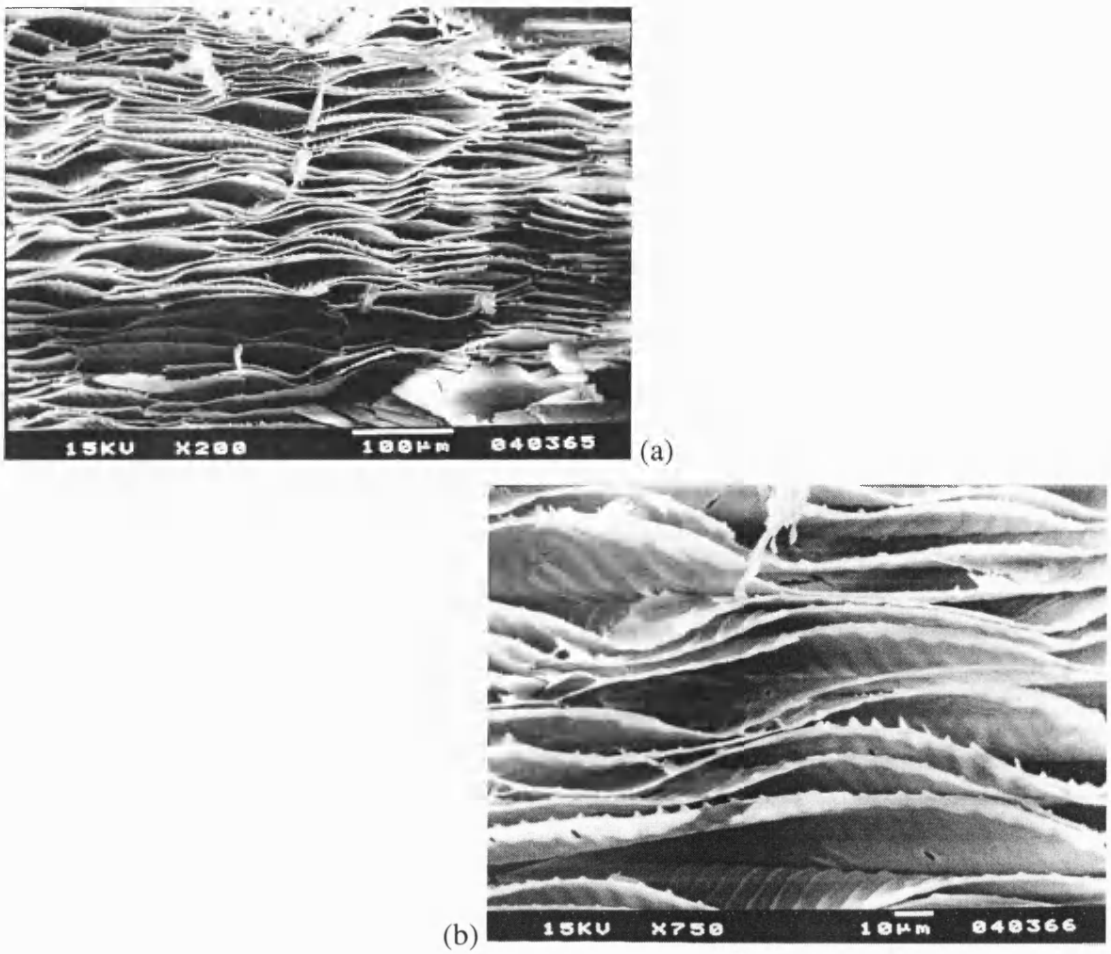

Figure 4.26. SEM images of a flake-like alumina gel prepared by freeze-drying.

Freezing of ceramic colloids has been widely discussed (*e.g.* Scherer, 1993; Statham *et al.*, 1998), but all morphological description of the products have been of small particulates, especially powders, flakes, ribbed flakes, interconnected cells, and granules. The variables determining the product morphology include the concentration of solutes, extent of polymerisation, pH, freezing temperature and freezing rate.

In this study, the freezing of the alumina sol (10 wt% Al_2O_3) was carried out in the following steps:

- Dip-coating the cordierite monolith with alumina sols.
- Dipping the coated monolith in liquid nitrogen (T=77K).
- Freeze drying the coated monolith at -60°C for 20 hours.
- Calcining the freeze-dried gel on monolith at 450 °C.

The alumina coating produced by freezing was examined by SEM. The coating consisted of many layers of plates, ridged on one side and flat on the other. The thickness of the plate was between 0.8 μm and 2 μm. The freeze-dried alumina calcined at 450 °C was found to be γ-alumina (confirmed with XRD). The XRD pattern of the freeze-dried alumina is similar to the pattern of the xerogel as shown in Figure 4.20.

The nitrogen adsorption-desorption isotherm for the nonsupported alumina cryogel calcined at 450°C is Type IV, see Figure 4.27(a), which indicates that it has a mesoporous structure. The BET specific surface area of the sample was 282m^2/g and the average pore diameter was 2.8 nm, with a pore size distribution as shown in Figure 4.27(b). Compared to the xerogel calcined at 450°C (BET surface area=295.7 m^2/g, d_p=3.2 nm), both the BET specific area and the average pore diameter are close to the value for the xerogel with little deviation.

In a similar manner, the nitrogen adsorption-desorption isotherm and the pore size distribution of an unsupported freeze-dried gel are presented in Figure 4.28. It can be seen that the pore size distribution of a freeze-dried gel on a cordierite is close to the unsupported one with an average pore diameter of 3.1 nm. The characteristics of the freezing gel have no great change whether or not it is coated on the cordierite support. Therefore, it can be concluded that the characteristics of the freezing gel are determined by the nature of the starting material, and calcination temperature and are independent of the drying methods.

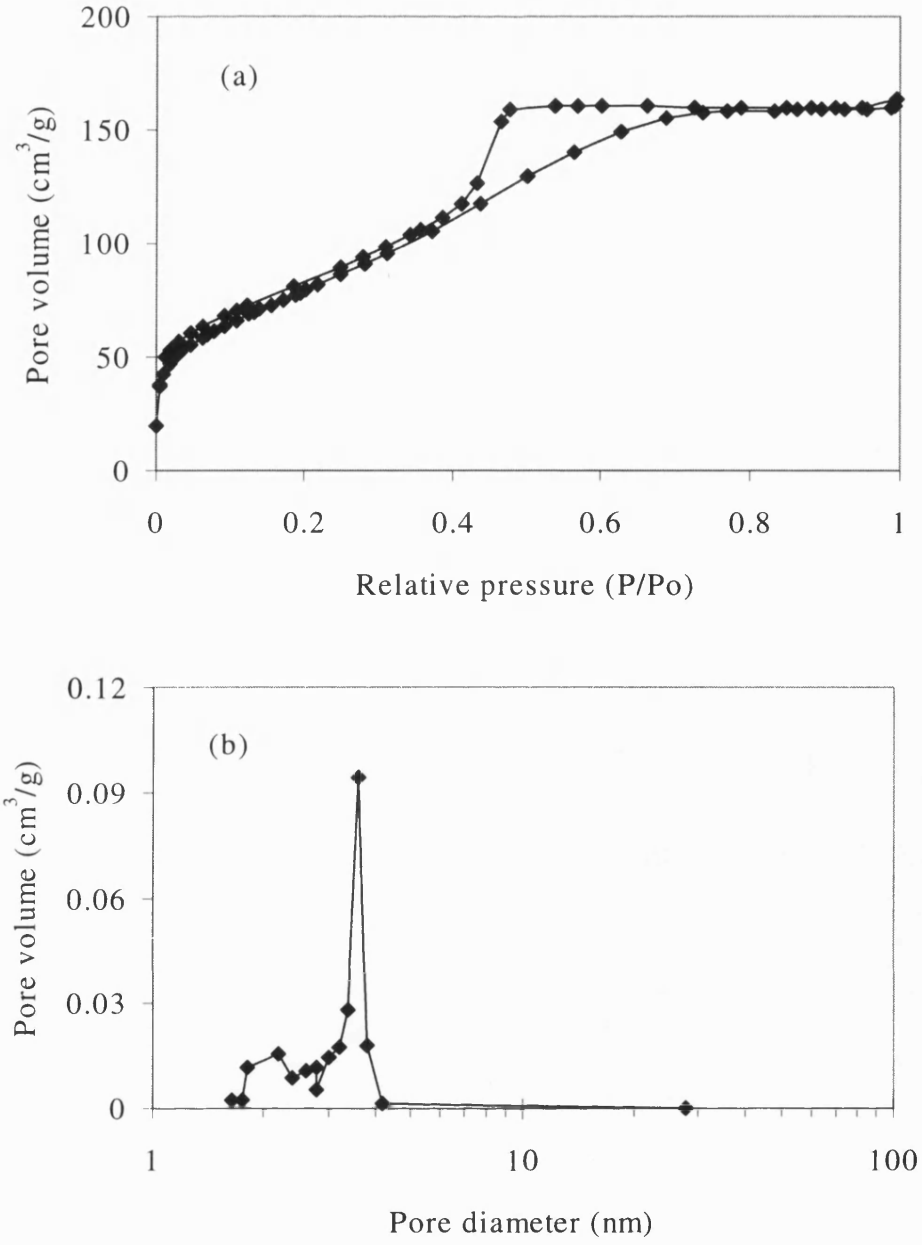

Figure 4.27. Nitrogen adsorption experiment for freeze-dried alumina calcined at 450°C: (a) nitrogen adsorption-desorption isotherm, (b) pore size distribution obtained from BJH desorption. BET surface area: 282 cm^3/g, d_p = 2.8 nm.

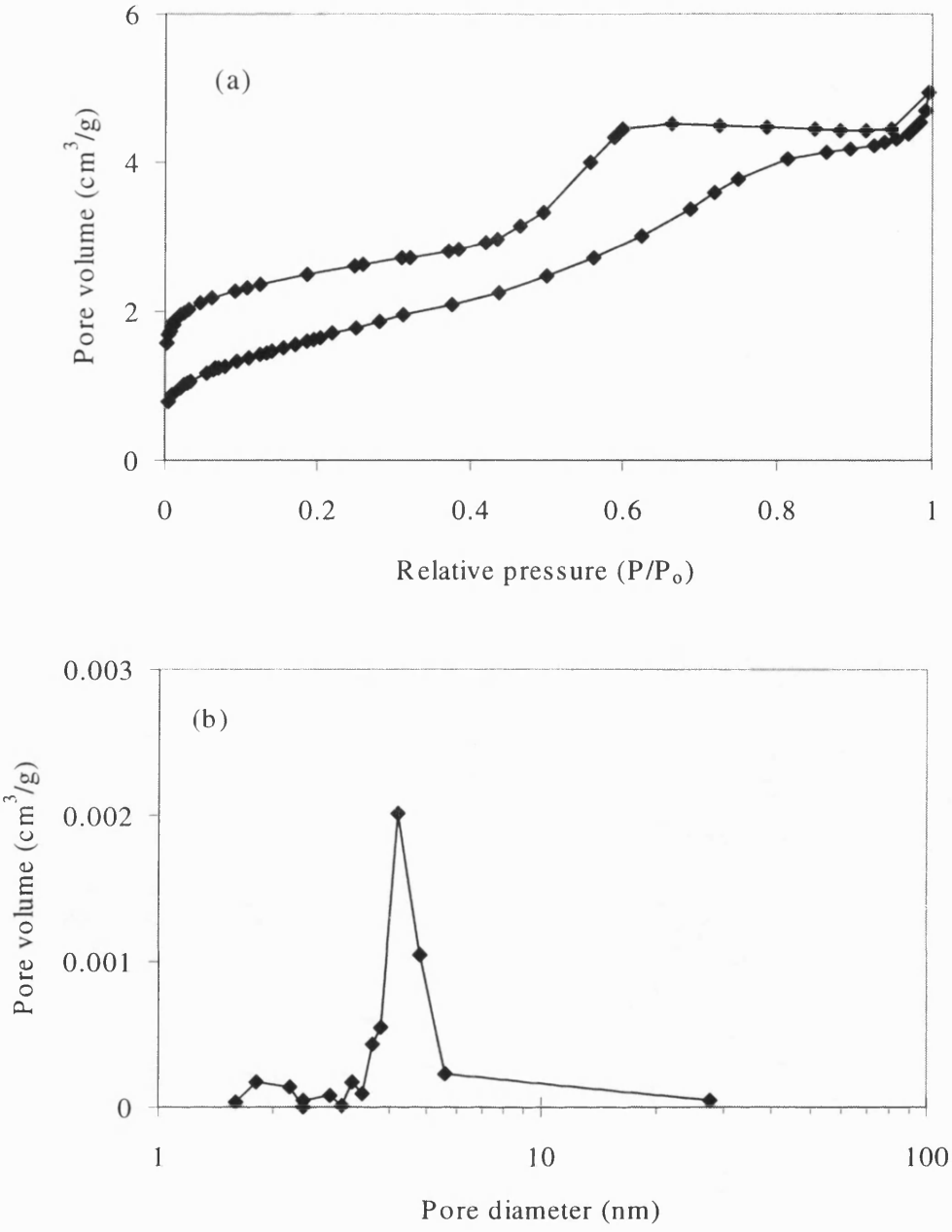

Figure 4.28. Nitrogen adsorption experiment for freeze-dried alumina on a cordierite monolith substrate calcined at 450°C: (a) nitrogen adsorption-desorption isotherm, (b) pore size distribution obtained from BJH desorption. BET surface area: 5.8 cm^3/g, d_p = 3.1 nm.

In summary, this part of the work was initiated to explore the validity of using freezing gels (or cryogels) in a catalyst application, as an alternative to xerogel. The cryogel was prepared using the same alumina sol as that used to prepare the alumina xerogel washcoat. The physical properties of the cryogel were found to be similar to the xerogel. The geometrical structure (macroporous structure) can be changed by the drying method.

Therefore, this cryogel can be used as a washcoat, where a high intraphase diffusion resistance exists, *e.g.* in high temperature catalytic combustion. This is because the cryogel generates a higher geometrical surface area than a xerogel, see Figure 4.29.

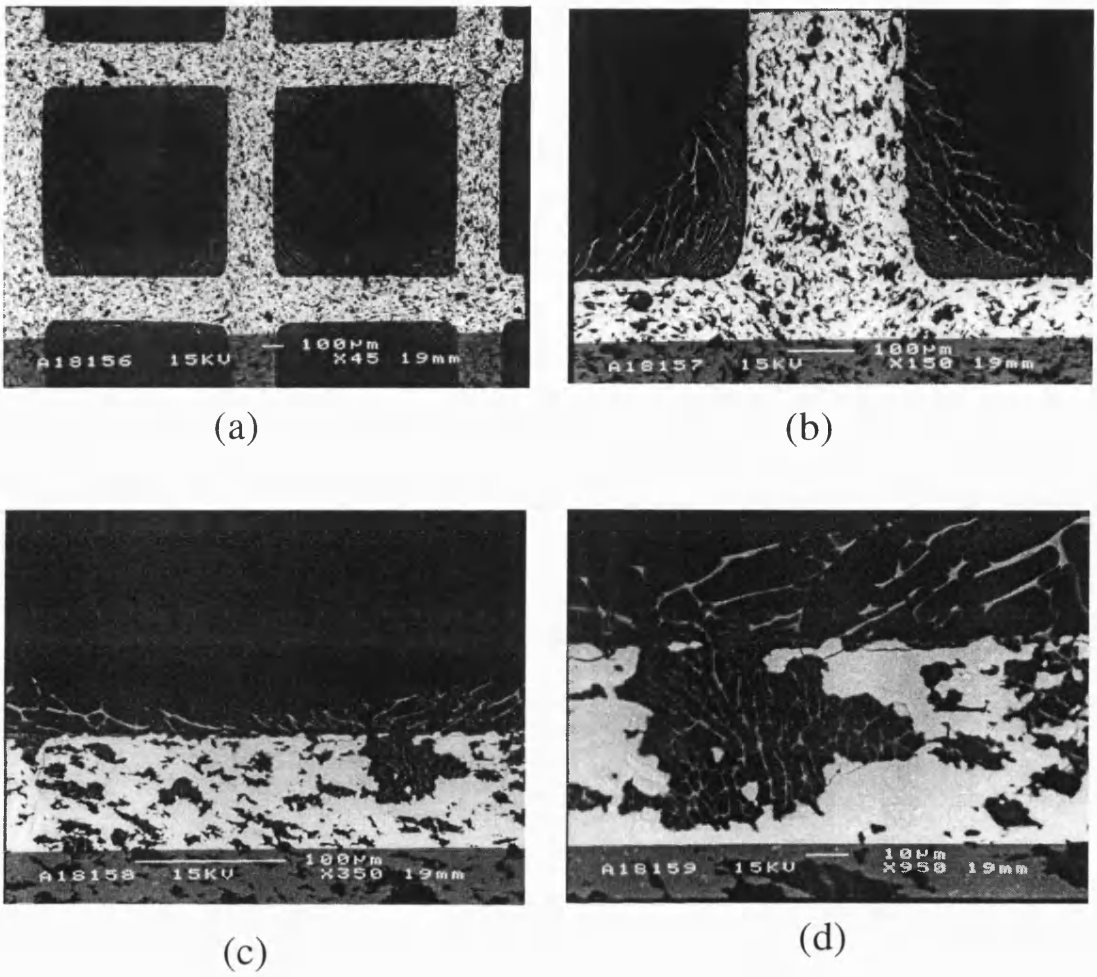

Figure 4.29. SEM images of an alumina cryogel on monolith from alumina sol (LAB2).

The sample was also examined by SEM at different angles as shown in Figure 4.30. The freeze-dried gel was also found to have anchored itself in the pores of the cordierite support. The void is the space where the water crystals existed and the shape and the size of them varies.

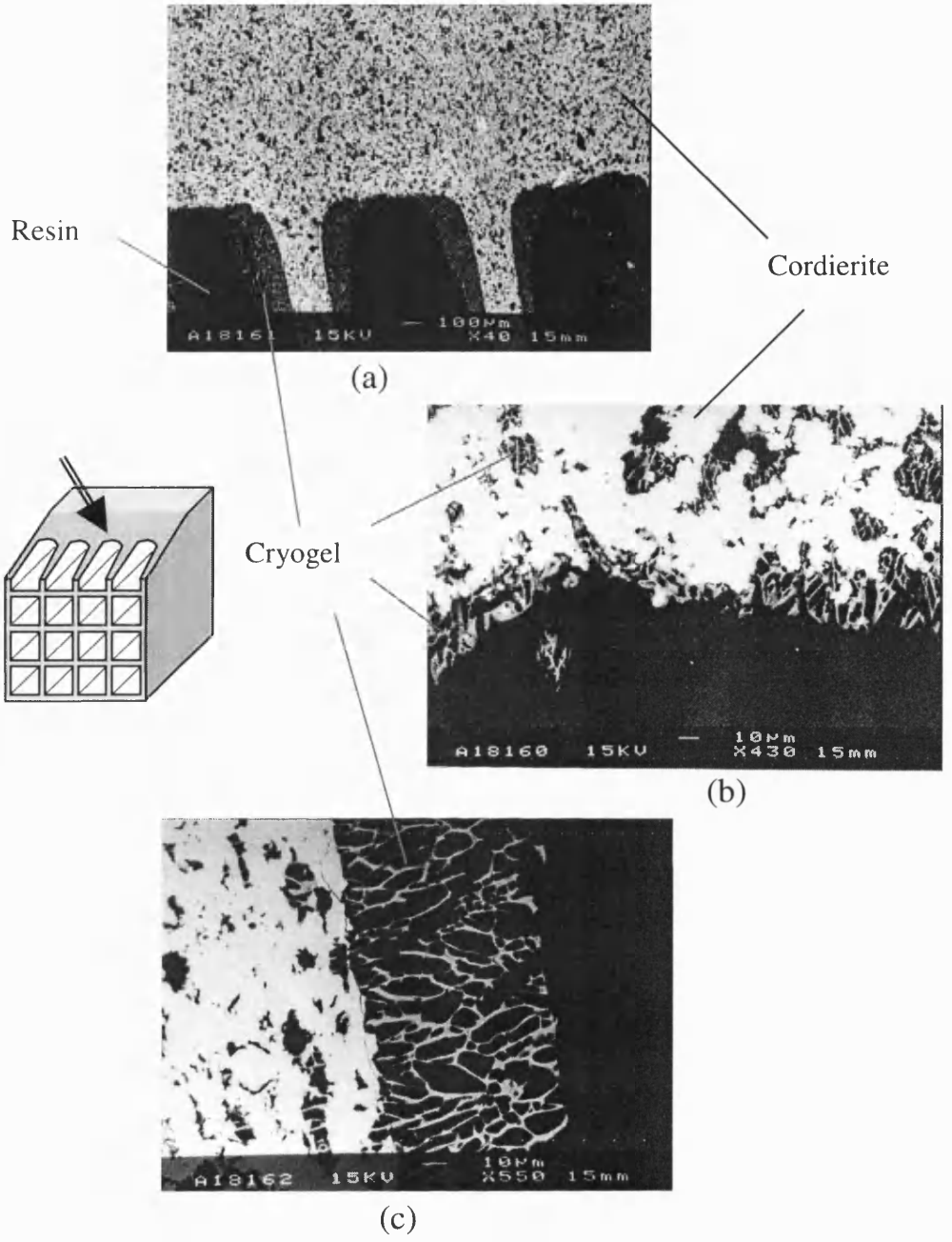

Figure 4.30. SEM images of alumina cryogel on monolith with a different angle from Figure 4.29. (a) Magnification: ×40, (b) Magnification: ×430, and (c) Magnification: ×550.

4.5.3. Effect of sintering temperature on characteristics of alumina washcoat

Specific surface area, average pore size and pore size distribution were measured using a nitrogen adsorption instrument, ASAP 2010 (Micrometrics, USA). Element analysis with XRD was also carried out.

As the calcination temperature is the main parameter for determining the physical properties of a washcoat material, the effect of calcination temperature on the characteristics of a washcoated cordierite plate was investigated. This was analysed by measuring the specific surface area and pore size of the washcoat. The dried gel was calcined at different temperatures using an electric furnace. The sintering time was fixed to 20 ± 2 hours. The calcination temperatures used in the study were 450, 600, 800, 1100, and 1200°C. As a phase change is taking place at certain temperatures, the calcined samples were compared with a reference sample obtained from Alfa Johnson Matthy plc (Herefordshire).

Figure 4.31 presents the nitrogen adsorption-desorption isotherms carried out for a washcoated cordierite monolith calcined at different temperatures. The isotherms have a hysteresis loop, which indicates the existence of a pore structure. It can be seen that the hysteresis loop occurs between 0.4 and 0.9 of relative pressure, and the extent of the loop become narrower with increasing calcination temperature. This may be due to the changing pore structure. The BET specific surface area of the washcoat monolith decreases with increasing calcination temperature and it can be seen that a sudden drop of surface area occurs at around 900°C, see Figure 4.32. Figure 4.33 illustrates the pore size distribution of the washcoat monoliths calcined at different temperatures.

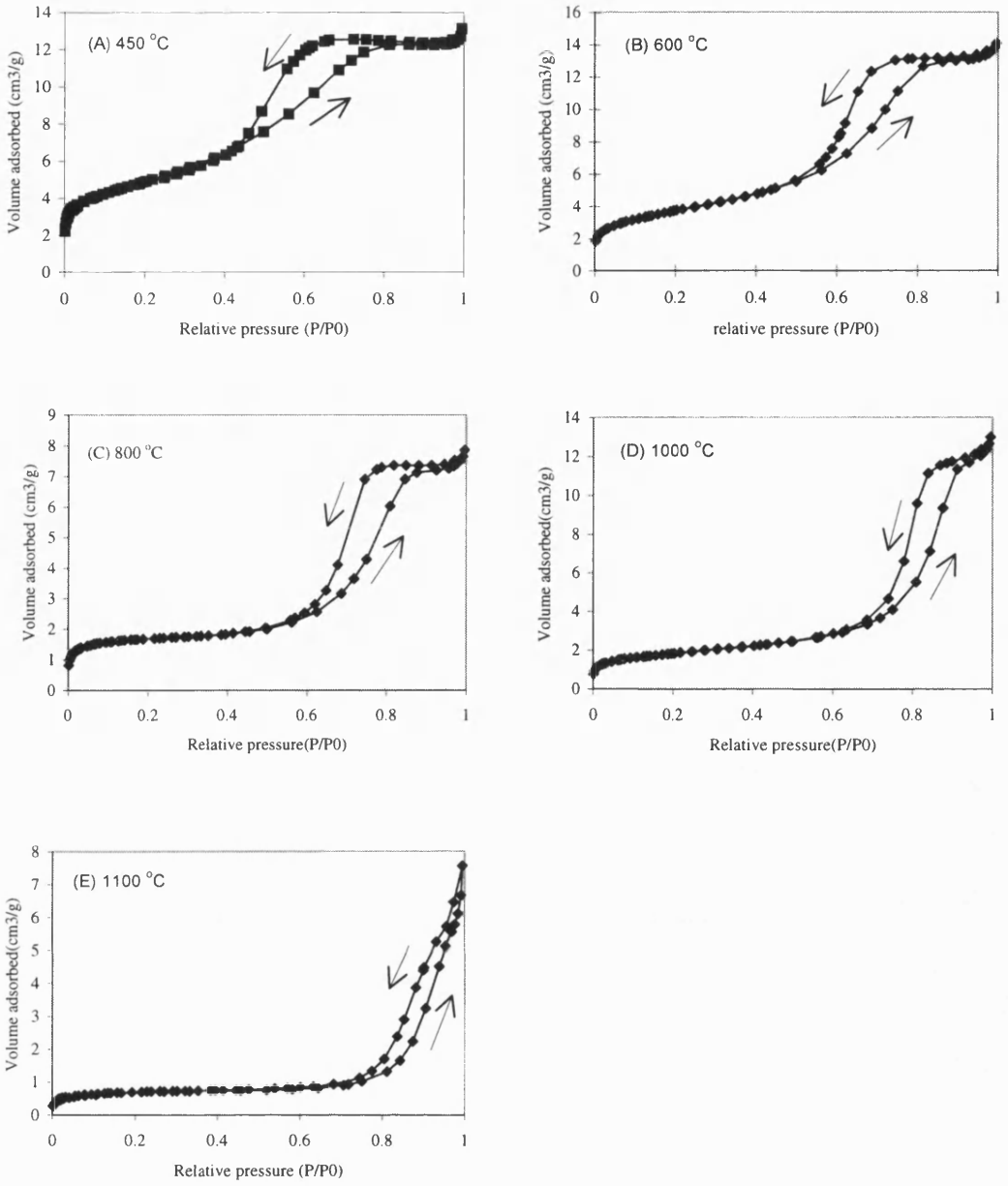

Figure 4.31. Nitrogen adsorption data of washcoated cordierites: calcined at different temperatures: (A) 450°C, (B) 600°C, (C) 800°C, (D) 1000°C, and (D) 1100°C.

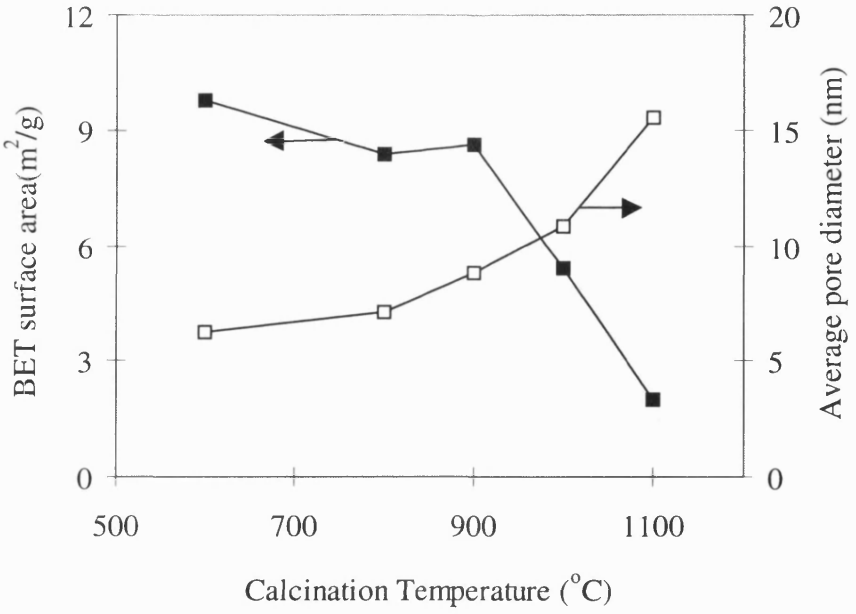

Figure 4.32. Surface area and average pore size for washcoated monolith (coated 4 times with LAB2) as a function of calcination temperature.

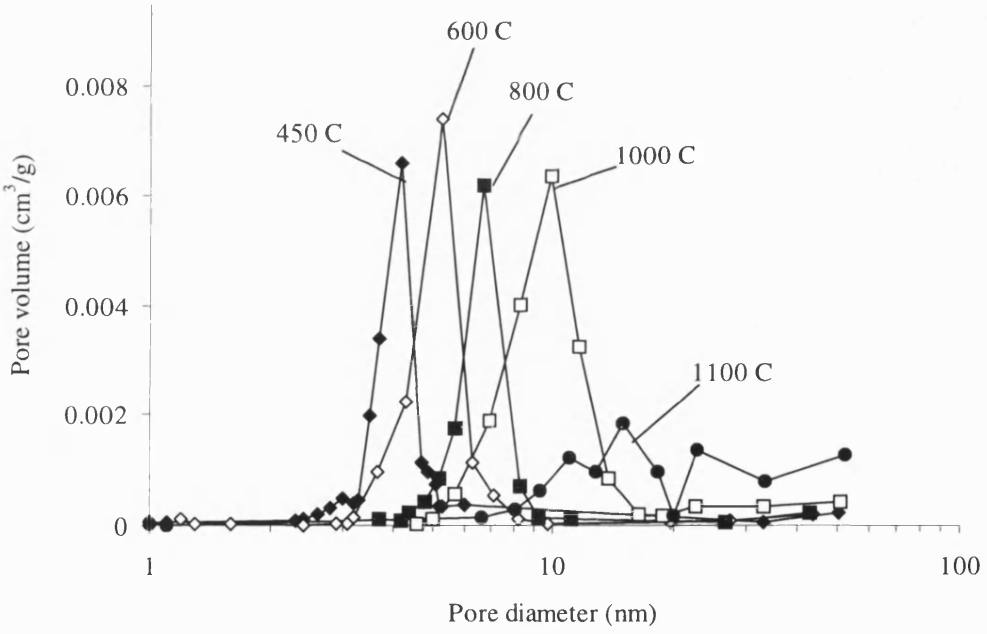

Figure 4.33. Pore size distribution of washcoated cordierite plates calcined at different temperatures.

4.5.4. The effect of doped ZrO_2 on the alumina washcoat

The thermal stability of an unsupported alumina washcoat was investigated by determining the pore size distribution, average pore size, pore volume, and surface area as a function of sintering temperature and the content of dopants. In general, composite metal oxides have a higher thermal stability than pure metal oxides. Zirconia was used as a dopant to prepare an Al_2O_3-ZrO_2 composite.

Two different ways to prepare the composite were considered:

1. Gels were formed from an alumina-zirconia sol complex, by using aluminium *i*-propoxide and zirconium *n*-propoxide as precursors before the sol synthesis process.
2. Gels were formed from an alumina sol mixed with different amounts of zirconium nitrate. The ratio of zirconium to alumina was 5, 10, 15, and 20 wt% of ZrO_2/Al_2O_3.

Zirconium *n*-propoxide (98%) was purchased from Johnson Matthey plc (Herefordshire, UK). Zirconium nitrate was obtained from MEL chemicals (Manchester, UK) which is a clear, acidic solution containing the equivalent of approximately 20 wt% ZrO_2.

The samples were also calcined at different temperatures (450, 600, 800, 1000, and 1200°C) and characterised with ASAP2010. The results were compared with the results obtained for pure alumina.

Although the transition aluminas (γ–, δ–, θ-alumina) have been used extensively as catalyst supports, use of these materials is limited at high temperatures. This is because a drastic decrease in specific surface area occurs as a result of the transformation of the metastable phase of alumina into the α-alumina form, which is the only thermodynamically stable phase. The temperature of the transformation is influenced by various factors such as particle size and morphology, crystalline forms, the nature of the gaseous atmosphere, additives, *etc.* Additives can influence the kinetics of the phase transformation by both accelerating and inhibiting. Since the thermal stability is due to the retardation of phase transformation, the additives with an inhibiting effect are of interest in this work. Additives of this kind include Mg^{2+}, La^{3+}, Zr^{4+} (Schaper and Van Reijen, 1982; Schaper *et al.*, 1983). A kinetic study on the effect of the additives on the phase transformation was carried by Burtin *et al.* (1987).

Zirconium ions were chosen to increase the thermal stability of the transition alumina catalyst support. The influence of zirconia additives on the thermal stability of alumina film prepared using the sol-gel method was investigated, in respect of the changes in surface area and pore size distribution. The zirconium-doped alumina was prepared in two different ways as described earlier. Figure 4.34 presents a comparison between zirconia-doped alumina gels, which were prepared in different ways and calcined at different temperatures. The plot labelled 'LAB3+Zr nitrate' corresponds to the catalyst support prepared by mixing alumina sol (LAB3) with an aqueous solution of zirconium nitrate. The plot labelled 'Al/Zr sol' refers to that prepared by hydrolysis of the mixture of aluminium *i*-propoxide and zirconium *n*-propoxide.

The doped alumina gel prepared by hydrolysis of zirconium *n*-propoxide was similar to the pure alumina gel. Therefore, the doped zirconia does not influence the specific surface area and the pore size distribution of alumina gel. It can be postulated that this is due to the incomplete hydrolysis of zirconium *n*-propoxide, as some white precipitates were found in the alumina/zirconia sol.

However, the doped alumina with zirconium nitrate was found to be more thermally stable as the changes of the specific surface area and the pore size distribution were smaller compared with the pure alumina gel. This may be because the nitrate is evenly dispersed in the alumina sol. However, Meijers *et al.* (1991) prepared a ZrO_2/SiO_2 catalyst, using zirconium ethoxide as the zirconia precursor and postulated that the ethoxide is hydrolysed more easily than the propoxide.

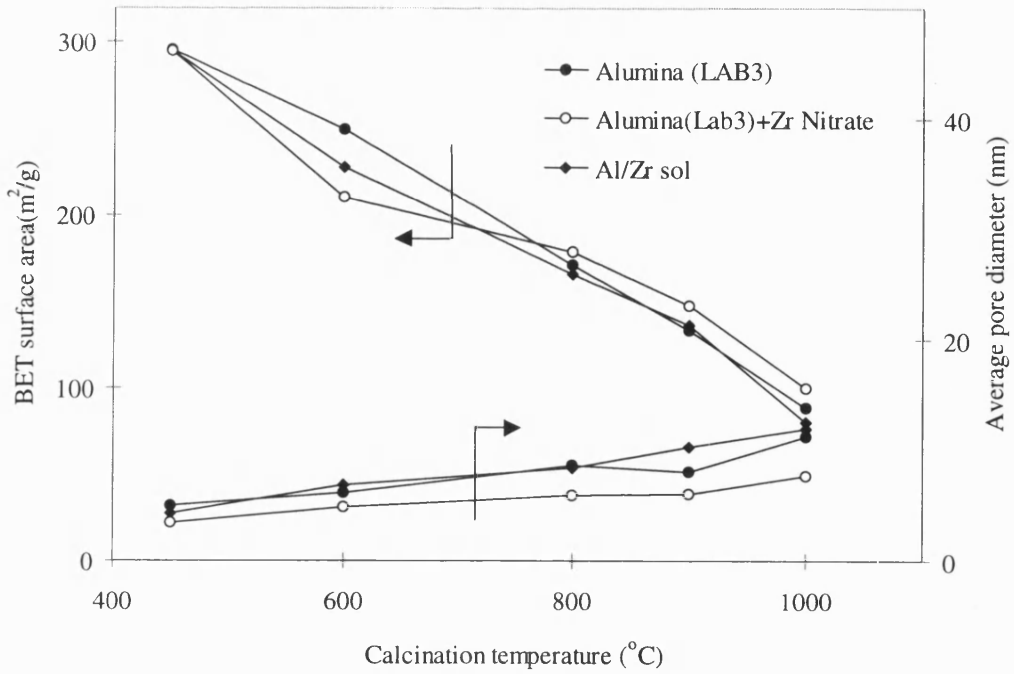

Figure 4.34. Comparison between zirconia-doped alumina gels which were prepared in two different ways and calcined at different temperatures.

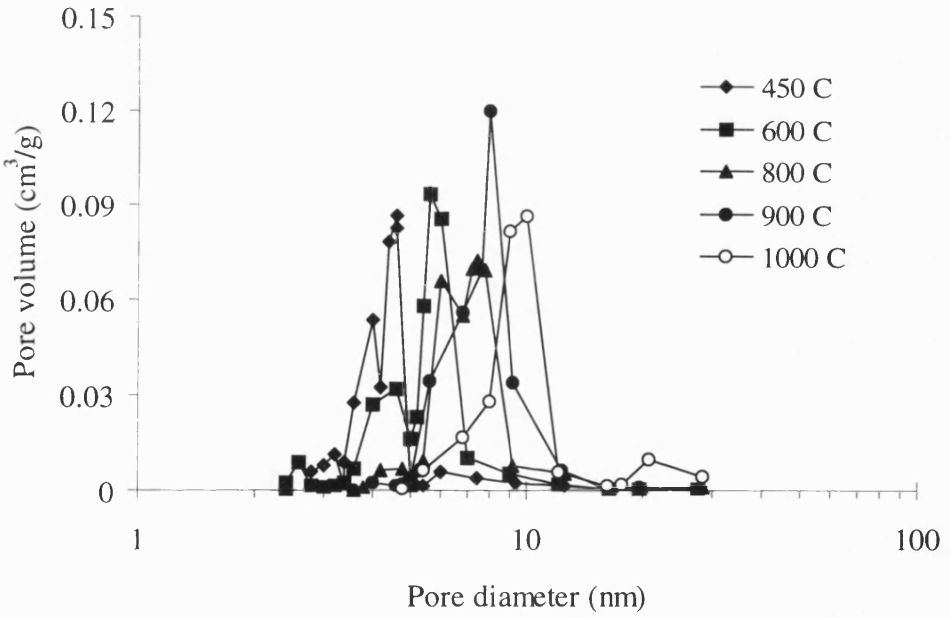

Figure 4.35. Pore size distribution for the zirconia-doped alumina gel prepared by hydrolysis of the mixture of aluminium *i*-propoxide and zirconium *n*-propoxide.

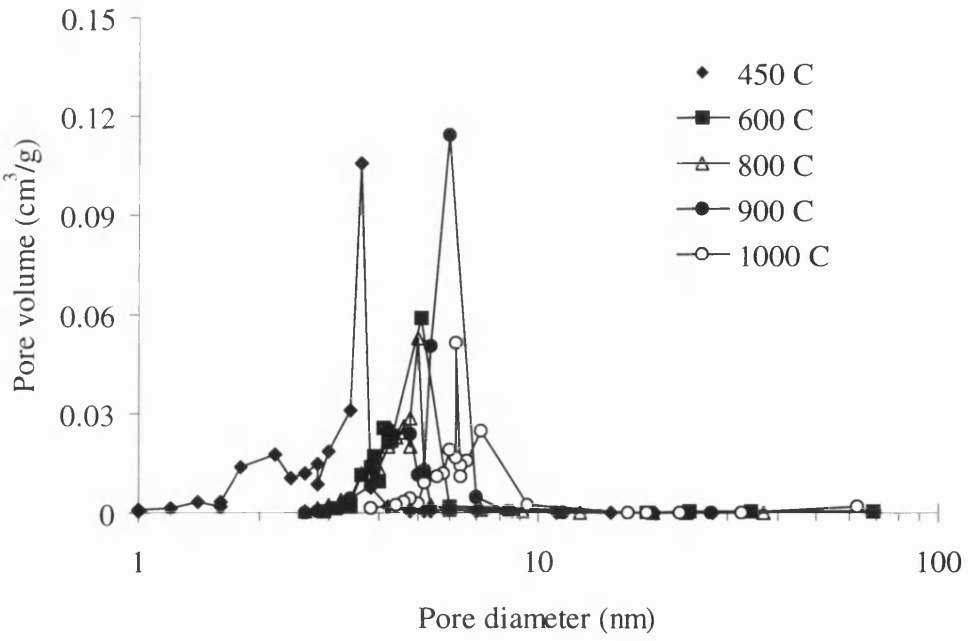

Figure 4.36. Pore size distribution for the zirconia-doped alumina gel prepared by mixing alumina sol (LAB3) with an aqueous solution of zirconium nitrate.

Average pore diameter and BET surface area for the pure alumina, for the alumina with different amounts of doped zirconium and for the pure zirconia at different calcination temperatures after 20 hours, are listed in Table 4.5. The specific surface area depends on the composition of the sample as shown in Figure 4.37. The highest BET surface area (295 m^2/g) was found in the sample of pure alumina calcined at 450°C. The difference between the samples became less marked at higher calcination temperatures, but for the alumina washcoat calcined at 1100°C zirconia-doped alumina samples had the high BET surface area and the sample containing 20 wt% zirconia had the highest surface area (29.2 m^2/g). This was due to the retention of θ-Al_2O_3 as shown by the XRD pattern. The effect of calcination temperature on the pore volume of the alumina washcoats is presented in Figure 4.38. In general, the pore volume decreases with an increase in calcination temperature and at about 1000°C a sudden decrease in pore volume was observed. The smaller pore volume of the zirconium-doped alumina washcoat at temperatures lower than 900°C was probably due to the filling of pores with zirconia (that has a lower surface area). The surface area shrinkage and pore volume densification with increasing sintering temperature are a common phenomena for alumina (Schaper & van Reijen, 1982; Lin *et al*, 1991). The alumina washcoat with 5 wt% zirconia was found to be less stable than pure alumina at temperatures higher than 1000°C, in respect of pore volume and surface area. The increase in the pore size of the

alumina washcoats is less significant at calcination temperature lower than 1000°C, but more significant at temperatures above 1000°C, see Figure 4.39. In general, the stability of pore size is improved by adding zirconium. The higher the amount of zirconium, the more stable the pore sizes are. However, the pore volume and the specific surface area decrease with an increase in zirconium content.

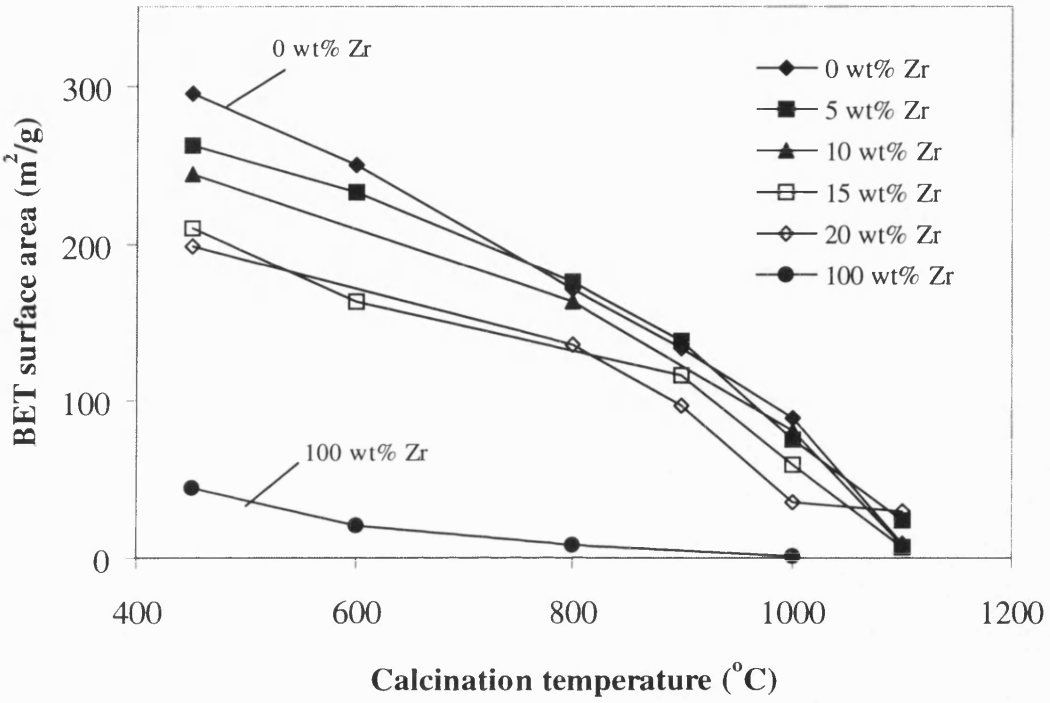

Figure 4.37. Effect of doped zirconia precursor (zirconium nitrate) on specific surface area of alumina washcoat (LAB3).

Table 4.5. Average pore diameter, d_p, and BET surface area, S, for the pure alumina, alumina with different amounts of doped zirconium, and pure zirconia at different sintering temperatures after 20 h.

Temp	pure Al_2O_3		5 wt% ZrO_2/Al_2O_3		10 wt% ZrO_2/Al_2O_3		15 wt% ZrO_2/Al_2O_3		20 wt% ZrO_2/Al_2O_3		pure ZrO_2	
(°C)	S (m^2/g)	d_p (nm)	S (m^2/g)	d_p (nm)	S (m^2/g)	d_p (nm)	S (m^2/g)	d_p (nm)	S (m^2/g)	d_p (nm)	S (m^2/g)	d_p (nm)
450	295.7	3.16	262.2	3.6	243.5	2.46	209.7	2.13	198.9	2.14	44.2	6.66
600	250	3.92	232.6	3.2	-	-	162.8	3.67	-	-	20.1	12.18
800	170.9	5.54	175.7	4.1	162.8	3.67	70.2	5.33	135.2	3.2	7.5	19.3
900	133.0	5.15	137.4	4.7	125.2	7.33	-	-	96.7	3.51	-	-
1000	88.6	7.22	75.3	7.7	80.5	5.2	59.2	4.25	34.8	3.3	1.4	13.59
1100	9.3	20.9	24.5	12.8	8.4	7.4	6.67	3.58	29.2	3.75	-	-

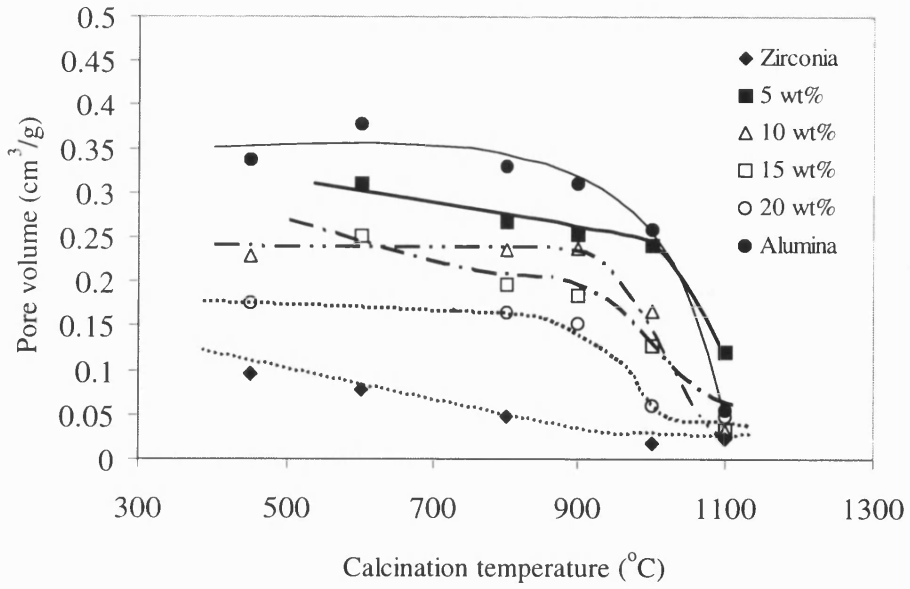

Figure 4.38. Effect of sintering temperature on pore volume for zirconium-doped alumina washcoat prepared using different doping amounts. Zirconia precursor: Zirconium nitrate.

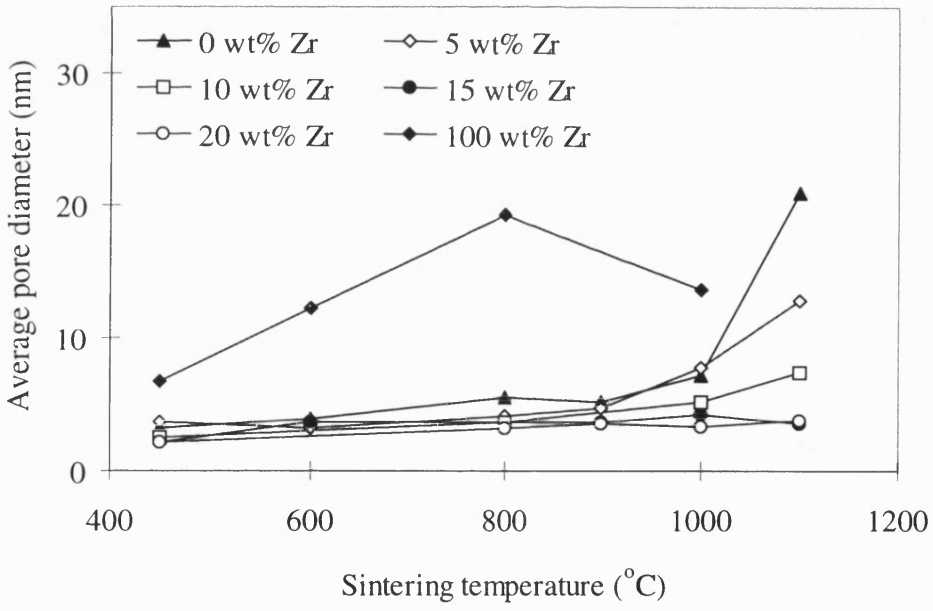

Figure 4.39. Effect of doped zirconium nitrate on the pore size distribution (BJH desorption) of the alumina washcoat.

Figure 4.40 shows the X-ray diffraction patterns for zirconia-doped alumina washcoat calcined at different temperatures. The XRD pattern for the washcoat calcined at 450°C is similar to the one without zirconia. However, the pattern for the washcoat calcined at 1000°C shows both the peaks of zirconia and the peaks of γ-alumina.

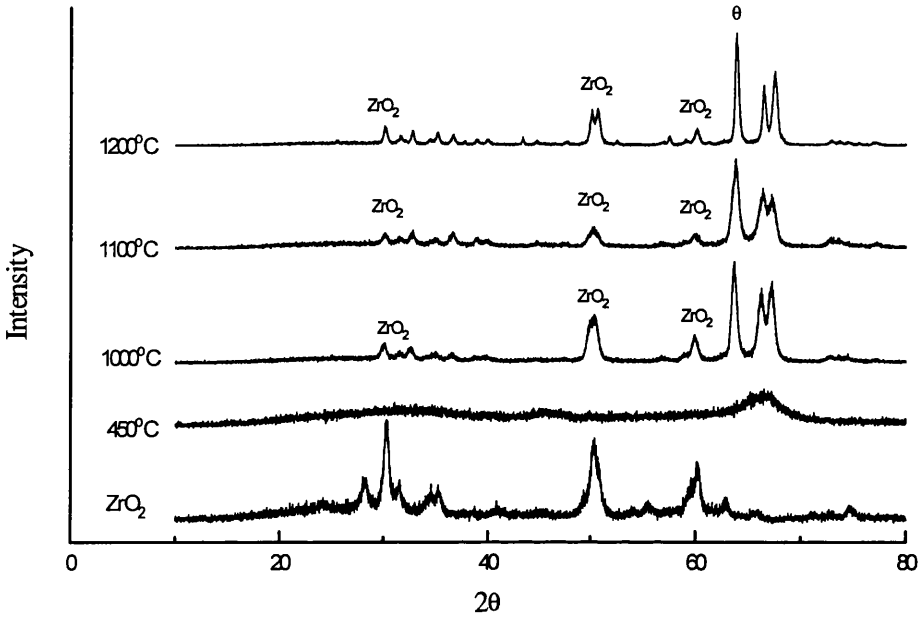

Figure 4.40. X-ray diffraction patterns for the zirconia-doped alumina washcoats sintered at different temperatures.

Figure 4.41 presents the X-ray mapping images for zirconia-doped alumina washcoats on the cordierite substrate. Washcoat layers can be distinguished from the cordierite substrate ($MgO\text{-}Al_2O_3\text{-}SiO_2$), the mixture of alumina, silica and magnesia. The washcoat layer can be clearly recognised in the SEM image shown in Figure 4.41(a). The doped zirconia is found only in the washcoat layer, see Figure 4.41(b). It can also be seen that the alumina in the washcoat is more densely populated than in the cordierite substrate, see Figure 4.41(d). In comparison, Figure 4.41(c) and Figure 4.41(e) shows the elements existed only in the substrate, Si and Mg, respectively.

(a)

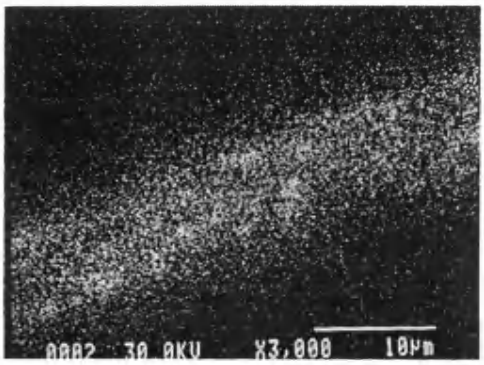

(b)

(c)

(d)

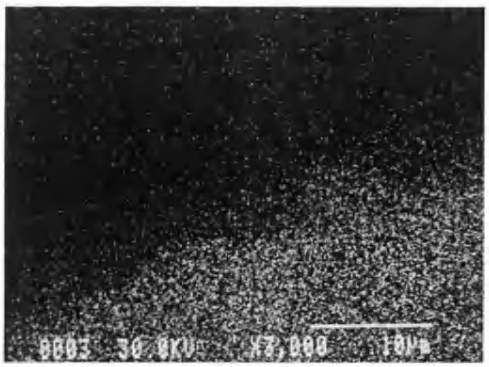

(e)

Figure 4.41. SEM image and X-ray mapping of specimen Zr-doped alumina calcined at 600°C: (a) SEM image, (b) Zr, (c) Si, (d) Al, and (e) Mg.

4.5.5. Effect of a drying additive

In order to prevent cracking of the alumina washcoat during the drying stage, formamide (98%, Aldrich) was added into the alumina sol as a drying control chemical additive (DCCA). This was added into alumina sol drop by drop in a stirred vessel and the total amount added was 0.1 wt%. The changes of physical properties were investigated by a nitrogen adsorption experiment. Cracking was investigated using scanning electron microscopy (SEM).

The addition of formamide did not have an influence on the characteristics of the alumina washcoat, see Figure 4.42. However, there were less cracks in the washcoat layer, see Figure 4.44. This can be noticed from a comparison with the washcoat prepared from formamide-free alumina sol, which was shown in Figure 4.43.

It can be concluded that the addition reduces the tendency for cracks to form in the washcoat, without a significant reduction in surface area or change in average pore size.

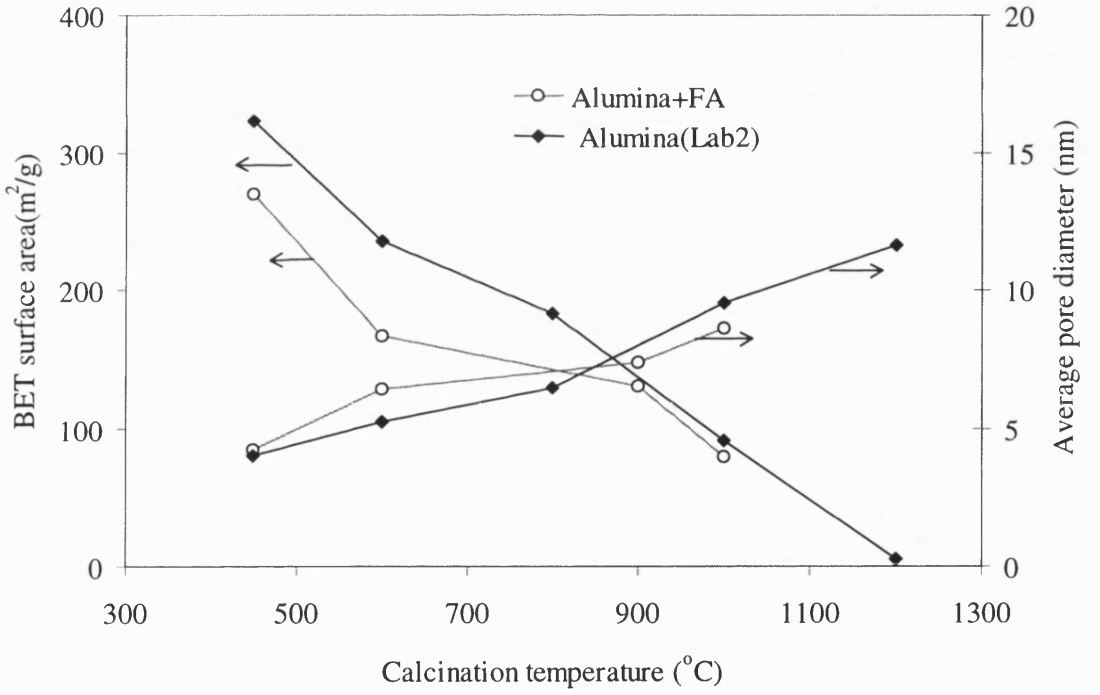

Figure 4.42. Effect of formamide on the characteristics of an alumina gel. The plot labelled 'Alumina+FA' corresponds to the alumina gel to which formamide was added into the stable sol.

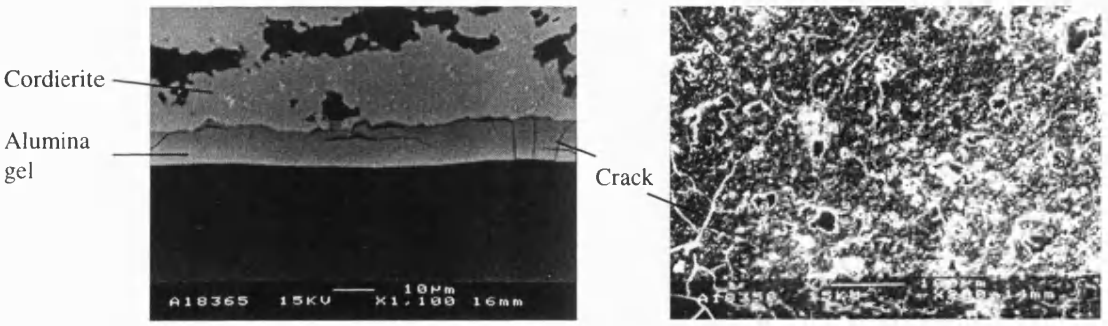

(a) Section view (b) Surface view

Figure 4.43. SEM images of an alumina gel (LAB2) on monolith.

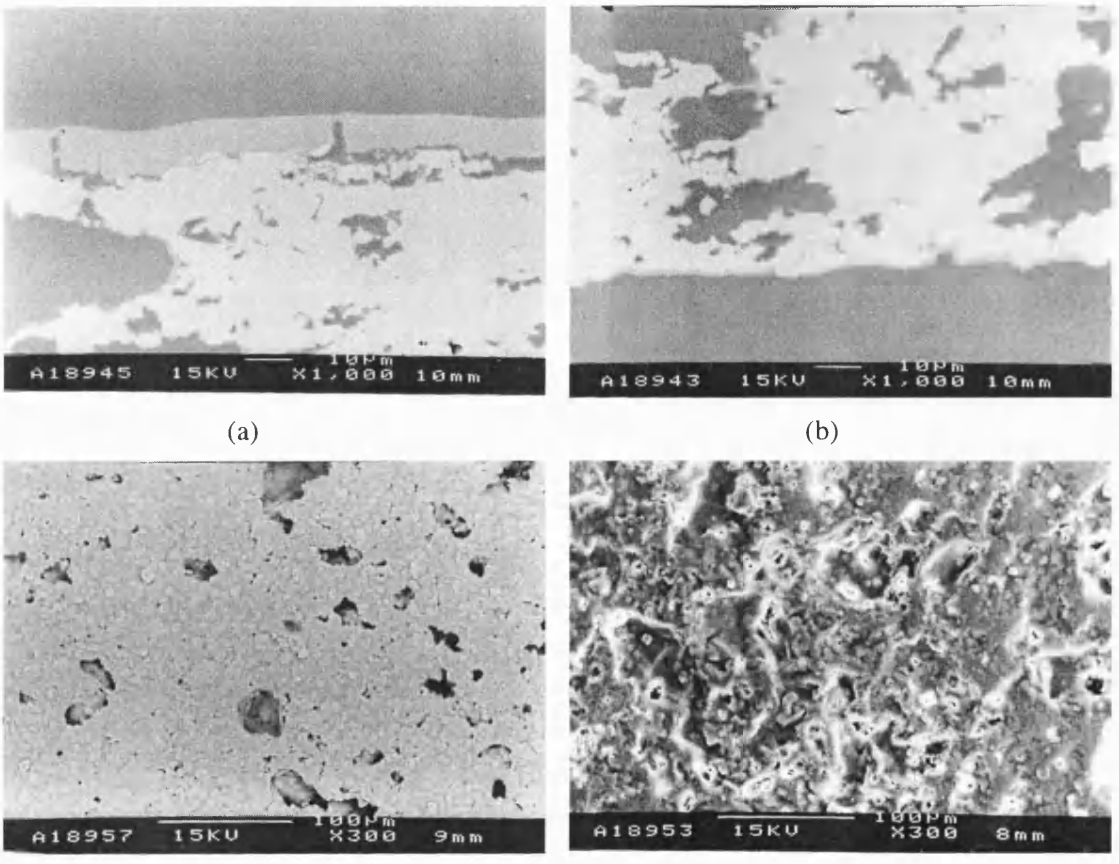

(a) (b)

(c) (d)

Figure 4.44. SEM images of alumina washcoat on cordierite substrate after adding formamide as a DCCA. (a) and (b): a section view of each side. (c) and (d): the surface view of (a) and (b), respectively.

4.5.6. Addition of active catalyst

Although the alumina washcoat was prepared as a catalyst support, it was necessary to investigate how the characteristics of the support might change after adding active catalysts. To achieve this, platinum were chosen and deposited on the washcoat. There are a variety of ways to prepare catalysts and the preparation of catalysts has been considered by some researchers as an art rather than science (Delmon *et al.*, 1976). According to Delmon *et al.* (1976), "there are two over-repeated explanations for this fact: 1) catalyst manufacturers are reluctant to reveal secret preparation details, many of which are of great importance; 2) catalyst fabrication is trial and error, foreman's know-how and tradition, and is not amenable to scientific analysis." The preparation techniques of metal catalysts on porous substrates can be broadly categorised into two groups, precipitation method and impregnation method.

(a) Precipitation methods

This method is frequently employed in the preparation of single- and multicomponent catalysts and applicable to materials, such as the hydrous oxides, sulphides, carbonates (Ciapretta and Plank, 1954). In general, it starts with aqueous solutions of the desired constituents and adds the required precipitating agents. According to Ciapretta and Plank (1954), the use of nitrates are generally recommended because other anions (*e.g.* chloride or sulphate) sometimes act as catalyst poisons or inhibitors if they are present in the final products.

(b) Impregnation methods

The technique of impregnating an active catalyst component on an inactive support is the simplest method of producing a catalyst. Impregnation of a support normally involves the use of a soluble compound of the desired constituent dissolved in a liquid, usually water. The method of catalyst preparation may involve the following steps:

(a) Evacuating the support.

(b) Contacting the support with the impregnating solution.

(c) Removing the excess solution.

(d) Drying.

(e) Calcination and activation.

Frequently, it is necessary to add a precipitation and washing step either before or after

drying. Evacuation of the support prior to contacting it with the impregnating solution provides a more uniform distribution of the active catalyst component.

In the case of preparation of a catalyst containing platinum or palladium, an acid solution of the metal chlorides, *e.g.* chloroplatinic acid, or from the alkali metal salts of this acid, *e.g.* sodium chloroplatinate, are widely used. It is important that the catalyst metal is reduced from its salt on the surface of the alumina. The impregnated support is dried at about 110°C and reduced in a hydrogen atmosphere between 100 to 500°C. The reduction of precious metals (*e.g.* Pt, Pd) from the chloride can proceed according one of the following reactions showed in Figure 4.45.

Reduction of platinum salts

$$H_2PtCl_6 + NH_2NH_2 \rightarrow Pt + N_2 + 6HCl$$

$$H_2PtCl_4 + \frac{1}{2}NH_2NH_2 \rightarrow Pt + \frac{1}{2}N_2 + 4HCl$$

Figure 4.45. Reduction of rare earth metals from chloride (adapted from Retallick, 1988).

When a solution of H_2PtCl_6 or H_2PtCl_4 is added first to alumina, and then hydrazine is added, the reduction is indicated by the colour of the alumina, which changes from white to black or grey with a time lag. The same is observed when the hydrazine is added first, followed by the platinate (Retallick, 1988). In general, a catalyst is impregnated on the washcoat after the sample has been calcined, otherwise some of the catalyst may be trapped inside the pores, as the alumina starts to sinter at elevated temperatures in the calcination process.

Development of the preparation methods of a catalyst for a catalytic combustion application is outside of the scope of this work. However, it would be interesting to know how the pore structure is changing after depositing catalyst onto the washcoat. This in turn may affect the effective diffusivity.

In this work, platinum was chosen in order to examine the change to the pore structure of the washcoat. This work focused on two features:

1. To examine the specific surface area change and pore size distribution change by

nitrogen adsorption-desorption study.

2. To examine the distribution of an active catalyst and the particle size of the catalyst by microscopic study (SEM-EDS, XRD, TEM).

Platinum catalyst was deposited by reduction of hexachloroplatinic acid (H_2PtCl_6, »37.5% Pt, Aldrich) with hydrazine (NH_2NH_2,, 64%, Sigma). To prepare 1 wt% Pt on alumina gel, the alumina gel was calcined at 600°C and then degassed before dipping into 10 wt% hexachloroplatinate solution. After dipping for a couple of minutes, it was then dried at 100°C for 2 hours. The platinate-impregnated alumina gel was yellowish in colour. This was dipped into 1 wt% hydrazine solution to reduce the platinate to metallic platinum. The reduction was noticed by a change in colour from yellowish to dark grey. The Pt-impregnated alumina gel was washed and dried. The samples were then characterised using the nitrogen adsorption experiment apparatus, ASAP2010 and investigated further with XRD, SEM-EDS, and TEM.

4.5.6.1. Comparison between an alumina washcoat and a platinised alumina washcoat.

A comparison was made between the microstructure of alumina washcoat and its platinised film in terms of the structural change of the washcoat after depositing platinum catalyst. Figure 4.46 presents the nitrogen adsorption-desorption isotherms of an alumina washcoat and a platinised alumina washcoat. Both have the same isotherm with the hysteresis loop appearing over the same range of relative pressures. However, the pore volume decreased by 9 % after the addition of platinum as the pore volume of alumina gel and platinised alumina gel are 0.322 cm^3/g and 0.295 cm^3/g, respectively. In Figure 4.47, the pore size distribution curves of both samples have overlapped with little change in the peak size. It can be concluded that the pore structure did not change much, even though the pore volume deceased when the platinum was added.

Figure 4.48 presents the X-ray diffraction patterns for both the alumina washcoat and the platinised washcoat calcined at 600°C. It can be seen that the peak for metallic platinum appears in a platinised washcoat as compared with the reference sample labelled as platinum marker.

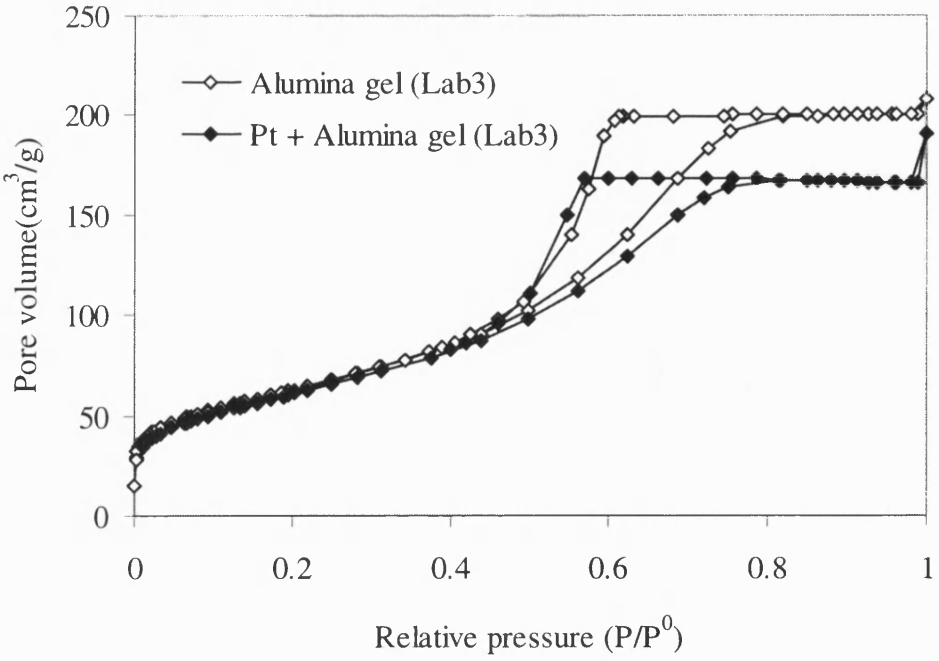

Figure 4.46. Nitrogen sorption isotherms of an alumina gel (LAB3) calcined at 600°C and its platinised alumina gel (Pt+Lab3). Pore volume of alumina gel and platinised alumina gel are 0.322 cm^3/g and 0.295 cm/g, respectively.

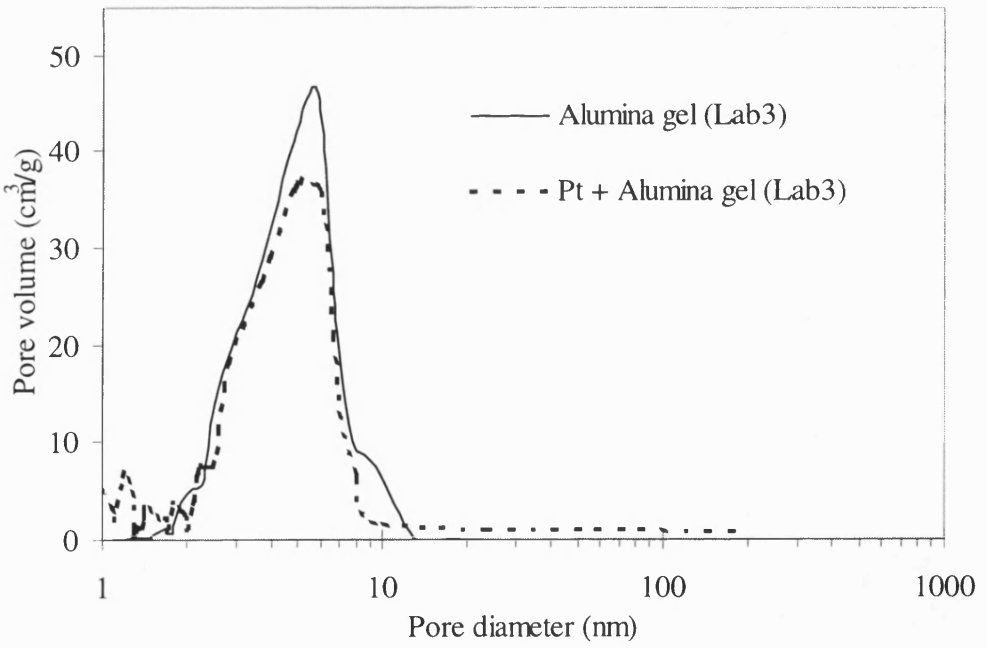

Figure 4.47. Pore size distribution determined by the BJH method for an alumina washcoat and a platinised alumina washcoat calcined at 600°C.

The clear peaks of metallic platinum may be more visible, because platinum particles

are more populated in the surface of the washcoat than in the pores. The transport of platinum salts into pores takes place by diffusion.

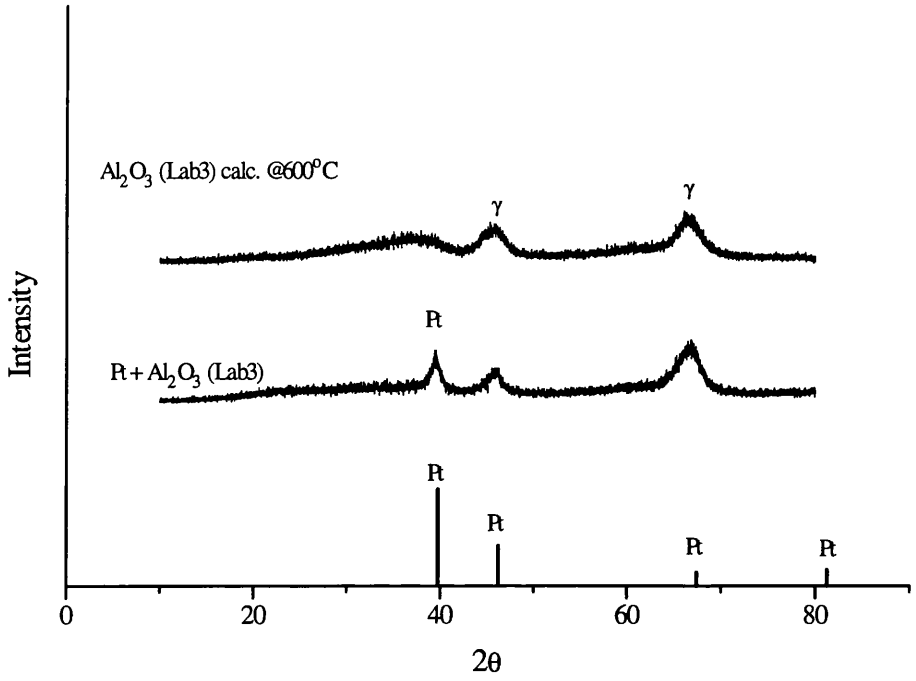

Figure 4.48. X-ray diffraction patterns for alumina gel (Lab3) and platinised alumina gel calcined at 600 °C for 20hr.

In Figure 4.49, a TEM image shows the distribution of platinum particles in the alumina washcoat. It can be seen that platinum particles were evenly dispersed in the alumina gel. The platinum particles were identified using EDS analysis. Figure 4.49(c) presents the spectrum of the white background area, and the spectrum of the black dotted areas is shown in Figure 4.49(d). The platinum aggregates vary in their diameter as shown in Figure 4.49(b). As the process of depositing platinum on the washcoat is a result of the reaction of two reactants, platinum salt and hydrazine, the area having a large platinum aggregate may be due to easy access of the reactants into the pores. Allowing a longer dipping time in the platinum salt solution may result in the formation of larger platinum aggregates. This is because a longer dipping time allows more platinum salts to diffuse into the pores of the washcoat. This can be supported by the finding of XRD investigation in which there is a distinctive platinum peak in the XRD pattern as shown in Figure 4.48. This can also be seen in the X-ray map of platinum on alumina washcoat as shown in Figure 4.50.

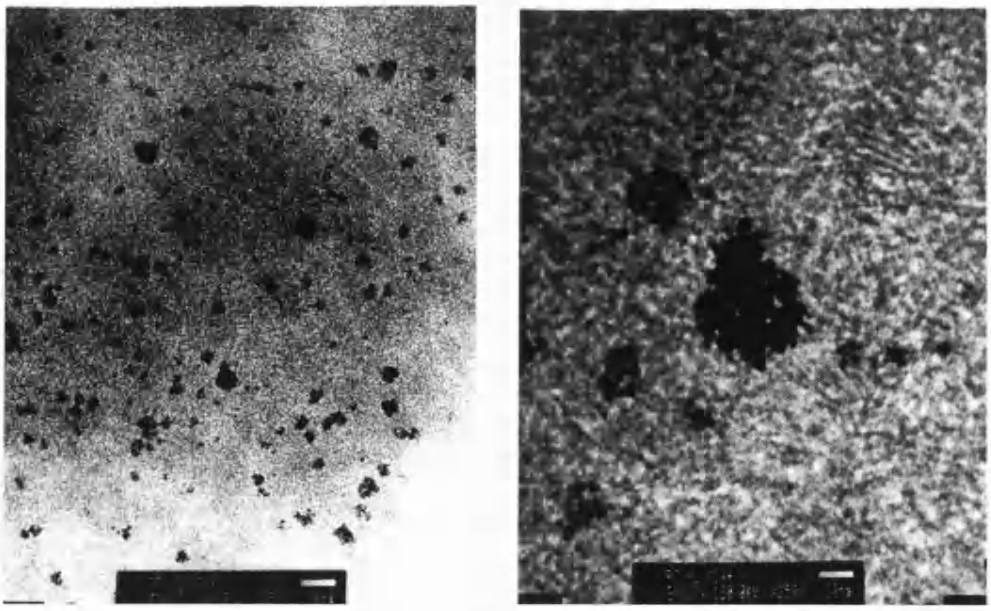

(a) (b)

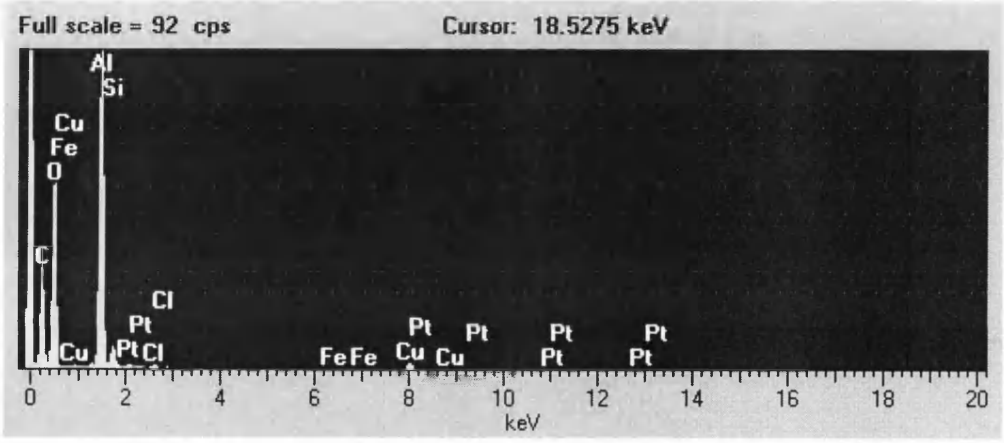

(c)

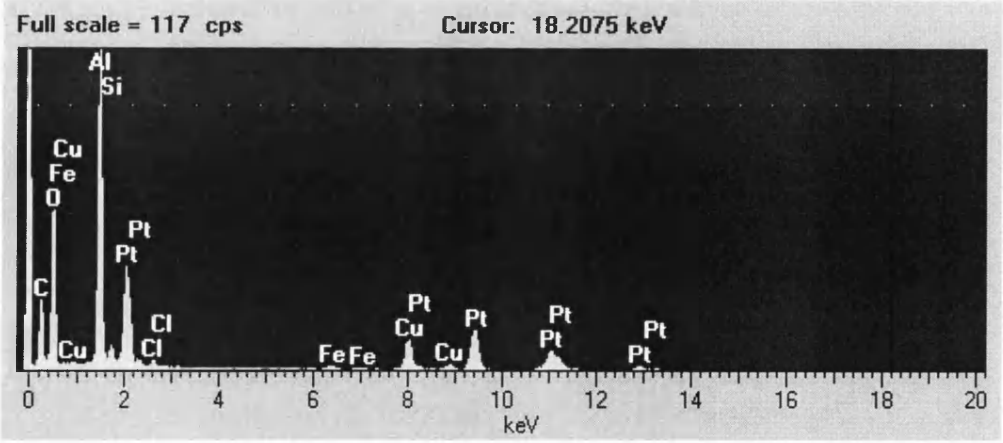

(d)

Figure 4.49. TEM images and X-ray analysis data of specimen Pt on Lab3 calcined at 600°C: (a) TEM image, Magnification: ×100,000, (b) TEM image, Magnification: ×500,000, (c) area A: white and (d) area B: dark spot.

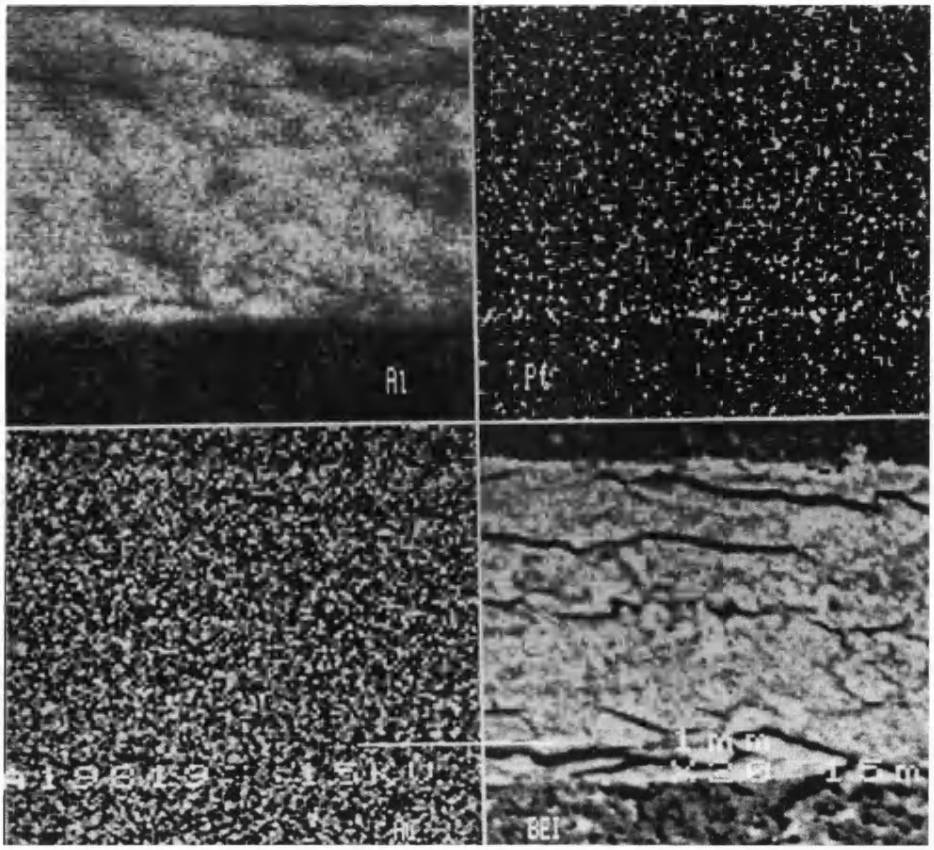

Figure 4.50. X-ray mapping image for platinum impregnated alumina gel calcined at 600°C: Left top: Al, Right top: Pt, Left bottom: Au, and Right bottom: SEM image.

Conclusions

- Use of the sol-gel method enables a uniform layer of washcoat to be deposited on the surface of a cordierite support. However, the washcoat loading per coating is relatively low, but it can be built up in a number of layers.
- Using the sol-gel method, the relative weight of sample increases in a linear manner with the number of coatings. After the first coating, the washcoat penetrates the pores and does not contribute to the thickness of the layer. After subsequent coatings, the thickness of the layer increases in a linear manner. Surface area and pore volume also increase in a linear manner.
- BET surface area decreases with calcination temperature and average pore diameter increases rapidly above a temperature of 900°C. These will have a significant impact on the effective diffusivity of components in the washcoat.
- Properties of cryogels (freeze-drying gels) and xerogels were compared. It was

shown that calcination temperature had more of a significant effect on the final properties of the washcoat than the method of drying.

- The addition of zirconia increases the stability of the pore size distribution, however, both pore volume and surface area decrease as zirconia content is increased. Addition of zirconia will affect effective diffusivity of components in the structure.
- In experiments, when 1 wt% platinum was added, the cumulative pore volume decreased by 9%, but pore size distribution was not affected. The addition of a catalyst may have a small effect on the effective diffusivity of components in the washcoat.
- The addition of 0.1 wt% of a drying additive was shown to reduce the tendency for cracks to form in the washcoat, without a significant reduction in surface area or change in average pore size.
- For the sol-gel to be used in the studies in the following chapter, the following characteristics have been selected:
  - Calcination temperature: 450 °C, 600 °C, 800 °C, and 1000 °C
  - Average pore size (mesopore): 3.6 nm (450 °C), 4.3 nm (600 °C), 5.5 nm (800 °C), and 7.5 nm (1000 °C)
  - Pore volume: 0.0006 ~ 0.022 cm^3/g
  - BET surface area: 0.65 ~ 14 m^2/g
  - Drying additives: none
  - Catalyst: none
  - Zirconia: none

Chapter 5. Measurement of Effective Diffusivity Using the Steady State Method

Using the sol-gel technique, plate samples from the cordierite were prepared and the series of experiments performed in this chapter is summarised in Figure 5.1. The steady state method described in Section 3.5.2 was employed. Operating conditions are summarised in Figure 5.2.

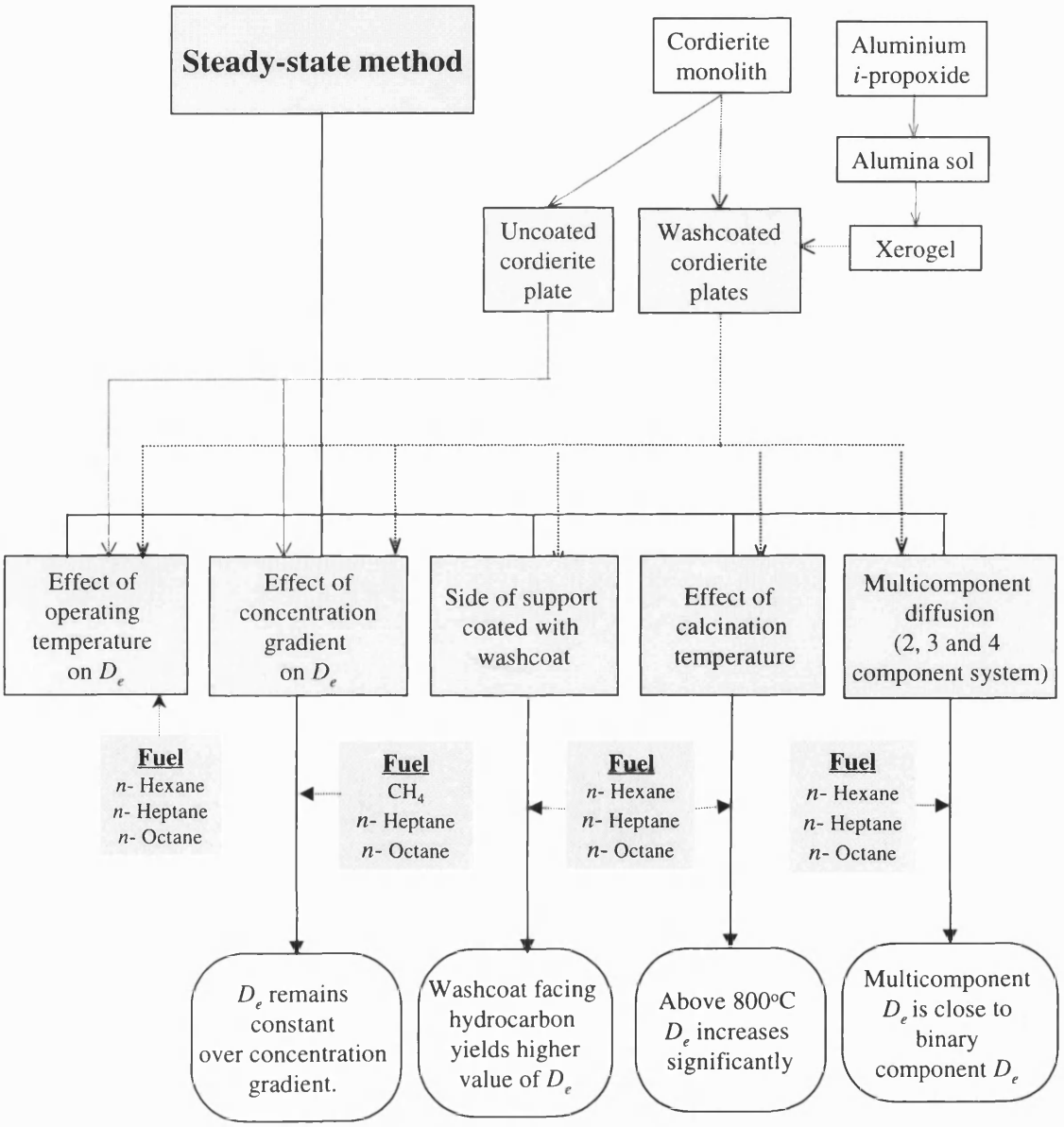

Figure 5.1. Schematic describing the link between the experiments in Chapter 5 (note: this links with Figure 1.2 in Chapter 1).

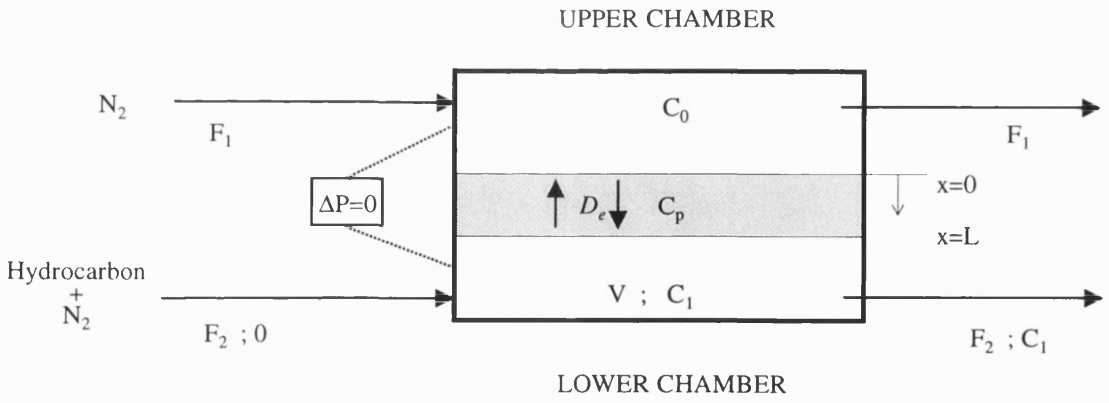

UPPER CHAMBER	LOWER CHAMBER
• Inlet : N_2 • Flowrate of N_2 (F_1) = 10 ~ 13 cm^3/s	• Inlet : Mixture of hydrocarbon and N_2 • Total flowrate (F_2): same as F_1 • Molar flowrate of hydrocarbon: 3.0×10^{-4} ~ 4.0×10^{-4} mol/s
• Operating temperature = 353 ~ 548 K, • Operating pressure = 1.35~ 1.5 bar • Pressure differential = ±1 mbar • Specimen : cordierite substrate Cross sectional area : 45 mm^2 Thickness : 0.25 mm Average pore diameter: 0.54 μm	

Figure 5.2. Operating conditions for the steady state method.

5.1. Measurement of effective diffusivity in uncoated cordierite substrate

A set of experiments was performed on the uncoated substrate to assess the influence of composition and temperature on the value of effective diffusivity and how it compares with values from the use of a random pore model (*e.g.* Wakao & Smith, 1962) and a parallel pore model (*e.g.* Johnson & Stewart, 1965).

Physical properties of the cordierite were determined in Section 4.4.1. In summary, the following data are relevant for this section:

Surface area, m^2/g	Apparent density, g/cm^3	Pore volume, cm^3/g	Porosity			Pore diameter, μm		
			total	macro	micro	Average	macro	micro
0.65	2.48	0.088	0.299	0.297	0.002	0.54	0.54	0.0036

5.1.1. Effective diffusivity of C5-C8 paraffins

A mixture of hydrocarbon and nitrogen was fed into the lower chamber and a flow of nitrogen was maintained in the upper chamber. Details of the apparatus were provided in Figure 3.9. The results of these experiments are shown in Table 5.1 and plotted against temperature in Figure 5.3.

Table 5.1. Experimental effective diffusivity of C_5-C_8 *n*-paraffins.

	Effective diffusivity (cm^2/s)			
T (K)	*n*-Pentane	*n*-Hexane	*n*-Heptane	*n*-Octane
353	$0.00289\pm3.5\times10^{-4}$	-	-	-
373	$0.00309\pm2.2\times10^{-4}$	-	-	-
398	-	$0.00273\pm1.3\times10^{-4}$	$0.00196\pm1.8\times10^{-4}$	-
403	-	-	$0.0021\pm1.2\times10^{-4}$	$0.00116\pm1.8\times10^{-4}$
423	$0.00360\pm4.5\times10^{-4}$	-	$0.00212\pm1.4\times10^{-4}$	-
448		$0.00305\pm1.3\times10^{-4}$	$0.00225\pm1.8\times10^{-4}$	$0.00149\pm5.7\times10^{-5}$
473	$0.00435\pm4.4\times10^{-4}$	-	$0.0026\pm2.7\times10^{-4}$	-
498	-	$0.00345\pm1.4\times10^{-4}$	-	$0.00160\pm9.8\times10^{-5}$
523	$0.00495\pm5.0\times10^{-4}$	-	$0.00285\pm1.4\times10^{-4}$	-
548	-	$0.00408\pm1.8\times10^{-4}$	-	$0.00187\pm1.3\times10^{-4}$

As expected, for the *n*-paraffins, the effective diffusivity decreases with an increase in molecular weight. This may be due to difference in the physico-chemical properties of the species, particularly, molecular weight and characteristic length. The molecular diffusivity estimated by Lenard-Jones expression shown in Equation 2.2 is inversely proportional to the square root of the molecular weight ($M^{-1/2}$), the square of the characteristic length (σ_{AB}) and the diffusion collision integral (Ω_D). The parameters for the C5-C8 *n*-paraffins are presented in Table 5.2.

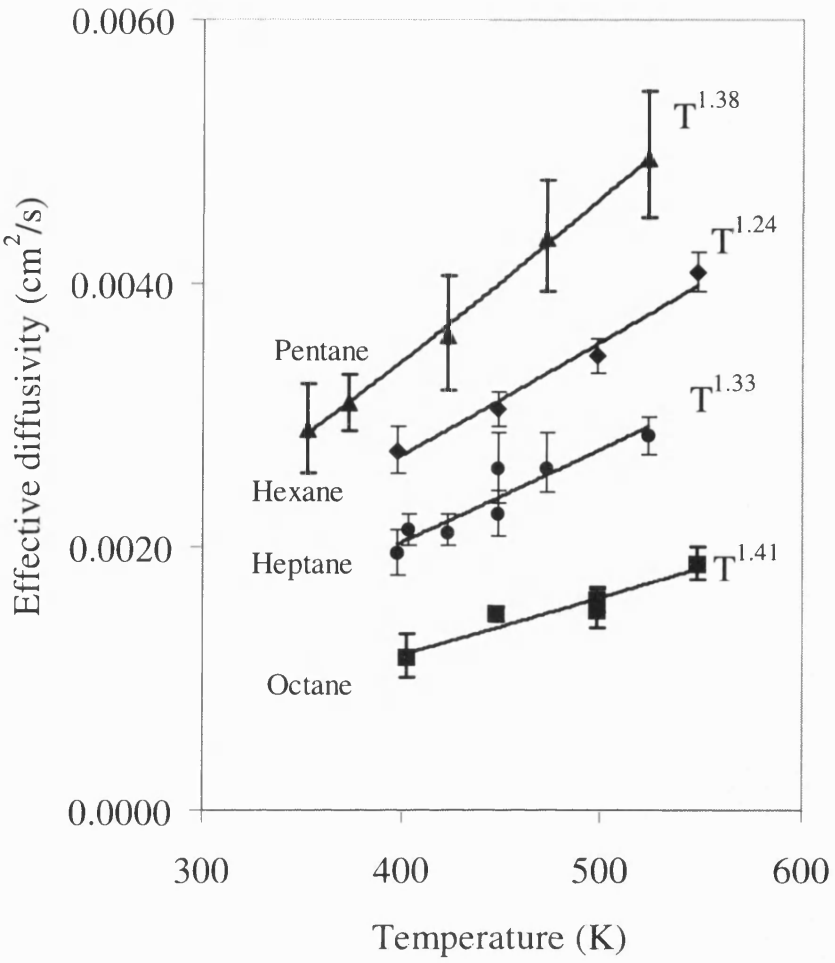

Figure 5.3. Temperature dependence of the effective diffusivity of C_5-C_8 *n*-paraffins in the uncoated cordierite substrate.

Table 5.2. The physical parameters for C5-C8 *n*-paraffins.

Component	Boiling point, °C	Molar mass, g/mol	Lenard-Jones constants*	
			σ	ε/k
n-Pentane	36.3	72.15	5.769	345
n-Hexane	69.0	86.18	5.909	413
n-Heptane	98.4	100.21	8.88	282
n-Octane	125.7	114.23	7.451	320
Nitrogen	-195.8	28	3.617	91.5

* Referred from Hirschfelder *et al.* (1954).

From data on porosity and pore diameter, it is clear that in the cordierite substrate macropores are dominant, therefore, bulk diffusion should prevail. Making use of Equation 2.2 and Equation 2.4:

$$D_{AB} = \frac{0.00266T^{3/2}}{PM_{AB}^{1/2}\sigma_{AB}^{2}\Omega_{D}} \tag{2.2}$$

$$D_{KA} = 2/3\ r\sqrt{\frac{8RT}{\pi M_A}} \tag{2. 4}$$

values of D_{KA} and D_{AB} were calculated and are compared with experimental values. As the solid has a bi-disperse structure, two Knudsen diffusion coefficients can be defined. They are D_{KAa}, the Knudsen diffusivity of species A in macropores (based on average macropore radius, r_a), and D_{KAi}, the Knudsen diffusivity of species A in the micropores (based on average micropore radius, r_i). From this data, it is clear that values of D_{AB} are smaller than D_{KAa}, but greater than D_{KAi}. However, none of the values are close to the measured values. It is noted that D_{AB} is about 30 times greater than measured values. This is clearly illustrated in the values of D_{KA} and D_{AB} presented in Figure 5.4. It is worth noting that in the reference (Hirschfelder *et al.*, 1954) the values of σ_{AB} and Ω_D for *n*-heptane have been determined using a different method than that for the other hydrocarbons. This may explain why calculated values of D_{AB} appear to be smaller for *n*-heptane than those for *n*-octane.

The temperature dependence of molecular diffusion is $T^{3/2}$ according to the theory based on the Lennard-Jones potential and the ideal gas law, although experimental data show them to be slightly different. Seager *et al.* (1963) reported experimental binary diffusion coefficients of gas-gas and gas-vapour mixtures up to 523 K and used a least square analysis to obtain the exponent (m) in assumed T^m dependence of the diffusion coefficients. The average value for all gases yields m = 1.70 and the average value for all vapours is also 1.70. For the microporous diffusion represented by Knudsen diffusion, the temperature dependence is $T^{1/2}$, as shown in Equation 2.4.

Pore diffusion occurs mostly in the transition diffusion regime so the exponent for effective diffusivities may be between two values. Yang & Liu (1982) reported the exponent for temperature dependence of effective diffusivities of between 1.1 and 1.2 for gaseous diffusion in porous graphite. Hou *et al.* (1999) measures the effective

diffusivities of H_2/N_2, CO_2/N_2 and CH_4/N_2 in an α-alumina pellet, which had a porosity of 0.39 and an average pore diameter of about 300 nm. They reported that their exponents were 1.06, 1.14 and 1.21, respectively.

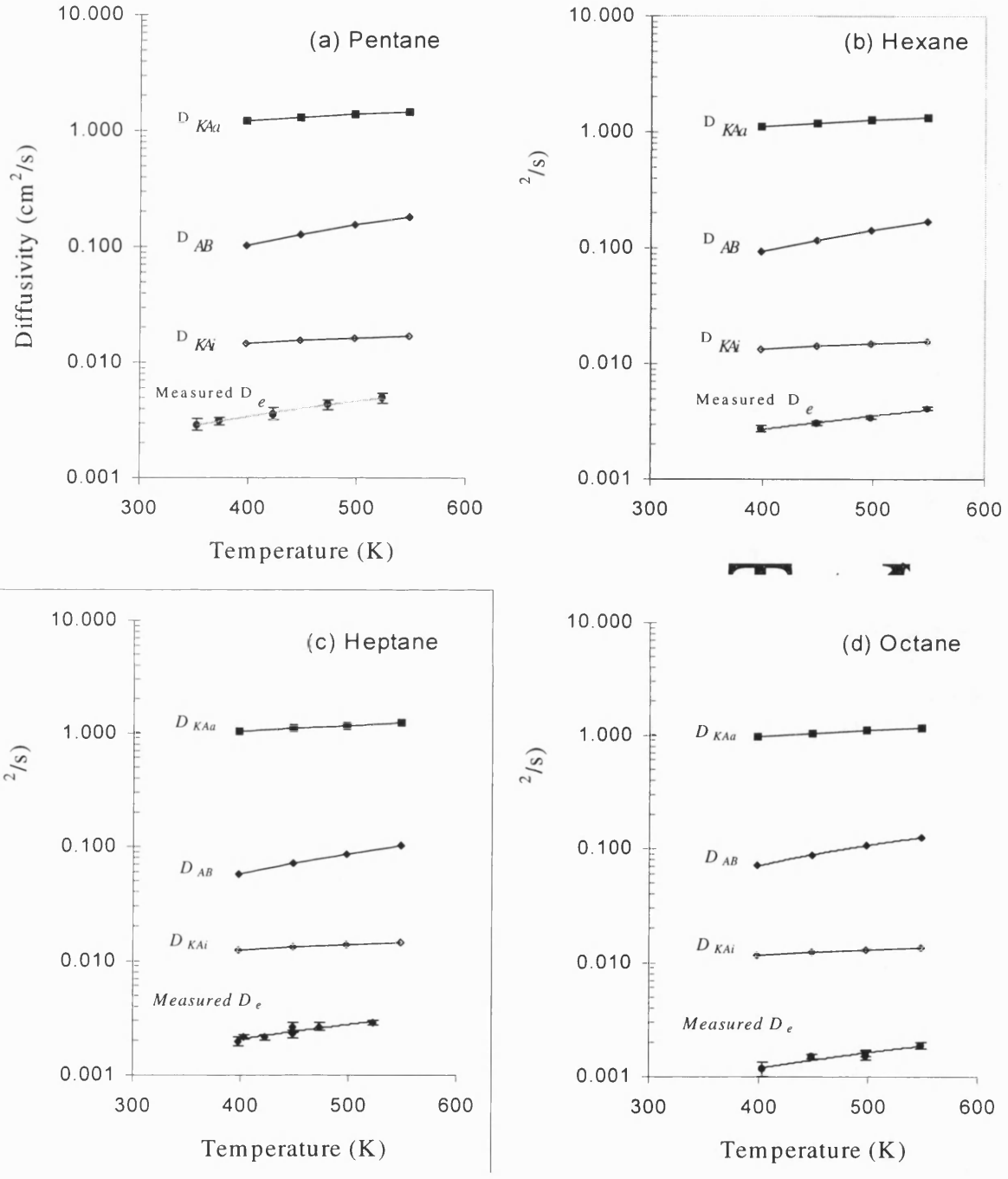

Figure 5.4. Experiments for the cordierite support: Comparison between measured effective diffusivity and calculated molecular diffusivity and Knudsen diffusivity.

The temperature dependence of effective diffusivities is presented in Table 5.3 and Figure 5.3. The values lie between 1.7 for molecular diffusion and 0.5 for Knudsen diffusion. This means that the diffusion is dominated by molecular diffusion as the cordierite substrate consists mainly of macropores.

Table 5.3. Temperature dependence of effective diffusivities of C5-C8 *n*-paraffins.

Components	Temperature dependence
n-pentane (C_5H_{12})	$8.6\times10^{-7}T^{1.38}$
n-hexane (C_6H_{14})	$1.6\times10^{-6}T^{1.24}$
n-heptane (C_7H_{16})	$7.1\times10^{-7}T^{1.33}$
n-octane (C_8H_{18})	$2.6\times10^{-10}T^{1.41}$

5.1.2. Comparison with the models

The results of theoretical calculations using a parallel pore model and a random pore model were compared with experimentally determined D_e. The parallel pore model described by Johnson and Stewart (1965) can be applied to a mono-disperse material (material consisted of pores of one size range only). The governing equation in the Johnson-Stewart model is:

$$D_e = \frac{\kappa\, D_{AB}\varepsilon}{(M_A/M_B)^{1/2}-1}\ln\left\{\frac{(M_A/M_B)^{1/2}+D_{AB}/D_{KA}}{1+D_{AB}/D_{KA}}\right\} \qquad (2.14)$$

The random pore model developed by Wakao and Smith (1962) is a model that is frequently used for a bi-disperse material (this consists of a structure with two distinct sizes of pores). The Wakao-Smith model has the form:

$$D_e\frac{\ln[1/(1-\alpha)]}{D_{AB}} = \varepsilon_a^2\ln\left\{\frac{1+D_{AB}/D_{AKa}}{1-\alpha+D_{AB}/D_{AKa}}\right\}+\frac{\varepsilon_i^2\alpha}{1-\alpha+D_{AB}/D_{AKi}}+\frac{4\varepsilon_a(1-\varepsilon_a)}{1+[(1-\varepsilon_a)^2/\varepsilon_i^2]}\times$$
$$\alpha/\left\{1-\frac{\alpha}{2}+\frac{D_{AB}}{D_{AKi}(1+\varepsilon_i^2)/(1-\varepsilon_a)^2}\right\} \qquad (2.16)$$

where $\alpha = 1-(M_B/M_A)^{1/2}$.

The values of D_e obtained by these two theoretical models, the Johnson-Stewart (1965) model and the Wakao-Smith (1968) model are listed in Table 5.4. They are compared with the measured D_e values in Figure 5.3. When the experimental results were compared with the use of the parallel pore model, it was found that the predicted D_e values are greater than the experimental values by a factor of 3 - 4, except in the case of octane which deviates by a factor of 8. When the experimental results were compared with the random pore model, it was found that the predicted effective diffusivities for *n*-pentane, *n*-hexane and *n*-heptane are greater than the experimental values by a factor of about 2 and 3, while D_e values for *n*-octane deviate by a factor of 5. Neither of the models, as they are constructed, provides a good match with the experimental data. Hayes and Kolaczkowski (2000) reported that values of D_e calculated using the random pore model were found to be 3.1 times larger than the experimental values.

In the Johnson-Stewart model, a tortuosity of 3 is assumed, as the geometric constant, κ, (or the reciprocal of tortuosity factor, $1/\tau$) is assumed a value of $1/3$, for an isotropic pore system. It is assumed that the pores are straight and nonconnecting, with no dead volume (Johnson & Stewart, 1965). The tortuosity factor is also assumed to be the reciprocal of macroporosity in the random pore model (Wakao and Smith, 1962). As the macroporosity of the cordierite is 0.299, the tortuosity used in random pore model is 3.34 and is greater than the tortuosity for the parallel pore model.

So, making use of the experimental data, tortuosity factors were calculated using an equation suggested by Satterfield (1970):

$$D_{eff} = D_T \frac{\varepsilon}{\tau} \qquad (5.1.a)$$

The transition diffusivity, D_T, is a function of concentration and is given by (Park *et al.*,1996):

$$\frac{1}{D_T} = \frac{1-\alpha \cdot y}{D_{AB}} + \frac{1}{D_{KA}} \qquad (5.1b)$$

For equimolar counterdiffusion (α=0) and also for dilute systems (y<<1), Equation (5.1b) reduces to Equation (5.1c):

$$\frac{1}{D_T} = \frac{1}{D_{AB}} + \frac{1}{D_{KA}} \qquad (5.1.c)$$

Table 5.4. Experimental and predicted (from J-S model and W-S model) effective diffusivities for C5-C8 *n*-paraffins-nitrogen at different temperatures and tortuosities. (macroporosity=0.299, average pore diameter=0.54 μm).

Temperature, K	Experimental D_e, cm^2/s	D_{AB}, cm^2/s	D_{KAa}, cm^2/s	D_{KAi}, cm^2/s	D_T, cm^2/s	D_e (J-S), cm^2/s (D_e(J-S)/D_e(expt))	D_e (W-S), cm^2/s (D_e(W-S)/D_e(expt))	Calculated tortuosity (τ)
				***n*-Pentane**				
353.15	0.00289 ±0.000347	0.0825	1.159	0.00353	0.0628	0.00946 (3.3)	0.00667 (2.3)	6.5
373.15	0.00309 ±0.000216	0.0913	1.191	0.00376	0.0692	0.0104 (3.4)	0.00734 (2.4)	6.7
423.15	0.0036 ±0.000448	0.115	1.269	0.00431	0.0862	0.0129 (3.6)	0.00908 (2.5)	7.2
473.15	0.00435 ±0.000436	0.140	1.341	0.00484	0.104	0.0155 (3.6)	0.0109 (2.5)	7.2
523.15	0.00495 ±0.000502	0.168	1.410	0.00534	0.123	0.0182 (3.7)	0.0129 (2.6)	7.4
								Average= 7.0 ±0.4
				***n*-Hexane**				
398.15	0.00273 ±0.000181	0.0947	1.126	0.00371	0.0683	0.011 (4.1)	0.00751 (2.7)	7.5
448.15	0.00305 ±0.000134	0.118	1.19	0.00420	0.0839	0.0135 (4.4)	0.00916 (3.0)	8.2
498.15	0.00345 ±0.000133	0.142	1.26	0.00468	0.101	0.0161 (4.7)	0.0109 (3.2)	8.7
548.15	0.00408 ±0.000145	0.169	1.32	0.00513	0.118	0.0188 (4.6)	0.0127 (3.1)	8.6
								Average= 8.3 ±0.6

The number in the parenthesis is the ratio of theoretically predicted D_e and experimentally determined D_e.
$D_T = ((1-\alpha \cdot y_A)/D_{AB}+1/D_{KA})^{-1}$ based on Equation (5.1.b).
τ calculated from Equation (5.1.a).

Table 5.4. Experimental and predicted (continue.....).

Temperature, K	Experimental D_e, cm^2/s	D_{AB}, cm^2/s	D_{KAa}, cm^2/s	D_{KAi}, cm^2/s	D_T, cm^2/s	D_e (J-S), cm^2/s (D_e(J-S)/D_e(expt))	D_e (W-S), cm^2/s (D_e(W-S)/D_e(expt))	Calculated tortuosity (τ)
				***n*-Heptane**				
398.15	0.00196 ±0.000167	0.0576	1.044	0.00279	0.0408	0.00721 (3.7)	0.00472 (2.4)	6.2
423.15	0.00212 ±0.000103	0.0643	1.076	0.00300	0.0454	0.00800 (3.8)	0.00524 (2.5)	6.4
448.15	0.0026 ±0.00233	0.0712	1.107	0.00321	0.0502	0.00881 (3.4)	0.00577 (2.2)	5.8
473.15	0.0026 ±0.000185	0.0784	1.138	0.00342	0.0550	0.00965 (3.7)	0.00632 (2.4)	6.3
523.15	0.00285 ±0.000137	0.0937	1.197	0.00382	0.0653	0.0114 (4.0)	0.00745 (2.6)	6.9
								Average= 6.3 ±0.4
				***n*-Octane**				
403.15	0.00116 ±0.000185	0.0726	0.984	0.00305	0.0490	0.0091 (7.8) 1	0.00579 (5.0)	12.6
448.15	0.00149 ±0.000057	0.0879	1.037	0.00343	0.0589	0.0108 (7.3)	0.00691 (4.6)	11.8
498.15	0.0016 ±0.000097	0.106	1.094	0.00383	0.0705	0.0129 (8.0)	0.00821 (5.1)	13.2
548.15	0.00187 ±0.00013	0.126	1.147	0.00421	0.0828	0.0151 (8.0)	0.00957 (5.1)	13.2
								Average= 12.7 ±0.7

The number in the parenthesis is the ratio of theoretically predicted D_e and experimentally determined D_e.
$D_T = ((1-\alpha \cdot y_A)/D_{AB}+1/D_{KA})^{-1}$ based on Equation (5.1.b).
τ calculated from Equation (5.1.a).

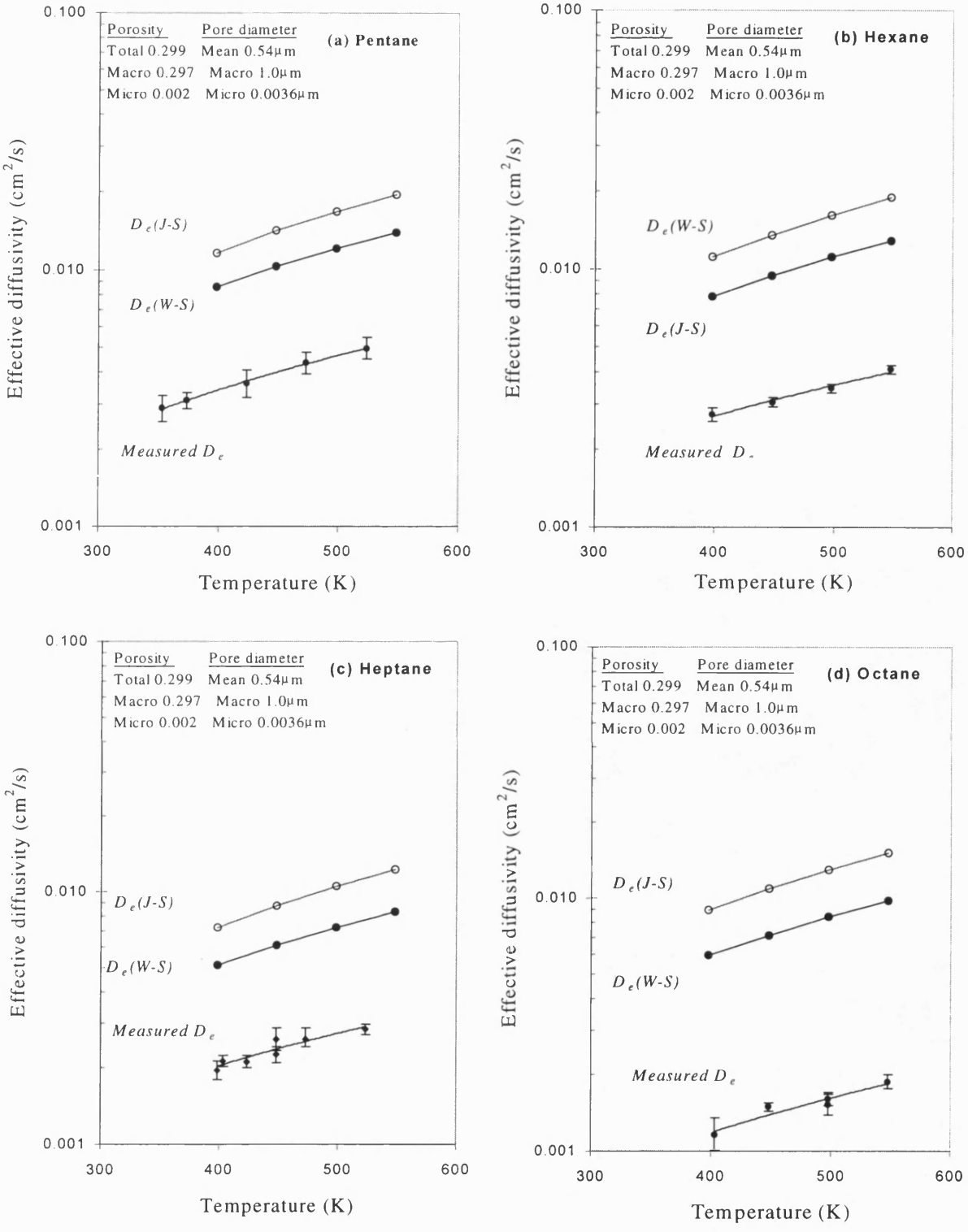

Figure 5.5. Comparing experimentally measured values of D_e, with the values calculated from the use of the parallel model (J-S) and the random pore model (W-S).

Table 5.5. Tortuosity factors obtained from a diffusion experiment for methane-nitrogen (CH_4-N_2).

Temperature, K	Experimental D_e, cm^2/s	D_{AB}, cm^2/s	D_{KAa}, cm^2/s	D_{KAb}, cm^2/s	D_T, cm^2/s	D_e(J-S), cm^2/s (D_e(J-S)/D_e(expt))	D_e(W-S), cm^2/s (D_e(W-S)/D_e(expt))	Tortuosity (τ)
294.15	0.00871 ±0.0018	0.153	2.246	0.00670	0.186	0.0125 (1.43)	0.01274 (1.46)	6.4
323.15	0.0114 ±0.0012	0.181	2.354	0.00744	0.217	0.0146 (1.28)	0.01496 (1.31)	5.7
373.15	0.0129 ±0.0013	0.233	2.529	0.00867	0.275	0.0186 (1.44)	0.01904 (1.48)	6.4
423.15	0.0144 ±0.0010	0.290	2.694	0.00983	0.336	0.0229 (1.59)	0.02341 (1.63)	7.0
473.15	0.0175 ±0.0023	0.352	2.848	0.0109	0.400	0.0274 (1.57)	0.02804 (1.60)	6.8
523.15	0.0185 ±0.0030	0.418	2.995	0.0120	0.467	0.0322 (1.74)	0.03291 (1.78)	7.6
573.15	0.0246 ±0.00071	0.489	3.135	0.0130	0.536	0.0372 (1.51)	0.03798 (1.54)	6.5
								Average=6.9 ± 0.5

The number in the parenthesis is the ratio of theoretically predicted D_e and experimentally determined D_e.
$D_T = ((1-\alpha \cdot y_A)/D_{AB}+1/D_{KA})^{-1}$ based on Equation (5.1.b).
τ calculated from Equation (5.1.a).

Using this method, tortuosity factors were calculated for the hydrocarbons and these are listed in Table 5.4. In addition, tortuosity factors were determined for a methane-nitrogen at different temperatures, see Table 5.5. The values lie between 5.7 and 7.6 with the least variation with temperature. The average value is 6.9 with a standard deviation of 0.5. In principle, tortuosity should be independent of temperature. Li (1997) performed experiment with methane and nitrogen and reported the tortuosity of a cordierite substrate was 8.5. In general, the tortuosity factors for commercial catalysts and supports are between 3 and 7.5 (Satterfield, 1970).

The calculated average values of τ are plotted as a function of molar mass in Figure 5.6. From this it is interesting to observe that the calculated τ increases with molecular weight. As the tortuosity should be constant for the material, this indicates that either the presence of the heavier species is increasing tortuosity (perhaps connecting micropores becomes blocked) or other factors (*e.g.* adsorption) are influencing the results.

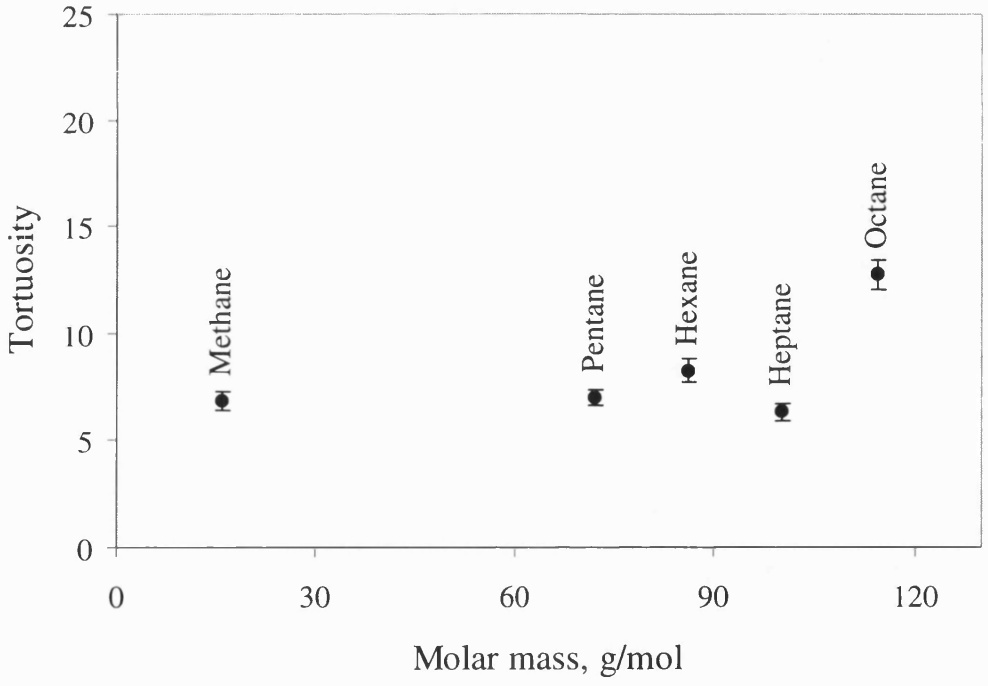

Figure 5.6. Tortuosity factors for the cordierite support obtained from different diffusing species.

5.2. Measurement of effective diffusivity in the alumina washcoat

In the case of a composite membrane composed of n sheets of thickness, l_1, l_2, l_3, ..., l_n and diffusion coefficient, $D_{e,1}$, $D_{e,2}$, $D_{e,3}$, ..., $D_{e,n}$, the concentration gradient through the whole membrane is the sum of the gradients through the component sheets (Crank, 1956). Since the mass transfer rate, F, is the same across each section, the total drop in concentration (by using a standard resistance in series concept):

$$\frac{Fl_1}{D_{e,1}} + \frac{Fl_2}{D_{e,1}} + \bullet\bullet\bullet + \frac{Fl_n}{D_{e,n}} = (R_1 + R_2 + \bullet\bullet\bullet + R_n)F = R_{overall}F \tag{5.2}$$

This approach was applied to a catalytic monolith by Hayes *et al.* (2000). As the alumina is washcoated on both sides of the cordierite substrate plate, then:

$$\frac{Fl_1}{D_{e,washcoat}} + \frac{Fl_2}{D_{e,cord}} + \frac{Fl_3}{D_{e,washcoat}} = \frac{l_{overall}}{D_{e,overall}}F \tag{5.3}$$

where, $D_{e,washcoat}$ = effective diffusivity in washcoat, cm^2/s

$D_{e,cord}$ = effective diffusivity in cordierite substrate, cm^2/s

$D_{e,overall}$ = overall effective diffusivity, cm^2/s

l_1, l_3 = thickness of washcoat layer, cm

l_2 = thickness of the cordierite substrate, cm

$l_{overall}$ = total thickness, cm

Dividing Equation (5.3) by F, then:

$$\frac{l_1 + l_3}{D_{e,washcoat}} + \frac{l_2}{D_{e,cord}} = \frac{l_{overall}}{D_{e,overall}} \tag{5.4}$$

To obtain the effective diffusivity in the washcoat, $D_{e,cord}$, the rate of diffusion is measured with two samples, a plain substrate and a washcoated substrate as shown in Figure 5.7. As l_1, l_2 and l_3 can be measured, and $D_{e,cord}$ and $D_{e,overall}$ can be determined from measurements of diffusion, then the value of $D_{e,washcoat}$ can be calculated from Equation (5.4).

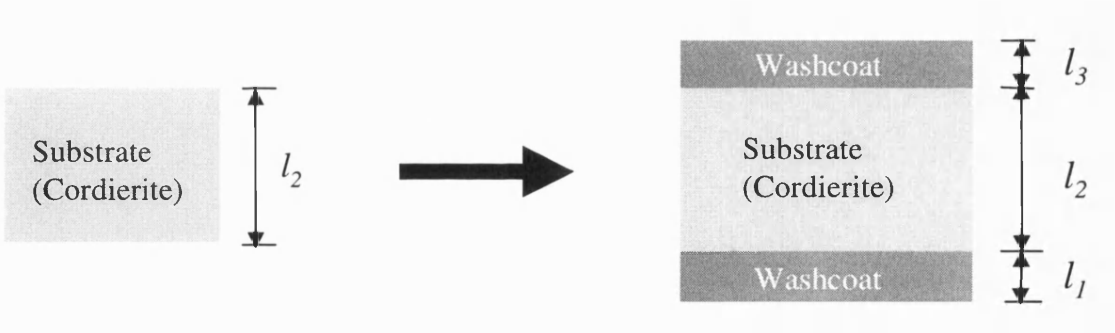

Figure 5.7. Diffusion experiments are performed on substrate and then the washcoated cordierite support.

Using this concept, Hayes *et al.* (2000) assumed that there is no effect of the interface between the washcoat and the support. However, they suggested that the assumption be tested by performing experiments with monolith samples with washcoat of differing thickness. Before these experiments were performed, it was decided to test if there is a concentration dependence.

5.2.1. Effect of concentration gradient on the value of overall effective diffusivity

In general, it is assumed that effective diffusivity is independent of concentration (*e.g.* Cussler, 1984). However, in many systems, *e.g.* the interdiffusion of metals or the diffusion organic vapours in high polymer substances, diffusion coefficient depends on the concentration of diffusing substance (Crank, 1956). In this thesis, the dependence of effective diffusivity on the concentration of hydrocarbons was investigated.

Figure 5.8 presents the effect of the feed concentration on the effective diffusivity of *n*-heptane and *n*-octane. Within experimental errors, the overall effective diffusivity of both *n*-heptane and *n*-octane appears constant over the range of mole fractions in the feed, while as expected, the diffusion fluxes of both hydrocarbons increase with an increase in mole fraction.

Figure 5.9 presents the effect of the feed concentration of methane on the value of the overall effective diffusivity. The experiment was performed on the same sample. It can be seen that within experimental errors the effective diffusivity remains constant over the whole range, while the flux increases linearly with mole fraction.

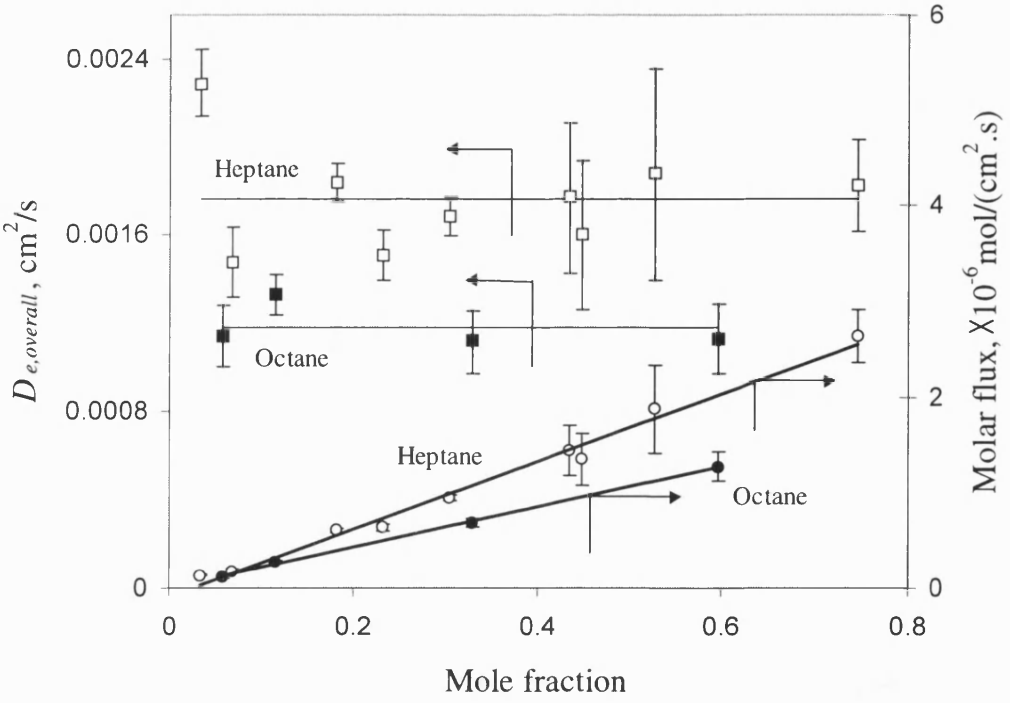

Figure 5.8. Effect of concentration gradient on the overall effective diffusivity of *n*-heptane and *n*-octane (T=225°C, P=1.57 bar, F_1=13 cm^3/s). The washcoat is alumina gel (LAB2) calcined at 600°C and alumina loading was 0.001 g/cm^2.

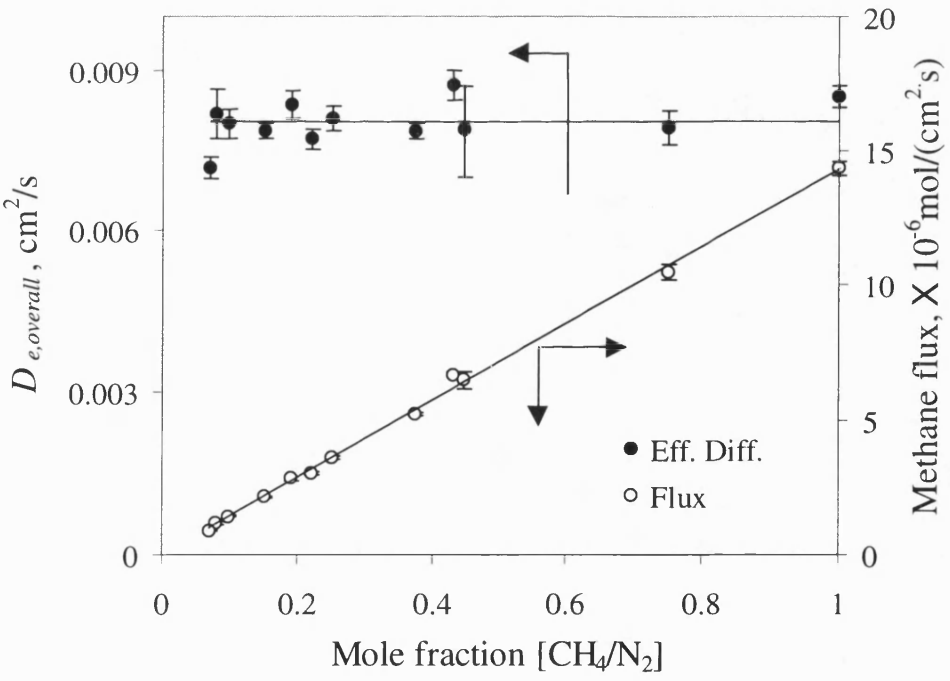

Figure 5.9. Effect of concentration gradient on the overall effective diffusivity of methane (T=225°C, P=1.57 bar, F_1=13 cm^3/s). The washcoat is alumina gel (LAB2) calcined at 600°C and alumina loading was 0.001 g/cm^2.

5.2.2. Effect of alumina loading on effective diffusivity

In order to explore the formation of the interface between the washcoat and the cordierite support, the overall effective diffusivity was determined for various loadings of washcoat. The washcoat was prepared by dipping and spinning with the alumina sol (LAB2) at different alumina washcoat loadings (the loading is expressed as grams of alumina per external geometrical area of substrate plate). This method was discussed in Section 4.3.2.1. The SEM images of the coated cordierite with different alumina loadings were presented in Figure 5.10. The results for *n*-hexane, *n*-heptane, and *n*-octane are presented in Table 5.6 and are also plotted in Figure 5.11. In the calculation of the overall effective diffusivity, the thickness of all of the samples was assumed to be same as the uncoated cordierite plate.

From this data, it is clear that an increase in the amount of loaded alumina from 0 to 0.0015 g/cm^2, decreases the overall effective diffusivity of *n*-hexane from 0.0031 to 0.0005 cm^2/s. For all of the hydrocarbon species, the overall effective diffusivities decreased with increasing amounts of loaded alumina, although the extent of the decrease differed in each case. However, the decrease in overall effective diffusivity with loading becomes constant above an alumina washcoat loading of 0.0012 g/cm^2. From this, it can be postulated that the pore filling keeps progressing until the external pore openings are filled with alumina, see Figure 5.10. Then the layer starts to build up in uniform manner and hence the effective diffusivity decreases in a linear manner. The effective diffusivity of hydrocarbons in the alumina washcoat can be calculated with Equation (5.4). Table 5.7 presents the calculated $D_{e,washcoat}$ values for three *n*-paraffins in the alumina washcoat. The calculation was performed using two different values of $D_{e,cord}$. Firstly, $D_{e,cord}$ values for uncoated cordierite were used. Secondly, $D_{e,overall}$ values for a surface pore filled cordierite with a washcoat of an alumina loading of 0.000747 g/cm^2 were used for the value of $D_{e,cord}$. The effective diffusivities of *n*-hexane, *n*-heptane and *n*-octane in the alumina washcoat at 175°C were 1.84×10^{-5} cm^2/s, 1.07×10^{-5} cm^2/s, and 1.26×10^{-5} cm^2/s, respectively. It is clear that it would be better to make use of a pre-treated cordierite plate with washcoat, to act as a reference for $D_{e,cord}$.

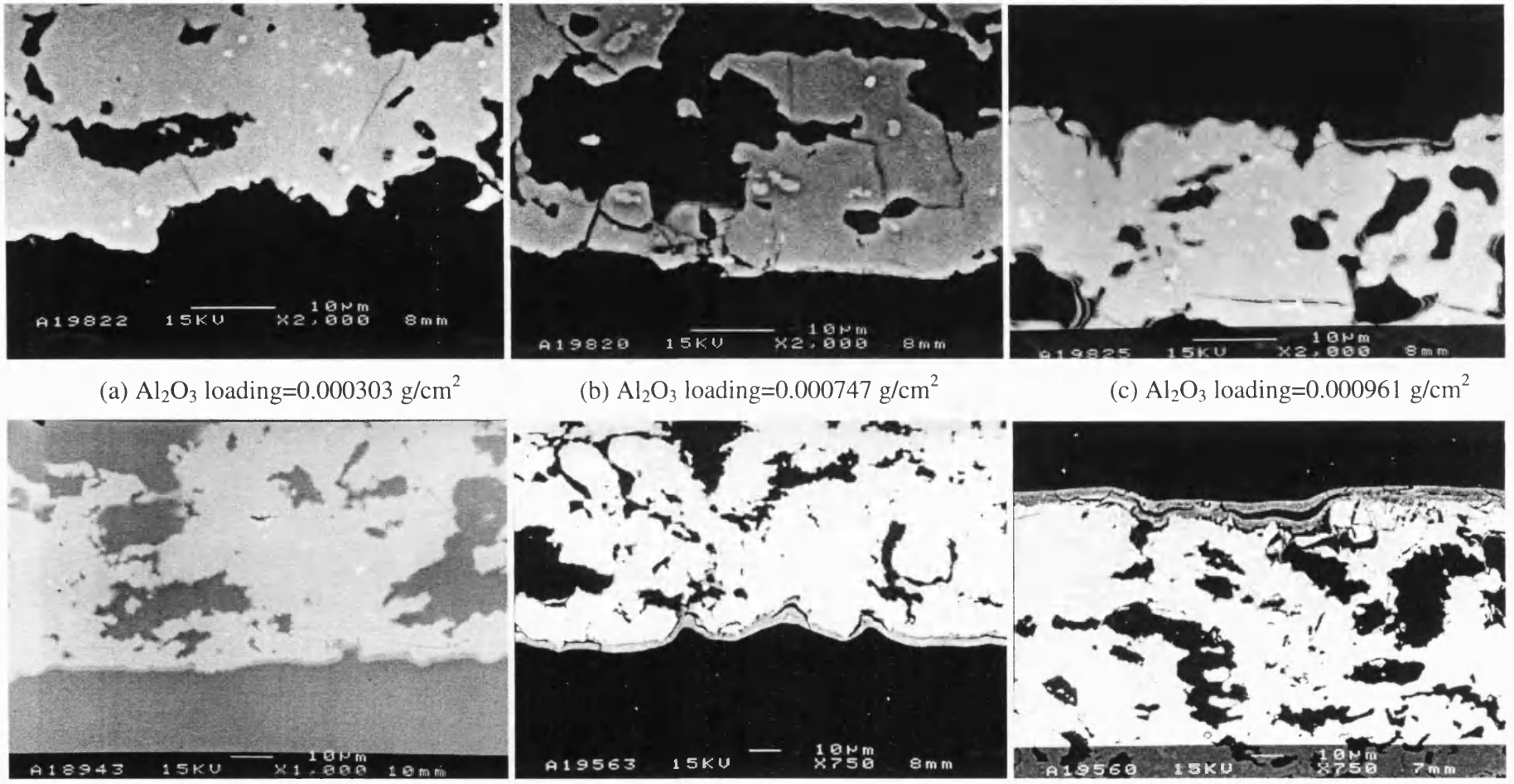

(a) Al_2O_3 loading=0.000303 g/cm^2 (b) Al_2O_3 loading=0.000747 g/cm^2 (c) Al_2O_3 loading=0.000961 g/cm^2

(d) Al_2O_3 loading=0.00121 g/cm^2 (e) Al_2O_3 loading=0.00132 g/cm^2 (f) Al_2O_3 loading=0.00149 g/cm^2

Figure 5.10. SEM images of the alumina coated cordierite with different alumina loadings.

Table 5.6. Effective diffusivities and molar fluxes of *n*-paraffins in washcoated substrate with alumina gel (LAB2) calcined at 600°C (T=175°C, P= 1.45 ~ 1.5 bar).

Alumina loading, g/cm^2	Washcoat thickness, μm	Effective diffusivity ($D_{e,overall}$), cm^2/s			Molar flux, mol/(cm^2.s)		
		n-Hexane	*n*-Heptane	*n*-Octane	*n*-Hexane	*n*-Heptane	*n*-Octane
none	0	0.00305 ±0.00013	0.00225 ±8.3×10^{-5}	0.0015 ±5.7×10^{-5}	-	-	-
0.000303	N/A	0.00244 ±0.00012	0.00230 ±9.2×10^{-5}	0.0012 ±0.00013	6.6×10^{-7} ±2.7×10^{-8}	3.6×10^{-7} ±1.3×10^{-8}	3.1×10^{-7} ±3×10^{-8}
0.000747	N/A	0.00142 ±0.00016	0.00104 ±0.00011	0.00091 ±6.3×10^{-5}	5×10^{-7} ±2.7×10^{-8}	3.4×10^{-7} ±1.1×10^{-8}	2.4×10^{-7} ±7.5×10^{-8}
0.000961	0.5	0.00107 ±0.00015	0.00081 ±6.8×10^{-5}	0.00045 ±6.9×10^{-5}	6.9×10^{-7} ±8.5×10^{-8}	4×10^{-7} ±2.9×10^{-8}	2.5×10^{-7} ±3.3×10^{-8}
0.00121	1.5	0.0008 ±0.00013	0.00077 ±5.5×10^{-5}	0.00061 ±0.00012	3.3×10^{-7} ±6.6×10^{-8}	2.1×10^{-7} ±5.4×10^{-8}	2×10^{-7} ±2×10^{-8}
0.00130	2	0.00087 ±0.00011	0.00053 ±3.0×10^{-5}	0.00051 ±2.6×10^{-5}	5.3×10^{-7} ±7×10^{-8}	3.9×10^{-7} ±2×10^{-8}	3.3×10^{-7} ±6.1×10^{-8}
0.00132	2.5	0.00053 ±0.00011	0.0004 ±2.0×10^{-5}	0.00034 ±4.0×10^{-5}	3.5×10^{-7} ±3.8×10^{-8}	1.9×10^{-7} ±6.8×10^{-8}	1.7×10^{-7} ±6.9×10^{-9}
0.00149	4	0.00052 ±3.3×10^{-5}	0.00037 ±3.2×10^{-5}	0.00034 ±1.1×10^{-5}	2.5×10^{-7} ±1.1×10^{-8}	1.6×10^{-7} ±1.2×10^{-8}	7.3×10^{-8} ±2.1×10^{-9}

N/A: not applicable.

Note: The thickness of cordierite plates is 0.025 cm.

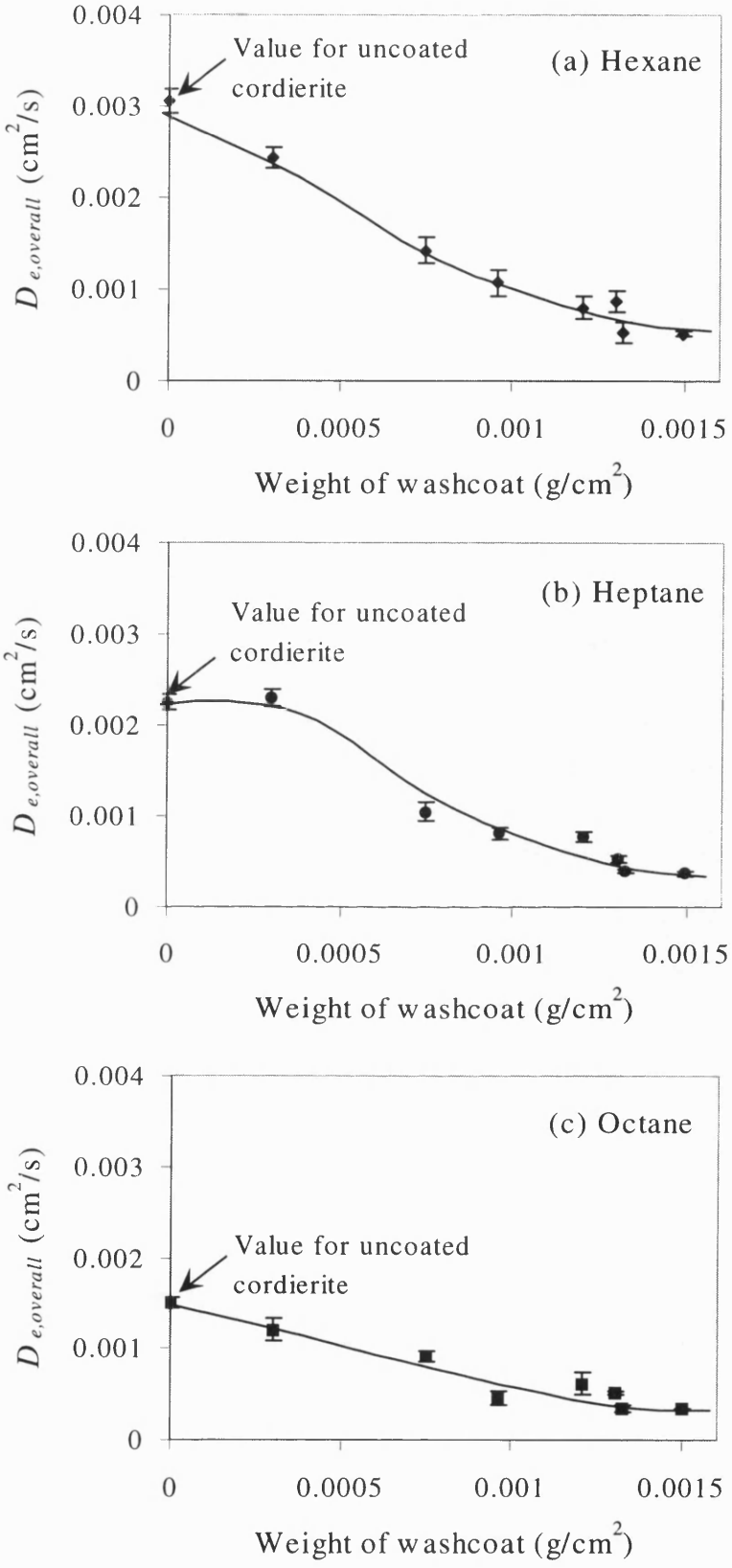

Figure 5.11. Alumina washcoat loading versus overall effective diffusivity (T=175°C, P=1.45~1.5bar). The washcoat is alumina gel (LAB2) calcined at 600°C (l_2=0.025 cm).

Table 5.7. Calculation of the effective diffusivity of hydrocarbons in an alumina washcoat using Equation (5.4).

Alumina loading, g/cm^2	Thickness of washcoat, μm	Effective diffusivity of washcoat, $D_{e,washcoat}$, cm^2/s		
		n-Hexane	*n*-Heptane	*n*-Octane
When $D_{e,overall}$ for uncoated cordierite is considered $D_{e,cord}$				
0.0013	2	1.91×10^{-5} $\pm4.08\times10^{-6}$	1.08×10^{-5} $\pm9.55\times10^{-7}$	1.22×10^{-5} $\pm1.23\times10^{-6}$
0.00132	2.5	1.25×10^{-5} $\pm3.51\times10^{-6}$	9.49×10^{-6} $\pm6.54\times10^{-7}$	8.51×10^{-6} $\pm1.48\times10^{-6}$
0.0015	4	1.21×10^{-5} $\pm1.91\times10^{-5}$	1.68×10^{-6} $\pm1.37\times10^{-5}$	1.35×10^{-5} $\pm6.94\times10^{-7}$
	Average	**1.46×10^{-5}**	**7.32×10^{-6}**	**1.14×10^{-5}**
When $D_{e,overall}$ for washcoated cordierite with alumina loading of 0.000747 g/cm^2 is considered $D_{e,cord}$				
0.0013	2	2.63×10^{-5} $\pm2.28\times10^{-5}$	1.26×10^{-5} $\pm3.38\times10^{-6}$	1.38×10^{-5} $\pm3.38\times10^{-6}$
0.00132	2.5	1.94×10^{-5} $\pm9.97\times10^{-6}$	1.50×10^{-5} $\pm2.38\times10^{-6}$	1.25×10^{-5} $\pm3.26\times10^{-6}$
0.0015	4	2.47×10^{-5} $\pm4.51\times10^{-6}$	1.76×10^{-5} $\pm3.71\times10^{-6}$	1.66×10^{-5} $\pm1.57\times10^{-6}$
	Average	**1.84×10^{-5}**	**1.07×10^{-5}**	**1.26×10^{-5}**

5.2.3. Effect of direction of flux in composite binary structure on effective diffusivity

The cordierite support contains mainly macropores whereas the washcoat contains micropores. An experiment was, therefore, designed to investigate whether the nature of the interface between the washcoat and the support against the hydrocarbon rich stream had any effect on diffusion. For this experiment, the cordierite plate was only coated on one side. The washcoat material was alumina gel calcined at 600°C. The washcoat loading was 0.0006 g/cm^2, which is of a value at which a uniform coating is formed. This corresponded to a washcoat thickness of about 1.5 μm. Using this sample, two experiments were performed, see Figure 5.12. Firstly, a hydrocarbon-rich gas was introduced on the side facing the washcoat (Exp. 1). Then the hydrocarbon-rich gas was introduced on the side without the washcoat (Exp. 2). The operating conditions and the experimental data are summarised in Table 5.8.

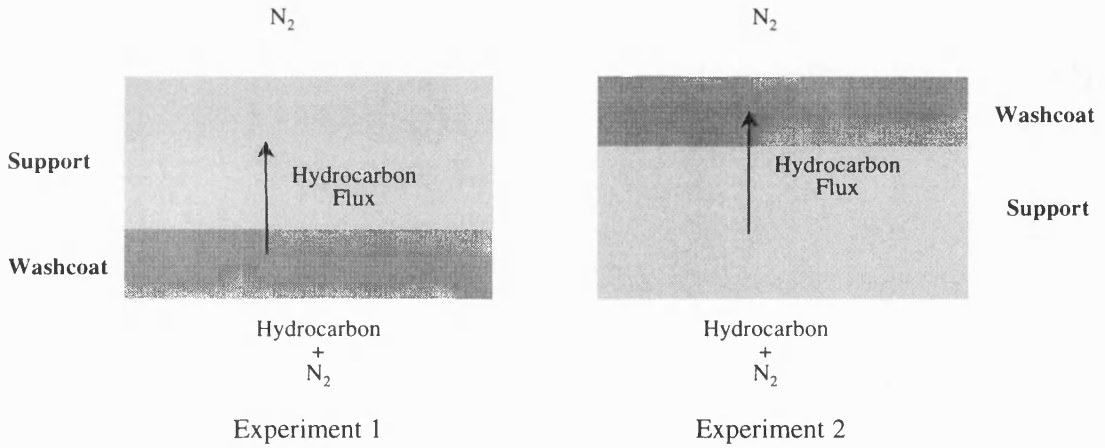

Figure 5.12. Direction of hydrocarbon flux in two different diffusion experiments. (Note: The coated support is the same in both of the experiments, only the position of the plate is reversed.).

Figure 5.13 shows the overall effective diffusivities across the composite, for *n*-hexane, *n*-heptane, and *n*-octane. The overall effective diffusivities for Exp. 2 (in which nitrogen faces the washcoat) are greater than those for Exp. 1. The differences in values of $D_{e,overall}$ between the two experiments are a factor of 1.43. 1.44, and 1.52 for *n*-hexane, *n*-heptane and *n*-octane, respectively.

Table 5.8. Experiments across the composite: Summary of experimental data (Washcoat: Alumina gel (LAB2) calcined at 600°C, washcoat thickness: 1.5 μm).

	n-Hexane		*n*-Heptane		*n*-Octane	
	Exp. 1	Exp. 2	Exp. 1	Exp. 2	Exp. 1	Exp. 2
Temperature,°C	175					
Pressure, bar	1.50		1.51		1.51	
Flowrate(F1), cm^3/s	12.97		12.97		13.09	
Concentration in upper chamber, mol/ml	0.00153 $\pm 1.2\times10^{-5}$	0.001 $\pm 5.7\times10^{-5}$	0.00084 $\pm 1.2\times10^{-5}$	0.00091 $\pm 6.3\times10^{-6}$	0.00076 $\pm 1.9\times10^{-5}$	0.00084 $\pm 1.2\times10^{-5}$
Concentration in lower chamber, mol/ml	1.485 ±0.0172	0.663 ±0.0107	0.945 ±0.00595	0.712 ±0.0258	2.057 ±0.0246	2.15 ±0.00966
$D_{e,overall}$, cm^2/s	0.00142 ±0.00004	0.00204 ±0.00017	0.00123 ±0.00003	0.00185 ±0.00009	0.00052 $\pm 1.9\times10^{-5}$	0.00079 $\pm 1.7\times10^{-5}$
$D_{e,washcoat}$, cm^2/s	2.1×10^{-5} $\pm 1.6\times10^{-6}$	4.8×10^{-5} $\pm 2\times10^{-6}$	2.1×10^{-5} $\pm 3.9\times10^{-6}$	6.5×10^{-5} $\pm 6.7\times10^{-6}$	6.2×10^{-6} $\pm 5.1\times10^{-7}$	1.3×10^{-5} $\pm 1.3\times10^{-6}$

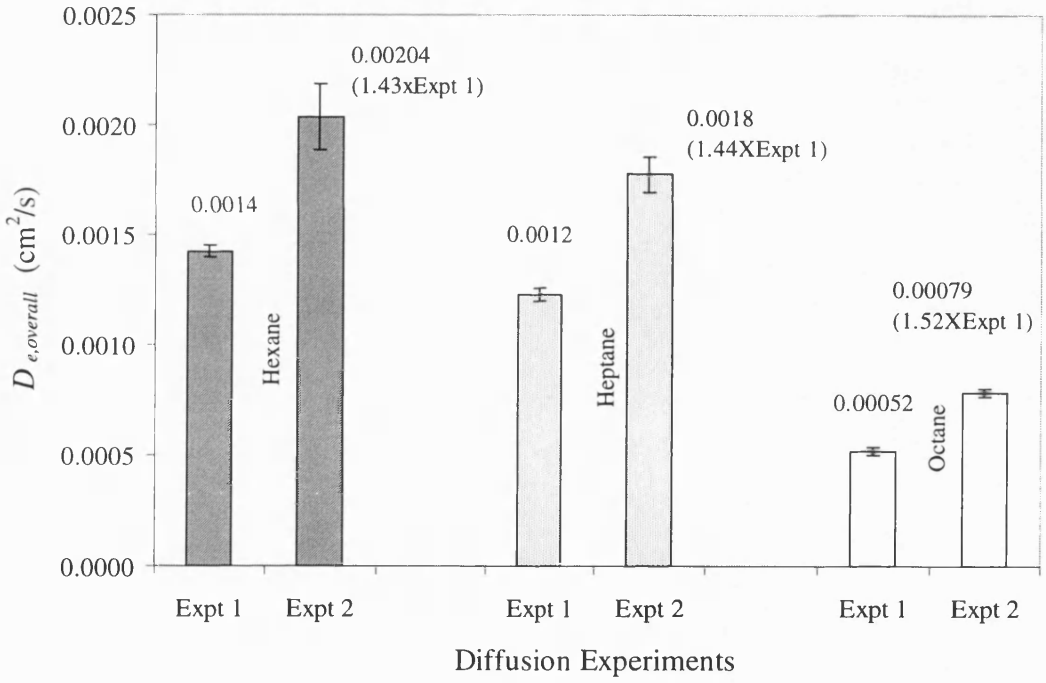

Figure 5.13. Experiments in a two layered structure – choice of layer to face the hydrocarbon and its effect on the overall effective diffusivity across the composite layer. (T=175°C, F_1= 12.9~13.2 cm^3/s, P=1.56 bar): Exp. 1: hydrocarbon facing washcoat, Exp. 2: nitrogen facing washcoat.

These differences are very intriguing. It is difficult to postulate the cause of the difference between the two experiments as many parameters are involved in the transport process in the composite layer, see Figure 5.14. Flux decline can be caused by several factors, such as concentration polarisation, adsorption, pore blocking and surface diffusion

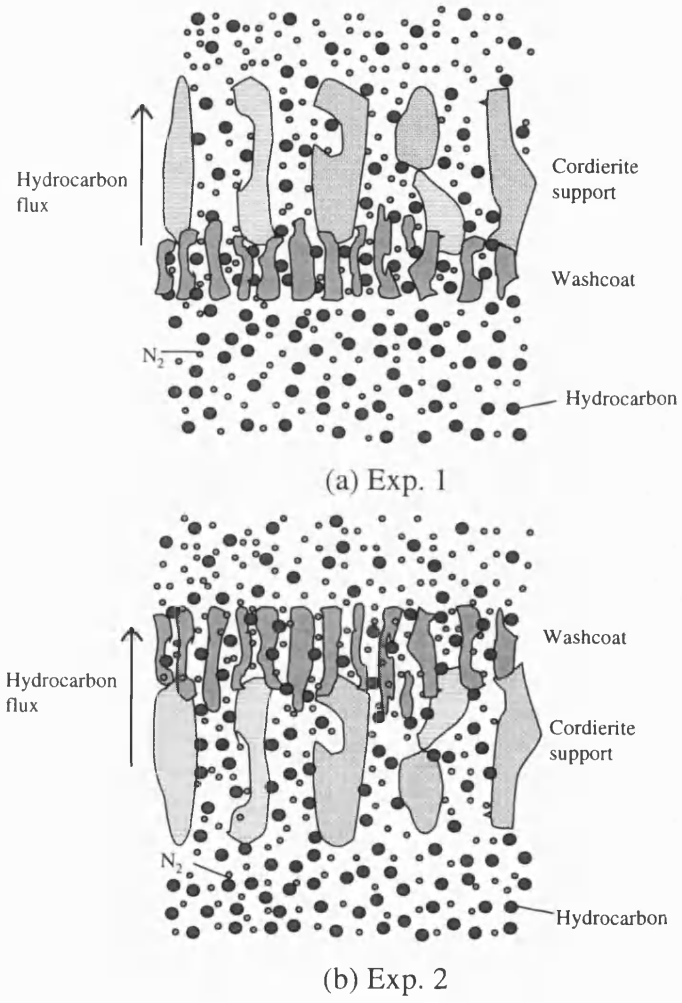

Figure 5.14. Hydrocarbon flux in the composite structure.

In order to explore if capillary condensation may be influencing the results, use was made of the Kelvin equation (Gregg and Sing, 1982). As described in Ruthven (1984), "in a porous adsorbent there is a continuous progress from multilayer adsorption to capillary condensation in which the smaller pores become completely filled with liquid sorbate. This occurs because the saturation vapour pressure in a small pore is reduced, in accordance with the Kelvin equation, by the effect of surface tension."

The Kelvin equation may be written as (Ruthven, 1984):

$$\frac{dV}{dA} = \frac{-V_L \sigma \cos\theta}{RT \ln(\frac{p}{p^\circ})} \tag{5.5}$$

where for the cylindrical pore

$$\frac{dV}{dA} = \frac{r_m}{2} \tag{5.6}$$

substituting Equation (5.6) into (5.5), then

$$\frac{r_m}{2} = \frac{-V_L \sigma \cos\theta}{RT \ln(\frac{p}{p^\circ})} \tag{5.7}$$

and after rearranging

$$\ln\frac{p}{p^\circ} = \frac{-2\sigma V_L}{RT}\frac{\cos\theta}{r_m} \tag{5.8}$$

Assuming that the surface is wetted, then θ=0 and $\cos\theta$=1 and substituting values into Equation (5.8), values of p/p° can be calculated. Table 5.9 presents the values of the relative pressure, p/p°, at different values of pore radius, r_m, for *n*-hexane, *n*-heptane and *n*-octane at T=20°C, T=125°C, T=175°C, and T=275°C. The pore radii are assigned values of the average pore radius of the alumina calcined at different temperatures. This data may be compared with calculated values of p/p°, over the range of experimental conditions studied, see Table 5.10. If $(p/p^\circ)_{\text{experiment}} > (p/p^\circ)_{\text{theoretical}}$, then there is a possibility that condensation could occur.

By comparing the data in Table 5.9 and Table 5.10, it is clear that for *n*-hexane and *n*-heptane that is unlikely to occur. However, for *n*-octane there is a possibility at $T \leq 125$°C. This may help to explain, why the tortuosity of *n*-octane was found to be higher in Figure 5.6.

Table 5.9. Theoretically calculated values of the relative pressure ($p/p°$) at which condensation will occur. For an alumina gel (LAB2) calcined at different temperatures.

r_m, nm (Calc. temp.,°C)	$p/p°$ at T=298K(25°C)			$p/p°$ at T=398K(125°C)*		
	n-Hexane	*n*-Heptane	*n*-Octane	*n*-Hexane	*n*-Heptane	*n*-Octane
1.83 (450)	0.313	0.230	0.155	0.425	0.339	0.253
2.15 (600)	0.372	0.287	0.204	0.483	0.399	0.310
2.6 (800)	0.442	0.357	0.270	0.549	0.468	0.381
3.75 (1000)	0.568	0.489	0.403	0.659	0.591	0.512
10.48 (1100)	0.817	0.774	0.722	0.862	0.828	0.787
18.93 (1200)	0.894	0.868	0.835	0.921	0.901	0.876
r_m, nm (Calc. temp.,°C)	$p/p°$ at T=448K(175°C)*			$p/p°$ at T=548K(275°C)*		
	n-Hexane	*n*-Heptane	*n*-Octane	*n*-Hexane	*n*-Heptane	*n*-Octane
1.83 (450)	0.468	0.383	0.295	0.537	0.456	0.368
2.15 (600)	0.524	0.442	0.354	0.589	0.513	0.428
2.6 (800)	0.587	0.510	0.424	0.647	0.576	0.496
3.75 (1000)	0.691	0.627	0.552	0.739	0.683	0.615
10.48 (1100)	0.876	0.846	0.808	0.897	0.872	0.840
18.93 (1200)	0.929	0.912	0.889	0.942	0.927	0.908

* The parameters, σ and V_L for T=298K were used.

Adsorptive	T, K	Surface tension (σ)**, mN/m	Molar volume (V_L)***, m^3/mol	$\sigma.V_L/T$, $N.m^2/(mol.K)$
n-Hexane	298	18.44	1.4×10^{-4}	8.82×10^{-9}
n-Heptane	298	20.14	1.62×10^{-4}	1.11×10^{-8}
n-Octane	298	23.38	1.78×10^{-4}	1.42×10^{-8}

** Calculated by Macleod-Sugden correlation (Reid *et al.*, 1987).
*** Calculated from $V_L=0.285V_c^{1.048}$ from Tyn & Calus method (Reid *et al*, 1987).

Table 5.10. Values of relative pressure ($p/p°$), calculated at experimental conditions.

Temp., K(°C)	Partial pressure (p)*, bar	Saturation pressure ($p°$)**, bar			Relative pressure ($p/p°$)		
		n-Hexane	*n*-Heptane	*n*-Octane	*n*-Hexane	*n*-Heptane	*n*-Octane
298(25)	0.6	0.200	0.0603	0.0184	2.997	9.954	32.543
398(125)	0.6	4.446	2.073	0.992	0.135	0.289	0.605
448(175)	0.6	11.85	6.201	3.341	0.0506	0.0968	0.18
548(275)	0.6	-	-	18.623	-	-	0.0322

* Total pressure is 1.5 bar and the mole fraction of hydrocarbons is 0.4.
** Calculated by using the Antoine equation (Reid *et al.*, 1987)

The effect of temperature was also studied. Figure 5.15 shows the results for an *n*-octane-nitrogen system. It can be seen that the flux of *n*-octane increases with an increase in temperature and hence the calculated value of $D_{e,overall}$ increases with temperature. The temperature dependence is consistent with a Knudsen diffusion mechanism which is $T^{0.5}$.

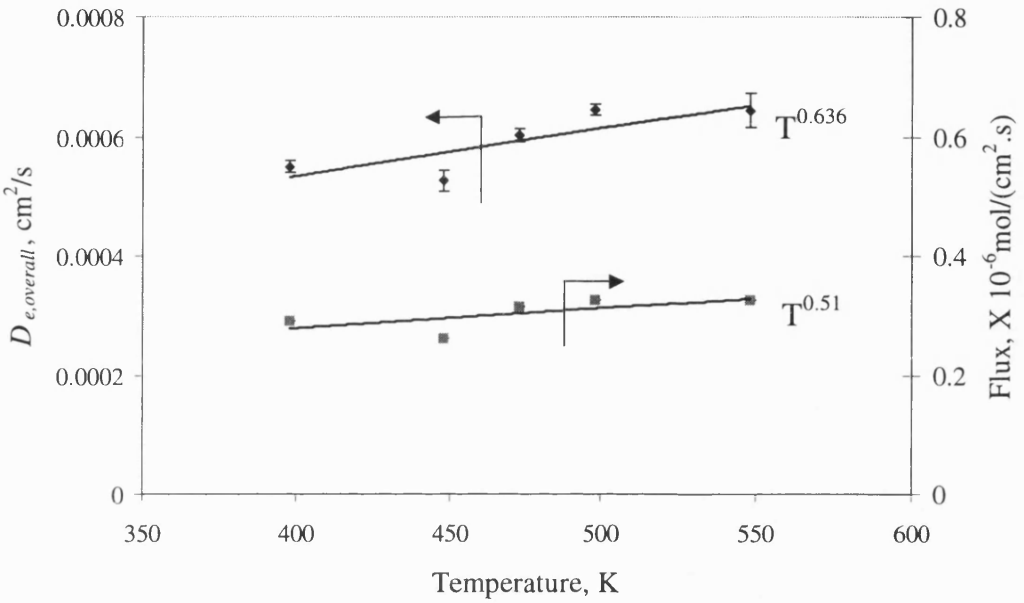

Figure 5.15. Diffusion experiment for *n*-octane-N_2 on one side of a coated cordierite (F_1= 12.8~13.2 cm^3/s, P=1.59~1.55 bar). The experiment was performed at conditions that relate to Exp. 1.

Table 5.11. Summary of experimental data in diffusion for *n*-otane-N_2. The cordierite is coated only one side with alumina gel (LAB2) and calcined at 600°C (l_1= 1.5 μm, l_2= 0.25 cm, d_w=4.3 nm and d_c=0.54 μm).

	T= 125°C	T= 175°C	T= 200°C	T= 225°C	T= 275°C
Pressure, bar	1.49	1.51	1.525	1.53	1.55
Flowrate (F_1), cm^3/s	13.2	13.1	13.0	12.8	12.8
Concentration in upper chamber, mol/cm^3	0.00084 $\pm 1.2\times10^{-5}$	0.00076 $\pm 1.9\times10^{-5}$	0.00093 $\pm 5.8\times10^{-6}$	0.000974 $\pm 7.6\times10^{-6}$	0.00097 $\pm 1.2\times10^{-5}$
Concentration in bottom chamber, mol/cm^3	2.154 ±0.00996	2.07 ±0.0166	2.13 ±0.0194	2.05 ±0.0144	2.06 ±0.063
Flux, $mol/(cm^2.s)$	2.9×10^{-7} $\pm 4.2\times10^{-9}$	2.6×10^{-7} $\pm 6.6\times10^{-9}$	3.2×10^{-7} $\pm 2.7\times10^{-9}$	3.25×10^{-7} $\pm 2.6\times10^{-9}$	3.3×10^{-7} $\pm 4.1\times10^{-9}$
$D_{e,overall}$, cm^2/s	0.000549 $\pm 1.0\times10^{-5}$	0.00053 $\pm 1.8\times10^{-5}$	0.0006 $\pm 1.1\times10^{-5}$	0.000645 $\pm 9.5\times10^{-5}$	0.00064 $\pm 2.9\times10^{-5}$
$D_{e,washcoat}$, cm^2/s	6.2×10^{-6} $\pm 5.1\times10^{-7}$	6.9×10^{-6} $\pm 3.7\times10^{-7}$	8×10^{-6} $\pm 4.6\times10^{-7}$	8.9×10^{-6} $\pm 1.0\times10^{-6}$	8.9×10^{-6} $\pm 2.8\times10^{-7}$

5.2.4. Effect of calcination temperature on the overall effective diffusivity

In Figure 4.20(b), pore size distribution was shown to be a function of calcination temperature. Figure 5.16 shows the effect of calcination temperature on the value of the overall effective diffusivity of *n*-hexane, *n*-heptane and *n*-octane. Four different specimens were prepared by washcoating alumina gel and calcining at 450°C, 600°C, 800°C, and 1000°C. To get the same thickness of washcoat, the coating conditions, and in particular the number of coatings was kept constant.

It can be seen that below a calcination temperature of 800°C, the overall effective diffusivities are almost constant. It is well known that a phase change occurs at about 900°C. This will result in a decrease in surface area, pore volume and tortuosity, but an increase in average pore size, see Table 4.1 (from Chapter 4).

Table 4. 1. Physical properties of alumina gel (LAB2).

Calcination temperature, °C	Apparent density, g/cm^3	Pore volume, cm^3/g	Porosity*	Average pore diameter, nm	BET surface area, m^2/g
450	3.93	0.360	0.591	3.65	285.3
600	3.91	0.372	0.599	4.3	235.1
800	4.24	0.353	0.586	5.2	176.1
1000	4.27	0.229	0.480	7.5	90.5
1100	3.89	0.056	0.184	20.95	9.3
1200	3.84	0.018	0.067	37.86	5.3

The results of these experiments are compared with theoretically calculated values based in the Wakao-Smith model and Knudsen diffusivity model applied to the micropores. As the washcoat penetrates and fills the pores of the support, the structure was modelled as a pseudo-homogeneous plate. The model was selected as the structure has two distinctive pores, macropores (from cordierite support) and micropores (from alumina washcoat). Physical properties are listed in Table 5.12.

Table 5.12. Parameters needed for prediction of D_e by models (Alumina washcoat loading: 0.00132 g/cm^2, Cross sectional area: 0.45 cm^2).

Calcination temperature, °C	Porosity			Pore diameter, μm	
	total	macro	micro	Macro	micro
450	0.237	0.218	0.019	0.54	0.00365
600	0.238	0.218	0.0196	0.54	0.00429
800	0.237	0.218	0.0186	0.54	0.0052
1000	0.230	0.218	0.0121	0.54	0.0075

An increase in pore size should increase the value of $D_{e,overall}$, but a decrease in pore volume, should act to decrease the value of $D_{e,overall}$. A decrease in tortuosity should increase the value of $D_{e,overall}$. From Figure 5.17, as expected the value of D_{KAi}, (micropore Knudsen diffusivity) increases with an increase in pore size, but its increase is not as dramatic as the experimental value of $D_{e,overall}$. Moreover, it can be seen that the predicted value of $D_e(W\text{-}S)$ does not increase with an increase in calcination temperature. Therefore, it is reasonable to assume that the increase of $D_{e,overall}$ is as a result of a decrease in tortuosity.

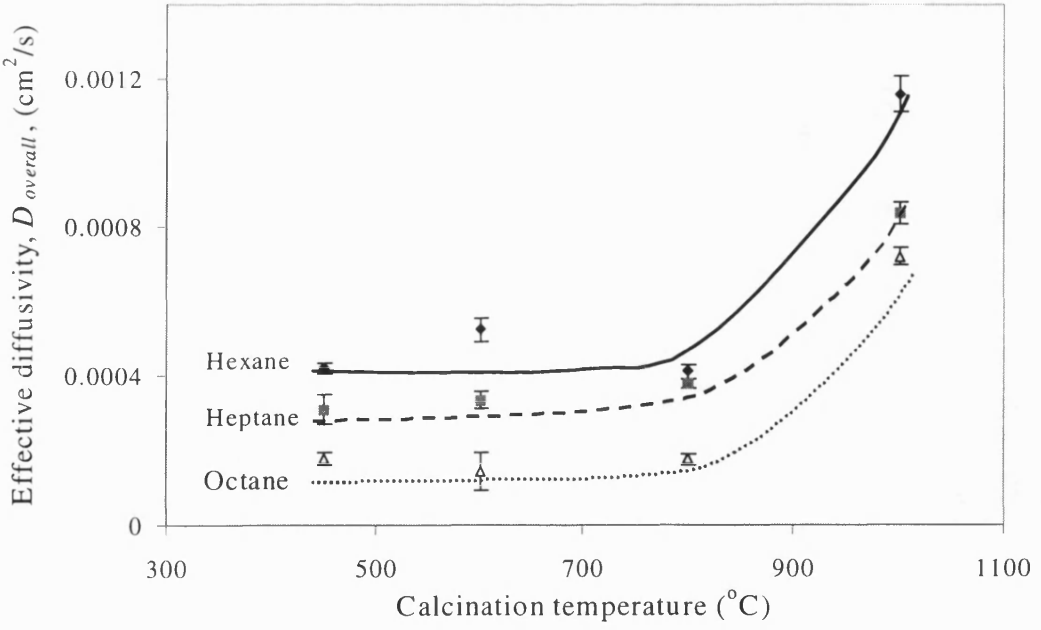

Figure 5.16. Effect of calcination temperature of the alumina washcoat on the overall effective diffusivity (T=175 °C, P=1.4~1.5 bar).

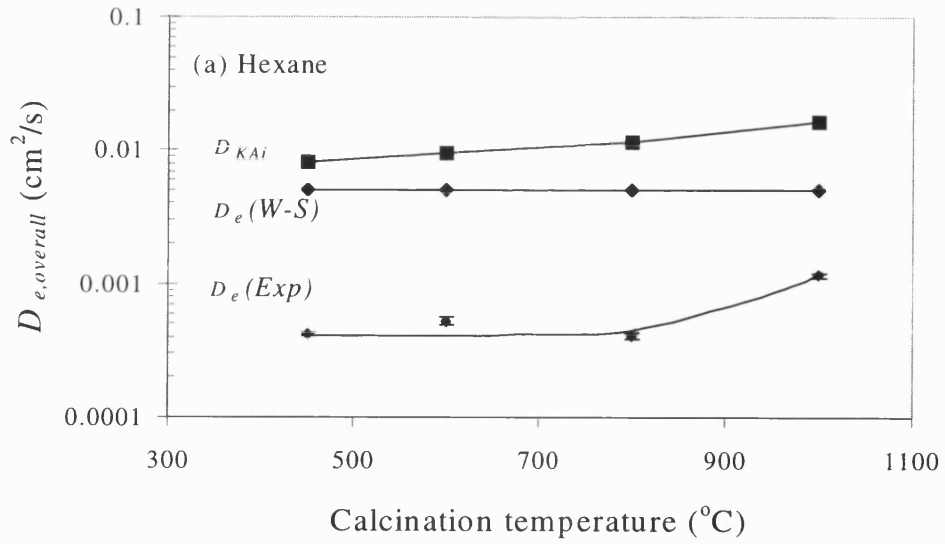

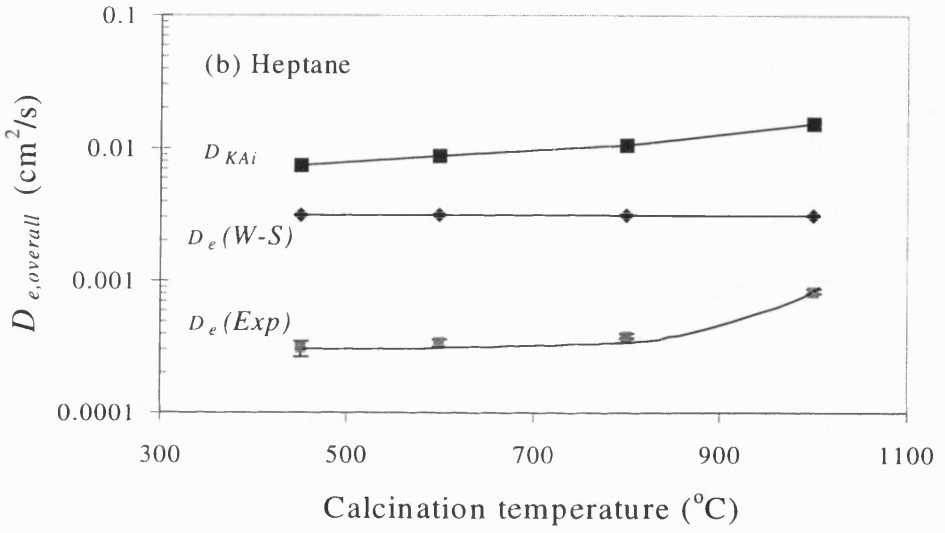

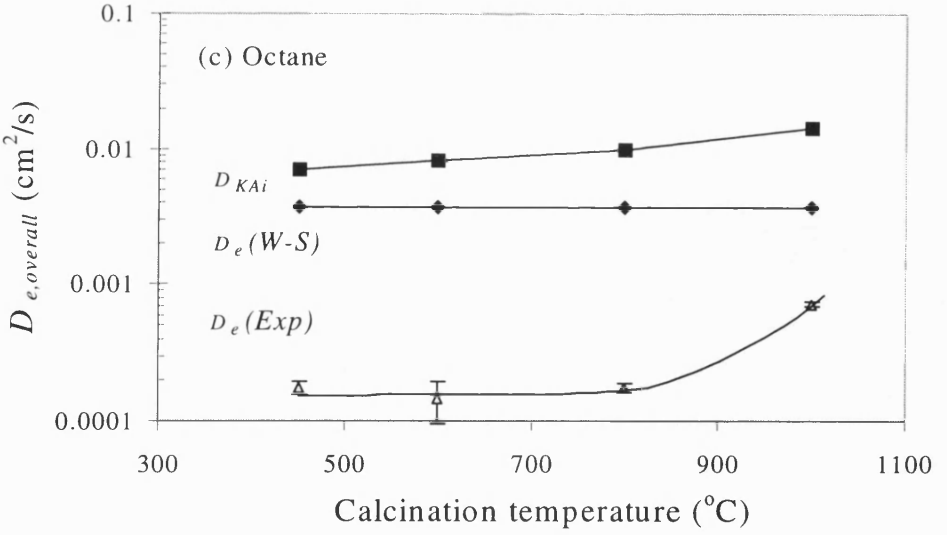

Figure 5.17. Effect of calcination temperature on the overall effective diffusivity.

5.2.5. Multicomponent diffusion

Returning to the application area of interest in this thesis, as gasoline is a complex mixture of various hydrocarbons, multicomponent diffusion will occur. In this final section of the thesis, the interaction between the hydrocarbons in two, three and four component mixtures was studied. Both sides of the cordierite plate were coated with the washcoat to a thickness of about 2 μm. The experiments were classified into five types and are listed in Table 5.13. The multicomponent experiment was carried out using the same apparatus as for the binary diffusion experiment, but for the analysis of the concentration of each component, a gas chromatography column was employed. The operating conditions are summarised in Table 5.14.

Table 5.13. Types of experiments.

Type	Feed to upper chamber	Feed to lower chamber		
		Components	Mole fraction of total hydrocarbon	Composition of hydrocarbon
A	N_2	*n*-Hexane+N_2, *n*-Heptane+N_2, *n*-Octane+N_2	0.4	
B	N_2	*n*-Hexane+*n*-Heptane+N_2	0.4	1:1
C	N_2	*n*-Hexane+*n*-Octane+N_2	0.4	1:1
D	N_2	*n*-Heptane+*n*-Octane+N_2	0.4	1:1
E	N_2	*n*-Hexane+*n*-Heptane+*n*-Octane+N_2	0.4	1:1:1

Table 5.14. Summary of experimental conditions for multicomponent diffusion.

- Operating temperature = 125, 175, and 225°C,
- Operating pressure = 1.5~ 1.58 bar
- Pressure differential = ±1 mbar
- Flowrate(F_1) = 12.9 ~ 13.1 cm^3/s
- Specimen : coated cordierite substrate (Cross sectional area : 46.5 mm^2)
- Washcoat: Alumina gel (LAB2) calcined at 600°C
  - Thickness: 2 μm each side
  - Average pore diameter: 4.3 nm
- Analysis : Gas chromatography
  - Detector: FID
  - GC column (1.8m long): packed with 10% CP-Sil5/Chromosorb WHP
  - Oven temp.: 75°C
  - Detector temp.: 200°C

The overall effective diffusivity across the washcoated plate was calculated from:

$$D_{e,overall_i} = -\frac{J_i}{\frac{\Delta C_i}{\Delta x}} \tag{5.9}$$

The flux, J_i, and concentration difference, ΔC_i, were easily determined for each of the components. The thickness Δx was the overall thickness of the coated plate.

The results of these experiments at T=125°C, T=175°C and T=225°C are presented in Table 5.15 and Table 5.16. In addition, to facilitate the identification of any trends, the results are also presented in Figure 5.18, Figure 5.19, and Figure 5.20.

From this data, it would appear that the presence of the additional hydrocarbon components is not having a major effect on the overall effective diffusivity of the species. To see more clearly any temperature dependence, the results are also presented in Figure 5.21. What is useful to note from this data, is that within experimental errors, values of $D_{e,overall}$ are not significantly affected by the presence of other hydrocarbon species.

In order to obtain a good match between theoretically calculated values and experimental data, the inclusion of an appropriate value of the tortuosity factor remains the dominant factor. For Type E experiment, it appears from the results that $D_{e,overall}$ has a stronger dependence on temperature. The presence of *n*-hexane (C_6H_{14}) may be a contributing factor, although the mechanism is unclear.

Table 5.15. Multicomponent diffusion experiments with different combinations of diffusing species (P=1.577 bar, F_1=13.0 cm^3/s). Washcoat is alumina gel (LAB2) calcined at 600°C.

Type of experiment	$D_{e,overall}$ (cm^2/s) at T=125°C			$D_{e,overall}$ (cm^2/s) at T=175°C			$D_{e,overall}$ (cm^2/s) at T=225°C		
	n-Hexane	*n*-Heptane	*n*-Octane	*n*-Hexane	*n*-Heptane	*n*-Octane	*n*-Hexane	*n*-Heptane	*n*-Octane
Case A (binary diffusion)	0.000799 ($\pm 1.7\times10^{-5}$)	0.000571 ($\pm 3.1\times10^{-5}$)	0.00045 ($\pm 1.2\times10^{-5}$)	0.000779 ($\pm 1.9\times10^{-5}$)	0.000592 ($\pm 1.4\times10^{-5}$)	0.0004 ($\pm 2.3\times10^{-5}$)	0.000998 ($\pm 3.4\times10^{-5}$)	0.000660 ($\pm 2.1\times10^{-5}$)	0.00051 ($\pm 4.6\times10^{-5}$)
Case B (ternary diffusion)	0.00093 ($\pm 2.2\times10^{-5}$)	0.000608 ($\pm 2.8\times10^{-5}$)	-	0.0009 ($\pm 1.8\times10^{-5}$)	0.000651 ($\pm 4.7\times10^{-5}$)	-	0.00098 ($\pm 1.6\times10^{-5}$)	0.000700 ($\pm 2.4\times10^{-5}$)	-
Case C (ternary diffusion)	0.00079 ($\pm 2.9\times10^{-5}$)	-	0.000419 ($\pm 1.0\times10^{-5}$	0.00072 ($\pm 2.7\times10^{-5}$)	-	0.000386 ($\pm 2.1\times10^{-5}$)	0.00096 ($\pm 1.9\times10^{-5}$)	-	0.000411 ($\pm 2.0\times10^{-5}$)
Case D (ternary diffusion)	-	0.000672 ($\pm 2.4\times10^{-5}$)	0.000414 ($\pm 3.3\times10^{-5}$)	-	0.000606 ($\pm 3.3\times10^{-5}$)	0.000374 ($\pm 2.2\times10^{-5}$)	-	0.000676 ($\pm 1.9\times10^{-5}$)	0.000411 ($\pm 9.4\times10^{-6}$)
Case E (quaternary diffusion)	0.00079 ($\pm 2.5\times10^{-5}$)	0.000579 ($\pm 3.2\times10^{-5}$)	0.000357 ($\pm 1.5\times10^{-5}$)	0.00079 ($\pm 6.2\times10^{-5}$)	0.000668 ($\pm 5.6\times10^{-5}$)	0.00037 ($\pm 2.7\times10^{-5}$)	0.00108 ($\pm 6.0\times10^{-5}$)	0.000863 ($\pm 4.1\times10^{-5}$)	0.000461 ($\pm 1.8\times10^{-5}$)

Standard errors are shown in the parenthesis.

Table 5.16. Summary of experimental data for multicomponent diffusion.

Type of experiment	P, bar	F_1, cm^3/s	Concentration, mol/cm^3		Flux, $mol/(cm^2.s)$
			in upper chamber	in lower chamber	
T= 125 °C					
Case A (binary diffusion)	1.5 ~ 1.53	12.98 ~ 13.14	Hexane: 0.00108 ($\pm 1.5\times10^{-5}$) Heptane: 0.00085 ($\pm 3.3\times10^{-5}$) Octane: 0.000846 ($\pm 2.0\times10^{-5}$)	Hexane: 0.944 (±0.0072) Heptane: 1.04 (±0.015) Octane: 1.3 (±0.0041)	Hexane: 2.3×10^{-7} ($\pm 3.2\times10^{-9}$) Heptane: 1.63×10^{-7} ($\pm 6.3\times10^{-9}$) Octane: 1.46×10^{-7} ($\pm 3.5\times10^{-9}$)
Case B (ternary diffusion)	1.51	13.1	Hexane: 0.00052 ($\pm 9.9\times10^{-6}$) Heptane: 0.00043 ($\pm 1.4\times10^{-5}$)	Hexane: 0.384 (±0.0016) Heptane: 0.495(±0.0055)	Hexane: 9.8×10^{-8} ($\pm 3.6\times10^{-9}$) Heptane: 8.18×10^{-8} ($\pm 2.8\times10^{-9}$)
Case C (ternary diffusion)	1.51	13.13	Hexane: 0.00062 ($\pm 1.3\times10^{-5}$) Octane: 0.00021 ($\pm 2\times10^{-6}$)	Hexane: 0.557(±0.00835) Octane: 0.362 (±0.00537)	Hexane: 1.2×10^{-7} ($\pm 2.5\times10^{-9}$) Octane: 3.7×10^{-8} ($\pm 3.5\times10^{-10}$)
Case D (ternary diffusion)	1.51	13.07	Heptane: 0.00029 ($\pm 3.7\times10^{-6}$) Octane 0.00038 ($\pm 6.2\times10^{-6}$)	Heptane: 0.302 (±0.0069) Octane: 0.642 (±0.03734)	Heptane: 5.6×10^{-8} ($\pm 7.2\times10^{-10}$) Octane: 6.53×10^{-8} ($\pm 1.1\times10^{-9}$)
Case E (quaternary diffusion)	1.5	13.05	Hexane: 0.00041 ($\pm 8.1\times10^{-6}$) Heptane: 0.00066 ($\pm 2.7\times10^{-6}$) Octane: 0.000303 ($\pm 7.8\times10^{-6}$)	Hexane: 0.363 (±0.004) Heptane: 0.80 (±0.0139) Octane: 0.89 (±0.0155)	Hexane: 7.9×10^{-8} ($\pm 1.5\times10^{-9}$) Heptane: 1.27×10^{-8} ($\pm 4.9\times10^{-9}$) Octane: 7.82×10^{-8} ($\pm 1.9\times10^{-9}$)

Standard errors are shown in the parenthesis.

Table 5.16. Summary of experimental data for multicomponent diffusion (continue……).

Type of experiment	P, bar	F_1, cm^3/s	Concentration, mol/cm^3		Flux, $mol/(cm^2.s)$
			in upper chamber	in lower chamber	
T= 175 °C					
Case A (binary diffusion)	1.49 ~ 1.5	12.80 ~ 12.89	Hexane: 0.00193 ($\pm 2.6\times10^{-5}$) Heptane: 0.00162 ($\pm 2.7\times10^{-5}$) Octane: 0.00158 ($\pm 5.4\times10^{-5}$)	Hexane: 1.71 (±0.0184) Heptane: 1.88 (±0.012) Octane: 2.7 (±0.059)	Hexane: 4.09×10^{-7} ($\pm 5.5\times10^{-9}$) Heptane: 3.03×10^{-7} ($\pm 5.34\times10^{-9}$) Octane: 2.68×10^{-7} ($\pm 9.2\times10^{-9}$)
Case B (ternary diffusion)	1.50	12.9	Hexane: 0.00137 ($\pm 2.7\times10^{-5}$) Heptane 0.0012 ($\pm 5.6\times10^{-5}$)	Hexane: 1.078 (±0.0089) Heptane: 1.29 (±0.0322)	Hexane: 2.64×10^{-7} ($\pm 3.0\times10^{-9}$) Heptane: 2.28×10^{-7} ($\pm 1.0\times10^{-8}$)
Case C (ternary diffusion)	1.50	13.07	Hexane: 0.00142 ($\pm 4.33\times10^{-5}$) Octane: 0.000491 ($\pm 2\times10^{-5}$)	Hexane: 1.38 (±0.00865) Octane: 0.894 (±0.0109)	Hexane: 2.71×10^{-7} ($\pm 8.3\times10^{-9}$) Octane: 8.5×10^{-8} ($\pm 3.5\times10^{-9}$)
Case D (ternary diffusion)	1.51	13.05	Heptane: 0.00104 ($\pm 4.7\times10^{-5}$) Octane: 0.0006 ($\pm 3.3\times10^{-5}$)	Heptane: 1.205 (±0.012) Octane: 1.09 (±0.021)	Heptane: 1.99×10^{-7} ($\pm 9\times10^{-9}$) Octane: 1.0×10^{-7} ($\pm 3.8\times10^{-9}$)
Case E (quaternary diffusion)	1.5	12.98	Hexane: 0.00108 ($\pm 5.8\times10^{-5}$) Heptane: 0.000601($\pm 3.9\times10^{-5}$) Octane: 0.000314 ($\pm 1.9\times10^{-5}$)	Hexane: 0.953 (±0.0216) Heptane: 0.625 (±0.0108) Octane: 0.594 (±0.00483)	Hexane: 2.06×10^{-7} ($\pm 1.1\times10^{-8}$) Heptane: 1.15×10^{-7} ($\pm 7.4\times10^{-9}$) Octane: 5.4×10^{-8} ($\pm 3.4\times10^{-9}$)

Standard errors are shown in the parenthesis.

Table 5.16. Summary of experimental data for multicomponent diffusion (continue……).

Type of experiment	P, bar	F_1, cm^3/s	Concentration, mol/cm^3		Flux, $mol/(cm^2.s)$
			in upper chamber	in lower chamber	
T= 225 °C					
Case A (binary diffusion)	1.5 ~ 1.52	12.82 ~ 12.98	Hexane: 0.0019 ($\pm 3.7\times10^{-5}$) Heptane: 0.00169 ($\pm 3.6\times10^{-5}$) Octane: 0.00142 ($\pm 1.2\times10^{-4}$)	Hexane: 1.37 (±0.021) Heptane: 1.76 (±0.0172) Octane: 2.88 (±0.038)	Hexane: 4.03×10^{-7} ($\pm 8.5\times10^{-9}$) Heptane: 3.18×10^{-7} ($\pm 6.8\times10^{-9}$) Octane: 3.61×10^{-7} ($\pm 2.75\times10^{-9}$)
Case B (ternary diffusion)	1.58	13.02	Hexane: 0.00224 ($\pm 2.5\times10^{-5}$) Heptane 0.00126 ($\pm 2.8\times10^{-6}$)	Hexane: 1.608 (±0.0127) Heptane: 1.26 (±0.0142)	Hexane: 4.3×10^{-7} ($\pm 4.2\times10^{-9}$) Heptane: 2.4×10^{-7} ($\pm 5.3\times10^{-9}$)
Case C (ternary diffusion)	1.57	13.03	Hexane: 0.0024 ($\pm 4.54\times10^{-5}$) Octane: 0.000534 ($\pm 1.2\times10^{-5}$)	Hexane: 1.75 (±0.013) Octane: 0.911 (±0.0221)	Hexane: 4.6×10^{-7} ($\pm 8.6\times10^{-9}$) Octane: 9.2×10^{-8} ($\pm 2.1\times10^{-9}$)
Case D (ternary diffusion)	1.51	13.09	Heptane: 0.00132 ($\pm 2.1\times10^{-5}$) Octane: 0.00086 ($\pm 2.3\times10^{-5}$)	Heptane: 1.37 (±0.0175) Octane: 1.84 (±0.051)	Heptane: 2.54×10^{-7} ($\pm 4.0\times10^{-9}$) Octane: 1.60×10^{-7} ($\pm 3.6\times10^{-9}$)
Case E (quaternary diffusion)	1.56	12.86	Hexane: 0.00202 ($\pm 6.3\times10^{-5}$) Heptane: 0.00149($\pm 5.2\times10^{-5}$) Octane: 0.000726 ($\pm 3.7\times10^{-5}$)	Hexane: 1.25 (±0.0082) Heptane: 1.156 (±0.0134) Octane: 0.911(±0.0093)	Hexane: 3.67×10^{-7} ($\pm 1.0\times10^{-8}$) Heptane: 2.7×10^{-7} ($\pm 9.8\times10^{-9}$) Octane: 1.2×10^{-7} ($\pm 3.4\times10^{-9}$)

Standard errors are shown in the parenthesis.

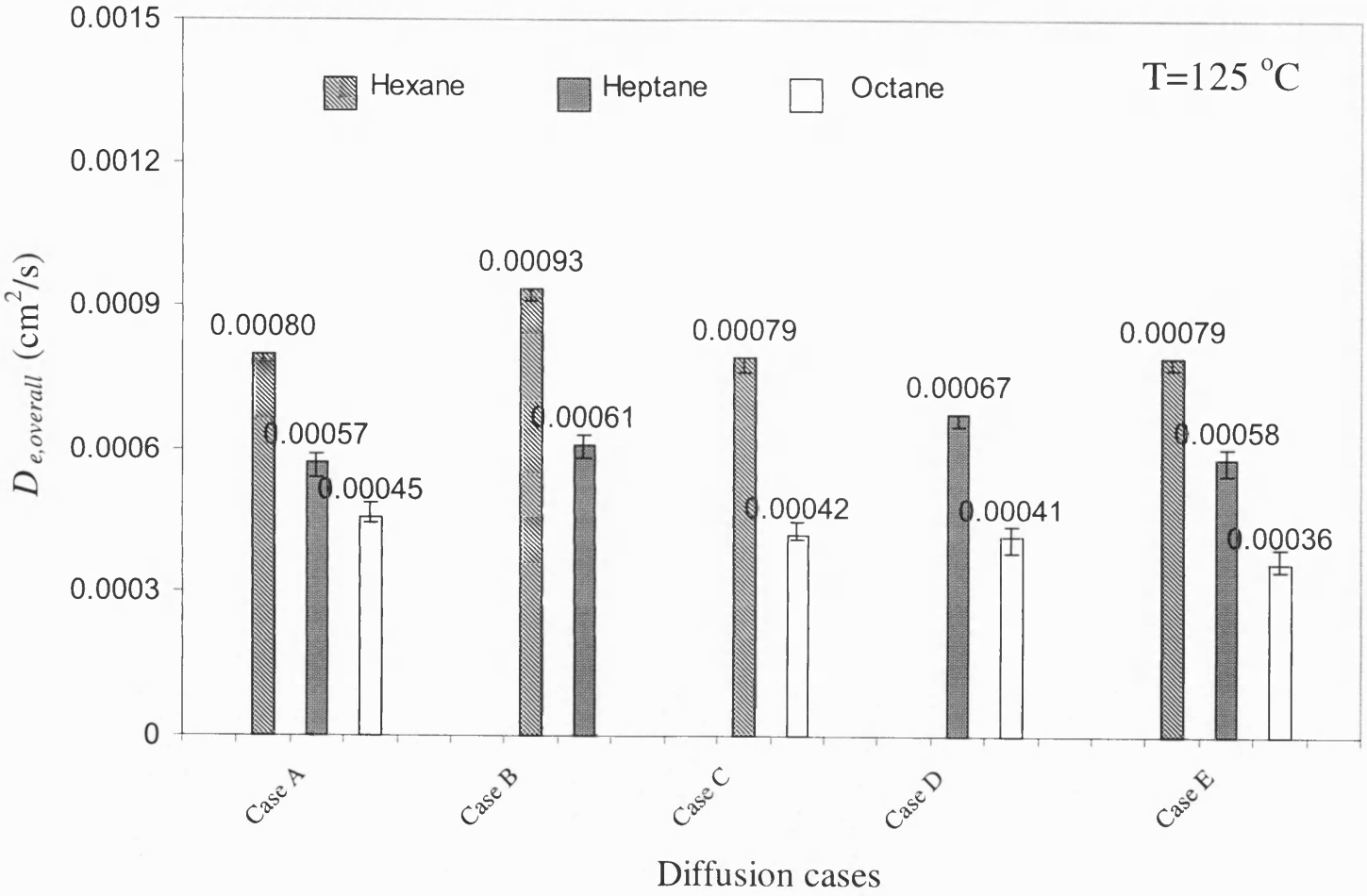

Figure 5.18. Comparisons between binary diffusion experiments and multicomponent diffusion experiments with different combinations of diffusing species (T=125°C, P≈1.51 bar, F_I≈13 cm^3/s).

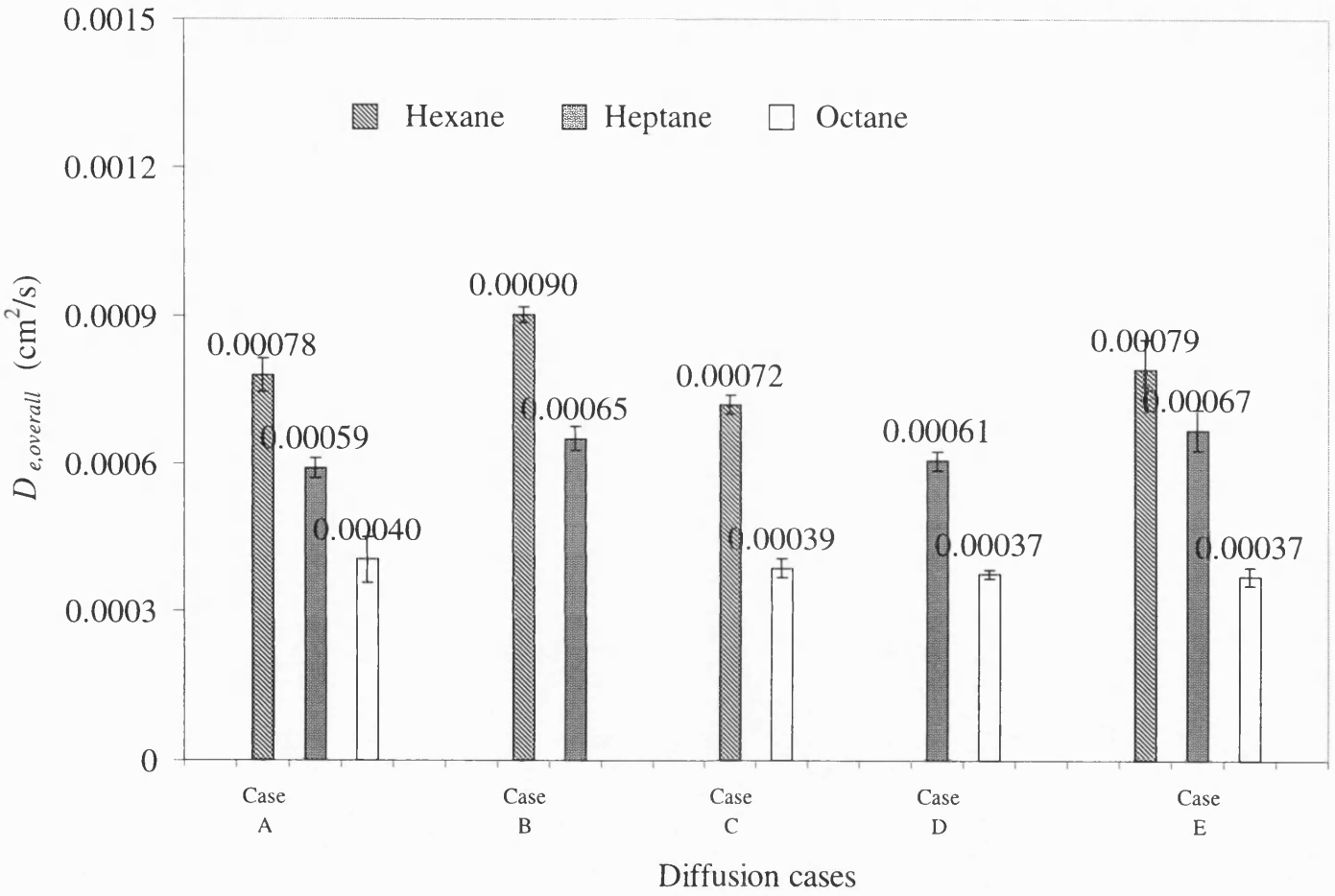

Figure 5.19. Comparisons between binary diffusion experiments and multicomponent diffusion experiments with different combinations of diffusing species (T=175°C, P≈1.5 bar, F_l≈13 cm^3/s).

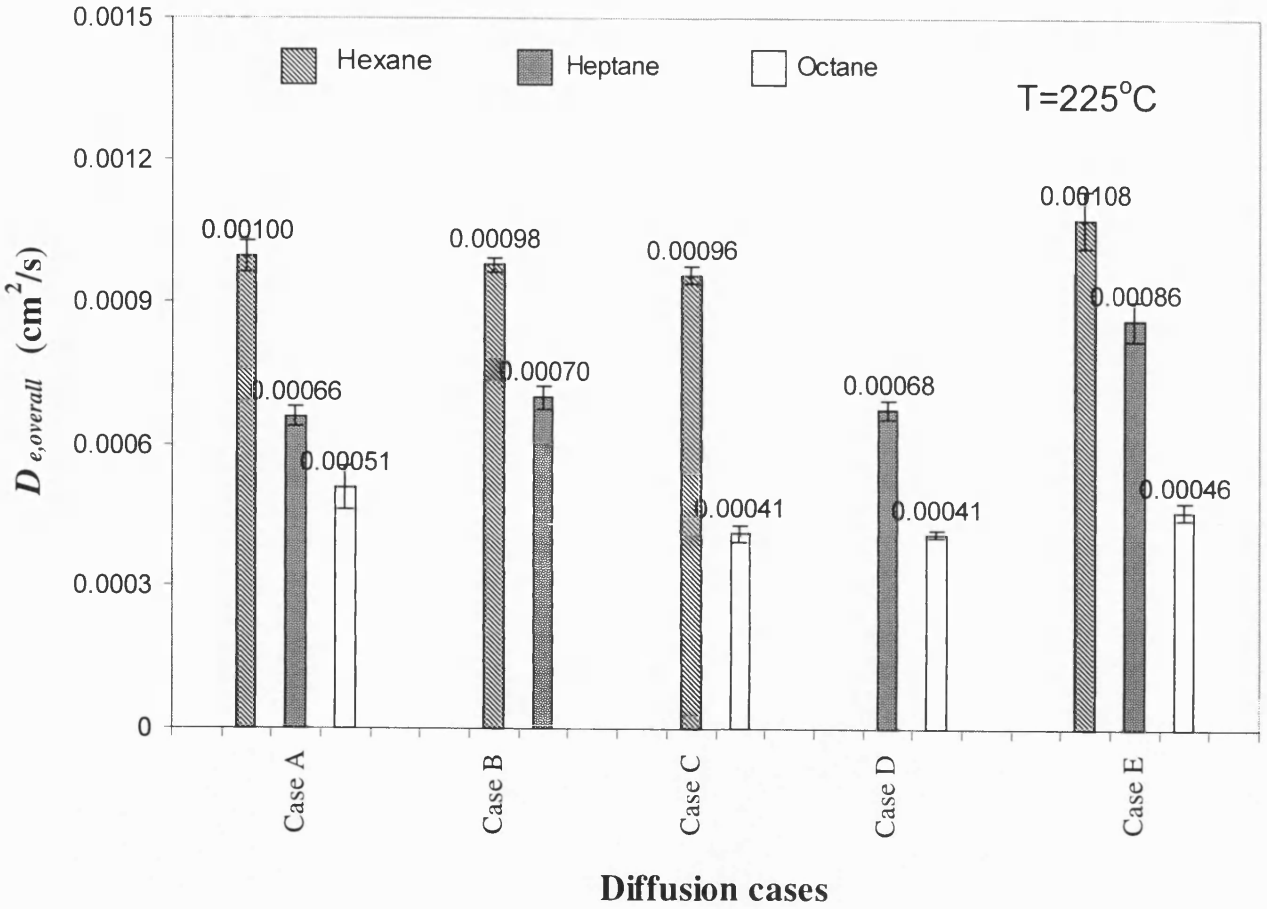

Figure 5.20. Comparisons between binary diffusion experiments and multicomponent diffusion experiments with different combinations of diffusing species (T=225°C, P≈1.55 bar, F_1≈13 cm^3/s).

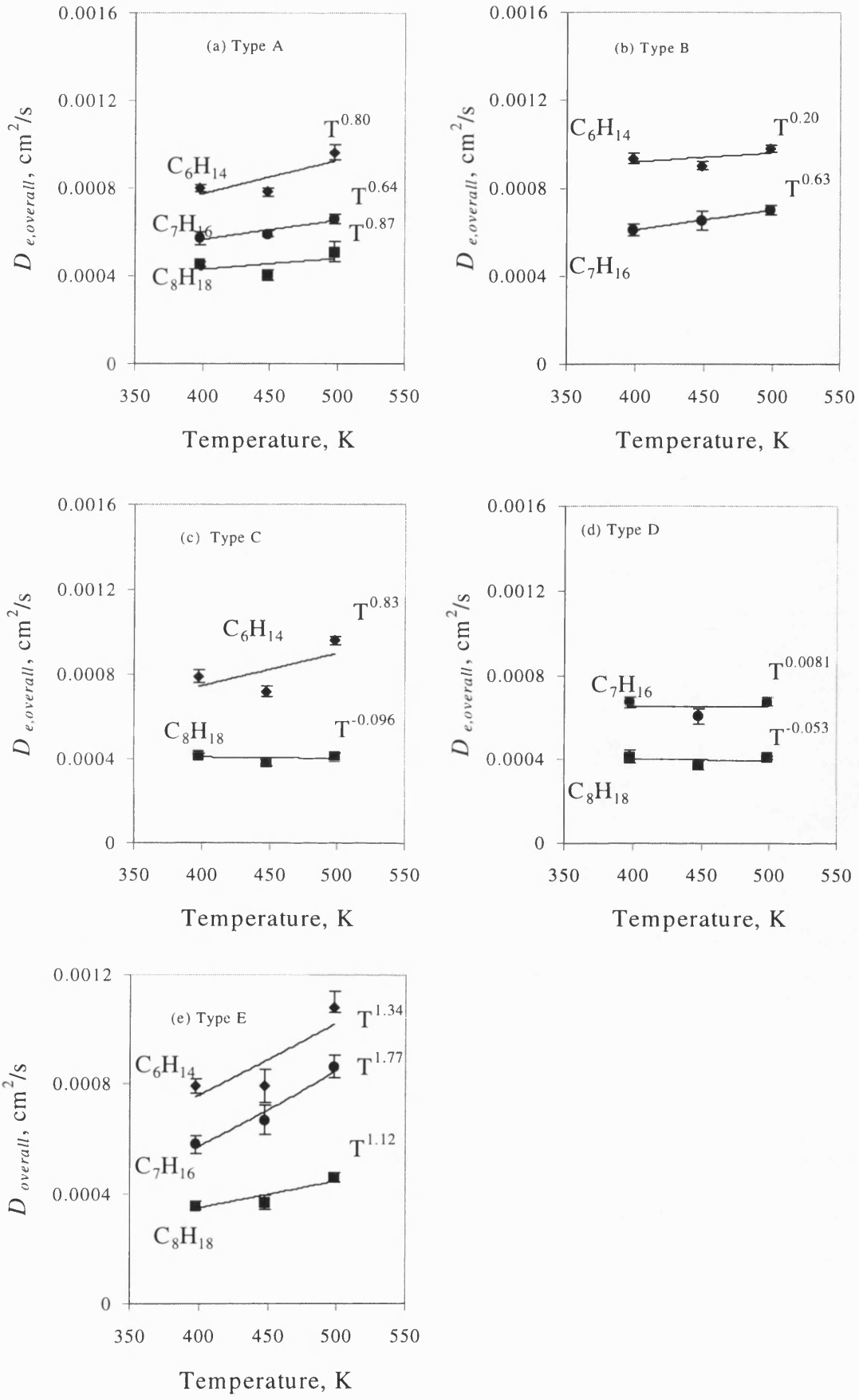

Figure 5.21. Temperature dependence of effective diffusivity in multicomponent diffusion.

5.3. Conclusions

5.3.1. Diffusion in the cordierite support

- For the uncoated cordierite, the binary effective diffusivities of the four components for T= 125°C ~ 275°C were shown to be represented by:
  - *n*-Pentane: $D_e = 8.6\times10^{-7} T^{1.38}$
  - *n*-Hexane: $D_e = 1.6\times10^{-6} T^{1.24}$
  - *n*-Heptane: $D_e = 7.1\times10^{-7} T^{1.33}$
  - *n*-Octane: $D_e = 2.6\times10^{-10} T^{1.41}$

- When the experimental results were compared with the use of the parallel pore model, it was found that the predicted D_e values are greater than the experimental values by a factor of 3 - 4, except in the case of octane which deviates by a factor of 8. When the experimental results were compared with the random pore model, it was found that the predicted effective diffusivities for *n*-pentane, *n*-hexane and *n*-heptane are greater than the experimental values by a factor of about 2 to 3, while D_e values for octane deviate by a factor of 5. Neither of these models provides a good match with experimental data. This confirms earlier findings by Hayes *et al.* (2000), that values of D_e calculated using the random pore model were found to be 3.1 times larger than the experimental values.
- When calculated average values of tortuosity, τ, were plotted as function of molar mass, τ was seen to increase with molar mass. As the tortuosity should be constant for the material, this indicates the either the presence of the heavier species is increasing tortuosity (perhaps connecting micropores becomes blocked) or other factors (*e.g.* adsorption) are influencing the results.

5.3.2. Diffusion in the alumina washcoat

- For the washcoated cordierite plate, by treating the diffusion in the washcoat and plate as a combined resistance in series, it was possible to calculate the value of D_e in the washcoat.

- It was found that over the range of conditions tested, the experimentally measured value of D_e is independent of the concentration of the species.

- From experiments with *n*-hexane, *n*-heptane and *n*-octane, it was shown that D_e decreases with an increase in the weight and hence thickness of washcoat loadings. Above a washcoat loading of 0.0012 g/cm^2 (corresponded to 1.5 μm), the decrease was linear with loading. This indicates that care must be taken with the prediction of values of D_e in very thin layers of catalyst (< 2 μm). Also, that the resistance in the interfacial layer can be significant at low washcoat thickness.

- It was shown that if one side of a cordierite plate is coated (forming a binary composite layer), then the value of D_e varies depending on whether the hydrocarbon stream is on the washcoated or on uncoated side of the support. If the hydrocarbons are on the washcoat side, then there is a 40% reduction in flux hence the value of D_e.

- From experiments with *n*-hexane, *n*-heptane and *n*-octane, above a calcination temperature of 800°C, hydrocarbon flux and hence value of D_e increased with calcination temperature. It is postulated that the combined effect of an increase in mean pore size and reduction in tortuosity increases the flux across the plate. Changes in tortuosity are likely to be the dominant factor.

- Multicomponent diffusion experiments show that the D_e values of each diffusing species in multicomponent diffusion system are close to the values obtained from binary diffusion. It can be postulated that a diffusing species does not have a significant effect on the transport of the other species across the washcoat. By assigning an appropriate value to the tortuosity factor, a reasonable match can be obtained between modelled and experimental data.

Chapter 6. Conclusions and Recommendations for Future Work

Several important conclusions can be drawn from discussions that have been presented in this thesis.

6.1 Development of diffusion measurement technique

- A method was developed in which a metal ring was formed around the perimeter of a sample of cordierite, such that it could be sealed in a diffusion cell. The method involved electroplating and the sample was tested at temperatures up to 320°C, without fracture occurring.

- Both transient and steady state experiments were performed to measure the effective diffusivity of hydrocarbons in a cordierite substrate. The transient method was shown to be unsuitable for such a thin sample, as the time delay for diffusion is insufficient to discriminate from the other time delays in the system.

6.2 Sol-gel method to be applied in catalyst preparation

- Use of the sol-gel method enables a uniform layer of washcoat to be deposited on the surface of a cordierite support. However, the washcoat loading per coating is relatively low, but it can be built up in a number of layers.
- Using the sol-gel method, the relative weight of sample increases in a linear manner with the number of coatings. After the first coating, the washcoat penetrates the pores and does not contribute to the thickness of the layer. After subsequent coatings, the thickness of the layer increases in a linear manner. Surface area and pore volume also increase in a linear manner.
- BET surface area decreases with calcination temperature and average pore diameter increases rapidly above a temperature of 900°C. These will have a significant impact on the effective diffusivity of components in the washcoat.
- Properties of cryogels (freeze-drying gels) and xerogels were compared. It was shown that calcination temperature had more of a significant effect on the final properties of the washcoat, than the method of drying.
- The addition of zirconia increases the stability of the pore size distribution, however, both pore volume and surface area decrease as zirconia content is increased. Addition of zirconia will affect effective diffusivity of components in the structure.

- In experiments, when 1 wt% platinum was added, the cumulative pore volume decreased by 9%, but pore size distribution was not affected. The addition of a catalyst may have a small effect on the effective diffusivity of components in the washcoat.
- The addition of 0.1 wt% of a drying additive was shown to reduce the tendency for cracks to form in the washcoat, without a significant reduction in surface area or change in average pore size.

6.3 Measurement of effective diffusivity using the steady state method

6.3.1 Diffusion in the cordierite support

- For the uncoated cordierite, the binary effective diffusivities of the four components for T= 125°C ~ 275°C were shown to be represented by:
  - *n*-Pentane: $D_e = 8.6\times10^{-7} T^{1.38}$
  - *n*-Hexane: $D_e = 1.6\times10^{-6} T^{1.24}$
  - *n*-Heptane: $D_e = 7.1\times10^{-7} T^{1.33}$
  - *n*-Octane: $D_e = 2.6\times10^{-10} T^{1.41}$

- When the experimental results were compared with the use of the parallel pore model, it was found that the predicted D_e values are greater than the experimental values by a factor of 3~4, except in the case of octane which deviates by a factor of 8. When the experimental results were compared with the random pore model, it was found that the predicted effective diffusivities for pentane, hexane and heptane are greater than the experimental values by a factor of about 2 to 3, while D_e values for octane deviate by a factor of 5. Neither of these models provides a good match with experimental data. This confirms earlier findings by Hayes *et al.* (2000), that values of D_e calculated using the random pore model were found to be 3.1 times larger than the experimental values.

- When calculated average values of tortuosity, τ, were plotted as function of molar mass, τ was seen to increase with molar mass. As the tortuosity should be constant for the material, this indicates that either the presence of the heavier species is increasing tortuosity (perhaps connecting micropores becomes blocked) or other factors (*e.g.* adsorption) are influencing the results.

6.3.2 Diffusion in the alumina washcoat

- It was found that over the range of conditions tested, the experimentally measured value of D_e is independent of the concentration of the species.

- From experiments with *n*-hexane, *n*-heptane and *n*-octane, it was shown that D_e decreases with an increase in the weight and hence thickness of washcoat loadings. Above a washcoat loading of 0.00132 g/cm^2 (corresponded to 1.5 μm), the decrease was linear with loading. This indicates that care must be taken with the prediction of values of D_e in very thin layers of catalyst (< 2 μm). Also, that the resistance in the interfacial layer can be significant at low washcoat thickness.

- It was shown that if one side of a cordierite plate is coated (forming a binary composite layer), then the value of D_e varies depending on whether the hydrocarbon stream is on the washcoated or uncoated side of the support. If the hydrocarbons are on the washcoat side, then there is a 40% reduction in flux hence the value of D_e.

- From experiments with *n*-hexane, *n*-heptane and *n*-octane, above a calcination temperature of 800°C, hydrocarbon flux and hence value of D_e increased with calcination temperature. It is postulated that the combined effect of an increase in mean pore size and reduction in tortuosity increases the flux across the plate. Changes in tortuosity are likely to be the dominant factor.

- Multicomponent diffusion experiments show that the D_e values of each diffusing species in multicomponent diffusion system are close to the values obtained from binary diffusion. It can be postulated that a diffusing species does not have a significant effect on the transport of the other species across the washcoat. By assigning an appropriate value to the tortuosity factor, a reasonable match can be obtained between modelled and experimental data.

6.4 Future work

(a) In a binary composite structure consisting of washcoat/cordierite, to investigate further why values of D_e varied depending on the direction of hydrocarbon flux through the structure.

(b) To explore why back calculated values of tortuosity appeared to increase with the molar mass of the hydrocarbon.

(c) To perform experiments with washcoated surfaces that are about 25 and 50 μm thick, and to make use of a combined resistance in series model to calculate values

of D_e in the washcoat layer. Then to compare these values with predictions from the use of mathematical model.

(d) To explore further the use of a cryogel (freezing gel), as a method of preparing a high surface area support. This was an exciting discovery in the thesis, but to have studied it further would have resulted in a distraction from the main thrust of the work.

(e) To use the sol-gel method, described in this thesis, to coat monoliths, and to perform catalytic combustion experiments. Then to compare the results with mathematical models in which data on factors that influence D_e values described in this thesis has been utilised.

REFERENCES

Abraham, A., *Thin-film Technology for Microelectronics*, FPH/OP, Israel (1975).

Agrafiotis, C. and A. Tsetsekou, "The effect of powder characteristics on washcoat quality. Part I: Alumina washcoats", *J. European Ceram. Soc.*, 20, 815-824 (2000).

Agrafiotis, C. and A. Tsetsekou, "The effect of processing parameters on the properties of γ-alumina washcoats deposited on ceramic honeycombs", *J. Mat. Sci.*, 35, 951-960 (2000).

Al-bayaty, S., Acharya, D.R., and Hughes, R., "Effect of coke deposition on the effective diffusivity of catalyst pellets", *Appl. Catal. A*, Vol.110, No.1, 109-119 (1994).

Al-Rqobah, H.A., Kam, E.K.T., and Hughes, R., "A simple technique for dead volume residence time evaluation", *AIChE J.*, Vol.32, No.2, 350-352 (1986).

Al-Rqobah, H.A., Kam, E.K.T., and Hughes, R., "Dynamic determination of diffusion in porous particles", *Chem. Eng. Res. Des.*, Vol.66, No.3, 275- 283 (1988).

Amenomiya, Y., "Methanol synthesis from CO_2+H_2 .2. Copper-based binary and ternary catalysts", *Appl. Catal.*, Vol.30, No.1, 57-68 (1987).

Anderson, D.N., "Effect of inlet temperature on the performance of a catalytic reactor", in *Proceedings of the 3rd Workshop on Catalytic Combustion*, edited by J.P. Kesseling, *US EPA report, EPA-600/7-79-038*, pp. 405-425 (1979).

Anold, W.D., Bond, W.D, and S.M. Robinson, *Radioact. Waste Manage. Nucl. Fuel Cycle*, 3, 57 (1982).

Arai, H. and M. Machida, "Thermal stabilization of catalyst supports and their application to high-temperature catalytic combustion", *Appl. Catal. A: General*, 138, 161-176 (1996).

Aris, R, *The Mathematical Theory of Diffusion and Reaction in Permeable Catalysts*, Volume 1, Clarendon Press, Oxford (1975).

Artaki, I., T.W. Zerda and J. Jonas, "Solvent effects on the condensation stage of the sol-gel process", *J. Non-Cryst. Solids*, Vol. 81, 381-395 (1986).

Ash, R., R.M. Barrer, C.G. Pope, "Flow of adsorbable gases and vapours in a microporous medium I. Single sorbates", *Proc. Roy. Soc. London, A.* 271, 1-18 (1963).

Baiker, A., New, M., and Richarz, W., "Determination of intraparticle diffusion coefficients in catalyst pellets - A comparative-study of measuring methods", *Chem. Eng. Sci.*, Vol.37, No.4, 643-656 (1982).

Barrer, R.M. and D.M. Grove, "Flow of gases and vapours in a porous medium and it bearing on adsorption problems", *Trans. Faraday Soc. London, Ser. A.*, 213, 250 (1952).

Barrer, R.M. and J.A. Barrie, "Sorption and surface diffusion in porous glass", *Proc. Roy. Soc.*, A213, 250-265 (1952).

Barrer, R.M., "A new approach to gas flow in capillary systems", *J. Phys. Chem.*, Vol. 57, 35-40 (1953).

Barrett, E.P., L.G. Joyner and P.P. Halenda, "The determination of pore volume of area

distributions in porous substances: I. Computations from nitrogen isotherms", *J. Chem. Phys.*, Vol. 73, 373-380 (1951).

Beebe, K.W., Cairns, K.D., Pareek, V.K., *et al.*, "Development of catalytic combustion technology for single-digit emissions from industrial gas turbines", Catal. Today, 59 (1-2), 95-115 (2000).

Beeckman, J. W., "Measurement of effective diffusion coefficient of nitrogen monoxide through porous monolith-type ceramic catalysts", *Ind. Eng. Chem. Res.*, 30, 428-430 (1991).

Bennett, C.J., Hayes, R.E., Kolaczkowski, S.T, *et al.*, "An experimental and theoretical-study of a catalytic monolith to control automobile exhaust emissions", *Proc. Roy. Soc. London A Mat.*, 439: (1907), 465-483 (1992).

Biswas, J., Do, D.D., Greenfield, P.F., and Smith, J.M., "Evaluation of bidisperse transport properties of a reforming catalyst using a diffusion cell. 2. Experimental study", *Appl. Catal.*, Vol.32, No.1-2, 235-247 (1987).

Boersma-Klein, W. and Moulijn J.A., "The evaluation in time domain of mass transfer parameters from chromatographic peaks", *Chem. Eng. Sci.*, Vol. 34, 959-969 (1979).

Boreskov, G.K, "Catalytic activation of dioxygen", in *Catalytic science and technology* (eds. J.R Anderson and M. Boudart), Springer-Verlag, Berlin, Vol. 3, pp 39-137 (1982).

Boreskov, G.K, *Heterogeneous catalysis*, Moskow, Nauka (1986).

Boreskov, G.K., "Scientific basis of catalyst preparation", *Preparation of catalysts*, edited by B. Delmon *et al.*, pp223-245, (1976).

Bower, P.E., M.P. Dudukovic, P.L. Mills and S.P. Waldrum, "Steady and unsteady state binary gas diffusion measurements in single spherical catalyst pellets", *I. Chem. E. Symp. Ser.*, 87, 9-16 (1984).

Brinker, C. J. and G. W. Scherer, *Sol-Gel Science: The Physics and Chemistry of Sol-Gel Processing*, Academic press, Inc., Boston (1990).

Brinker, C.J., A.J. Hurd, P.R. Schunk, *et al.*, "Review of sol-gel thin film formation", *J. Non-Cryst. Solids*, 147&148, 424-436 (1992).

Brinker, C.J., Keefer, K.D., Schaefer, D.W., and Ashley, C.S., "Sol-gel transition in simple silicates" *J. Non-Cryst. Solids*, 48, 47-64 (1982).

Brown, G.W., *Modern Mathematics for Engineers*, McGraw-Hill Book Co., p276 (1956).

Brown, L.F., H.W. Haynes, and W.H. Manogue, "The prediction of diffusion rates in porous materials at different pressures", *J. Catal.*, 14, 220-225 (1969).

Bruce, L.A., Hope, G.J., and Mathews, J.F., "Conversion of synthesis gas to aromatic-containing hydrocarbons under mild conditions", *Appl. Catal.*, Vol.9, No.3, 351-359 (1984).

Bullot, J., Gallais, O., Gautier, M. and J. Livage, "Semiconducting properties of amorphous V_2O_5 layers deposited from gels", *Appl. Phys. Lett.*, 36, 986 (1980).

Burghardt, A. and Smith J.M, "Dynamic response of a single catalyst pellet", *Chem. Eng. Sci.*, 34, 267 (1979)

Burtin, P., Brunelle, J.P., Pijolat, M., and Soustelle, M., "Influence of surface-area and additives on the thermal-stability of transition alumina catalyst supports .1. Kinetic data", *Appl. Catal.*, Vol.34, No.1-2, 225-238 (1987).

Carman, P.C., *Flow of gases through Porous Media*, Academic Press, New York (1956).

Carturan, G. and V. Gottardi, "Hydrogenation of 1-hexane catalysed by palladium supported on metal-organic glasses", *J. Mol. Catal.*, 4, 349-359 (1978).

Carturan, G., *et al.*, "Preparation of supports for catalysis by the gel route", *J. Non-Cryst. Solids*, 63, 273-281 (1984).

Carturan, G. G. Cocco, Schiffini, G. Strukul, "Role of molecular interactions during the preparation of Pd and Pt/glass hydrogenation catalysts", *J. Catal.*, 65, 359-368 (1980).

Caulton, K.G. and Hubert-Pfalzgraf, L.G., "Synthesis, structural principles, and reactivity of heterometallic alkoxides", *Chem. Rev.*, Vol.90, No.6, 969-995 (1990).

Childs, E.C. and Collis-George, N., "The permeability of porous materials", *Proc. Roy. Soc.*, A 201, 392 (1950).

Cho, I.-H., Park, S.-B., Cho, S,-J., *et al.*, "Investigation of Pt/γ-alumina catalysts prepared by sol-gel method", *J. Catal.*, 173, 295-303 (1998).

Ciambelli, P., Palma, V., Tikhov, S.F., Sadykov, V.A., Isupova, L.A., and Lisi, L, "Catalytic activity of powder and monolith perovskites in methane combustion", *Catal. Today*, Vol.47, No.1-4, 199-207 (1999).

Ciapretta F.G. and C.J. Plank, "Chapter 7 Catalyst preparation", in *Catalysis Volume 1* (ed. P.H. Emmett), Reinhold Publishing Corp., New York, pp 315 (1954).

Clements, W.C., Jr., "Determination of the parameters of the longitudinal dispersion model from experimental data", *Chem. Eng. Sci.*, 24, 957 (1969).

Crank, J., *The Mathematics of Diffusion*, Oxford University Press, London (1956).

Cresswell, D.L. and Orr, N.H., "Measurement of binary gas diffusion coefficients with porous catalysts", In *Residence Time Distribution Theory in Chemical Engineering* (edited by Petho, G., Noble, R.D.), Verlag Chemie GmbH, Weinheim, Germany, pp41-74 (1982).

Curl, R.R.L. and McMillan, M.L., "Accuracy in residence-time measurements", *AIChE J.*, 12, 819 (1966).

Cussler, E.L., *Diffusion: Mass transfer in fluid systems*, Cambridge University Press, Cambridge (1984).

Dalla Betta, R.A., "Catalytic combustion gas turbine system: the preferred technology for low emmission electric power production and co-generation", *Catal. Today*, 35,129-135 (1997).

de Boer, J.H., "The shapes of capillaries", in *Structure and Properties of Porous Materials* (edited by D. H. Everitt & F. S. Stone), Butterworths Scientific Pub., London, pp68-94 (1958).

Delmon, B., P. Jacobs and G. Poncelet, *Preparation of catalysts I*, Elsevier Scientific, Amsterdam, pp 1-11 (1976).

DeLuca, J.P. and L.E. Campbell, "Monolith catalyst supports", in *Advanced Materials in*

Catalysis (edited by Burton, J. J. and R. L. Carten), Materials Science Series, Academic Press, pp. 293-324 (1977).

Deriagin, B.V. and S.P. Bakanov, "Theory of the flow of a gas in a porous material in the near-Knudsen diffusion", *Tech. Phys.*, 2, 1904 (1957).

Dharmadhikari, S., "Gas turbines for process industries", *Chem. Engrs.*, 16-20 (1989).

Diggin, M.B., "Nickel plating from the sulphamate solution", *Trans. Inst. Met . Finishing*, 31, 243-256 (1954).

Djuricic, B., S. Pickering, P. Glaude, D. McGarry, P. Tambuyser, "Thermal stability of transition phases in zirconia-doped alumina", *J. Materials Sci.*, 32, 589-601 (1997).

Do, D.D. and Smith, J.M., "Transient response of diffusion cell containing a porous solids", *Chem. Eng. Sci.*, 39(12), 1689-1699 (1984).

Do, D.D., "Adsorption in porous solids having bimodal pore-size distribution", *Chem. Eng. Commum.*, 17, 1001 (1983).

Do, D.D., *Adsorption Analysis: Equilibria and Kinetics*, Imperial College Press, London, p399 (1998).

Dogu, G. and Ercan, C., "Dynamic analysis of adsorption on bidisperse porous catalysts" *Can. J. Chem. Eng.*, Vol. 61, No.5, 660- 664 (1983).

Dogu, G. and J. M. Smith, "A dynamic method for catalyst diffusivities", *AIChE J.*, Vol. 21, No. 1, 58 - 61 (1976).

Dogu, G., Keskin, A., and Dogu, T., "Macropore and micropore effective diffusion coefficients from dynamic single-pellet experiments", *AIChE J.*, Vol.33, No.2, 322-324 (1987).

Dogu, G., Pekediz, A. and Dogu, T., "Dynamic analysis of viscous-flow and diffusion in porous solids", *AIChE J.*, Vol.35, No.8, 1370-1375 (1989).

Dogu, T. and Dogu, G., "Testing the relative importance of temperature and concentration gradients in catalyst pellets", *AIChE J.*, Vol.30, No.6, 1002-1004 (1984).

Dogu, T., Cabbar, C., and Dogu, G., "Single-pellet technique for irreversible and reversible adsorption in soil", *AIChE J.*, Vol.39, No.11, 1895-1899 (1993).

Dogu, T., Keskin, A., Dogu, G. and Smith, J.M., "Single-pellet, moment method for analysis of gas-solid reactions", *AIChE J.*, Vol.32, No.5, 743-750 (1986).

Doong, S.-J. and Yang, R.T, "Bulk separation of multicomponent gas mixtures by pressure swing adsorption: pore/surface diffusion and equilibrium models, *AIChE J.*, 32, 397-410 (1986)

Evans, R. B., G. M. Watson and E. A. Mason, "Gaseous diffusion in porous media at uniform pressure", *J. Chem. Phy.*, Vol. 35, No. 6, 2076-2083 (1961).

Farrauto, R.J. T. Kennelly, E.M. Waterman, "Process conditions for operation of ignition catalyst for natural gas combustion", *US Pat. 4,893,465*, January 16 (1990).

Felder, R.M. and Stahal, E.P, "Non-isothermal chemical kinetics", *Chem. Eng. Commun.*, 1, 187 (1974).

Feng, C. and W.E. Stewart, "Practical models for isothermal diffusion and flow of gases in porous solids", *Ind. Eng. Chem. Fundam.*, Vol.12. No.2, 143-147 (1973).

Firsch, H.L., "The time lag in diffusion", *J. Phys. Chem.,* Vol. 61, 93-95 (1957).

Foster, A.G., "The sorption of condensable vapours by porous solids. Part 1. The applicability of the capillary theory", *Trans. Faraday Soc.*, 28, 645-657 (1932).

Foster, G.F. and H.E. Meissner, *Ger. Pat. DT 1317536* (1973).

Foster, R.N. and J.B. Butt, "A computational model for the structure of porous materials employed in catalysis", *AIChE J.*, Vol.12, No.1, 180-185 (1966).

Froment, G.F. and Bischoff, R.B., *Chemical Reactor Analysis and Design, 2nd ed.*, John Wiley & Sons, London. (1990).

Froment, G.F. and H. Hoffman, "Design of fixed-bed gas-solid catalytic reactors", in *Chemical reaction and reactor engineering* (eds Carberry, J.J. and Varma, A.), Dekker, New York, pp373-440 (1986).

Frost, A.C., "Measurement of effective diffusivity from effluent concentration of a flow through diffusion cell", *AIChE J.*, 27, 813 (1981).

Gangwal, S.K., Hudgins, R.R., Bryson, A.W. and Siverstone, P.L., "Interpretation of chromatographic peaks by Fourier analysis", *Can. J. Chem.*, Vol. 49, 113-119 (1971).

Glassman, I., *Combustion, 2nd ed.*, Academic Press Inc., London (1987).

Gregg, S.J. and K.S.W. Sing, *Adsorption, Surface Area and Porosity*, Academic press, London, (1982).

Guilhaume, N. and M. Primet, "Catalytic combustion of methane: CuO supported on high-specific area spinels synthesised by sol-gel process", *J. Chem. Soc. Faraday Trans.*, 90 (11), 1541-1545 (1994).

Guilhaume, N. and Primet, M., "Catalytic combustion of methane - copper-oxide supported on high- specific-area spinels synthesised by a sol-gel process", *J. Chem. Soc.-Faraday Trans.*, Vol.90, No.11, 1541-1545 (1994).

Gupta, A.K. and Lilly, D.D., "Review: the environmental challenge of gas turbine", *J. Inst. Energy*, 65, 106-117 (1992).

Hartley, J., "Will we ever drive gas turbine cars?", *Autocar*, w/e 28, January, 52-55 (1978).

Hashimoto, N. and Smith, J.M., "Macropore diffusion in molecular sieve pellets by chromatography", *Ind. Eng. Chem. Fundam.*, Vol. 12, No. 3, 353-359 (1973).

Hawtin, P., R.W. Dawson, and J. Roberts, "The diffusion of gases through graphite", *Trans. Instn. Chem. Engrs.,* Vol. 47, T109-T113 (1969).

Hayes, R.D. and Kolaczkowski, S.T, *Introduction to Catalytic Combustion*, Gordon and Beach Science Publishers, Amsterdam (1997).

Hayes, R.D. and Kolaczkowski, S.T., "Diffusion limitation effects in the washcoat of a catalytic monolith reactor", *Can. J. Chem. Eng.*, 74, 94-103 (1996).

Hayes, R.D. and Kolaczkowski, S.T., "Mass transfer and heat transfer effects in catalytic monolith reactors", *Chem. Eng. Sci.*, Vol. 49, No. 21, 3587-3599 (1994).

Hayes R.E., Kolaczkowski, S.T., Li, P.K.C., *et al.*, "Evaluating the effective diffusivity of methane in the washcoat of a honeycomb monolith", *Appl. Catal. B-Environ.*, 25: (2-3), p 93-104 (2000).

Haynes Jr H.W. and P.N. Sarma, "A model for the application of gas chromatography to measurements of diffusion in bidisperse structured catalysts", *AIChE J.*, 19, 1043-1046 (1973).

Haynes, H.W. Jr., "The determination of effective diffusivity by chromatography. Time domain solutions", *Chem. Eng. Sci.*, Vol. 30, 955-961 (1975).

Haynes, H.W. Jr., "The experimental evaluation of catalyst effective diffusivity", *Catal. Rev. - Sci. Eng.*, 30 (4), 567-627 (1988).

Hegedus, L.L., "Temperature excursions in catalytic monoliths", *AIChE J.*, 21 (5), 849-853 (1975).

Hench, L.L. and Ulrich, D.R., *Ultrastructure Processing of Ceramics, Glasses, and Composites*, Wiley, New York (1984).

Hewitt, G.F. and E.W. Sharratt, "Gaseous diffusion in porous media with particular reference to graphite", *Nature*, Vol. 198, No. 4884, 952-957 (1963).

Hirao, O. and R.K. Pefley, *Present and Future Automotive Fuels*, A Wiley-Interscience Pub., New York, p6, (1988).

Hirashima, H. *et al.*, "Oxide aerogel catalysts", *J. Non-Cryst. Solids*, 225, 153-156 (1998).

Hirschifelder, J.O., Curtiss, C.F., and Bird, R.B., *Molecular Theory of Gases and Liquids*, John Wiley & Sons, New York, pp 1110-1112 (1954).

Holmgren A. and Andersson B., "Mass transfer in monolith catalysts - CO oxidation experiments and simulations", *Chem. Eng. Sci.*, 53: (13), 2285-2298 (1998).

Hou, K., Fowles, M, Hughes, R., "Effective diffusivity measurements on porous catalyst pellets at elevated temperature and pressure", *Chem. Eng. Res. Des.*, 77: (A1), 55-61 (1999).

Hsu, L.-K. P. and H.W. Haynes, "Effective diffusivity by the gas chromatography technique: analysis and application to measurements of diffusion of various hydrocarbons in zeolite NaY", *AIChE J.*, Vol. 27, No.1, 81-91 (1981).

Iizuka, T., Tanaka, Y., and Tanabe, K., "Hydrogenation of CO and CO_2 over Rhodium Catalysts Supported on Various Metal-Oxides", *J. Catal.*, Vol.76, No.1, 1-8 (1982).

Irandoust, S. and B. Andersson, "Monolithic catalysts for non-automobile applications", *Catal. Rev. - Sci. Eng.*, 30 (3), 341-392 (1988).

Jackson, R., *Transport in Porous Catalysts*, Elsevier Scientific Pub., Amsterdam (1977).

Jefferson, C.P., "Dynamic testing-a unification", *Chem. Eng. Sci.*, 25, 1319-1329 (1970).

Johnson, M.F.L and W.E. Stewart, "Pore structure and gaseous diffusion in solid catalysts", *J. Catal.*, 4, 248-252 (1965).

Kajita, S., Y. and Tanaka, J. Kitajima, *ASME 90-GT-89* (1990).

Kamiya, K., S. Sakka and Y. Tatemichi, "Preparation of glass fibres of the ZrO_2-SiO_2 and Na_2O-ZrO-ZrO_2-SiO_2 systems from metal alkoxides and their resistance to alkaline solution", *J. Mat. Sci.*, 15, 1765 (1980)

Keith, C.D., P.M. Kennah and D.L. Bair, "Coated film of catalytically active oxide on a refractory support", *US Patent 3,565,830* (1971).

Kelly, J.F. and Fuller, O.M., "An evaluation a method for investigating sorption and diffusion in porous solids", *Ind. Eng. Chem. Fundam.*, 19, 11 (1980)

Kemp, M. K., *Physical Chemistry*, Marcel Dekker, New York (1979).

Kesselring, J.P., "Catalytic combustion", in *Advanced Combustion Methods* (eds. F.J. Weinberg), Academic Press, London, pp237-275 (1986).

Kokubo, T., Teranishi, Y., Maki, T., and Sakka, S., "Formation of zirconia fibers on unidirectional freezing of a gel", *J. Materials Sci.*, Vol.23, No.3, 1126-1130 (1988).

Kolaczkowski S. T. and Serbetcioglu S., "Development of combustion catalysts for monolith reactors: a consideration of transport limitations", *Appl. Catal. A*, 199-214 (1996).

Kolaczkowski, S.T., "Catalytic stationary gas-turbine combustors - a review of the challenges faced to clear the next set of hurdles", *Chem. Eng. Res. Des.*, (VOL 73, PG 168, 1995), 73: (A7) 865-865 (1995).

Kolaczkowski, S.T., S. Awdry and J.L. Scott-Scott, "Catalytic combustion chamber with pilot stage and a method of operation thereof", *US Patent* 600212 (1999).

Kolaczkowski, S.T., W.J. Thomas, J. Titiloye, and D.J. Worth, "Catalytic combustion of methane in a monolith reactor: Heat and mass transfer under laminar flow and pseudo-steady-state reaction conditions", *Combst. Sci. and Tech.*, Vol. 118, 79-100 (1996).

Komeya, K. and M. Matsui, "High temperature engineering ceramics", Chapter 10 in *Meterial Science and Technology, Volume II* (eds. R.W. Cahn *et al.*), VCH, Weinheim (1994).

Kondis, E. F. and J. S. Drankoff, "Kinetics of isothermal sorption of ethane on 4A molecular sieve pellets", *Ind. Eng. Chem. Proc. Des. Dev.*, 10, 108 (1971).

Krishna, R. and J.A. Wesselingh, "The Maxwell-Stefan approach to mass transfer", *Chem. Eng. Sci.*, Vol. 52, No. 6, 861-911 (1997).

Kucera, E., "Contribution to the theory of chromatography: linear non-equilibrium elution chromatography", *J. Chromatog.*, 19, 237-248 (1965).

Kyriacopoulou, V., Psyllos, A., Philippopoulos, C., "Diffusional effects and intrinsic kinetics for no reduction by CO over Pt-Rh gamma-Al_2O_3 monolithic catalysts", *Ind. Eng. Chem. Res.*, 33: (7), 1669-1673 (1994).

Lange, C., Storck, S., Tesche B., *et al.*, "Selective hydrogenation reactions with a microporous membrane catalyst, prepared by sol-gel dip coating", *J. Catal.*, 175, 280-293 (1998).

Leenaars, A.F.M. and A.J. Burggraaf, "The preparation and characterization of alumina membranes with ultra-fine pores, 2. The formation of supported membranes", *J. Colloid Interface Sci.*, Vol. 105, No. 1, 27-41 (1985).

Leenaars, A.F.M. and A.J. Burggraaf, "The preparation and characterization of alumina membranes with ultra-fine pores, part 3. The permeability for pure liquids", *J. Membrane Sci.*, 24, 245-260 (1985).

Leenaars, A.F.M. and A.J. Burggraaf, "The preparation and characterization of alumina membranes with ultra-fine pores, part 4. Ultrafiltration and hyperfiltration experiments", *J. Membrane Sci.*, 24, 261-270 (1985).

Leenaars, A.F.M., K. Keiser and A.J. Burggraaf, "Porous alumina membranes", *Chemtech*, Sept., 560-564 (1986).

Leenaars, A.F.M., K. Keiszer and A.J. Burgraaf, "The preparation and characterisation of alumina membranes with ultra-fine pores Part 1 Microstructural investigations on non-supported membranes", *J. Mat. Sci.*, Vol. 19, 1077-1088 (1984).

Leung, D., R.E. Hayes and S.T. Kolaczkowski, "Diffusion limitation effects in the washcoat of a catalytic monolith reactor", *Can. J. Chem. Eng.*, Vol. 74, 94-103 (1996).

Levenspiel, O., *Chemical Reaction Engineering, 2nd ed.*, John Wiley & Sons, Inc, New York (1972).

Levinson, W.A., A. Arnold, and O. Dehodgins, "Spin-coating behavior of polyimide precursor solutions", *Polymer Eng. Sci.*, 33, 980 (1993).

Li, B. and R.D. Gonzalez, "Sol-gel synthesis and catalytic properties of sulfate zirconia catalysts", *Ind. Eng. Chem. Res.*, 35, 3141-3148 (1996).

Li, P.K.C, *Catalytic Combustion of Methane in Monoliths and the Influence of Diffusion Barriers, PhD thesis*, University of Bath, pp. 188 - 220 (1997).

Lin, Y.S., Devries, K.J., and Burggraaf, A.J., "Thermal-stability and its improvement of the alumina membrane top-layers prepared by sol-gel methods", *J. Materials Sci.*, Vol.26, No.3, 715-720 (1991).

Livage, J., M. Henry and C. Sanchez, "Sol-gel chemistry of transition metal oxides", *Prog. Solid St. Chem.*, 18, 259-341 (1988).

Ma, Y.H. and Lee, T.Y., "Transient diffusion in solids with bipore distribution", *AIChE J.*, 22, 147 (1976).

Ma, Y.H. and S.Y. Ho, "Diffusion in synthetic faujasite powder and pellets", *AIChE J.*, 20 (2), 279-284 (1974).

Machida, M., K. Eguchi, and H. Arai, " High-temperature catalytic combustion over cation-substituted barium hexaaluminates", *Chem. Lett.*, No. 5, 767-770 (1987).

Mackay, R., "Gas turbine generator sets for hybrid vehicles", *SAE Special Publications R15069*, pp19-24 (1992).

Mahler, W. and M.F. Bechtold, "Freezing-formed silica fibres", *Nature*, Vol. 285, 27-28 (1980).

Maki, T. and S. Sakka, "Preparation of alumina fibres by sol-gel method", *J. Non-Cryst. Solids*, 100, 303-308 (1988).

Maki, T. and Sakka, S., "Formation of alumina fibres by unidirectional freezing of gel ", *J Non-Cryst. Solids*, Vol.82, No.1-3, 239- 245 (1986).

Maki, T. and Sakka, S., "Preparation of porous alumina fibers by unidirectional freezing of gel", *J Mat. Sci. Letters*, Vol.5, No.1, 28- 30 (1986).

Mason, E.A. and Malinauskas, A.P., *Gas Transport in Transport Media: The Dusty Gas Model*, Elsevier, Amsterdam, The Netherlands (1983).

Mason, E.A. and R.B. Evans III, "Graham's law: Simple demonstrations of gases in motion", *J Chem. Ed.*, Vol. 46, No 6, 358-364 (1969).

Mason, E.A., Evans, R.B., Watson, G.M., " Gaseous diffusion in porous media. III. Thermal transpiration", *J. Chem Phys.*, 38, 1808 (1963).

Mason, E.A., Malinauskas, A.P, Evans, R.B., "Flow and diffusion of gases in porous media", *J. Chem Phys.*, 46, 3199 (1967).

McBain, J.W., "An explanation of hysteresis in the hydration and dehydration of gels", *J. Amer. Chem. Soc.*, 57, 699 (1935).

McCarty J.G., Gusman M., Lowe D.M., *et al.*, "Stability of supported metal and supported metal oxide combustion catalysts", *Catal. Today*, 47: (1-4), 5-17 (1999).

McKewan and Olsson (1966), cited by Daken and Turkdogan (1970) in *Heterogeneous Kinetics at Elevated Temperatures* (edited by G.R. Belton and W.L. Worrell), Plenum Press, New York (1970).

Meijers, A.C.Q.M., Dejong, A.M., Van Gruijthuijsen, L.M.P., and Niemantsverdriet, J.W., "Preparation of zirconium-oxide on silica and characterization by X-ray photoelectron-spectroscopy, secondary ion mass-spectrometry, temperature programmed oxidation and infrared-spectroscopy", *Appl. Catal.*, Vol.70, No.1, 53-71 (1991).

Mercera, P.D.L., Vanommen, J.G., Doesburg, E.B.M., Burggraaf, A.J., and Ross, J.R.H., "Zirconia as a support for catalysts - Evolution of the texture and structure on calcination in air", *Appl. Catal.*, Vol.57, No.1, 127-148 (1990).

Miller, J.C. and J.N. Miller, *Statistics for Analytical Chemistry, 3rd Ed.*, Ellis Horwood Ltd, West Sussex (1993).

Nakhjavan, A., Bjornbom P., Zwinkels, M.F.M., *et al.*, "Numerical-analysis of the transient performance of high-temperature monolith catalytic combustors - effect of catalyst porosity", *Chem. Eng. Sci.*, 50: (14), 2255-2262 (1995).

Narula; C.K., Watkins, W.L.H., and Shelef; M., "Aluminium oxide catalyst supports from alumina sols", *US Patent 5210062* (1993).

Nelson, E. T. and P. L. Walker, "Some techniques for investigating the unsteady-state molecular flow of gas through a microporous medium", *J. Appl. Chem.*, 11, 358 (1961).

Nelson, R.L. Ramsay, J.D.F., Woodhead, J.L., *et al.*, "The coating of metals with ceramic oxides via colloidal intermediates", *Thin Solid Films*, 81, 329-337 (1981).

Oh, S.H. and Cavendish, J.C., "Design aspects of poison-resistant automobile monolithic catalysts", *Ind. Eng. Chem. Prod. Rd.*, 22: (4), 509-518 (1983).

Omata, H. and L.F. Brown, "Using the dusty gas diffusion equation in catalyst pores smaller than 50 Å radius", *AIChE J.*, Vol.18, No. 5, 967-975 (1972).

Otani, S. and J.M. Smith, "Effectiveness of large catalyst pellets-an experimental study", *J.*

Catal., 5, 332-347 (1966).

Paravar, A. and D.T. Hayhurst, "Direct measurement of diffusivity for butane across a single silicate crystal", *6TH P Int. Zeolite C.*, p.217 (1984).

Park, I.-S., D.D. Do, and A.E. Rodrigues, "Measurement of the effective diffusivity in porous media y the diffusion cell method", *Catal. Rev.-Sci. Eng.*, 38(2), 189-247 (1996).

Perry, J.A., *Introduction to Analytical Gas Chromatography*, Marcel Dekker, Inc., New York, p149 (1981).

Perry, R.H. and D. Green, *Perry's Chemical Engineers' Handbook, 6th ed.*, McGraw Hill, Inc, New York (1984).

Petersen, E.E., "Diffusion in a pore of varying cross section", *AIChE J.*, Vol.4, No.3, 343-345 (1958).

Pfefferie, W.C., "Methods of starting a combustion system utilizing a catalyst", *US Patent* 4,019,316 (1975).

Pfefferle, L.D. and W.C. Pfefferle, "Catalysis in combustion", *Catal. Rev.-Sci. Eng.*, 29 2 3, pp. 219-267 (1987).

Pletcher, D. and F.C. Walsh, *Industrial Electrochemistry, 2nd ed.*, Blakie Academic & Professional, London (1993).

Prasad, R., Kennedy, L.A., and Ruckenstein, E., "Catalytic Combustion", *Catal. Rev.*, 26: (1), 1-58 (1984).

Ramachandran, P.A. and Smith, J.M., Transport rates by moment analysis of dynamic data", *Ind. Chem. Fundamental*, 17(3), 148 (1978).

Rao, M.R., N. Wakao, and J.M. Smith, "Diffusion and reaction rates in the ortho-hydrogen conversion", *Ind. Eng. Chem. Fundamentals*, Vol. 3, No.2, 127-131 (1964).

Reid, R.C., J.M Prausnitz and B.R. Polling, *The Properties of Gas and Liquids*, 4th Ed., McGraw-Hill, New York (1986).

Retallick, W.R, "Washcoat for a catalyst support", *US Patent 4,762,567* (1988).

Reyes, S.C. and Iglesia E., "Effective diffusivities in catalyst pellets - new model porous structures and transport simulation techniques", *J. Catal.*, 129: (2), 457-472 (1991).

Rice, R.G, "Approximate solutions for batch, packed tube and radial flow adsorbers - comparison with experiment", *Chem. Eng. Sci.*, 37, 83 (1982).

Ritter, H.L. and L.C. Drake, "Pore-size distribution in porous materials: pressure porosimeter and determination of complete macropore-size distributions", *Ind. Eng. Chem. Anal. Ed.*, Vol.17, No.12, 782-786 (1945).

Roduit B., Baiker K., Bettoni F., *et al.*, "3-D modelling of SCR of NO_x by NH_3 on vanadia honeycomb catalysts", *AIChE J.*, 44: (12), 2731-2744 (1998).

Rothfeld, L.B., "Gaseous counterdiffusion in catalyst pellets", *AIChE J.*, Vol.9, No.1, 19-24 (1963).

Ruckensten, E., A. S. Vaidyanthan and G. R. Youngquist, "Sorption by solids with bidisperse

pore structures", *Chem. Eng. Sci.*, Vol. 26, 1305-1318 (1971).

Ruthven D.M. and Loughlin K.F., "Effects of particle shape and size distribution on the transient solution of the diffusion equation", *Chem. Eng. Sci.*, 26, 577 (1971).

Ruthven D.M., *Principles of Adsorption and Adsorption Processes*, A Wiley-Interscience Pub., New York, p58 (1984).

Sadamori, H., T. Tanioka and T. Matsuhisa, "Development of a high-temperature combustion catalyst system and prototype catalytic combustor turbine test results", *Catal. Today*, 26, No. 3-4, pp. 337-344 (1995).

Sadamori, H., T. Tanioka and T. Matsuhisa, *Proceedings of the 1995 Yokohama International Gas Turbine Congress*, Vol. 1, p. 247 (1995).

Sakka S., "Sol-gel fibers and coating films", in *Sol-Gel Science and Technology, Proceedings of the Winter School on Glasses and ceramics for Gels, Sao Carlos, Brazil* (ed.), World Scientific Pub, Singapore, pp346-374 (1989).

Sakka, S. and K. Kamiya, "The sol-gel transition in the hydrolysis of metal alkoxides in relation to the formation of glass fibres and films", *J. Non-Cryst. Solids*, Vol. 48, 31-46 (1982).

Sakka, S., Kamiya, K., Makita, K., and Yamamoto, Y., "Formation of sheets and coating films from alkoxide solutions", *J. Non-Cryst. Solids*, Vol.63, No.1-2, 223-235 (1984).

Santos, A, A. Bahamonde, P. Avila, and F. Garcia-Dchoa, "Measurement of the effective diffusivity for a vanadia-tungsta-titania/sepiolite catalyst for SCR of NO_x", *Appl. Catal. B.*, 8, 299-314 (1996).

Sarraco, G. and Montanaro, L., "Catalytic ceramic filters for flue gas cleaning. 1. Preparation and characterisation", *Ind. Eng. Chem. Res.*, 34, 1471-1479 (1995).

Satterfield, C. N. and T. K. Sherwood, *The Role of Diffusion in Catalysis*, Addison-Wesley Publishing Co., London (1963).

Satterfield, C.N. and P.J. Cadle, "Gaseous Diffusion and Flow in Commercial Catalysts at Pressure Levels above atmospheric", *Ind. Eng. Chem. Fundamentals*, Vol.7, No.2, 202-210 (1968).

Satterfield, C.N., *Mass Transfer in Heterogeneous Catalysis*, MIT Press, Cambridge (1970).

Schanel, L. and P. Schneider, "Axial dispersion due to molecular diffusion in gas chromatography", *Chem. Eng. J.*, 2, 274-279 (1971).

Schaper, H. and van Reijen, L.L., "The influence of dopes on the stability of γ-alumina catalyst support", *Mat. Sci, Monogra.*, 14, 173 (1982).

Schaper,H., Doesburg, E.B.M., and van Reijen, L.L., "The influence of lanthanum oxide on the thermal-stability of gamma alumina catalyst supports", *Appl. Catal.*, Vol.7, No.2, pp.211-220 (1983).

Scheidegger, A.E., *The Physics of Flow through Porous Media*, University of Toronto Press, Toronto (1957).

Scherer, G.W., "Freezing gels", *J. Non-Cryst. Solids*, Vol. 155, 1-25 (1993).

Scott, D.S. and F.A.L. Dullien, "Diffusion of ideal gases in capillaries and porous solids", *AIChE J.*, Vol.8, No.1, 113-117 (1962).

Seager, S.L, L.R. Geertson, and J.C. Giddings, "Temperature dependence of gas and vapor diffusion coefficients", *J. Chem. Eng. Data*, Vol. 8, No 2., 168-169 (1963).

Seker, E. and Gulari, "Improved N_2 selectivity for platinum on alumina prepared sol-gel technique in the reduction of NO_x by propene", *J. Catal.*, 179, 339-342 (1998).

Shah, D.B. and Ruthven, D.M., "Measurement of zeolite diffusivities and equilibrium isotherms by chromatography", *AIChE J.*, Vol. 23, No. 6, 804-809 (1977).

Sharma, R.K., Cresswell, D.L., Newson, E.J., "Effective diffusion-coefficients and tortuosity factors for commercial catalysts", *Ind. Eng. Chem. Res.*, 30: (7), 1428-1433 (1991).

Sherer, G.W. "Drying of gels", in *Sol-Gel Science and Technology, Proceedings of the WinterSchool on Glasses and ceramics for Gels, Sao Carlos, Brazil* (ed.), World Scientific Pub, Singapore, pp181-220 (1989).

Silveston, P.L., "Multicomponent diffusion in capillaries", *AIChE J.*, Vol. 10, No. 1, 132-133 (1964).

Sjöblom B., Rehn J., "The Volvo high speed generation hybrid drive and associated combustion system", *Energ. Convers. Manage.*, 38: (10-13), 1225-1235 (1997).

Smith, J.M., *Chemical Engineering Kinetics*, McGraw-Hill, New York (1981).

Statham, M.J., Hammett, E., Harris, B., *et al.*, "Net-shape manufacture of low-cost ceramic shapes by freeze-gelation", *J. Sol-Gel Sci. Tech.*, 13: (1-3), 171-175 (1998).

Stiles, A.B., *Catalyst Manufacture: Laboratory and Commercial Preparations*, Marcel Dekker, Inc., New York, pp. 89-91 (1983).

Strawbridge, I. and James, P.F., "The factors affecting the thickness of sol-gel derived silica coatings prepared by dipping", *J. Non-Cryst. Solids*, Vol.86, No.3, 381-393 (1986).

Svachula, J., N. Ferlazzo, P. Forzatti, *et al.*, "Selective reduction of NO_x by NH_3 over honeycomb DeNOxing catalysts", *Ind. Eng. Chem. Res.*, 32, 1053-1060 (1993).

Takeuchi, K. and Uraguchi, Y., "Chromatographic studies of CO and CO_2 adsorption on activated alumina by weighted Fourier analysis", *J. Chem. Eng. Japan*, 10 (4), 297-302 (1977).

Thiele, E.W., "Relation between catalytic activity and size of particle", *Ind. Eng. Chem.*, 31, 916 (1939).

Touchton, G.L., Szema, L.C., Cutrone, M.B., *et al.*, "Design of a catalytic combustor for heavy-duty gas-turbines", *J. Eng. Power-T. ASME*, 105 (4), 797-805 (1983).

Trimm, D.L., "Catalytic combustion (review)", *Appl. Catal.*, 7, 249-282 (1983).

Tronconi, E., A. Beretta, A.S. Elmi, *et al.*, "A complete model of SCR monolith reactors for the analysis of interacting NO_x reduction and SO_2 oxidation reactions", *Chem. Eng. Sci.*, Vol. 49, No. 24A, 4277-4287 (1994).

Tucci, E. R., "Use catalytic combustion for LHV gases", *Hydrocarbon Processing*, March, 159-166 (1982).

Ulrich, D.R., "Prospects of sol-gel processes", *J. Non-Cryst. Solids*, Vol. 100, 174-193 (1988).

Wakao, H. and Smith, J.M., "Diffusion in catalyst pellets", *Chem. Eng. Sci.*, Vol. 17, 825-834 (1968).

Wakao, N. and S. Kaguei, *Heat and Mass Transfer in Packed Beds*, Gordon and Breach, New York (1982).

Wang, C.T. and Smith, J.M., "Tortuosity Factors for Diffusion in Catalyst Pellets", *AIChE J.*, Vol.29, No.1, 132-136 (1983).

Wang, Z.-M. and Y.S. Lin, "Sol-gel-derived alumina-supported copper oxide sorbent for flue gas desulfurization", *Ind. Eng. Chem. Res.*, 37, 4675-4681 (1998).

Wehrenberg II, R.H, *Materials Engineering*, October 1 (1978).

Weisz, P.B. and Schwartz, A.B., "Diffusivity of porous-oxide0gel derived catalyst particles", *J. Catal.*, 1, 399 (1962).

Wheeler, A, "Reaction rates and selectivity in catalyst pores", *Catalysis*, 2, 105-116 (1955).

Wheeler, A., "Reaction rate and selectivity in catalyst pores", in *Advances in Catalysis* (ed. W.G. Frankerberg *et al.*), Vol. 3, p294 (1951).

Wicke, von E. and Kallenbach, R., "The surface diffusion of carbon dioxide in activated charcoals (Die oberflachendiffusion von kohlendioxyd in aktiven kohlen)", *Kolloid Z.*, 17, 135 (1941).

Wyllie, M.R.J. and Gardner, G.H.F., "The generalised Kozeny-Carman equation", *World Oil*, 149, 210 (1958).

Xie, Y.-C. and Y.-Q. Tang, "Spontaneous monolayer dispersion of oxides and salts onto surfaces of supports: Applications to heterogeneous catalysis", *Adv. Catal.*, 37, 1-43 (1990).

Xie, Y.C. *et al.*, in *Adsorption and catalysis on oxide surfaces,* Proceedings of a symposium, Brunel University, Uxbridge, 1984 (eds. M. Che and G.C. Bond), Elsevier, Amsterdam, p139, (1985).

Yang, R.T. and R.-T. Liu, "Gaseous diffusion in porous solids at elevated temperatures", *Ind. Eng. Chem. Fund.*, Vol.21, No.3, 262-268 (1982).

Yoldas, B.E., "Alumina gels that form porous transparent Al_2O_3", *J. Mat. Sci.*, 10, 1856-1860 (1975).

Yoldas, B.E., "A transparent porous alumina", *Ceramic Bulletin*, Vol. 54, No 3, 286-289 (1975).

Yoldas, B.E., "Alumina sol preparation from alkoxides", *Ceramic Bulletin*, Vol. 54, No 3, 289-290 (1975).

Youngquist, G. R., J. L. Allen, and J. Eisenberg, "Adsorption of hydrocarbons by synthetic zeolites", *Ind. Eng. Chem. Prod. Res. Dev.*, Vol. 10, No.3, 308-314 (1971).

Youngquist, G.R., "Diffusion and flow of gases in porous solids", *Ind. Eng. Chem.*, Vol.62, No.8, 52-63 (1970).

Zarzycki, J., "Monolithic xero- and aerogels for gel-glass processes", in *Science of Ceramic Chemical Processing* (eds. L.L. Hench and D.R. Urlich), Wiley, New York, pp27-42 (1986).

Zarzycki, J., "Proceedings Of The 3rd International Workshop On Glasses And Glass-Ceramics From Gels - Montpellier, France, September 12-14, 1985 – Preface", *J. Non-Cryst. Solids*, 82: (1-3), R7-R7 (1986).

Zarzycki, J., M. Prassas and J. Phalippou, "Synthesis of glasses from gels - the problem of monolithic gels", *J. Mat. Sci.,* 17, 3371-3379 (1982).

Zwinkels, M.F.M, S.G. Jaras and P.G. Menon, "Preparation of combustion catalysts by washcoating alumina whiskers-covered metal monoliths using a sol-gel method", *Preparation of Catalysts, VI*, 85-94 (1995).

Zwinkels, M.F.M, S.G. Jaras, P.G. Menon and T.A. Griffin, "Catalytic materials for high temperature combustion", *Catal. Rev.-Sci. Eng.,* 35(3), 319-358 (1993).

Zygourakis, K. and Aris, R., "Multiple oxidation reactions and diffusion in the catalytic layer of monolith reactors", *Chem. Eng. Sci.*, 38: (5), 733-744 (1983).

Appendix 1. Effective diffusivity experimental data

To obtain effective diffusivity, the following quantities should be determined:

1. Dimensions of the sample plate.
2. Volumetric flowrates on both chambers of the plate (at S.T.P.).
3. Concentration of diffusing gas in both chambers of the diffusion cell.

An example calculation is shown below.

The experimental quantities are:

$T = 398$ K	$A = 0.45$ cm^2
$P = 1.5$ bar	$L = 0.025$ cm
$F_1 = 12.89$ cm^3/s	$C_{1,Hex} = 1.48\times10^{-8}$ mol/cm^3
	$C_{2,Hex} = 1.03\times10^{-5}$ mol/cm^3

The hexane flux is calculated from a material balance in the upper chamber (on the nitrogen side) of the diffusion cell:

$$N_{Hex} = \frac{C_{1,Hex} \cdot F_1 \cdot}{A} = \frac{(1.48\times10^{-8}\,\text{mol/cm}^3)(12.89\ \text{cm}^3/\text{s})}{0.45\ \text{cm}^2}$$

$$= 4.24\times10^{-7}\ \text{mol/(cm}^2\text{.s)}$$

From Fick's law:

$$N_{Hex} = -D_e \cdot \frac{\Delta C}{\Delta x} = -\frac{D_e(C_{1,Hex} - C_{2,Hex})}{L}$$

Therefore, the effective diffusivity is:

$$D_{eff} = \frac{N_{Hex} \cdot L}{(C_{2,Hex} - C_{1,Hex})} = \frac{(4.24\times10^{-7}\,\text{mol/cm}^2 \cdot \text{s})(0.025\ \text{cm})}{(1.03\times10^{-5} - 1.48\times10^{-8})\ \text{mol/cm}^3}$$

$$= 0.00103\ \text{cm}^2/\text{s}$$

Appendix 2. Use of the transient method in a Wicke-Kallenbach type of diffusion cell: summary of experimental conditions reported in a selection of publications.

Author	Pellet: L(cm), ID(cm), ε, R_μ, r_P(Å), S_g(cm^2/g)	Tracer/carrier	Conditions: T(°C), P(atm), F_1 and F_2(cm^3/min)	Remark
Gibilaro *et al.*(1970)	Alumina: ε=0.8 Particle size=30/50, 50/80, 180/270 mesh size	CH_4/N_2	T=95	V=0.1 cm^3 pulse=0.2 cm^3 D_e=0.016 cm^2/s
Wakao (1974)	Silica-alumina L=1.15, ID=2.76, S_g=339, ε=0.58-0.73	H_2/N_2	T=21 P=1	D_e=0.010-0.013 cm^2/s
Dogu and Smith (1975)	Alumina L=2.44, ID=1.35, S_g=339, ε=0.771, R_μ=24,35	He/N_2	T=24 P=1 F_1=60 F_2=20-150	V_1=0.45,V_2=0.5 cm^3 Pulse=1.0cm^3 D_e=0.079cm^2/s
Dogu and Smith (1975)	Alumina L=0.57, ID=1.35, S_g=339, ε=0.58-0.73, R_μ=35	He and cyclopropane(2%)/N_2	T=24 P=1 F_1 and F_2=30-300	D_e=0.291 cm^2/s Pulse =1.0-3.0 cm^3
Moffat (1978)	Alumina (14%CoMoO4) L=2.48, ID=1.27, S_g=284, ε=0.56, r_p=41 Silica(6.8% WO) L=1.33, ID=0.48, S_g=345, ε=0.59, r_p=57	He/Ar	T=20,100 P=0.3-2 F_1 and F_2=100	$\tau=\varepsilon D_c/D_e$=5.0 (alumina), 9.9 (silica)
New *et al.* (1979)	BASF H3-10 L=1 and 2, ID=1.27, S_g=284, ε=0.656, $20<r_p<10^6$,R_μ=50	Ar/He	T=40 P=1 F = 12-60	V_2=0.4 cm^3 D_e=0.05 cm^2/s
Baiker *et al.* (1982)	L=1 and 2, ID=2.0, R_μ<50, ε=0.524 - 0.651	Ar/He	T=40 P=1 F_1 and F_2=6-30	D_a=0.0267, $D_i=4.6\times10^{-7}$ cm^2/s

Appendix 2. Use of the transient method (continued.....).

Author	Pellet: L(cm), ID(cm), ε, R_μ, r_P(Å), S_g(cm^2/g)	Tracer/carrier	Conditions: T(°C), P(atm), F_1 and F_2(cm^3/min)	Remark
Cresswell and Orr (1982)	Silica-alumina L=0.33, 0.426, ID=0.318, S_g=264, ε=0.5, r_p=35	He/N_2	T=50 F_1 and F_2=4.3-14.3	$V_2=2.38\times10^{-3}cm^3$ D_e=0.00381 cm^2/s τ=3.97
Wang and Smith (1983)	HDS-20A L=0.476, ID=0.952, Sg=201,ε=0.569,0.677, 15<r_p<5×10^5, R_μ=30.5-52	He and H_2/N_2	T=23-229 P=1 F_1=30-60 F_2=30-300	V=0.226 cm^3 τ=6-8
Dogu and Ercan (1983)	α-Alumina L=0.6,ID=1.34,ε=0.73	Ethylene/He	T=45 P=1 F=19-200	D_a=0.0334,$D_i=8.9\times10^{-6}$ cm^2/s
Dogu (1984)	Alumina (0.5% Pt) L=0.6,ID=1.34, S_g=339, ε=0.74	Benzene (3%)/H_2	T=202 P=0.93-1.74 F_2=40-200	D_e=0.045-0.056 cm^2/s Pulse=0.2 cm^3
Dogu *et al.* (1986)	Activated soda L=3,1.3,ID=1.35,ε=0.56	N_2,CO_2,SO_2/He	T=202 P=0.93-1.74 F_2=40-200	V=0.5 cm^3 Pulse=5 cm^3 D_e=0.22 for CO_2, 0.23 cm^2/s for SO_2
Al-Rqobah *et al.* (1986)	Silica-alumina ε=0.64	He/N_2	T=20-305 P=1	D_e=0.02-0.05 cm^2/sec
Dogu *et al.*(1987)	Activated soda L=3,1.14,ID=1.35,S_g=5, ε=0.47,R_μ=42	N_2/He	T=200 P=1 F_1=300 F_2=80-400	D_a=0.15,$D_i=1.5\times10^{-6}$ cm^2/s

Appendix 2. Use of the transient method (continued.....).

Author	Pellet: L(cm), ID(cm), ε, R_μ, r_P(Å), S_g(cm^2/g)	Tracer/carrier	Conditions: T(°C), P(atm), F_1 and F_2(cm^3/min)	Remark
Biswas *et al.*(1987)	γ-Alumina L=0.5, 1, ID=0.95, ε=0.77, $r_{p,m}$=2000, $r_{p,\mu}$=18	He(10%)/N_2, Ethane(10%)/He	T=25-305 P=1 F=30-300	V_1=0.523,V_2=0.172 cm^3 Pulse=0.226 cm^3 τ=2.8
Al-Rqobah et al. (1988)	Silica-Alumina L=1.27, ID=1.27, S_g=381-427, ε=0.4-0.7, $r_{p,m}$=1900-4000, $r_{p,\mu}$=19-29	H_2 and He/N_2	T=22-277 P=1 F_2=40-66	τ=4.7-13.9
Dogu et al. (1989)	γ-Alumina L=1.3, ID=1.4, ε=0.68, 30<rp<10,000	He/N_2	T=45 P=1	D_e =00234
Dogu et al. (1993)	Soil L=0.29, ID=1.35, ε=0.49	Bezene/N_2	T=35-90 F_2=48-120	D_e=0.0177 cm2/s Pulse=0.5 μl of liquid benzene
Sun et al. (1994)	5A (RP5A) L=0.35, ID=0.16, ε=0.393, S_g=48,r_p=129	O_2,N_2,Ar (3.5-20 %)/He	T=70 F=7.6	D_a=0.0267, D_i=4.6×10-7 cm^2/s
Al-Bayaty, et al. (1994)	Chromia-alumina, silica-alumina, zeolites L=1.2, ID=1.27	He/N_2	T=25-300 F=250	At 25 °C, D_e= 1.86 $T^{1.31}$±0.032×10^5 for Silica-alumina, D_e= 4.97 $T^{1.12}$±0.028×10^5 for zeolite, D_e=2.04 $T^{1.21}$±0.049×10^5 for chromia-alumina

Appendix 3. Mercury porosimetry data for the cordierite monolith

```
SAMPLE DIRECTORY/NUMBER: KIM     /11
OPERATOR: S Kim                                  LP  11:49:38 07/15/98
SAMPLE ID: Cordierite                            HP  12:40:45 07/15/98
SUBMITTER: S Kim                                 REP 10:37:31 07/02/99

PENETROMETER NUMBER:07-0586          ADVANCING CONTACT ANGLE: 130.0deg
PENETROMETER CONSTANT:10.79 µL/pF    RECEDING CONTACT ANGLE:  130.0deg
PENETROMETER WEIGHT:63.1607 g        MERCURY SURFACE TENSION:485.0dyn/cm
STEM VOLUME:          0.3920 mL      MERCURY DENSITY:       13.5438 g/mL
MAXIMUM HEAD PRESSURE:4.4500 psia    SAMPLE WEIGHT:          1.0404 g
PENETROMETER VOLUME:   6.1812 mL     SAMPLE+PEN+Hg WEIGHT: 143.7671 g

   LOW PRESSURE:
          EVACUATION PRESSURE:           50 µmHg
          EVACUATION TIME:                5 min
          MERCURY FILLING PRESSURE:  3.9763 psia
          EQUILIBRATION TIME:             5 sec

   HIGH PRESSURE:
          EQUILIBRATION TIME:             5 sec

                        INTRUSION DATA SUMMARY
                 (FROM PRESSURE     0.00 TO 60000.00 psia )

                     TOTAL INTRUSION VOLUME =    0.0880 mL/g
                            TOTAL PORE AREA =     0.652 sq-m/g
               MEDIAN PORE DIAMETER (VOLUME) =    3.2953 µm
                MEDIAN PORE DIAMETER (AREA) =    0.0264 µm
               AVERAGE PORE DIAMETER (4V/A) =    0.5397 µm
                                 BULK DENSITY =    3.3946 g/mL
              APPARENT (SKELETAL) DENSITY =    4.8409 g/mL
                                    POROSITY =     29.88 %
                          STEM VOLUME USED =        23 %
```

PRESSURE psia	PORE DIAMETER µm	MEAN DIAMETER µm	CUMULATIVE VOLUME mL/g	INCREMENTAL VOLUME mL/g	DIFFEREN. VOL dV/dD mL/g-µm
3.98	45.4855	45.4855	0.0000	0.0000	4.332E-05
4.96	36.4798	40.9827	0.0004	0.0004	5.884E-05
5.96	30.3687	33.4243	0.0009	0.0004	7.982E-05
6.96	25.9872	28.1780	0.0013	0.0004	1.327E-04
7.95	22.7382	24.3627	0.0019	0.0006	1.532E-04
8.95	20.2040	21.4711	0.0022	0.0003	1.521E-04
9.95	18.1693	19.1866	0.0027	0.0005	1.810E-04
10.96	16.5044	17.3368	0.0027	0.0000	2.818E-04
11.95	15.1333	15.8189	0.0035	0.0008	4.043E-04
12.95	13.9708	14.5521	0.0039	0.0004	4.568E-04
13.94	12.9712	13.4710	0.0044	0.0005	4.920E-04
14.94	12.1050	12.5381	0.0047	0.0003	6.046E-04
15.94	11.3496	11.7273	0.0054	0.0006	7.435E-04
16.93	10.6850	11.0173	0.0059	0.0005	9.261E-04
17.92	10.0929	10.3890	0.0065	0.0006	1.026E-03
18.92	9.5598	9.8264	0.0071	0.0006	1.227E-03
19.92	9.0788	9.3193	0.0079	0.0008	1.532E-03
20.93	8.6431	8.8609	0.0081	0.0002	1.933E-03
21.90	8.2571	8.4501	0.0091	0.0010	2.335E-03
22.90	7.8968	8.0769	0.0105	0.0014	2.482E-03
23.91	7.5656	7.7312	0.0109	0.0004	2.481E-03
24.91	7.2616	7.4136	0.0128	0.0019	2.219E-03
26.55	6.8129	7.0373	0.0130	0.0003	1.539E-03
27.85	6.4953	6.6541	0.0133	0.0003	1.098E-03
29.08	6.2193	6.3573	0.0134	0.0001	7.857E-04
30.91	5.8515	6.0354	0.0137	0.0003	8.748E-04

32.18	5.6210	5.7363	0.0139	0.0001	1.078E-03
33.81	5.3494	5.4852	0.0143	0.0004	1.858E-03
35.67	5.0704	5.2099	0.0146	0.0003	3.901E-03
40.85	4.4275	4.7490	0.0195	0.0049	1.349E-02
43.06	4.1999	4.3137	0.0239	0.0044	1.733E-02
45.94	3.9370	4.0684	0.0293	0.0054	2.054E-02
50.99	3.5468	3.7419	0.0381	0.0088	2.218E-02
55.48	3.2602	3.4035	0.0448	0.0068	2.155E-02
61.79	2.9271	3.0937	0.0516	0.0068	1.939E-02
66.77	2.7087	2.8179	0.0557	0.0041	1.761E-02
71.63	2.5249	2.6168	0.0590	0.0034	1.645E-02
76.57	2.3621	2.4435	0.0614	0.0023	1.544E-02
81.09	2.2304	2.2963	0.0634	0.0021	1.495E-02
86.83	2.0829	2.1567	0.0655	0.0021	1.494E-02
91.02	1.9870	2.0350	0.0671	0.0016	1.491E-02
101.16	1.7879	1.8875	0.0701	0.0030	1.468E-02
112.20	1.6120	1.7000	0.0727	0.0026	1.391E-02
127.49	1.4186	1.5153	0.0753	0.0026	1.323E-02
150.69	1.2002	1.3094	0.0782	0.0029	1.209E-02
176.50	1.0247	1.1125	0.0801	0.0019	9.124E-03
201.94	0.8956	0.9602	0.0811	0.0010	6.513E-03
251.59	0.7189	0.8073	0.0821	0.0009	5.427E-03
302.30	0.5983	0.6586	0.0828	0.0007	6.087E-03
354.11	0.5108	0.5545	0.0833	0.0006	6.028E-03
501.98	0.3603	0.4355	0.0840	0.0007	3.407E-03
598.69	0.3021	0.3312	0.0842	0.0002	3.018E-03
701.19	0.2579	0.2800	0.0843	0.0001	2.375E-03
815.90	0.2217	0.2398	0.0844	0.0001	8.214E-04
903.94	0.2001	0.2109	0.0844	0.0000	8.450E-05
1010.30	0.1790	0.1896	0.0844	0.0000	0.000E+00
1254.66	0.1442	0.1616	0.0844	0.0000	7.830E-04
1508.98	0.1199	0.1320	0.0845	0.0001	1.040E-02
1752.21	0.1032	0.1115	0.0848	0.0003	1.470E-02
2011.83	0.0899	0.0966	0.0849	0.0001	1.352E-02
2510.83	0.0720	0.0810	0.0852	0.0003	1.216E-02
3007.75	0.0601	0.0661	0.0853	0.0001	2.179E-03
3504.97	0.0516	0.0559	0.0853	0.0000	9.299E-03
4506.29	0.0401	0.0459	0.0856	0.0003	4.005E-02
5506.29	0.0328	0.0365	0.0860	0.0004	7.686E-02
6492.73	0.0279	0.0304	0.0865	0.0005	9.386E-02
7481.73	0.0242	0.0260	0.0868	0.0003	9.442E-02
8997.06	0.0201	0.0221	0.0872	0.0004	7.795E-02
11954.45	0.0151	0.0176	0.0874	0.0001	1.130E-01
14956.17	0.0121	0.0136	0.0880	0.0006	1.045E-01
19955.22	0.0091	0.0106	0.0880	0.0000	0.000E+00
24906.05	0.0073	0.0082	0.0880	0.0000	0.000E+00
29872.31	0.0061	0.0067	0.0880	0.0000	0.000E+00
34933.07	0.0052	0.0056	0.0880	0.0000	0.000E+00
39822.25	0.0045	0.0049	0.0880	0.0000	0.000E+00
44805.93	0.0040	0.0043	0.0880	0.0000	0.000E+00
49816.63	0.0036	0.0038	0.0880	0.0000	0.000E+00
54771.42	0.0033	0.0035	0.0880	0.0000	0.000E+00
59705.13	0.0030	0.0032	0.0880	0.0000	0.000E+00

Appendix 4. Nitrogen adsorption experimental data for the alumin (BET surface area and BJH average pore diameter).

1. Sample: Alumina gel(Lab2) calcined at 450°C

Summary report

ASAP 2010 V2.00 D Unit 1 Serial # 180

Sample Id: Al Sol LAB2-1(Calc, @450,24Hr)
Operator Id: S KIM
Submitter Id: S KIM
File Name: C:\2000M\KIM\0000024.SMP

Started: 21/02/99 17:43:03 Analysis Adsorptive: N2
Completed: 22/02/99 09:18:01 Analysis Bath: 77.07 K
Report Time: 17/03/00 23:17:08 Thermal Correction: Yes
Sample Weight: 0.1020 g Smoothed Pressures: Yes
Warm Freespace: 28.3800 cm^3 Cold Freespace: 91.5081 cm^3
Equil. Interval: 10 secs Low Pressure Dose: 2.00 cm^3/g STP

Analysis Log

Relative Pressure	Pressure (mmHg)	Vol Adsorbed (cm^3/g STP)	Elapsed Time (HR:MN)	Saturation Press.(mmHg)
			02:14	736.00787
0.000001417	0.00104	2.0535	02:51	
0.000003234	0.00238	4.1072	03:19	
0.000007230	0.00532	6.1574	03:39	
0.000017158	0.01262	8.2040	03:58	
0.000029464	0.02167	10.2462	04:15	
0.000048374	0.03558	12.2806	04:30	
0.000076104	0.05597	14.3055	04:42	
0.000115397	0.08486	16.3166	04:53	
0.000169531	0.12466	18.3108	05:04	
0.000242484	0.17829	20.2830	05:12	
0.000339619	0.24970	22.2254	05:21	
0.000467384	0.34362	24.1326	05:28	
0.000632987	0.46535	25.9951	05:35	
0.000844415	0.62076	27.8031	05:42	
0.001108545	0.81490	29.5478	05:48	
0.001458449	1.07207	31.3339	05:56	
0.001892620	1.39116	33.0490	06:04	
0.002421939	1.78016	34.6847	06:11	
0.004232447	3.11071	38.4772	06:22	
			06:25	734.95465
0.008143159	5.98453	43.0386	06:30	
0.017532379	12.88369	48.7262	06:38	
0.021826694	16.03868	50.4631	06:42	
0.026536740	19.49887	52.0694	06:46	
0.032202657	23.66083	53.7317	06:51	
0.046289860	34.00953	57.2969	06:56	
0.062553018	45.95572	60.4407	07:01	
0.066356349	48.74832	61.0745	07:04	
0.070511928	51.79951	61.7988	07:07	
0.078258974	57.48816	63.0960	07:11	
0.093611229	68.76202	65.5203	07:16	
0.109527246	80.44963	67.8387	07:20	
0.125092530	91.87862	70.0161	07:24	
0.132982771	97.67071	71.1074	07:27	
			07:30	734.43750
0.140736140	103.35937	72.2409	07:34	
0.156231505	114.73666	74.3101	07:38	
0.171798055	126.16566	76.4511	07:42	
0.187379486	137.60504	78.6383	07:46	

0.195319533	143.43330	79.6766	07:49	
0.203190738	149.20988	80.7793	07:53	
0.218647190	160.55615	82.8971	07:57	
0.249290134	183.05215	87.3119	08:02	
0.281343626	206.58250	92.0707	08:07	
0.312645419	229.55948	97.0252	08:12	
0.372853023	273.75510	107.6473	08:19	
0.436977926	320.82098	121.2759	08:27	
0.499628813	366.79562	137.9086	08:37	
			08:39	734.12726
0.562407901	412.87360	158.6146	08:51	
0.623991902	458.07257	182.2087	09:13	
0.678791615	498.29132	202.8032	09:31	
0.687762683	504.87466	205.6504	09:35	
0.718624546	527.52582	214.1301	09:42	
			09:44	734.07550
0.751044877	551.31995	220.3538	09:50	
0.814446142	597.85828	224.7064	09:54	
0.847984963	622.47455	225.4115	09:59	
0.882299176	647.65973	225.5292	10:04	
0.916471978	672.74158	225.6865	10:08	
0.933545195	685.27197	225.7364	10:11	
0.950575556	697.77161	225.7828	10:13	
0.967626947	710.28662	225.8143	10:15	
0.984679599	722.80170	225.8809	10:18	
0.996244673	731.28284	233.0267	10:28	
0.961601116	705.84442	226.2131	10:39	
0.927690990	680.94879	226.3524	10:45	
			10:47	734.02380
0.893627680	655.97040	226.5047	10:53	
0.876652307	643.52252	226.5925	10:56	
0.859586158	631.00751	226.7674	10:59	
0.808185914	593.30731	226.9229	11:07	
0.739588713	542.98865	227.0467	11:18	
0.688159065	505.25732	227.0543	11:26	
0.619480796	454.86621	226.8572	11:37	
0.602354153	442.29953	226.7809	11:40	
0.585231958	429.73273	226.7100	11:42	
0.558094706	409.82248	226.4960	11:48	
			11:50	734.33411
0.520125310	381.99460	195.5697	12:13	
0.504573733	370.62253	171.4674	12:37	
0.495035810	363.64093	161.7669	12:49	
0.467962809	343.78244	143.5614	13:04	
			13:06	734.64441
0.437207786	321.23465	128.5235	13:18	
0.420353366	308.87479	122.9521	13:25	
0.404233359	297.05270	118.6368	13:32	
0.372437701	273.70859	111.6603	13:39	
0.341480910	250.97466	105.8168	13:45	
0.310380495	228.13216	100.4555	13:51	
0.279181694	205.21207	95.4923	13:56	
0.248173569	182.43163	90.8439	14:02	
0.186962651	137.44473	82.2828	14:08	
			14:10	735.16156
0.124396801	91.46490	73.6981	14:19	
0.108775498	79.98418	71.5741	14:23	
0.093296825	68.60688	69.3349	14:27	
0.061994821	45.59370	64.2508	14:34	
0.046458588	34.16986	61.2682	14:38	
0.030908298	22.73567	57.4711	14:46	
0.023868522	17.55900	55.2248	14:52	
0.019234658	14.15098	53.5557	14:56	
0.015437828	11.35837	51.7769	15:00	
0.011640741	8.56576	49.6421	15:08	
0.009601857	7.06603	48.2099	15:13	
			15:16	735.93726
0.008055436	5.92830	46.9609	15:19	
0.005877037	4.32513	44.7703	15:26	
0.004049993	2.98054	42.0695	15:37	

BJH Desorption Pore Distribution Report

t = [13.9900 / (0.0340 - log(P/Po))] 0.5000

Diameter Range: 1.0000 to 500.0000 nm
Adsorbate Property Factor: 0.953000 nm
Density Conversion Factor: 0.001547
Fraction of Pores Open at Both Ends: 0.000

Pore Diameter Range (nm)	Average Diameter (nm)	Incremental Pore Volume (cm^3/g)	Cumulative Pore Volume (cm^3/g)	Incremental Pore Area (m^2/g)	Cumulative Pore Area (m^2/g)
51.8- 4.1	4.3	0.090343	0.090343	84.110	84.110
4.1- 3.9	4.0	0.071947	0.162290	71.613	155.723
3.9- 3.9	3.9	0.028215	0.190505	28.960	184.683
3.9- 3.6	3.7	0.050730	0.241234	54.533	239.216
3.6- 3.4	3.5	0.039279	0.280513	45.273	284.489
3.4- 3.2	3.3	0.012664	0.293178	15.414	299.903
3.2- 3.1	3.2	0.008735	0.301913	11.047	310.950
3.1- 2.9	3.0	0.012104	0.314017	16.208	327.158
2.9- 2.7	2.8	0.008527	0.322544	12.270	339.428
2.7- 2.5	2.6	0.006751	0.329295	10.435	349.862
2.5- 2.3	2.4	0.005191	0.334486	8.625	358.487
2.3- 2.2	2.2	0.003940	0.338426	7.046	365.533
2.2- 1.9	2.0	0.004527	0.342954	9.152	374.685
1.9- 1.5	1.7	0.001012	0.343966	2.431	377.116

Summary Report

Area

Single Point Surface Area at P/Po 0.17179806 :	275.6314	m^2/g
BET Surface Area:	285.2609	m^2/g
BJH Adsorption Cumulative Surface Area of pores between 1.000000 and 500.000000 nm Diameter:	322.5918	m^2/g
BJH Desorption Cumulative Surface Area of pores between 1.000000 and 500.000000 nm Diameter:	377.1159	m^2/g

Volume

Single Point Total Pore Volume of pores less than 510.5549 nm Diameter at P/Po 0.99624467:	0.360446 cm^3/g
BJH Adsorption Cumulative Pore Volume of pores between 1.000000 and 500.000000 nm Diameter:	0.323220 cm^3/g
BJH Desorption Cumulative Pore Volume of pores between 1.000000 and 500.000000 nm Diameter:	0.343966 cm^3/g

Pore Size

Average Pore Diameter (4V/A by BET):	5.0543	nm
BJH Adsorption Average Pore Diameter (4V/A):	4.0078	nm
BJH Desorption Average Pore Diameter (4V/A):	3.6484	nm

2. Sample: Alumina gel(Lab2) calcined at 600°C

Summary report

ASAP 2010 V2.00 D Unit 1 Serial # 180

Sample Id Al Sol Lab2(calc. 600C,16hrs)
Operator Id: S KIM
Submitter Id: S KIM
File Name: C:\2000M\KIM\0000028.SMP

Started: 25/02/99 11:05:12 Analysis Adsorptive: N2
Completed: 26/02/99 01:22:18 Analysis Bath: 77.20 K
Report Time: 17/03/00 23:19:11 Thermal Correction: Yes
Sample Weight: 0.1170 g Smoothed Pressures: Yes
Warm Freespace: 28.2727 cm^3 Cold Freespace: 90.8570 cm^3
Equil. Interval: 10 secs Low Pressure Dose: 3.00 cm^3/g STP

Analysis Log

Relative Pressure	Pressure (mmHg)	Vol Adsorbed (cm^3/g STP)	Elapsed Time (HR:MN)	Saturation Press.(mmHg)
0.001159700	0.86560	23.5730	03:54	
0.002102819	1.56942	26.3946	04:17	
0.004186814	3.12460	30.4352	04:33	
			04:36	746.28827
0.008573323	6.39811	34.9262	04:45	
0.017857143	13.32629	39.8068	04:56	
0.022422801	16.73344	41.4068	05:00	
0.027307729	20.37881	42.8468	05:05	
0.032722019	24.41920	44.2417	05:09	
0.046346417	34.58639	47.3231	05:14	
0.062701359	46.79114	50.0102	05:19	
0.066305211	49.48032	50.5958	05:23	
0.070595100	52.68148	51.1468	05:26	
0.078218424	58.37013	52.1962	05:30	
0.093679725	69.90775	54.1473	05:34	
0.109480842	81.69878	56.0282	05:39	
			05:41	746.23651
0.125106878	93.35534	57.7993	05:46	
0.132913919	99.17845	58.7002	05:49	
0.140749058	105.02223	59.5096	05:52	
0.156209983	116.55468	61.1638	05:56	
0.171963083	128.30434	62.8375	06:00	
0.187689536	140.03331	64.4305	06:04	
0.195527080	145.87709	65.2529	06:07	
0.203365086	151.72092	66.0710	06:10	
0.218754241	163.19646	67.6504	06:14	
0.249480820	186.11136	70.9757	06:19	
0.281721369	210.15367	74.4753	06:24	
0.312938575	233.43059	78.1941	06:29	
0.373416206	278.52609	86.0334	06:36	
0.437156689	326.04700	95.9036	06:44	
			06:46	745.82281
0.499488066	372.54395	108.3741	06:56	
0.561678105	418.94785	124.8493	07:08	
0.623677289	465.21725	147.3161	07:22	
0.673361834	502.32275	171.4545	07:45	
0.690691201	515.27216	180.7627	07:56	
			07:58	746.02966
0.719825219	537.04938	195.8030	08:11	
0.751373622	560.62103	209.1924	08:22	
0.819394300	611.40009	221.6541	08:30	
0.861886632	643.11682	222.8837	08:33	
0.893667993	666.83856	223.3815	08:35	
0.925004831	690.22913	223.7212	08:37	
0.956245908	713.55267	224.0076	08:40	
0.987484270	736.87091	224.2567	08:42	
0.996856132	743.90930	240.4199	08:53	

0.958608088	715.37830	224.6459	08:56	
0.912701764	681.12738	224.7300	08:58	
			09:01	746.28827
0.880863236	657.39014	224.6548	09:03	
0.849033132	633.65295	224.6823	09:06	
0.786917756	587.31122	224.6211	09:09	
0.724888851	541.03143	224.4195	09:12	
0.662938883	494.80338	224.1336	09:14	
0.603638870	450.57666	220.7295	09:22	
0.594376068	443.72452	210.8550	09:37	
0.575932559	430.07175	175.8575	10:06	
			10:08	746.75366
0.561831953	419.60455	156.8075	10:32	
0.532285664	397.58951	133.6026	10:56	
0.501537751	374.64877	119.7311	11:09	
			11:12	747.01227
0.470332764	351.28906	109.7743	11:22	
0.435705235	325.37985	101.6345	11:31	
0.420717737	314.15768	98.5477	11:37	
0.403372523	301.17725	95.5605	11:43	
0.372862815	278.37094	90.7718	11:49	
0.341446724	254.89232	86.3118	11:55	
0.310509688	231.77571	82.2867	12:01	
0.279428215	208.55566	78.6605	12:07	
0.248683470	185.59422	75.1943	12:12	
			12:18	746.23651
0.187319491	139.76439	68.7115	12:24	
0.124700163	93.02435	62.0770	12:32	
0.108766036	81.12991	60.3618	12:36	
0.093385778	69.64917	58.5425	12:41	
0.062124133	46.32571	54.4368	12:48	
0.046456345	34.63812	51.8601	12:53	
0.030960432	23.07981	48.6113	13:01	
0.023852573	17.77903	46.6616	13:06	
0.019344643	14.41755	45.1775	13:10	
0.015391002	11.46980	43.6076	13:14	
			13:24	745.04712
0.011715903	8.72890	41.7989	13:26	
0.009633554	7.17745	40.5589	13:30	
0.008037084	5.98801	39.4156	13:34	
0.005815908	4.33313	37.4747	13:42	
0.003941792	2.93682	35.1218	13:52	
0.001998263	1.48880	31.1391	14:19	

BJH Desorption Pore Distribution Report

t = [13.9900 / (0.0340 - log(P/Po))] 0.5000

Diameter Range: 1.0000 to 500.0000 nm
Adsorbate Property Factor: 0.953000 nm
Density Conversion Factor: 0.001547
Fraction of Pores Open at Both Ends: 0.000

Pore Diameter Range (nm)	Average Diameter (nm)	Incremental Pore Volume (cm^3/g)	Cumulative Pore Volume (cm^3/g)	Incremental Pore Area (m^2/g)	Cumulative Pore Area (m^2/g)
48.2- 9.8	11.0	0.000055	0.000055	0.020	0.020
9.8- 7.5	8.3	0.000474	0.000529	0.228	0.248
7.5- 6.1	6.6	0.000689	0.001218	0.416	0.664
6.1- 5.1	5.5	0.008943	0.010161	6.550	7.215
5.1- 4.9	5.0	0.027315	0.037476	21.880	29.095
4.9- 4.7	4.8	0.097070	0.134546	80.901	109.996
4.7- 4.5	4.6	0.051986	0.186532	45.288	155.284
4.5- 4.2	4.3	0.060573	0.247104	56.036	211.319
4.2- 3.9	4.0	0.032556	0.279660	32.564	243.883
3.9- 3.6	3.7	0.020635	0.300296	22.306	266.189
3.6- 3.3	3.4	0.014060	0.314356	16.477	282.666
3.3- 3.2	3.2	0.004749	0.319105	5.892	288.559
3.2- 3.0	3.1	0.003670	0.322774	4.732	293.291

3.0-	2.8	2.9	0.005078	0.327852	6.938	300.229
2.8-	2.6	2.7	0.003802	0.331654	5.587	305.815
2.6-	2.4	2.5	0.002586	0.334240	4.090	309.905
2.4-	2.3	2.3	0.001185	0.335426	2.018	311.923
2.3-	2.1	2.2	0.000716	0.336141	1.313	313.236

Summary Report

Area

Single Point Surface Area at P/Po 0.17196308 :	226.5048	m^2/g
BET Surface Area:	235.0540	m^2/g
BJH Adsorption Cumulative Surface Area of pores between 1.000000 and 500.000000 nm Diameter:	269.2365	m^2/g
BJH Desorption Cumulative Surface Area of pores between 1.000000 and 500.000000 nm Diameter:	313.2361	m^2/g

Volume

Single Point Total Pore Volume of pores less than 609.2838 nm Diameter at P/Po 0.99685613:	0.371882	cm^3/g
BJH Adsorption Cumulative Pore Volume of pores between 1.000000 and 500.000000 nm Diameter:	0.351293	cm^3/g
BJH Desorption Cumulative Pore Volume of pores between 1.000000 and 500.000000 nm Diameter:	0.336141	cm^3/g

Pore Size

Average Pore Diameter (4V/A by BET):	6.3284	nm
BJH Adsorption Average Pore Diameter (4V/A):	5.2191	nm
BJH Desorption Average Pore Diameter (4V/A):	4.2925	nm

3. Sample: Alumina gel(Lab2) calcined at 800°C

Surface Area Reports

ASAP 2010 V2.00 D Unit 1 Serial # 180

Sample Id: Al Sol lab2(cal. 800C,4hrs)
Operator Id: S KIM
Submitter Id: S KIM
File Name: C:\2000M\KIM\0000025.SMP

Started: 22/02/99 10:40:18
Completed: 23/02/99 02:25:02
Report Time: 11/07/80 11:59:54
Sample Weight: 0.1184 g
Warm Freespace: 28.5838 cm³
Equil. Interval: 10 secs
Analysis Adsorptive: N2
Analysis Bath: 77.14 K
Thermal Correction: Yes
Smoothed Pressures: Yes
Cold Freespace: 89.9419 cm³
Low Pressure Dose: 2.00 cm³/g STP

Analysis Log

Relative Pressure	Pressure (mmHg)	Vol Adsorbed (cm³/g STP)	Elapsed Time (HR:MN)	Saturation Press.(mmHg)
			05:22	740.30023
0.000004645	0.00344	2.0452	05:51	
0.000019246	0.01425	4.0799	06:05	
0.000053320	0.03948	6.0977	06:18	
0.000127266	0.09424	8.0884	06:27	
0.000228862	0.16947	10.0423	06:35	
0.000380184	0.28153	11.9458	06:41	
0.000596796	0.44195	13.7844	06:47	
0.000912423	0.67570	15.6278	06:56	
0.001342298	0.99408	17.3899	07:04	
0.001906577	1.41201	19.0533	07:11	
0.002620547	1.94083	20.6074	07:18	
0.004124567	3.05484	22.8957	07:28	
			07:30	740.65143
0.008320686	6.16289	26.5598	07:35	
0.018077831	13.39038	30.8892	07:44	
0.022525300	16.68501	32.1797	07:48	
0.027292361	20.21651	33.3262	07:52	
0.032437307	24.02809	34.3961	07:56	
0.046410608	34.37962	36.9178	08:00	
0.062675911	46.42923	39.0272	08:03	
0.066374850	49.17013	39.4614	08:06	
0.070492131	52.22131	39.9606	08:10	
0.078309441	58.01339	40.7541	08:13	
0.093658611	69.38552	42.2812	08:16	
0.109509886	81.13000	43.7438	08:19	
0.125073806	92.66246	45.1083	08:23	
0.132959474	98.50624	45.7806	08:26	
0.140761148	104.28798	46.3803	08:29	
0.156247581	115.76353	47.6143	08:32	
			08:35	740.90997
0.171967965	127.41493	48.8620	08:38	
0.187669359	139.05080	50.1309	08:41	
0.195539171	144.88426	50.7369	08:44	
0.203326087	150.65565	51.3665	08:46	
0.218719161	162.06398	52.6142	08:49	
0.249701962	185.02542	55.0601	08:53	
0.281590717	208.65921	57.7057	08:57	
0.312919652	231.87923	60.3999	09:01	
0.373688488	276.91785	66.0329	09:06	
0.437112609	323.92673	72.9000	09:11	
0.499418195	370.11349	81.3624	09:18	
0.561851299	416.39841	92.3596	09:25	
0.623292058	461.95929	107.7908	09:35	
			09:37	741.16858
0.684907071	507.62360	131.3299	09:51	
0.720510549	534.00354	150.5229	10:04	

0.751077605	556.64941	170.9777	10:18	
0.788007209	584.00671	195.4554	10:37	
			10:39	741.11682
0.816234124	604.99780	207.4489	10:49	
0.843899618	625.53381	212.0971	10:53	
0.892844598	661.83783	213.7131	10:56	
0.924993817	685.69385	214.1811	10:59	
0.956301414	708.91913	214.4985	11:01	
0.987572592	732.11853	214.7215	11:03	
0.998671506	740.44470	228.4533	11:14	
0.956507380	709.20862	215.0551	11:17	
0.912488591	676.58691	215.0401	11:19	
0.880568785	652.94281	214.9341	11:22	
0.848525683	629.20557	214.8693	11:25	
0.786427698	583.17926	214.7013	11:28	
0.724552072	537.30804	214.3528	11:30	
0.681932095	505.72052	214.0018	11:33	
0.652300615	483.89160	177.8608	11:58	
			12:00	741.84088
0.637987058	473.28488	150.8849	12:25	
0.623068701	462.21783	133.1819	12:45	
0.607592724	450.73712	121.1366	12:58	
0.591349940	438.68756	112.0011	13:08	
			13:11	741.84088
0.558875385	414.58835	99.8131	13:20	
0.498375414	369.69971	85.7675	13:30	
0.452090872	335.36093	78.5134	13:36	
0.418354092	310.33087	74.2238	13:42	
0.403995177	299.67758	72.5402	13:45	
0.372208374	276.09555	69.2477	13:50	
0.341465870	253.28923	66.2802	13:54	
0.310305219	230.17264	63.4698	13:59	
0.279282052	207.15945	60.8966	14:02	
0.248454225	184.29106	58.3738	14:06	
0.187046787	138.74052	53.5988	14:11	
			14:14	741.73743
0.124117917	92.06772	48.6076	14:20	
0.108686532	80.62319	47.3369	14:23	
0.093207153	69.14246	45.9697	14:26	
0.061957495	45.96380	42.6633	14:33	
0.046410163	34.43135	40.6456	14:38	
0.030933618	22.95062	38.0672	14:44	
0.023474556	17.41712	36.3753	14:48	
0.019292004	14.31422	35.2828	14:51	
0.015667114	11.62504	34.0656	14:55	
0.011484620	8.52214	32.3846	15:02	
0.009463296	7.02240	31.3778	15:05	
0.007790455	5.78124	30.3152	15:09	
0.005699514	4.22979	28.7234	15:15	
			15:18	742.15112
0.003741285	2.77660	26.5476	15:27	
0.002041030	1.51475	23.6999	15:46	

BJH Desorption Pore Distribution Report

t = [13.9900 / (0.0340 - log(P/Po))] 0.5000

Diameter Range: 1.0000 to 500.0000 nm
Adsorbate Property Factor: 0.953000 nm
Density Conversion Factor: 0.001547
Fraction of Pores Open at Both Ends: 0.000

Pore Diameter Range (nm)	Average Diameter (nm)	Incremental Pore Volume (cm^3/g)	Cumulative Pore Volume (cm^3/g)	Incremental Pore Area (m^2/g)	Cumulative Pore Area (m^2/g)
45.9- 23.3	27.7	0.000028	0.000028	0.004	0.004
23.3- 17.2	19.3	0.000210	0.000238	0.043	0.047
17.2- 13.7	15.0	0.000129	0.000367	0.034	0.082
13.7- 9.7	11.0	0.000354	0.000721	0.129	0.211

9.7-	7.5	8.3	0.000786	0.001507	0.380	0.591
7.5-	6.4	6.8	0.000818	0.002325	0.478	1.069
6.4-	5.8	6.1	0.092447	0.094772	60.830	61.899
5.8-	5.6	5.7	0.069396	0.164168	48.862	110.760
5.6-	5.3	5.4	0.044485	0.208653	32.764	143.524
5.3-	5.1	5.2	0.029076	0.237730	22.411	165.935
5.1-	4.8	5.0	0.020960	0.258690	16.919	182.854
4.8-	4.4	4.6	0.025312	0.284002	21.929	204.782
4.4-	3.8	4.1	0.023499	0.307501	23.205	227.988
3.8-	3.4	3.6	0.008287	0.315788	9.332	237.319
3.4-	3.1	3.2	0.003359	0.319147	4.161	241.480
3.1-	3.0	3.1	0.001072	0.320219	1.404	242.884
3.0-	2.8	2.9	0.001176	0.321394	1.630	244.514
2.8-	2.6	2.7	0.000632	0.322026	0.944	245.458
2.6-	2.4	2.5	0.000141	0.322167	0.226	245.684

Summary Report

Area

Single Point Surface Area at P/Po 0.17196797 :	176.1275	m^2/g
BET Surface Area:	183.0491	m^2/g
BJH Adsorption Cumulative Surface Area of pores between 1.000000 and 500.000000 nm Diameter:	203.3301	m^2/g
BJH Desorption Cumulative Surface Area of pores between 1.000000 and 500.000000 nm Diameter:	245.6842	m^2/g

Volume

Single Point Total Pore Volume of pores less than 1437.7774 nm Diameter at P/Po 0.99867151:	0.353372	cm^3/g
BJH Adsorption Cumulative Pore Volume of pores between 1.000000 and 500.000000 nm Diameter:	0.328153	cm^3/g
BJH Desorption Cumulative Pore Volume of pores between 1.000000 and 500.000000 nm Diameter:	0.322167	cm^3/g

Pore Size

Average Pore Diameter (4V/A by BET):	7.7219	nm
BJH Adsorption Average Pore Diameter (4V/A):	6.4556	nm
BJH Desorption Average Pore Diameter (4V/A):	5.2452	nm

4. Sample: Alumina gel(Lab2) calcined at 1000°C

Summary report

ASAP 2010 V2.00 D Unit 1 Serial # 180

Sample Id: Al Sol Lab2(calc 1000C,4hrs)
Operator Id: S Kim
Submitter Id: S Kim
File Name: C:\2000M\KIM\0000026.SMP

Started: 23/02/99 11:57:16
Completed: 24/02/99 04:03:16
Report Time: 17/03/00 23:17:48
Sample Weight: 0.1165 g
Warm Freespace: 28.3474 cm³
Equil. Interval: 10 secs
Analysis Adsorptive: N2
Analysis Bath: 77.15 K
Thermal Correction: Yes
Smoothed Pressures: Yes
Cold Freespace: 90.9664 cm³
Low Pressure Dose: 1.00 cm³/g STP

Analysis Log

Relative Pressure	Pressure (mmHg)	Vol Adsorbed (cm³/g STP)	Elapsed Time (HR:MN)	Saturation Press.(mmHg)
			03:16	745.05804
0.000004963	0.00370	1.0366	03:37	
0.000018491	0.01378	2.0650	03:47	
0.000049166	0.03663	3.0756	03:56	
0.000130596	0.09731	4.0574	04:03	
0.000231610	0.17257	5.0006	04:09	
0.000378628	0.28212	5.8972	04:15	
0.000577103	0.43001	6.7401	04:20	
0.000830397	0.61875	7.5255	04:26	
0.001139717	0.84923	8.2518	04:31	
0.002143332	1.59707	9.8260	04:40	
0.004070513	3.03312	11.5741	04:49	
			04:51	745.14581
0.009016445	6.71799	13.8338	04:58	
0.018864815	14.05461	15.8942	05:05	
0.023570108	17.55949	16.5203	05:08	
0.028032721	20.88332	17.0199	05:11	
0.032837685	24.46193	17.4946	05:14	
0.046701267	34.78854	18.6943	05:16	
0.062601665	46.63129	19.6758	05:19	
0.066533664	49.55836	19.9045	05:22	
0.070590064	52.57852	20.1370	05:24	
0.078369208	58.37060	20.5597	05:27	
0.093994007	70.00647	21.2499	05:29	
0.109690365	81.69405	21.9216	05:32	
0.125386349	93.38165	22.5010	05:34	
0.133112920	99.13235	22.8459	05:37	
0.140949442	104.96581	23.1240	05:39	
0.156578098	116.60168	23.6811	05:41	
0.172279122	128.28929	24.2516	05:44	
0.187978969	139.97688	24.7816	05:46	
0.195831575	145.82066	25.0230	05:48	
0.203617669	151.61276	25.2636	05:51	
			05:53	744.57697
0.218980419	163.04175	25.8116	05:56	
0.250106901	186.21007	26.8570	05:59	
0.281791400	209.79211	27.9796	06:02	
0.313057613	233.06389	29.0670	06:04	
0.374830472	279.03854	31.3155	06:08	
0.437715492	325.84058	33.7752	06:11	
0.499979957	372.17722	36.7425	06:14	
0.562742413	418.87595	40.3970	06:18	
0.624823835	465.05743	45.4030	06:23	
			06:55	744.00806
0.662100140	492.56979	50.2522	07:02	
0.689658073	513.04889	53.2602	07:06	
0.717156980	533.47638	57.9489	07:11	

0.732875168	545.06049	62.9000	07:29	
0.744614521	553.74860	64.9911	07:36	
0.798892123	594.03461	83.8583	07:48	
			07:58	743.49091
0.805375704	598.74585	90.4968	08:03	
0.809496532	601.79187	91.4932	08:05	
0.833904667	619.81970	106.2632	08:18	
0.838331942	623.04675	110.8093	08:25	
0.844287800	627.39075	116.4132	08:34	
0.850687766	632.04510	122.8288	08:45	
0.857989181	637.37689	129.0056	08:55	
			09:00	742.81866
0.864207210	641.87103	134.3342	09:07	
0.870967210	646.83557	136.9391	09:12	
0.879267522	652.88623	142.3322	09:22	
0.900997678	668.78864	146.2067	09:42	
0.934472494	693.43079	146.7193	09:59	
			10:04	741.99121
0.949235205	704.28583	146.9087	10:09	
0.968988755	718.92633	147.0715	10:11	
0.973892795	722.54120	147.1271	10:14	
0.984666396	730.51038	147.2428	10:17	
0.992356011	736.19916	147.3996	10:19	
0.995671095	738.57806	148.4403	10:29	
0.969062530	718.66785	147.4286	10:51	
			11:08	741.47406
0.935804824	693.84467	147.5516	11:14	
0.900027837	667.28894	147.6485	11:20	
0.884191440	655.52380	147.7039	11:25	
0.868325311	643.73279	147.7080	11:31	
0.806066645	597.55121	147.7945	11:37	
0.753151571	558.26331	137.4124	11:52	
0.750884457	556.54633	132.4531	12:01	
0.748642044	554.83978	124.9472	12:12	
			12:15	741.11206
0.747386020	553.73309	118.9520	12:23	
0.745321919	551.93854	111.1835	12:36	
0.742439475	549.58038	104.1332	12:47	
0.739079394	546.87054	97.5806	12:58	
0.734885126	543.56586	91.6385	13:08	
0.730394209	540.04413	85.9358	13:18	
			13:23	739.25031
0.727262308	537.46362	80.4704	13:33	
0.719887378	531.80072	75.1541	13:46	
0.711304864	525.20197	69.6824	14:02	
0.700982334	517.34125	64.7785	14:17	
0.682700457	503.74020	60.2905	14:24	
			14:29	737.75055
0.629370985	464.74191	49.3214	14:37	
0.620621876	458.43784	47.9764	14:40	
0.603852653	446.25381	46.0686	14:44	
0.588438527	435.01096	44.5588	14:47	
0.556915501	411.89435	41.9187	14:51	
0.494542892	365.97141	38.1305	14:56	
0.464544506	343.88913	36.7284	14:59	
0.432890420	320.56564	35.4109	15:02	
0.417126178	308.99701	34.8215	15:05	
0.401585653	297.55246	34.2397	15:07	
0.370609671	274.69443	33.1941	15:10	
0.339585029	251.78470	32.2261	15:13	
0.308581500	228.87498	31.3189	15:16	
0.277668696	206.01695	30.4668	15:19	
0.246846525	183.21060	29.6199	15:22	
0.185265287	137.55144	28.0347	15:25	
0.123266254	91.57164	26.1856	15:30	
			15:33	743.12891
0.107670860	80.01333	25.6959	15:35	
0.093161160	69.23075	25.2465	15:37	
0.061984422	46.06242	23.9080	15:43	
0.046535253	34.58169	23.0509	15:46	
0.031086079	23.10096	21.9510	15:51	
0.023013531	17.10202	21.0953	15:55	

0.019325214	14.36112	20.6167	15:58
0.015567304	11.56851	20.0777	16:01
0.011878990	8.82762	19.3187	16:04
0.009325004	6.92968	18.7182	16:08

BJH Desorption Pore Distribution Report

t = [13.9900 / (0.0340 - log(P/Po))] 0.5000

Diameter Range: 1.0000 to 500.0000 nm
Adsorbate Property Factor: 0.953000 nm
Density Conversion Factor: 0.001547
Fraction of Pores Open at Both Ends: 0.000

Pore Diameter Range (nm)	Average Diameter (nm)	Incremental Pore Volume (cm^3/g)	Cumulative Pore Volume (cm^3/g)	Incremental Pore Area (m^2/g)	Cumulative Pore Area (m^2/g)
63.8- 8.4	9.1	0.023112	0.023112	10.164	10.164
8.4- 8.3	8.3	0.011844	0.034957	5.686	15.850
8.3- 8.2	8.3	0.017967	0.052924	8.706	24.556
8.2- 8.2	8.2	0.014379	0.067302	7.017	31.573
8.2- 8.1	8.1	0.018603	0.085905	9.141	40.714
8.1- 8.0	8.1	0.016796	0.102701	8.337	49.051
8.0- 7.9	8.0	0.015542	0.118243	7.812	56.863
7.9- 7.8	7.8	0.013962	0.132205	7.124	63.987
7.8- 7.6	7.7	0.013343	0.145548	6.926	70.913
7.6- 7.5	7.6	0.012959	0.158507	6.826	77.739
7.5- 7.3	7.4	0.011943	0.170451	6.420	84.159
7.3- 7.1	7.2	0.012154	0.182604	6.732	90.891
7.1- 6.9	7.0	0.010468	0.193072	6.003	96.894
6.9- 6.4	6.6	0.008076	0.201148	4.876	101.770
6.4- 5.4	5.8	0.019031	0.220179	13.056	114.826
5.4- 5.3	5.3	0.001991	0.222169	1.489	116.315
5.3- 5.0	5.1	0.002090	0.224259	1.624	117.939
5.0- 4.8	4.9	0.001347	0.225606	1.097	119.035
4.8- 4.4	4.6	0.001782	0.227388	1.553	120.588
4.4- 3.8	4.0	0.000382	0.227771	0.380	120.968
3.8- 1.0	1.0	0.000129	0.227900	0.496	121.464
1.0- 1.0	1.0	0.000054	0.227954	0.215	121.680

Summary Report

Area

Single Point Surface Area at P/Po 0.17227912 :	87.3842	m^2/g
BET Surface Area:	90.5404	m^2/g
BJH Adsorption Cumulative Surface Area of pores between 1.000000 and 500.000000 nm Diameter:	90.5150	m^2/g
BJH Desorption Cumulative Surface Area of pores between 1.000000 and 500.000000 nm Diameter:	121.6796	m^2/g

Volume

Single Point Total Pore Volume of pores less than 443.2914 nm Diameter at P/Po 0.99567110:	0.229608	cm^3/g
BJH Adsorption Cumulative Pore Volume of pores between 1.000000 and 500.000000 nm Diameter:	0.214956	cm^3/g
BJH Desorption Cumulative Pore Volume of pores between 1.000000 and 500.000000 nm Diameter:	0.227954	cm^3/g

Pore Size

Average Pore Diameter (4V/A by BET):	10.1439	nm
BJH Adsorption Average Pore Diameter (4V/A):	9.4993	nm
BJH Desorption Average Pore Diameter (4V/A):	7.4936	nm

Appendix 5. Measurement of apparent density

1. Method

The density of the specimens is measured by helium displacement using a pycnometer (*AccuPyc 1330, Micrometrics Instrument Co.*). Pycnometer measures the volume of solids of irregular shape by gas displacement whether powdered or in one piece. A general diagram of the instrument is shown in Figure A5.1. It was assumed that both the cell volume (V_{CELL}) and the expansion volume (V_{EXP}) are at ambient pressure (P_a) and at ambient temperature (T_a). After the valve is closed, V_{CELL} is changed to an elevated pressure. The working equation is:

$$V_{sam} = V_{CELL} - \frac{V_{EXP}}{\frac{p_{1g}}{p_{2g}} - 1}$$

where $p_{1g} = p_1 - p_a$

$p_{2g} = p_2 - p_a$

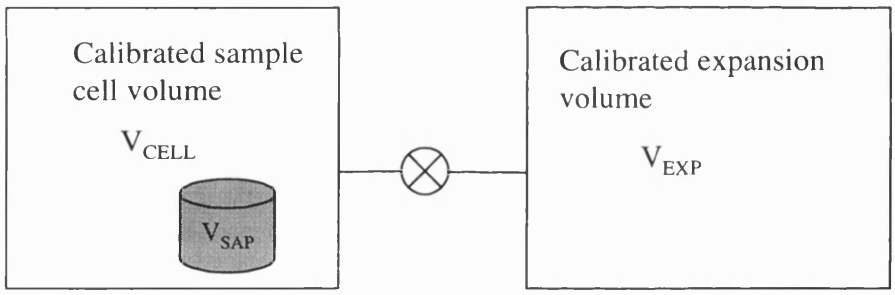

Figure A5.1. Schemcatic diagram of pycnometer

2. Results

1. Sample: Cordierite substrate
   - Sample weight: 1.656 g
   - Apparent density : 2.48 ± 1.2 g/cm^3

Run	Density (g/cm^3)	Run	Density (g/cm^3)
1	2.503	6	2.476
2	2.492	7	2.472
3	2.487	8	2.462
4	2.475	9	2.469
5	2.472	10	2.464

2. Sample: Alumina gel

A. Calcination temperature: 450 °C

- Sample weight: 0.4516 g
- Apparent density : 3.41 ± 0.06 g/cm^3

Run	Density (g/cm^3)	Run	Density (g/cm^3)
1	3.279	6	3.451
2	3.353	7	3.415
3	3.404	8	3.436
4	3.407	9	3.479
5	3.421	10	3.481

B. Calcination temperature: 600 °C

- Sample weight: 0.4932 g
- Apparent density : 3.93 ± 0.06 g/cm^3

Run	Density (g/cm^3)	Run	Density (g/cm^3)
1	4.052	6	3.889
2	3.914	7	3.906
3	3.965	8	3.876
4	3.988	9	3.919
5	3.869	10	3.873

C. Calcination temperature: 800 °C

- Sample weight: 0.3728 g
- Apparent density : 4.24 ± 0.07 g/cm^3

Run	Density (g/cm^3)	Run	Density (g/cm^3)
1	4.306	6	4.263
2	4.327	7	4.136
3	4.327	8	4.184
4	4.248	9	4.172
5	4.278	10	4.157

D. Calcination temperature: 1000 °C

- Sample weight: 0.7048 g
- Apparent density : 4.27 ± 0.03 g/cm^3

Run	Density (g/cm^3)	Run	Density (g/cm^3)
1	4.310	6	4.289
2	4.304	7	4.257
3	4.304	8	4.238
4	4.273	9	4.23
5	4.298	10	4.217

E. Calcination temperature: 1100 °C

- Sample weight: 0.5506 g
- Apparent density : 3.84 ± 0.16 g/cm^3

Run	Density (g/cm^3)	Run	Density (g/cm^3)
1	4.146	6	3.781
2	4.071	7	3.776
3	3.899	8	3.682
4	3.899	9	3.675
5	3.841	10	3.668

F. Calcination temperature: 1200 °C

- Sample weight: 0.3049 g
- Apparent density : 3.89 ± 0.36 g/cm^3

Run	Density (g/cm^3)	Run	Density (g/cm^3)
1	4.546	6	3.727
2	4.360	7	3.669
3	4.138	8	3.582
4	3.998	9	3.492
5	3.887	10	3.527